AWARD NUMBER: W81XWH-16-1-0039
BC150580

TITLE: Transient Nuclear Envelope Rupture during Cell Migration: A Cause of Genomic Instability and a Novel Opportunity for Therapeutic Intervention

PRINCIPAL INVESTIGATOR: Jan Lammerding

CONTRACTING ORGANIZATION: Cornell University
Ithaca, NY 14853-7202

REPORT DATE: MARCH 2019

TYPE OF REPORT: Annual Report

PREPARED FOR: U.S. Army Medical Research and Materiel Command
Fort Detrick, Maryland 21702-5012

REPORT DOCUMENTATION PAGE

Form Approved
OMB No. 0704-0188

1. REPORT DATE	2. REPORT TYPE	3. DATES COVERED
MARCH, 2019	ANNUAL	2/15/2018-2/14/2019

4. TITLE AND SUBTITLE
Transient Nuclear Envelope Rupture during Cell Migration: A Cause of Genomic Instability and a Novel Opportunity for Therapeutic Intervention

5a. CONTRACT NUMBER
W81XWH-16-1-0039

5b. GRANT NUMBER
BC150580

5c. PROGRAM ELEMENT NUMBER

6. AUTHOR(S)
Jan Lammerding

E-Mail: jan.lammerding@cornell.edu

5d. PROJECT NUMBER

5e. TASK NUMBER

5f. WORK UNIT NUMBER

7. PERFORMING ORGANIZATION NAME(S) AND ADDRESS(ES)

Cornell University
Weill Hall, Room 235
Ithaca, NY 14853

8. PERFORMING ORGANIZATION REPORT NUMBER

9. SPONSORING / MONITORING AGENCY NAME(S) AND ADDRESS(ES)

U.S. Army Medical Research and Materiel Command
Fort Detrick, Maryland 21702-5012

10. SPONSOR/MONITOR'S ACRONYM(S)

11. SPONSOR/MONITOR'S REPORT NUMBER(S)

12. DISTRIBUTION / AVAILABILITY STATEMENT

Approved for Public Release; Distribution Unlimited

13. SUPPLEMENTARY NOTES

14. ABSTRACT
We have demonstrated that the physical stress associated with confined cancer cell migration can result in transient nuclear envelope rupture in vitro and in vivo, and that the nuclear deformation and nuclear envelope rupture result in nuclear fragmentation and DNA damage. We were able to further show that ESCRT-III proteins play a critical role in the nuclear envelope repair, and that depleting or inhibiting ESCRT-III and associated proteins delays nuclear envelope repair. In addition, we showed that exposure of genomic DNA to the cytoplasm following nuclear envelope rupture activates the cGAS/STING pathway and promotes cancer metastasis. Inhibition of the cGAS/STING pathway or preventing nuclear envelope rupture by overexpression of lamin B2 significantly reduced metastasis in a mouse xenograft model. These findings suggest that targeting these pathways could be a potential therapeutic approach to prevent or reduce metastasis. During the current project period, our work on this project has so far resulted in 7 peer-reviewed publications (plus one currently in revision), as well as 13 seminar, conference or poster presentations by the PI or students/postdocs from the PI's laboratory. All tasks have been completed according to or ahead of the schedule listed in the original SOW.

15. SUBJECT TERMS
Breast cancer; metastasis; invasion; confined migration; nuclear envelope; lamins; DNA damage; genomic instability; mechanics; biophysics

16. SECURITY CLASSIFICATION OF:			17. LIMITATION OF ABSTRACT	18. NUMBER OF PAGES	19a. NAME OF RESPONSIBLE PERSON
a. REPORT	b. ABSTRACT	c. THIS PAGE			USAMRMC
Unclassified	Unclassified	Unclassified	Unclassified	204	19b. TELEPHONE NUMBER *(include area code)*

Table of Contents

Page

1. INTRODUCTION

During invasion and metastasis, cancer cells move through narrow openings in dense extracellular matrix networks, tight interstitial spaces, and small capillaries. We found that the physical forces acting on the cell nucleus during passage through such confined spaces result in repetitive nuclear envelope rupture, as indicated by transient loss of nuclear envelope integrity, protrusion of chromatin from the nucleus, formation of micronuclei, and nuclear fragmentation. The major goal of this project is to investigate whether the nuclear deformation and nuclear envelope rupture during confined migration can promote genomic instability, i.e., an increased occurrence of gene deletions, amplifications, alterations, and rearrangements. At the same time, migration-induced nuclear envelope rupture and DNA damage could also offer an opportunity to specifically target invasive cancer cells, motivating us to study the mechanism of nuclear envelope repair, and the consequences of inhibiting nuclear envelope repair and DNA damage repair pathways in invasive cancer cells. Lastly, we are examining whether particularly invasive and metastatic cancer cells are particularly prone to nuclear envelope rupture, or have evolved adaptive molecular mechanisms to tolerate nuclear envelope rupture. Our experimental approach utilizes a broad panel of breast cancer cell lines and is carried out in vitro using novel microfluidic devices that mimic physiological microenvironments, collagen matrices, and in vivo breast cancer models. Insights from these studies could provide relevant information for new diagnostic, prognostic, and therapeutic approaches.

2. KEYWORDS

Breast cancer; metastasis; invasion; confined migration; nuclear envelope; lamins; DNA damage; genomic instability; mechanics; biophysics

3. ACCOMPLISHMENTS

Major goals and accomplishments

Aim 1 – Task 1: Generation of additional materials and reagents (month 1-36)

We have generated and analyzed a large panel of human and mouse breast cancer cell lines to measure the incidence and extent of nuclear envelope rupture during confined migration. To facilitate the generation of cells expressing NLS-GFP and histone H2B-tdTomato, which enables automated detection of nuclear envelope rupture, we created a novel retroviral vectors. We have generated more than 20 cell lines so far, including MDA-MB-231, MDA-MB-468, BT-549, HCC70, SKBR3, BT474, T47D, and MCF7 human breast cancer cell lines, the MCF10A human breast epithelial cell line tumor progression series, the 4T1 mouse breast cancer progression series, mouse PyMT breast cancer cells, and the highly metastatic Met1 cell line derived from the PyMT cells. We have additionally modified the 4T1 and MDA-MB-231 cells with luciferase to enable visualization of tumor growth and metastatic distribution in live animals.

In terms of technologies, we continue to refine the microfluidic devices that mimic interstitial spaces to provide realistic three-dimensional environments for in vitro studies. We have optimized both the geometries of the constrictions, as well as the fabrication process (using reactive ion etching to directly create the geometries in silicon wafers, resulting in more precise and consistent fabrication). We recently published a detail protocol of how to use the devices (Keys et al., *Methods in Molecular Biology* 2018) and are currently in the process of writing up the revised fabrication process for publication. In addition, we developed a microfluidic micropipette aspiration assay that enables high throughput measurements of nuclear mechanics and which we also used to study nuclear envelope rupture (submitted for publication to *Lab on a Chip*: Davidson et al.).

Status: Stated goals completed; further improvements continuing.

Aim 1 – Task 2: Optimization of experimental parameters (months 1-9)
We have successfully established the experimental conditions for all of the current cell lines, including coating of microfluidic devices with suitable extracellular matrix proteins, fabrication of collagen matrices, cell seeding, etc. Since we experienced difficulties stably expressing the original full length 53BP1 reporter construct to detect double stranded DNA breaks used in our *Science* publication (Denais et al. 2016), we have obtained a new, truncated 53BP1 reporter construct that produces more consistent results. We have already validated this construct as suitable reagent to detect double stranded DNA breaks. We have generated a lentiviral vector to express an mCherry-tagged version of this reporter constructs and already modified several cell lines with this construct (See Task A1.1)
Status: Stated goals completed.

Aim 1 – Task 3: Development of nuclear rupture sensor (months 1-15)
The goal of this task is to develop a genetically encoded sensor/reporter to label cells that underwent nuclear envelope rupture. In addition to the NLS-GFP reporter, which helps to visualize the dynamics of nuclear envelope rupture, we have generated a nuclear rupture reporter based on the cytoplasmic DNA binding protein cGAS, which strongly binds to genomic DNA exposed to the cytoplasm upon nuclear rupture, and which is retained at the rupture site even after nuclear envelope integrity has been restored. We published the use of this reporter in our *Science* publication describing nuclear envelope rupture and repair in confined migration (Denais et al., *Science* 2016) and subsequent work to investigate the forces requires for nuclear envelope rupture (Zhang et al. *Mol Biol Cell* 2019). We have modified a large panel of cell lines with this reporter (see Task A1.1). In addition, we continue to develop novel nuclear rupture sensors, with the goal to stably label cells after nuclear envelope rupture. We have already designed various constructs that we are currently testing in vitro.
Status: Stated goals completed; additional approaches for further improvements ongoing.

Aim 1 – Task 4: Nuclear rupture analysis (months 6-24)
The goal of this task was to quantitatively describe nuclear envelope rupture during confined and unconfined migration, and to assess the effect on cell viability. We have tested an extensive panel of breast cancer cell lines in the microfluidic migration devices and in collagen matrices. Additional experiments were performed in vivo, using intravital imaging. We showed that migration through tight spaces results in transient nuclear envelope rupture in vitro and in vivo, and that the incidence of nuclear envelope rupture substantially increases with confinement, i.e., decreasing pore size. Intriguingly, the vast majority of cells survived nuclear envelope rupture. These results were published in *Science* during a first report period (Denais et al., 2016). Following up on these studies, we have analyzed more than 20 cell lines expressing our nuclear rupture reporter. We did observe an increased likelihood of nuclear fragmentation during confined migration in highly aggressive breast cancer cells in the isogenic 4T1 progression series (Figure 1). Unexpectedly, however, we did not detect any correlation between the aggressiveness of various human and mouse cancer cell lines (based on published in vivo studies) and the frequency or duration of nuclear envelope rupture. Instead, all cell lines showed similar frequency and duration of nuclear envelope rupture during confined migration (Figures 2 & 3). We did not detect any significant correlation between the aggressiveness of the cancer cell lines and their survival/death following nuclear envelope rupture, either, indicating that all tumor cells are capable of efficiently restoring nuclear envelope integrity. Consistent with this interpretation, we found that the various breast cancer cells expressed similar levels of ESCRT-III proteins (Figure 4), which we previously identified as crucial components for nuclear envelope repair (Denais et al. *Science* 2016).
Status: Stated goals completed. Follow-up experiments with additional cell lines in process.

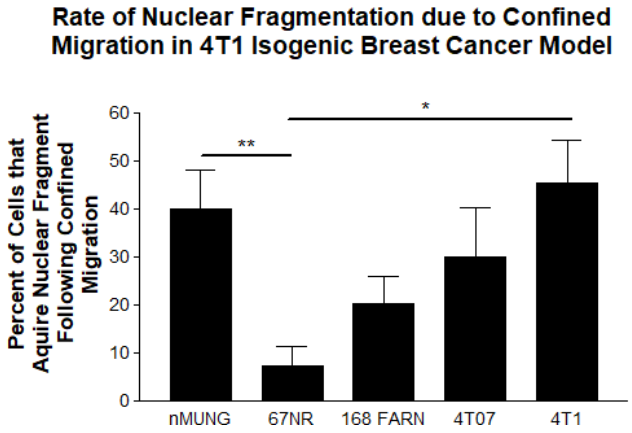

Figure 1. Nuclear fragmentation due to confined migration. Percentage of cells from 4T1 mouse breast cancer progression series that exhibit nuclear fragmentation following migration through confined constrictions. The 67NR, 168 FARN, 4T07 and 4T1 cells are isogenic mouse breast cancer cell lines with increasing metastatic potential. The mMUNG cells represent normal mouse breast epithelial cells, but from a different genetic background, making comparison challenging. Percentage of cells with nuclear fragmentation shown as mean of experimental averages ± SEM (*, $p < 0.05$; **, $p < 0.01$, by one-way ANOVA with Bonferroni's multiple comparison test). Data presented are from at least three independent experiments per cell line.

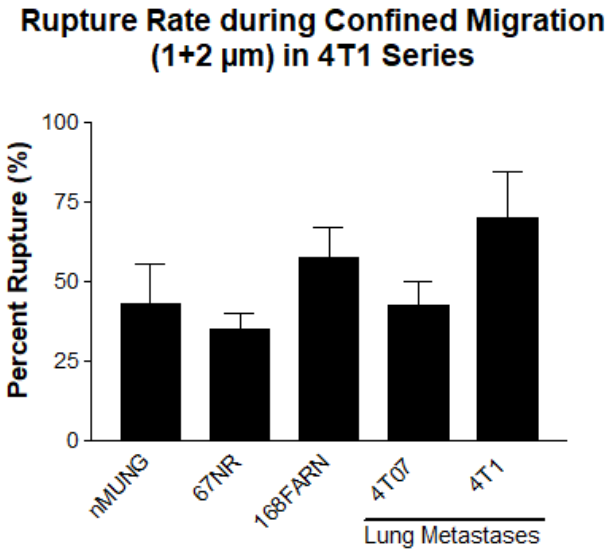

Figure 2. Rate of NE rupture in increasingly metastatic cell lines. Percentage of cells from 4T1 mouse breast cancer progression series that exhibit nuclear envelope rupture following migration through confined constrictions. Percentage of cells with nuclear envelope rupture shown as mean of experimental averages ± SEM by one-way ANOVA. Data shown are from at least three independent experiments per cell line.

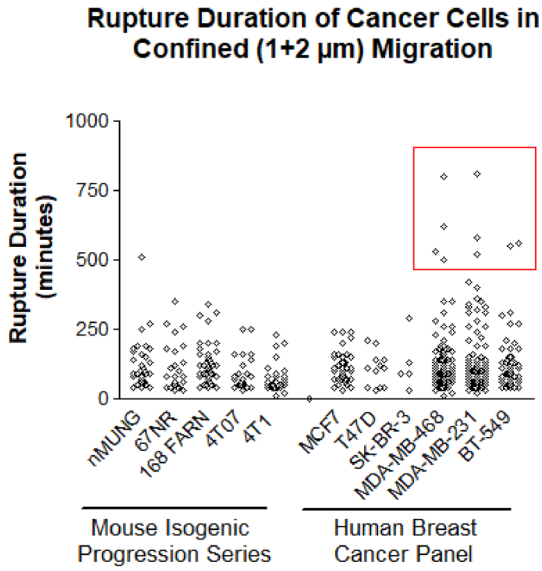

Figure 3. NE rupture duration for the 4T1 mouse isogenic breast cancer cell line series and the human breast cancer cell line panel. Scatterplot of NE rupture duration across cell lines. Red box indicates significant outliers in highly metastatic cell lines MDA-MB-468, MDA-MB-231, and BT-549. *n* = 36 for nMUNG cells; *n* = 31 for 67NR cells; *n* = 49 for 168 FARN cells; *n* = 26 for 4T07 cells; *n* = 42 for 4T1 cells; *n* = for 45 MCF7 cells; *n* = 13 for T47D cells; *n* = 5 for SK-BR-3 cells; *n* = 115 for MDA-MB-468 cells; *n* = 115 for MDA-MB-231 cells; *n* = 64 for BT-549 cells. At least three independent experiments per cell line.

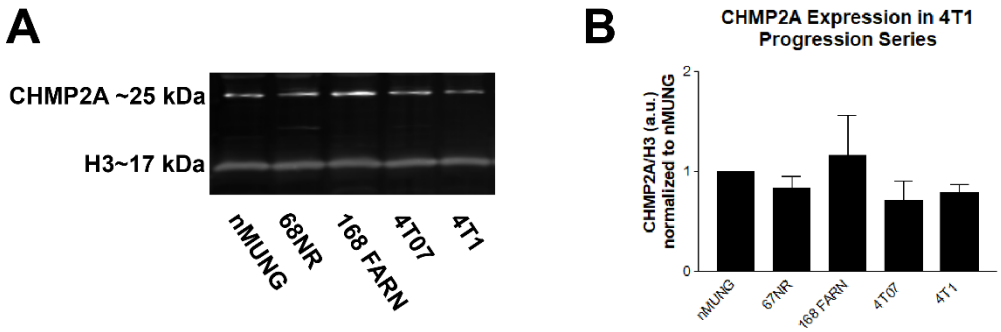

Figure 4. ESCRT-III proteins are conserved across cell lines of various metastatic potential. (**A**) Representative Western blot for CHMP2A, a protein part of the ESCRT-III machinery, in the isogenic 4T1 mouse breast cancer progression series and the normal breast epithelial control cell line, nMUNG. Histone H3 was used as loading control. (**B**) Analysis of CHMP2A Western blot results, normalized to histone H3 loading control, and relative to the nMUNG control breast epithelial cell line. Mean ± standard error of the mean from three independent blots. One-way ANOVA with Dunn's multiple comparison did not reveal any statistically significant differences.

Aim 1 – Task 5: Consequences of nuclear envelope rupture on genomic instability (months 8-24)

To assess the effect of nuclear envelope rupture on genomic integrity, we assessed cells during confined and confined migration for DNA damage and chromatin fragmentation. We found that increasing

confinement resulted in a substantial fraction of cells displaying chromatin protrusions, and, in severe cases, complete chromatin fragmentation, i.e., chromatin fragments separating from the main nucleus. More than 60% of the chromatin fragments were positive for γH2AX, indicating DNA damage, closely resembling previous findings in micronuclei. Our initial findings were published during the previous report period (Denais et al. *Science* 2016). Since then, we have analyzed the mechanism of DNA damage in more detail. Using live-cell imaging of cells co-expressing NLS-GFP and a 53BP1-mCherry reporter for DNA double strand breaks, we found that migration through confined spaces can result in DNA damage, even in the absence of nuclear envelope rupture, but that nuclear envelope rupture can further contribute to DNA damage (Figure 5).

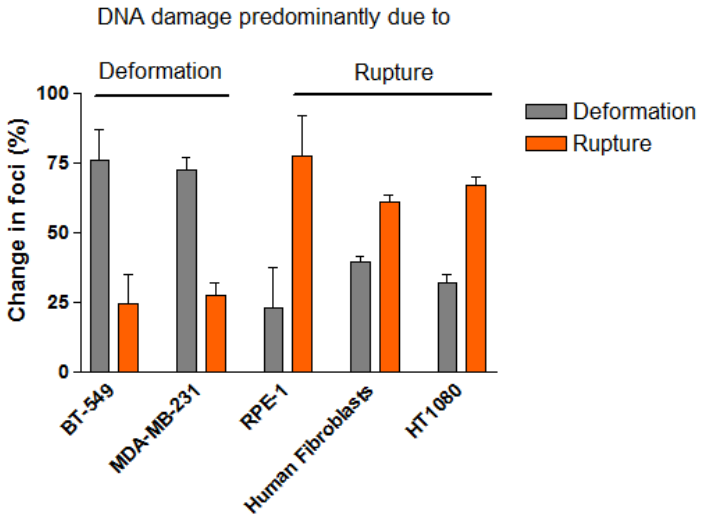

Figure 5. DNA damage can arise from nuclear envelope rupture or from nuclear deformation alone. Time-lapse microscope of cells expressing the DNA damage reporter 53BP1-mCherry together with the nuclear envelope rupture reporter NLS-GFP revealed that while in some cell lines (RPE-1, human fibroblasts, HT1080 cells) confined migration induced DNA damage is primarily due to nuclear envelope rupture, in triple negative breast cancer cells (BT-549 ad MDA-MB-231) nuclear deformation alone can cause DNA damage, even in the absence of nuclear envelope rupture.

We are currently in the process of determining the precise molecular mechanisms responsible for the DNA damage. Our preliminary studies suggest that confined migration lead to increased replication stress, which results in DNA damage at the replication fork.

In addition, we have been working on assessing the long term consequences of nuclear protrusion and fragmentation. We have generated clonal populations of MDA-MB-231 cells and collected cells that have repeatedly migrated through tight spaces (1×5μm^2 constrictions) and cells that have migrated through larger control channels (15×5μm^2), which do not require nuclear deformation and which do not induce nuclear envelope rupture. We have analyzed the first of the experiments by copy number abnormality (CNA)analysis (based on single cell sequencing, in collaboration with Dr. Nicholas Navin at MD Anderson). The preliminary data suggest that migration through 3D environments can increase CAN, but further studies are required to confirm these results. Nonetheless, recent publications by the Discher group support our hypothesis that confined migration results in increased genomic instability (Irianto et al. *Curr Biol*. 2017; Pfeiffer et al. *Curr Opin Syst Biol*. 2018)

Working with Dr. Lew Cantley at Weill Cornell Medicine, we have further unraveled an intriguing connecting between genomic instability and nuclear envelope rupture. Dr. Cantley's group had generated MDA-MB-231 breast cancer cells depleted for mitotic centromere-associated kinesin (MCAK), which leads to increased formation of micronuclei and genomic instability. Our collaboration revealed that nuclear envelope rupture of the micronuclei results cytoplasmic genomic DNA, which activates the cGAS/STING pathway and promotes metastatic spreading of the cancer cells in a mouse xenograft model. Intriguingly, reducing nuclear envelope rupture by overexpression of lamin B2, or inhibiting the cGAS/STING pathway by depletion of STING, significantly reduced metastatic progression (Figure 1). These results were recently published in Nature (Bakhoum et al. *Nature* 2018).
Status: Chromatin herniation and DNA damage detection completed. Analysis of long-term changes in genomic stability ongoing.

Aim 2 – Task 1. Acquisition of additional cell lines and patient samples (months 8-36)
As described under Aim 1, Task 1, we have acquired additional breast cancer cell lines and modified these cells with the various fluorescent reporters. We have also obtained the MCF10A human breast cancer progression series and the 4T1 mouse breast cancer progressions series, which enable comparison of isogenic cell lines with different metastatic potential, and we have already used these progression series in our experiments (see above). We have also obtained a large sets of human breast cancer patient samples, including tissue microarrays of 122 patient samples that includes 54 triple negative samples. Patients did not receive systemic adjuvant treatment and were followed up for at least 5 years. We have already used these samples to assess whether specific nuclear envelope proteins or indicators of nuclear envelope rupture correlate with clinical outcome in these patients (see prior project period report and below). In addition, we used publically available data bases such as the Human Protein Atlas to analyze correlations between changes in ESCRT protein levels and patient survival (see below).
Status: Progress according to schedule described in the SOW.

Aim 2 – Task 2. Comparison of nuclear rupture incidence in cells/tissues (months 8-36)
In our analysis of more than 20 different breast cancer cell lines, we did not detect any significant correlation between the incidence of nuclear envelope rupture and metastatic potential/aggressiveness. Some of these findings were reported as part of our work with the Cantley group (Bakhoum et al. *Nature* 2018), while others are still in preparation for publication. Our comparison between the different breast cancer cell lines, including an isogenic cancer progression series, however, revealed another striking finding: breast cancer cell lines that are particularly invasive and metastatic have reduced levels of the nuclear envelope protein lamin A and increased nuclear deformability, which may increase their ability to migrate through tight spaces smaller than the nuclear diameter. To test whether this correlation could yield prognostic value, we assessed levels of lamin A (normalized by lamin B) in a large panel of tumor samples (tissue micro array) from breast cancer patients who did not received systemic adjuvant therapy and who had been followed up for at least 5 years. Patients whose tumor cells had low levels of lamin A had significantly reduced disease free survival compared to patients whose tumors had high levels of lamin A. We are currently preparing a manuscript with these results for publication. Another manuscript describing lower levels of lamin A/C and enhanced migration in confined environments in an isogenic metastatic breast cancer model was published in the previous project period (Mekhdjian et a. *Mol Biol Cell*. 2017).
Intriguingly, although we did not detect any differences in the levels of ESCRT proteins between different cell lines in an isogenic breast cancer panel (Figure 4), our analysis of available gene expression data from the Human Protein Atlas revealed that breast cancer patients with low expression levels of the ESCRT

proteins CHMP2A and CHMP7, which we previously identified as having a critical role in nuclear envelope repair (Denais et al. *Science* 2016; Isermann et al. *Nucleus* 2017), had significantly lower survival rates than individuals with high levels of these proteins (Figure 6).
Status: Progress mostly completed.

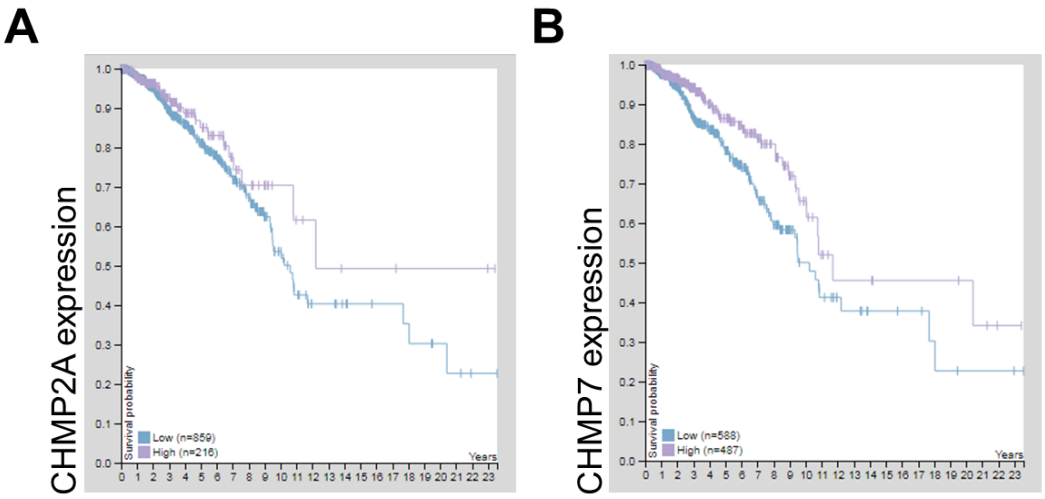

Figure 6. Kaplan-Meier plots for patients with high and low expression of the ESCRT-III proteins, CHMP2A (A) and CHMP7 (B). Blue line represents survival curve for low expression of ESCRT-III protein CHMP2A (*n = 859*; A) and CHMP7 (*n = 588*; B). Purple line represents survival curve for high expression of ESCRT-III protein CHMP2A (*n = 216*; A) and CHMP7 (*n = 487*; B). Plots created using microarray data from the Human Protein Atlas (Uhlen et al. 2017).

Aim 2 – Task 3. Investigate the mechanism(s) of nuclear envelope rupture and survival (months 12-24)
By varying the degree of confinement (pore size) in our microfluidic migration devices and collagen matrices, we demonstrated that nuclear envelope rupture increases dramatically with increasing confinement. The formation of nuclear membrane blebs that collapse upon nuclear envelope rupture indicate that nuclear rupture is caused by intranuclear pressure. The intranuclear pressure results from compression of the nucleus by the cytoskeleton, particularly the actin-myosin network, and inhibition of myosin II with blebbistatin significantly reduces nuclear envelope rupture. Our findings were published in *Science* (Denais et al. 2016), together with an independent study by Matthieu Piel's group (Raab et al. *Science* 2016) that produced very similar results in dendritic cells. Subsequent work by Emily Hatch and Martin Hetzer (*JCB* 2016, published with a commentary by Jan Lammerding) confirmed these results. In collaboration with Vivek Shenoy (University of Pennsylvania), we carried out computational modeling to describe the biophysical aspects of nuclear deformation during confined migration in more detail, showing that the front of the nucleus, where most of the nuclear envelope ruptures occurs, is exposed to particularly large mechanical stresses (Cao et al. *Biophys J* 2016). Most recently, we demonstrated that in addition to increased nuclear pressure, nuclear envelope rupture can also result from tensile stress applied to the outside of the nuclear envelope (Zhang et al. *Mol Biol Cell* 2019), as could be the case when cytoskeletal structures pull on the nucleus during cell migration.
Status: Task completed.

Aim 2 – Task 4. In vivo experiments with xenograft mouse model (months 1-33)
We have already obtained the regulatory approval for the proposed experiments by USAMRMC ACURO. During my sabbatical in Val Weaver's laboratory at UCSF (2015/16), I was trained in the procedures of mammary fat pad injection, observation of tumor growth, and harvest of primary tumors and other tissues for analysis of metastatic spreading. We have already generated cells for the in vivo experiments by stably modifying MDA-MB-231 cells and cells from the 4T1 progression series to express luciferase (for bioluminescence imaging of metastatic progression), along with fluorescent reporters for nuclear envelope rupture, and variations in their lamin A/C levels. The start of the in vivo experiments itself was unexpectedly delayed as the postdoctoral fellow trained on the procedure become pregnant, and the Cornell Environmental Health & Safety Office advised her against working with isoflurane during the pregnancy. Following the birth of her daughter and subsequent maternity leave, the postdoctoral fellow has now resumed her full time work in the lab and is in the process of initiating the first pilot experiments to confirm experimental conditions and procedures before then embarking on the full set of studies. Due to the delay, we have requested and been approved for a no-cost extension, allowing us to carry out the proposed experiments. In the meantime, our collaboration with the Cantley group at Weill Cornell Medicine revealed that cells from metastases had increased genomic instability compared to cells from the primary tumor, and that increasing genomic instability increases metastasis in a mouse model (Bakhoum et al. *Nature* 2018).
Status: In progress.

Aim 3 – Task 1. Identification of nuclear membrane repair mechanism (months 1-27)
Motivated by previous reports of a role of ESCRT-III proteins in mediating nuclear envelope re-sealing in late mitosis, we investigated the localization of the ESCRT-III proteins CHMP4B, CHMP7, and the ESCRT-III associated protein VPS4B during confined migration and nuclear envelope rupture induced by laser ablation or physical cell compression. Using time-lapse microscopy and superresolution imaging, we showed that these proteins rapidly accumulated at sites of nuclear envelope rupture, and that depletion of ESCRT-III proteins or expression of a dominant negative VPS4B mutant significantly delayed nuclear envelope repair after nuclear envelope rupture. Intriguingly, while inhibiting nuclear envelope repair alone (using the dominant negative VPS4B mutant) had no effect on cell viability after nuclear envelope rupture, inhibiting both nuclear envelope repair and DNA damage repair using the ATM inhibitor Ku-55933 resulted in significantly increased cell death after migrating, suggesting that this approach could potentially be used as a therapeutic strategy to target invasive cancer cells. These findings were described in detail in our *Science* publication (Denais et al. *Science*. 2016) and confirmed in an independent study published in parallel (Raab et al. *Science* 2016), as well as in a subsequent study by the De Vos group (Robijns et al. *Sci Reports* 2016). We recently published an extended description with additional details of the nuclear envelope repair (Isermann and Lammerding, *Nucleus.* 2017). We tried generating cells stably expressing (inducible) shRNA against ESCRT-III proteins or non-target controls, but these cells were not viable, possibly due to the critical role of ESCRT proteins in cellular function, so that even the low levels of knockdown resulting from leakage of the inducible system may interfere with cell proliferation.
Status: All items completed.

Aim 3 – Task 2. Targeting DNA damage and stress response pathways in vitro (months 18-24)
We have already conducted experiments using the ATM inhibitor Ku-55933, showing that combined inhibition of nuclear envelope repair and DNA damage repair significantly increases cell death after nuclear envelope rupture (Denais et al. *Science* 2016). Experiments with the HSP90 inhibitor 17-AAG resulted in overall decreased cell viability and proliferation, independent of confined migration. We also

conducted experiments exploring inhibition of alternative DNA damage response pathways, including ATR (VE-821 inhibitor) and DNA-PK (NU-7741 inhibitor). In addition, we analyzing cells lacking specific DNA damage response genes (e.g. ATM, ATR) from Robert Weiss' lab at Cornell and 4T1 cells with inducible ATM depletion from Sandra Demaria at Weill Cornell Medicine to complement pharmaceutical inhibition of DNA damage response pathways. Intriguingly, deletion of these DNA damage response pathways did not negatively affect cell survival. Instead, cells lacking ATM or treated with an ATM inhibitor migrated significantly faster through tight constrictions than wild-type controls. Our biophysical assays revealed significantly more deformable nuclei in the ATM-null and ATM inhibited cells, providing a possible explanation for this behavior. We are currently investigating the molecular mechanism by which ATM depletion alters lamin A/C levels and nuclear deformability.
Status: Proposed experiments completed. Additional work ongoing.

Aim 3 – Task 3. Targeting DNA damage and stress response pathways in vivo (months 12-36)
We have already obtained regulatory approval for the experiments by USAMRMC ACURO. We have already generated cells for the in vivo experiments by stably modifying MDA-MB-231 cells and cells from the 4T1 progression series to express luciferase (for bioluminescence imaging of metastatic progression), along with fluorescent reporters for nuclear envelope rupture, and variations in their lamin A/C levels. In parallel, we are testing different combinations of nuclear envelope repair inhibition and DNA damage repair inhibition to determine the best strategy to specifically target metastatic cells. Due to the pregnancy and subsequent maternity leave of the postdoctoral fellow (see above), the start of the in vivo experiments has been pushed back. We anticipate that the experiments will be completed during the no-cost extension period. In the meantime, working with the Cantley group at Weill Cornell Medicine, which has established protocols for in vivo models, we showed that preventing nuclear envelope rupture of micronuclei by overexpression of lamin B2, or inhibiting cGAS/STING signaling, which is activated by exposure of genomic DNA to the cytoplasm, significantly reduces metastasis in a mouse xenograft model (Bakhoum et al. *Nature* 2018)
Status: In progress.

Opportunities for training/professional development
The project, coupled with additional funds from other sources (NSF graduate research fellowship, start-up funds from the Lammerding lab) has provided excellent opportunities to train undergraduate students, graduate students, and a postdoctoral fellow in multidisciplinary research. It also has provided opportunities for trainees to present their research at national conferences, interact with breast cancer patients through outreach efforts (coordinated with the Cancer Resource Center of the Finger Lakes), and thus contributed to the training and professional development of the next generation of researchers.

Dissemination of results to communities of interest
We have disseminated the research results from this project through peer-reviewed publications, conference presentations, and invited seminars (see Products). To reach the local patient community, Alexandra McGregor, a graduate student in the Lammerding lab working on this project, is organizing regular presentations by cancer researchers to breast cancer patients through a joint project with the Cancer Resource Center of the Finger Lakes.

Plans for the next reporting period (no cost extension)
During the first 36 months of the project, we have generated a large array of assays, reagents, and tools to study the role of nuclear mechanics and nuclear envelope rupture in breast cancer progression, yielding already several new and important insights. We have already completed most of the tasks originally

proposed. Our main effort during the next project period will be on the in vivo studies, utilizing mouse models of breast cancer progression to study nuclear envelope rupture in vivo, and to test whether inhibiting nuclear envelope repair and DNA damage can serve as effective therapeutic approaches.
In addition, we will continue the use of in vitro experiments to investigate in more detail the molecular mechanism by which migration through confined environments causes DNA damage and may contribute to long-term genomic instability in tumor cells.

4. IMPACT

Impact on the development of the principal discipline(s) of the project

Our group, together with a Matthieu Piel's group, were the first to demonstrate that the physical stress associated with confined migration can result in transient nuclear envelope rupture in vitro and in vivo, and that the nuclear deformation and nuclear envelope rupture result in nuclear fragmentation and DNA damage. These findings suggest that the physical process of invasion could further drive genomic instability in metastatic cancer cells. Subsequent work by the Discher group (Irianto et al. *Curr Biol* 2017; Irianto et al. *Mol Biol* 2017; Pfeiffer et al. *Mol Biol Cell* 2018) further support these findings. We were able to show that ESCRT-III proteins play a critical role in the nuclear envelope repair, and that depleting or inhibiting ESCRT-III and associated proteins delays nuclear envelope repair. We also showed that combined inhibition of nuclear envelope repair and DNA damage repair results in significantly increased cell death after nuclear envelope rupture. These findings suggest that targeting these pathways could be a potential therapeutic approach to induce cell death in invasive cancer cells. Our finding that nuclear envelope rupture allows cytoplasmic cGAS to bind to genomic DNA (Denais et al. *Science* 2016) has stimulated tremendous interest in) the cytosolic DNA-sensing protein cyclic-GMP-AMP synthase (cGAS), which was first described as a key component of the innate immune system inflammatory response. Several recent reports demonstrate that loss of nuclear envelope integrity ('nuclear envelope rupture') exposes genomic DNA to the cytoplasm, enabling cytosolic cGAS to activate pro-inflammatory cytokine signaling and senescence (Mackenzie et al. *Nature* 2017; Dou et al *Nature* 2017; Gluck et al. *Nat Cell Bio*. 2017). In our work with the Cantley group, we showed that binding of cGAS to genomic DNA activates non-canonical NF-kB signaling and pro-inflammatory cytokine signaling, which is required for metastatic progression. Inhibiting nuclear envelope rupture or cGAS/STING signaling was sufficient to significantly reduce metastatic progression in a mouse model with breast cancer cells with increased chromosomal instability (Bakhoum et al. *Nature* 2018). Furthermore, recent findings from Sandra Demaria's group suggest that exposure of nuclear DNA following radiotherapy can amplify the effect of treatment by stimulating inflammatory signaling pathways (Diamond et al. *Cancer Immunol Res* 2018; Vanpouille-Box et al. *Cancer Cell* 2018).

Impact on other disciplines

Our work was also positively received in the membrane trafficking and ESCRT community, as our results showed an important role of ESCRT-III proteins, particularly the previously not well characterized CHMP7 protein, in nuclear envelope repair. Two other publications following our work have since then provided further insights into how CHMP7 can mediate nuclear envelope repair/reformation (Olmos et al. *Curr Biol* 2016; Gu et al. *PNAS* 2017). As discussed above, the finding that exposure of genomic DNA to cytoplasmic cGAS can activate the cGAS/STING pathway has resulted in a flurry of recent publications in a variety of field, ranging from immune cells to cell senescence research.

Impact on technology transfer
We have been working with a team of engineering students to develop a stand-alone version of our microfluidic assay to perform high-throughput measurements of nuclear stiffness, which could have important applications in cancer prognosis. In addition, *The Scientist* published an article highlighting our microfluidic cell migration device as a novel tool in mechanobiology: http://www.the-scientist.com/?articles.view/articleNo/49860/title/The-Mechanobiology-Garage/

Impact on society beyond science and technology
The You-Tube video produced by *Science* featuring the results (https://www.youtube.com/watch?v=-lg91eM8c7U) has already had more than 14,000 views, raising broad public awareness for this research.
We used our research on cancer cell invasion as a topic for outreach work "Squishing cells to stop cancer in its tracks" with female high school students interested in engineering through the Cornell CURIE Academy: https://www.bme.cornell.edu/news/index.cfm?news_id=96011
We collaborated with the Cancer Resource Center of the Finger Lakes to connect breast cancer patients with cancer researchers: https://ejs349.wixsite.com/website
The project has enabled us to train several undergraduate students in cancer research, including one student featured in the Cornell student newspaper: https://cornellsun.com/2019/02/18/student-spotlight-on-connor-mcguigan-a-biomedical-approach-to-treating-cancer/

5. CHANGES/PROBLEMS

We have not encountered any substantial problems in the project. The in vivo studies had been delayed as the postdoctoral fellow working on the project became pregnant (and gave birth to a baby girl in December 2018). The postdoctoral fellow was advised by the Cornell Environmental Health & Safety Officers to avoid exposure to isoflurane during the pregnancy, which prevented her from continuing with the in vivo studies. We have used this time to prepare the genetically modified cells, obtain/renew approval for all animal protocols, and are now (May 2019) resuming the in vivo experiments. Due to the incurred delay, we have requested and received approval for a no-cost extension to continue the studies.

6. PRODUCTS

The work performed for this project has already resulted in 8 journal publications (+ 2 submitted/in revision), and numerous seminar and conference presentations during the project period. Three additional manuscripts are currently in preparation for submission. Our work on nuclear envelope rupture, DNA damage, and nuclear envelope repair has also been covered by numerous news outlets and websites.

Journal publications

1. Kirby TJ. Lammerding J. Emerging views of the nucleus as a cellular mechanosensor. ***Nat Cell Biol*****.** 2018. 20(4): 373-381. Federal support acknowledged.
2. Yadav S, Feigelson S, Roncato F, Antman-Passig M, Shefi O, Lammerding J, Alon R. Elevated nuclear lamin A is permissive for granulocyte transendothelial migration but not for motility through collagen I barriers. ***J Leuk Biol***. 2018. 104(2): 239–251. Federal support acknowledged.
3. Singh A, Brito I, Lammerding J. Beyond tissue stiffness and bioadhesivity: advanced biomaterials to model tumor microenvironments and drug resistance. ***Trends in Cancer***. 2018. 4(4): 281-291. Federal support acknowledged.

4. Elacqua JJ, McGregor AL, Lammerding J. Automated analysis of cell migration and nuclear envelope rupture in confined environments. ***PLoS One***. 2018. 13(4): e0195664. Federal support acknowledged.
5. Keys J, Windsor A, Lammerding J. Assembly and use of a microfluidic device to study cell migration in confined environments. ***Methods Mol Biol***. 2018. 1840:101-118. Federal support acknowledged.
6. Zhang Q, Tamashunas A, Agrawal A, Torbati M, Katiyar A, Dickinson RB, Lammerding J, Lele TP. Local, transient tensile stress on the nuclear membrane causes membrane rupture. ***Mol Biol Cell***. 2019. 30(7): 899-906. Federal support acknowledged.
7. Maurer M, Lammerding J. The driving force: Nuclear mechanotransduction in cellular function, fate, and disease. ***Annu Rev Biomed Eng***. 2019. Published online March 27, 2019. Federal support acknowledged.
8. Zuela-Sopilniak N, Lammerding J. Engineering approaches to study cancer cell migration in 3D environments. ***Phil Trans Royal Society B***. Accepted for publication.
9. Picariello HS, Kenchappa RS, Rai V, Crish JF, Dovas A, Pagoda K, McMahon M, Bell ES, Chandrasekharan U, Luu A, West R, Lammerding J, Canoll P, Odde DJ, Janmey PA, Egelhoff1 T, Rosenfeld SS. Myosin IIA suppresses glioblastoma development in a mechanically sensitive manner. Currently in revision for ***PNAS***. Federal support acknowledged.
10. Davidson PM, Fedorchack GR, Mondesert-Deveraux S, Bell ES, Isermann P, Aubry D, Allena R, Lammerding J. High-throughput microfluidic micropipette aspiration device to probe time-scale dependent nuclear mechanics in intact cells. Submitted to ***Lab on a Chip***. Federal support acknowledged.

Conferences/Seminars/Meetings

1. Nuclear mechanobiology in cancer cell migration. Invited seminar as part of the Anderson Center for Cancer Research Seminar Series at Rockefeller University. New York, NY (May 2, 2019)
2. Nuclear deformability and expression of lamin A/C as predictors of metastatic potential in breast cancer cells. Invited platform presentation at the Gordon Research Conference on Physical Science of Cancer. Galveston, TX (Feb. 12, 2019)
3. Squish and Squeeze: Confined cancer cell migration and its impact on DNA damage. Shah P, McGuigan C, Chen S, Weiss R, Lammerding J. Poster presentation selected from submitted abstract. Gordon Research Conference on Physical Science of Cancer. Galveston, TX (Feb. 13, 2019)
4. Metabolic requirements for migration in confined 3D environments. Bell ES, Isermann P, Gopalan T, Zuela-Sopilniak N, Rodriguez NZ, Fedorchak G, Zipfel W, Lammerding J. Poster presentation selected from submitted abstract. Gordon Research Conference on Physical Science of Cancer. Galveston, TX (Feb. 13, 2019)
5. Nuclear deformability and expression of lamin A/C as predictors of metastatic potential in breast cancer cells. Invited platform presentation at the NCI Emerging Topic Symposium at the American Society for Cell Biology Annual Meeting. San Diego, CA (Dec. 12, 2018)
6. Confined migration induces heterochromatin formation in cancer cells. Chieh-Ren Hsia, Chao-Yuan Chang, Lammerding J. Poster presentations based on submitted abstract. American Society for Cell Biology Annual Meeting. San Diego, CA (Dec. 11, 2018)
7. Metastatic Nuclear Mechanobiology. Invited platform presentation at Special Interest Subgroup at the American Society for Cell Biology Annual Meeting. San Diego, CA (Dec. 8, 2018)

8. Nuclear envelope rupture, DNA damage, and DNA damage response activation as drivers of lamin-associated muscular dystrophy. Invited platform presentation at Special Interest Subgroup at the American Society for Cell Biology Annual Meeting. San Diego, CA (Dec. 8, 2018)
9. Lamin mutations cause mechanically-induced nuclear envelope rupture, DNA damage, and DNA-PK activation in muscle. Invited presentation. Pennsylvania Muscle Institute Annual Retreat and Symposium. Philadelphia, PA (Nov. 12, 2018)
10. Squish and squeeze – Nuclear mechanics in physiology and disease. Invited seminar at the Department of Biochemistry and Molecular Biology, Saint Louis University School of Medicine. St Louis, MO (Nov. 5, 2018)
11. Lamin mutations cause mechanically-induced nuclear envelope rupture and DNA damage in muscle fibers. Earle A, Fedorchak G, Kirby T, Isermann P, Patel J, Iruvanti S, Lammerding J. Platform presentation selected from submitted abstract. Biomedical Engineering Society Annual Meeting. Atlanta, GA (Oct. 20, 2018)
12. Nuclear deformability and expression of lamin A/C as predictors of metastatic potential in breast cancer cells. Bell ES, Shah P, McGregord AL, Isermann P, Kim DS, Smolka M, Span P, Lammerding J. Platform presentation selected from submitted abstract. Biomedical Engineering Society Annual Meeting. Atlanta, GA (Oct. 20, 2018)
13. Squish and squeeze – Nuclear mechanics in physiology and disease. Invited seminar. Department of Biomedical Engineering. University of Michigan. Ann Arbor, MI (Oct. 4, 2018)
14. Squish and squeeze - the role of the nucleus and lamins in breast cancer metastasis. Platform presentation based on submitted abstract. Cancer Systems Biology Consortium (CSBC) & Physical Sciences-Oncology Network (PS-ON) Annual Investigators Meeting 2018. Bethesda, MD (Sept. 27, 2018)
15. Elucidating the impact of cancer cell migration through confined environments on DNA damage and genomic instability. Shah P, McGuigan C, Lammerding J. Physical Science Oncology Network Annual Meeting. Bethesda, MD (Sept. 25, 2018)
16. Lamin mutations cause mechanically-induced nuclear envelope rupture and DNA damage in muscle fibers. Invited platform presentation at the German Society for Cell Biology (DGZ) Annual Meeting. Leipzig, Germany (Sept. 18, 2018)
17. Engineering extracellular environments to study nuclear mechanobiology. Invited platform presentation at the Gordon Research Conference on Signal Transduction from Engineered Extracellular Matrices. Andover, NH (July 23, 2018)
18. Nuclear mechanics and mechanotransduction in physiology and disease. Invited seminar at the Vienna Doctoral School “Molecules of Life”, an umbrella program of the PhD programs in molecular biology at universities in Vienna. Vienna, Austria (June 21, 2018)
19. Squish and squeeze – the role of the nucleus and lamins in breast cancer metastasis. Invited platform presentation at the Royal Society Meeting “Forces in cancer: interdisciplinary approaches in tumour mechanobiology”. London, UK (June 18-19, 2018)
20. Squish and squeeze – Nuclear mechanics and mechanotransduction in physiology and disease. Invited seminar at the GRK 2154 “Materials for Brain”, Department of Material Science, Christian-Albrechts-Universität zu Kiel (University of Kiel). Kiel, Germany (June 11, 2018)
21. Lamin mutations cause mechanically-induced nuclear envelope rupture and DNA damage in muscle fibers. Invited presentation at the EMBO Workshop on Nuclear Mechano-Genomics. Singapore (April 19, 2018)
22. Squish and squeeze – Nuclear mechanics and mechanotransduction in physiology and disease. Invited seminar in the Department of Chemical Engineering. University of Florida. Gainesville, FL (April 2, 2018)

Websites and other media

- Coverage of our recent *Nature* article with the Cantley group on chromosomal instability in cancer and activation of the STING pathway upon nuclear envelope rupture of micronuclei (February 23, 2018): https://www.nature.com/articles/nrc.2018.16
- Coverage of our research through the Cornell Research website: https://research.cornell.edu/news-features/cell-mechanics-cancer-and-muscle-disease
- Article in the Cornell Daily Sun featuring Connor McGuigan, an undergraduate student in the lab, and his research on cancer metastasis: https://cornellsun.com/2019/02/18/student-spotlight-on-connor-mcguigan-a-biomedical-approach-to-treating-cancer/
- Editorial in the *Journal of Leukocyte Biology* on our work with Ronen Alon demonstrating the importance of nuclear deformability in neutrophil transendothelial migration: https://jlb.onlinelibrary.wiley.com/doi/full/10.1002/JLB.1CE0318-099R

Technologies or techniques

We have already distributed several of the microfluidic migration devices developed in our laboratory to other laboratories, both as prepared devices and by providing design plans to recreate the devices. We have published manuscripts with a detailed protocol describing the fabrication and use of the devices (Keys et al. *Meth Mol Bio* 2018) and the automated image analysis of migration experiments and detection of nuclear envelope rupture (Elacqua et al. *PLoS one* 2018). We just submitted a manuscript describing a novel microfluidic micropipette aspiration assay to measure nuclear stability, including nuclear envelope rupture (Davidson et al.). This manuscript is currently under review at *Lab on a Chip*.

Other products

We have already generated more than 20 different breast cancer cell lines, including human and mouse, expressing various fluorescent reporters to monitor nuclear deformation and nuclear envelope rupture. We have modified these cells with a variety of fluorescent reporters to detect nuclear envelope rupture, nuclear fragmentation, and double strand DNA breaks by time-lapse microscopy. In addition, we have generated clonal populations of MDA-MB-231 cells that we will use to assess long-term DNA damage after confined migration through tight spaces, as the heterogeneity of standard MDA-MB-231 cell cultures would preclude drawing meaningful conclusions after karyotyping or other genomic analysis.

7. PARTICIPANTS

Individuals working on the project during the most recent project period

Name:	Jan Lammerding
Project Role:	PI
Researcher Identifier:	ORCID ID: 0000-0003-4335-8611
Person Months:	3 (25%)
Contribution:	Planning and analysis of experiments; supervision of researchers; coordination with collaborators; writing/editing publications
Funding Support:	This award

Name:	Pragya Shah
Project Role:	Graduate student
Person Months:	9 (75%)
Contribution:	Generation of cell lines; in vitro migration experiments; generation of new 53BP1-mCherry lentiviral vector; analysis of migration-induced DNA damage and molecular mechanism of DNA damage.
Funding Support:	This award

Name:	Noam Zuela-Sopilniak
Project Role:	Postdoctoral fellow
Person Months:	2 (17%)
Contribution:	Generation of human and mouse cell lines for in vivo experiments; pilot experiments for optimization of in vivo experiments.
Funding Support:	This award

Name:	Alexandra McGregor
Project Role:	Graduate student
Person Months:	7 (58%)
Contribution:	Generation of cell lines; in vitro migration experiments to assess nuclear envelope rupture and migration efficiency; assessment of DNA fragmentation in confined migration; dissemination of work to local breast cancer community
Funding Support:	This award

Name:	Gerald Sarubbe
Project Role:	Undergraduate student
Person Months:	1 (8%)
Contribution:	Analysis of chromatin fragmentation during confined migration.
Funding Support:	This award; research credit

Name:	Chieh-Ren (Jeremiah) Hsia
Project Role:	Graduate student
Person Months:	1.2
Contribution:	Generation of cell lines; in vitro migration experiments. Detection of chromatin modifications induced by confined migration.
Funding Support:	NIH Physical Science Oncology Network – Transnetwork Project

Change in the support of the PI

Nothing to report

Other organizations involved as partners

Organization Name:	MD Anderson Cancer Center
Location:	Houston, TX
Contribution:	Collaboration on nuclear envelope rupture studies in fibrosarcoma cells, performing intravital imaging studies and single cell sequencing studies to detect increases in genomic instability following confined migration.

Organization Name:	Radboud University Medical Center
Location:	Nijmegen, Netherlands
Contribution:	Collaboration on nuclear envelope rupture studies, performing migration assays in collagen matrix. De-identified tissue microarrays.

8. SPECIAL REPORTING REQUIREMENTS

Not applicable.

9. APPENDIX

The appendix contains reprints of the following publications:

1. Kirby TJ. Lammerding J. Emerging views of the nucleus as a cellular mechanosensor. ***Nat Cell Biol*****.** 2018. 20(4): 373-381. Federal support acknowledged.
2. Yadav S, Feigelson S, Roncato F, Antman-Passig M, Shefi O, Lammerding J, Alon R. Elevated nuclear lamin A is permissive for granulocyte transendothelial migration but not for motility through collagen I barriers. ***J Leuk Biol***. 2018. 104(2): 239–251. Federal support acknowledged.
3. Singh A, Brito I, Lammerding J. Beyond tissue stiffness and bioadhesivity: advanced biomaterials to model tumor microenvironments and drug resistance. ***Trends in Cancer***. 2018. 4(4): 281-291. Federal support acknowledged.
4. Elacqua JJ, McGregor AL, Lammerding J. Automated analysis of cell migration and nuclear envelope rupture in confined environments. ***PLoS One***. 2018. 13(4): e0195664. Federal support acknowledged.
5. Keys J, Windsor A, Lammerding J. Assembly and use of a microfluidic device to study cell migration in confined environments. ***Methods Mol Biol***. 2018. 1840:101-118. Federal support acknowledged.
6. Zhang Q, Tamashunas A, Agrawal A, Torbati M, Katiyar A, Dickinson RB, Lammerding J, Lele TP. Local, transient tensile stress on the nuclear membrane causes membrane rupture. ***Mol Biol Cell***. 2019. 30(7): 899-906. Federal support acknowledged.
7. Maurer M, Lammerding J. The driving force: Nuclear mechanotransduction in cellular function, fate, and disease. ***Annu Rev Biomed Eng***. 2019. Published online March 27, 2019. Federal support acknowledged.
8. Zuela-Sopilniak N, Lammerding J. Engineering approaches to study cancer cell migration in 3D environments. ***Phil Trans Royal Society B***. Accepted for publication.
9. Picariello HS, Kenchappa RS, Rai V, Crish JF, Dovas A, Pagoda K, McMahon M, Bell ES, Chandrasekharan U, Luu A, West R, Lammerding J, Canoll P, Odde DJ, Janmey PA, Egelhoff1 T, Rosenfeld SS. Myosin IIA suppresses glioblastoma development in a mechanically sensitive manner. Currently in revision for ***PNAS***. Federal support acknowledged.
10. Davidson PM, Fedorchack GR, Mondesert-Deveraux S, Bell ES, Isermann P, Aubry D, Allena R, Lammerding J. High-throughput microfluidic micropipette aspiration device to probe time-scale dependent nuclear mechanics in intact cells. Submitted to ***Lab on a Chip***. Federal support acknowledged.

https://doi.org/10.1038/s41556-018-0038-y

Emerging views of the nucleus as a cellular mechanosensor

Tyler J. Kirby[1,2] and Jan Lammerding[1,2*]

The ability of cells to respond to mechanical forces is critical for numerous biological processes. Emerging evidence indicates that external mechanical forces trigger changes in nuclear envelope structure and composition, chromatin organization and gene expression. However, it remains unclear if these processes originate in the nucleus or are downstream of cytoplasmic signals. Here we discuss recent findings that support a direct role of the nucleus in cellular mechanosensing and highlight novel tools to study nuclear mechanotransduction.

Cells are constantly exposed to mechanical forces, such as shear forces on endothelial cells[1], compressive forces on chondrocytes[2] and tensile forces in myocytes[3]. The ability of cells to sense and respond to these mechanical cues is critical for numerous biological processes, including embryogenesis[4,5], development[4,5] and tissue homeostasis[6,7]. Although it has long been recognized that mechanical forces can influence cell morphology and behaviour[8,9], the understanding of the molecular pathways involved in mechanosensing, and how disruption of these pathways can give rise to various diseases, is still in progress[10–13]. Stretch-activated ion channels, adhesion complexes, cell–cell junctions and cytoskeletal components have all been identified as mechanosensitive elements that can activate cellular signalling pathways, such Rho-family GTPases or the mitogen-activated protein kinase–extracellular signal-regulated kinase (MAPK–ERK), induce nuclear translocation of the transcriptional regulators YAP/TAZ and MKL1, and ultimately result in expression of mechanoresponsive genes (see refs[14–18] for review). Over the last two decades, the question whether the nucleus itself can sense mechanical stimuli has received increasing attention[19,20]. Such 'nuclear mechanotransduction' could provide a more rapid and direct method to transduce forces into cellular events[21,22] and act in concert with or independent of cytoplasmic mechanotransduction pathways. In this scenario, forces applied to the nucleus through the cytoskeleton may modulate the effect of cytoplasmic signals or even be sufficient to directly trigger changes in gene expression. Such multi-faceted mechanotransduction may enable cells to distinguish between small forces that only affect the cell surface, and larger forces that result in large-scale deformations of the cell and nucleus. Encouraged in part by advances in biophysical, biochemical and imaging assays, multiple mechanisms have been proposed to explain how forces acting on the nucleus could influence chromatin organization, transcription and other cellular processes[19,22–24]. However, distinguishing between nuclear events that are downstream of cytoplasmic mechanosensitive signalling pathways, and those that reflect true nuclear mechanotransduction events, remains challenging.

One aspect, which is commonly accepted now, is that extracellular and cytoplasmic forces are transmitted across the nuclear envelope to the nuclear interior, where they can cause deformation of chromatin and nuclear bodies[20,25–27]. Intriguingly, a recent study has demonstrated that force application to the nucleus can induce chromatin stretching and expression of a reporter transgene[28]. These findings provide some of the most direct evidence to date for the nucleus as a mechanoresponsive organelle. Below we discuss current findings that support nuclear mechanotransduction, explain potential molecular mechanisms and highlight emerging technologies to study nuclear mechanotransduction.

The nucleus and the nuclear lamina

The nucleus is the largest and stiffest organelle in the cell[29,30]. It can broadly be separated into the nuclear interior (which contains chromatin), nuclear bodies and other intranuclear elements, and the surrounding nuclear envelope. The nuclear envelope consists of the outer and inner nuclear membranes (ONM and INM, respectively), which contain a large number of membrane-bound proteins[31,32], as well as nuclear pore complexes (NPCs) that control entry of large molecules into the nuclear interior[33]. Underneath the INM lies the nuclear lamina, a filamentous protein network that consists of A-type and B-type lamins, and lamin-binding proteins[34,35]. In mammalian somatic cells, the major A-type lamin isoforms are lamin A and C, encoded by the *LMNA* gene. One major reason to study the role of the nucleus in mechanotransduction came from the identification of *LMNA* mutations as the genetic cause for various forms of muscular dystrophy and cardiomyopathy[36–38]. Diseases caused by lamin mutations (commonly referred to as laminopathies) remain both intriguing and perplexing. Although A-type lamins are nearly ubiquitously expressed, many of the *LMNA* mutations predominantly affect mechanically active tissue, such as skeletal muscle, cardiac muscle and tendons. These tissue-specific disease phenotypes suggest that defects in the nucleus can impair the ability of cells to respond appropriately to mechanical forces. It is now well-recognized that the nuclear lamina governs numerous biological functions, both biophysical and biochemical, including determining nuclear size and stiffness[39–43], regulating translocation and activity of transcription factors[44–47], interacting with chromatin and regulating its epigenetic state[48,49], and controlling cell polarization and migration[50–52]. Consequently, cells lacking lamin A/C or expressing lamin A/C mutations linked to human diseases display severe defects in nuclear stability[53–55], cytoskeletal dynamics[47,51] and nucleo-cytoskeletal force transmission[55,56]. Furthermore, lamin-A/C-deficient and -mutant cells fail to adequately activate mechanoresponsive genes when subjected to mechanical stimulation[43,57,58], suggesting an important role of the nucleus, and lamin A/C in particular, in cellular mechanotransduction. However, it remains incompletely understood to what extent lamins directly respond to mechanical stress in vivo,

[1]Nancy E. and Peter C. Meinig School of Biomedical Engineering, Cornell University, Ithaca, NY, USA. [2]Weill Institute for Cell and Molecular Biology, Cornell University, Ithaca, NY, USA. *e-mail: jan.lammerding@cornell.edu

and whether changes in lamin levels and organization are downstream of other mechanotransduction pathways[26,59–61]. The importance of the nuclear lamina in fundamental biological processes is highlighted by the early death of mice that lack functional lamin A/C. These mice are born without any overt defects, but develop severe muscular dystrophy and dilated cardiomyopathy and die at 2–8 weeks of age[62,63]. Uncovering how lamins mediate nuclear processes and mechanosensitive gene expression will not only enhance our understanding of mechanotransduction per se, but may also provide insights into the pathophysiology of laminopathies, with the potential to inform therapeutic approaches for these currently incurable diseases.

Force transmission to the nucleus

Work by the Ingber group in the 1990s provided some of the first evidence that forces can be transmitted from the cell surface to the nucleus through the cytoskeleton[20]. It is now recognized that these forces are transmitted across the nuclear envelope through the 'linker of nucleoskeleton and cytoskeleton' (LINC) complex[64,65]. The LINC complex consists of nesprin proteins that reside within the ONM and contain a C-terminal KASH (Klarsicht, ANC-1, Syne homology) domain, which interacts with SUN (Sad1 Unc-84) domain-containing proteins located on the INM. The SUN proteins in turn bind to the nuclear lamina, nuclear pores and chromatin[66] (Fig. 1a). On the cytoplasmic side, nesprins can interact with each other and with all major cytoskeletal filaments. The composition of the LINC complex and LINC complex-associated proteins varies depending on the cell type. Furthermore, both nesprin-1 and nesprin-2 contain alternative start and stop sites that produce a number of isoforms, including the so-called 'giant' variants, which contain an N-terminal actin-binding domain[67]. Nesprin-1 and nesprin-2 can bind to actin filaments[67] and the microtubule-associated motor proteins kinesin[68] and dynein[69], nesprin-3 binds to plectin[70], which connects to intermediate filaments, whereas nesprin-4 interacts with kinesin-1[71] (Fig. 1a). Additional KASH-domain-containing proteins and LINC complex-associated proteins have recently been characterized and are often cell-type-specific. We refer the readers to recent reviews on the LINC complex for further details[34,66,67,72].

Whereas external forces can be applied to the nucleus independently of the LINC complex, for example, during compression of the nucleus[73] or cell migration through confined environments[74], cells in many cases require an intact LINC complex to effectively transmit forces between the cytoskeleton and the nucleus. Consequently, depletion or expression of dominant-negative nesprin or SUN proteins severely impairs nucleo-cytoskeletal force transmission[27] and mechanosensitive gene expression[28,75]. Nonetheless, it remains to be tested whether impaired mechanotransduction is due to the role of components of the LINC complex in intracellular force transmission, or whether these proteins contribute through other functions, such as serving as signalling scaffolds or regulating other aspects of nuclear organization including chromatin mobility and nuclear envelope tethering[49,76]. Force-induced nuclear deformation further requires an intact and adequately tensed cytoskeletal network[77,78] to transmit forces from the cell surface to the nucleus[22]. If the actin cytoskeleton is disrupted through pharmacological or genetic approaches, force transmission to the nucleus is impaired[78,79], which is accompanied by changes in chromatin dynamics[77]. Notably, mechanically induced changes in the nucleus, cytoskeleton and extracellular matrix appear to be interrelated. For example, the mechanical properties of the extracellular matrix affect both cytoskeletal organization[80] and expression of lamin A/C[61,81], resulting in cells that are finely tuned to their physical environment.

The intricate relationship between the cytoskeletal network, nuclear mechanics and the mechanical environment is particularly important for skeletal and cardiac muscle cells. These contractile cells have a highly organized cytoskeleton, including a specialized perinuclear network that anchors the nucleus in place (Fig. 1b). Desmin is a muscle-specific cytoplasmic intermediate filament that interacts with the nuclear envelope through plectin 1[82]. This interaction is important for myofibre health[83] and functional loss of plectin releases tension on the nucleus resulting in altered expression of mechanoresponsive genes[82]. LINC-complex proteins have similarly important functions in muscle cells. The LINC complex is required for myonuclear movement[84–87], including the effective spacing of nuclei along the myofibre length. Loss of LINC-complex function causes muscular dystrophies[88–90], suggesting that adequately connecting the nucleus to the cytoskeleton is crucial for skeletal muscle health and maintenance. This idea is further supported by the finding that *LMNA* mutations that cause muscular dystrophy and dilated cardiomyopathy result in impaired nucleo-cytoskeletal coupling[55,91,92] and loss of structural function, whereas *LMNA* mutations associated with lipodystrophy have little or no effect on nuclear mechanics and nucleo-cytoskeletal force transmission[55,91].

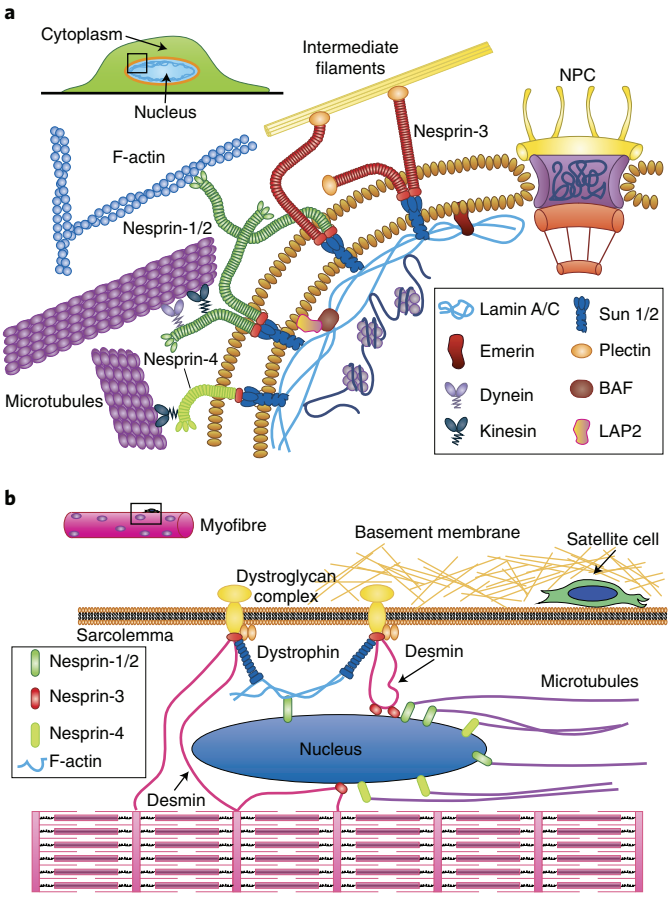

Fig. 1 | Schematic overview of nuclear envelope proteins involved in force transmission to the nucleus. a, Force transmission to the nucleus involves interaction of cytoskeletal elements (actin filaments, intermediate filaments, microtubules) with nesprin proteins on the ONM that transmit force through SUN domain proteins on the INM to the nuclear lamina and interior. **b**, Organization of the cytoskeletal network within muscle cells, including the highly ordered actin–myosin structures that form contractile sarcomeres and myofibrils. Nuclei are positioned at the periphery of the cell, where they interact with the muscle-specific proteins dystrophin (through actin filaments) and desmin. Additional proteins, such as LINC-complex proteins and lamins, may be involved in anchoring the myonuclei as well as generating and transmitting forces between the nucleus and cytoskeleton.

Although striated muscle tissues are affected the most by disruption in nuclear mechanics and nucleo-cytoskeletal coupling, many other cell types are also affected by impaired nucleo-cytoskeletal force transmission[93,94]. For example, T cell activation requires lamin A/C and the LINC complex to function properly to regulate T cell receptor clustering and F-actin formation[93]. In fibroblasts and endothelial cells, depletion of lamin A/C or disruption of the LINC complex reduces migration capabilities[94–96]. Similarly, the LINC complex is important in outer hair cells for hearing[97], proper function of the ciliary rootlets in photoreceptors and ependymal cells[98], hair follicle structure[99] and radial neuronal migration during neurogenesis[100]. These findings demonstrate the broad importance of nucleo-cytoskeletal force transmission on cellular function.

Potential mechanisms for nuclear mechanotransduction

The negative effects of lamin mutations and LINC complex disruption are well-documented, but the underlying molecular mechanisms remain incompletely understood. External forces are transmitted across the cytoskeleton to the nucleus, where they result in substantial deformation[101–103]. These forces and deformations could modulate transcriptional activity and chromatin organization through a number of mechanisms.

One potential mechanism to transduce forces acting on the nucleus into altered transcriptional activity is by modulating the physical organization of chromatin. The spatial location of the DNA within the nucleus exists in a non-random organization. This '4D nucleome' (meaning the 3D chromatin architecture and its change over time) is important for transcriptional regulation and cellular functions[104–107]. Heterochromatic DNA, which is tightly wrapped around histones and largely inaccessible for the transcriptional machinery, is often localized at the nuclear periphery[49]. This peripheral localization promotes gene silencing, whereas repositioning of genes towards the interior of the nucleus generally facilitates gene activation[108], although additional regulatory networks exist. Thus, force-induced changes in gene positioning relative to the nuclear periphery could alter the transcriptional activity of specific genes and contribute to nuclear mechanotransduction. Supporting this idea, altering cytoskeletal organization and tension by culturing cells on micropatterned substrates alters nuclear shape and chromosome distribution, accompanied by changes in gene expression[103,109]. It remains unclear to what extent these changes are the direct result of altered cytoskeletal forces acting on the nucleus versus upstream signalling pathways that may be sensitive to cytoskeletal organization. Extrinsic force application to cells can also induce repositioning of nuclear bodies and the associated chromatin[110–112], which could affect additional nuclear processes. Lastly, whereas changes in chromatin organization may be downstream of forces acting on the nucleus, the epigenetic state of chromatin also contributes to the mechanical properties of the nucleus: chromatin decondensation increases nuclear deformability and chromatin condensation decreases nuclear deformability[110,113–116], both of which may occur independently of changes in lamin levels[117]. Thus, changes in nuclear organization, even when downstream of other pathways, can have a direct effect on nuclear deformation and may thus modulate other nuclear mechanotransduction processes.

In addition to changes in gene or chromosome positioning, mechanical forces may directly alter chromatin organization and transcription. In vitro experiments indicate that 5 pN of force is sufficient to decondense single chromatin fibres[118]. Recent work from the Wang and Belmont laboratories demonstrated that applying force to the cell surface results in instantaneous stretching of chromatin inside the nucleus, associated with rapid induction of transcription of a transgene that is located within the stretched region of chromatin[28]. Notably, the level of transcription correlated with the frequency and magnitude of the applied forces, and disruption of the LINC complex abolished the force-mediated transcription response[28]. The finding that force-induced transcription occurred extremely rapidly (<30 seconds) suggests that the stretching of chromatin alters the accessibility of the transcriptional machinery to the gene or its activity, rather than altering the epigenetic state of the locus. Although highly intriguing, the directly mediated modulation of gene expression has not yet been demonstrated for endogenous genes. Furthermore, it remains to be investigated whether this mechanism of modulating gene transcription only applies to genes that are already 'primed' for transcription, or if it could also activate silenced genes, such as those in heterochromatic regions. Notably, prolonged force application induces an increase in heterochromatin and transcriptional repression[4], which could serve as a negative feedback mechanism. Lastly, it remains unclear how force-induced chromatin stretching would be able to confer specificity, as it is likely that multiple genomic loci are subjected to a similar level of mechanical force, and a direct association between mechanoresponsive genes and components of the LINC complex has not been demonstrated to date.

Force-induced molecular crowding could present another potential nuclear mechanotransduction mechanism. Nuclear deformation could also alter nuclear processes by local crowding and exclusion of soluble factors in areas where chromatin has been compacted. For example, exclusion of DNA-damage repair factors delays repair of DNA breaks[119,120]. Similarly, exclusion of transcriptional regulators or chromatin remodelling proteins could alter transcriptional activity.

Recent studies revealed that mechanical stress can induce conformational and post-translational changes (for example, phosphorylation) in nuclear envelope proteins[26,60,61,121] (Fig. 2). Force application on the nucleus results in apical-to-basal differences in the conformation of lamin A/C, as shown by the masking of certain C- and N-terminal epitopes under tension[60]. Exposing isolated nuclei to shear stress exposes a cryptic cysteine residue (Cys552) in the Ig-domain of lamin A/C, which is normally inaccessible during periods of low mechanical stress[61]. It remains to be investigated whether this residue becomes exposed under physiological forces in intact cells, as the N-terminal portion of the Ig-domain appears to be mostly inaccessible during periods of high mechanical stress in vivo[60]. Recent findings further indicate that reduced cytoskeletal tension, for example when cells are cultured on soft substrates, results in increased lamin A/C phosphorylation, which is associated with increased solubility and degradation[61,121]. By contrast, increased cytoskeletal tension results in decreased lamin A/C phosphorylation and higher lamin A/C levels[121]. Similarly, force application to isolated nuclei through the LINC complex causes phosphorylation of the INM protein emerin[26], which binds to lamin AC. It is unclear whether these phosphorylation events are triggered by increased residue accessibility after force-induced conformational changes, or whether force application modulates the activity of nuclear kinases such as Src[122]. Regardless of the specific mechanism, mutating the relevant Tyr74 and Tyr95 sites in emerin leads to decreased stress-fibre formation and decreased expression of SRF-dependent genes[26]. In response to prolonged force application, emerin may also serve to reinforce the actin network at the ONM and facilitate chromatin remodelling[4]. Although additional work is needed to elucidate the specific pathways involved, including whether emerin and lamin are downstream of other mechanosensitive signalling events and which biochemical signals are activated by their phosphorylation, these findings demonstrate the relevance of nuclear envelope proteins for modulation of transcriptional activity as well as nuclear and cytoskeletal organization.

Force-induced stretching of nuclear membranes could present an additional mechanism for nuclear mechanotransduction. Hypotonic swelling of the nuclear membranes results in translocation of nucleoplasmic phospholipase A2 (cPLA2) to the INM, which is inhibited when the nucleus is stabilized by either F-actin or lamin A/C[123]. This translocation directly activates cPLA2 and 5-LOX[123],

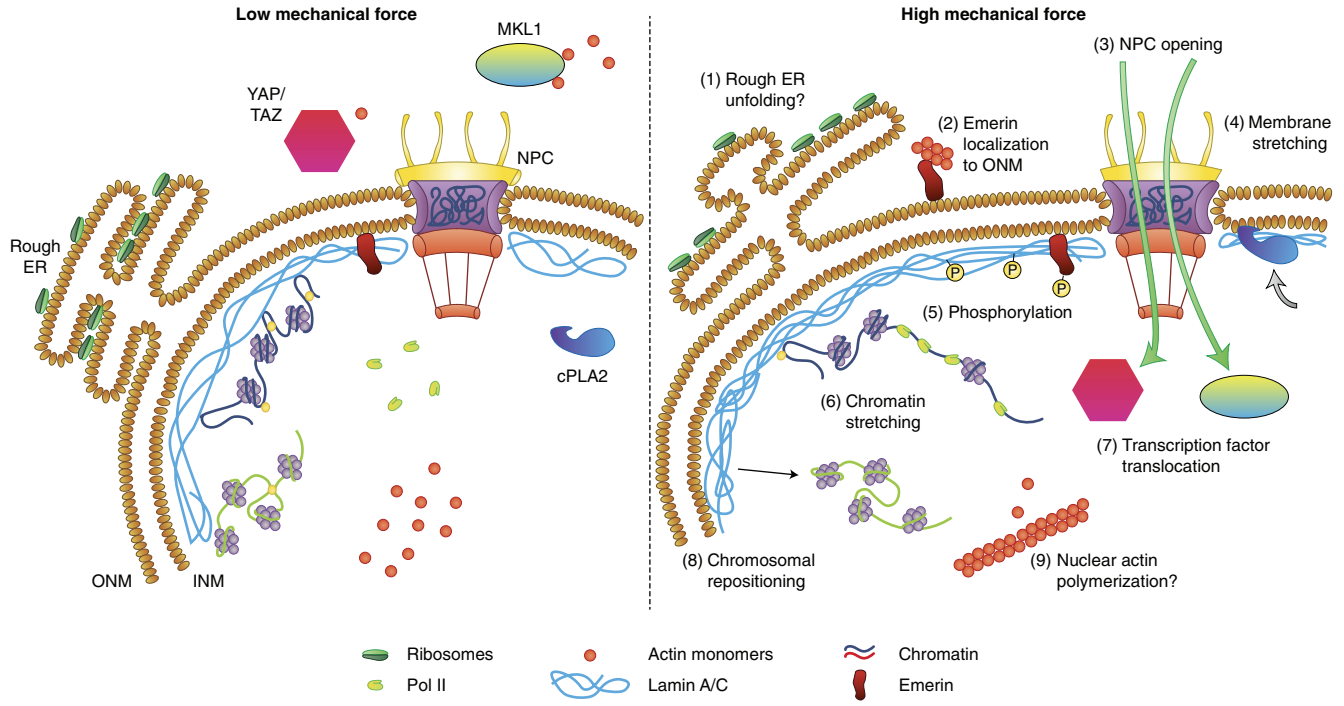

Fig. 2 | Proposed mechanisms for how the cell nucleus could respond directly to mechanical forces. (1) Stretching of the nuclear membrane could alter the conformation of the rough endoplasmic reticulum (ER), exposing more ribosomes to the cytoplasm. (2) Force application promotes translocation of emerin from the INM to the ONM, modulating chromatin organization and facilitating actin polymerization at the ONM. (3) Increased membrane tension could open NPCs and modulate NPC permeability. (4) Stretching of the nuclear membrane recruits cPLA2 to the INM. (5) Force transmission to the nucleus results in post-translational modification and altered dynamics of lamin A/C and INM proteins, such as emerin (see also (2)), which can modulate the mechanical properties of the nucleus and induce downstream signalling. (6) External forces can induce chromatin stretching, altering polymerase and transcription factor accessibility and activity. (7) Nuclear-pore opening and sequestration at the nuclear envelope can modulate localization and activity of transcription factors. (8) Forces acting on the nucleus may reposition chromatin domains, altering their transcriptional activity. (9) Mechanically induced polymerization of nuclear actin can modulate the export and activity of the transcriptional regulator MKL1, and affect other nuclear processes that require monomeric actin.

which are required for production of the chemotactic eicosanoids that attract leukocytes to sites of injury in vivo[123]. Because the underlying nuclear lamina is substantially stiffer than the nuclear membranes, it mechanically shields the nuclear membranes from large forces. At the same time, the nuclear lamina can tolerate substantially larger area strains than lipid membranes[115,116]. Thus, nuclear envelope composition and organization could markedly modulate the stretch response of the nuclear membrane. Furthermore, because the nuclear membranes are continuous with the endoplasmic reticulum, stretching of the nuclear membrane is expected to increase the membrane tension in the adjacent rough endoplasmic reticulum[124]. It will be interesting to determine whether increased membrane tension on the nucleus can alter the organization of the rough endoplasmic reticulum, and possibly the distribution of membrane-bound proteins in the endoplasmic reticulum[125]. For example, polysomes are enriched in the sheets rather than tubules of the endoplasmic reticulum[126], thus reducing membrane curvature could increase their exposure to the cytosol (Fig. 2).

An extreme form of nuclear mechanotransduction is force-induced nuclear membrane rupture. Compressive forces on the nucleus generated by actomyosin contractility can increase intranuclear pressure and result in nuclear membrane blebbing and transient loss of nuclear envelope integrity (that is, nuclear envelope rupture)[79,127–130]. Although these phenomena were first observed in cells that were deficient in lamin A/C, carried lamin A/C mutations[91] or had lower levels of B-type lamins[79], as well as in cancer cells with a compromised nuclear lamina[54], it is now apparent that all cells regularly exhibit transient nuclear envelope rupture. Defects in the nuclear lamina, increased actomyosin contractility and external confinement can markedly increase the incidence of nuclear envelope rupture from a few per cent to the majority of cells[79,131]. Cells typically restore nuclear envelope integrity and remain viable, but loss of nuclear envelope integrity results in uncontrolled exchange of cytoplasmic and nuclear proteins[91,128], mislocalization of organelles[54] and DNA damage[128,129]. The effect of nuclear envelope rupture on cell signalling, chromatin organization, gene expression and long-term outcomes remain incompletely understood and are topics of active investigation. Transcriptome analysis of nuclear rupture induced by severe cell compression revealed activation of DNA-damage response pathways, metabolism and nucleolar RNA production[132]. Recent findings additionally point to an important function of cGAS, a cytoplasmic DNA-binding protein first recognized for its activation of the STING pathways when encountering viral DNA in the cytoplasm[133]. The latest findings indicate that cGAS can also be activated when exposed to genomic DNA after nuclear envelope breakdown of micronuclei[134–137].

Increased nuclear membrane tension could also potentiate cytoplasmic signalling pathways by altering the permeability of NPCs (Fig. 2). Current models generated from the atomic structures of NPC components suggest that the NPCs can undergo conformational changes that constrict or dilate the NPC in response to mechanical force[138–140]. Force-mediated alterations to NPC conformations could arise from an increase in nuclear membrane tension or force transmission through LINC-complex proteins and nuclear lamins. Both Sun1 and lamin A/C interact with NUP153[141,142], a protein that comprises a portion of the NPC

basket[143]. In support of this mechanism, recent work by the Roca-Cusachs group found that direct force application to the nucleus is sufficient to promote nuclear entry of YAP, a mechanosensitive transcription factor[73]. The increase in nuclear YAP localization occurs through increased nuclear import of YAP, mediated by an increase in the permeability of the NPC for larger proteins, and the partial unfolding of YAP to further promote transition through the NPC[73]. Besides an increase in NPC permeability, other nuclear envelope proteins may modulate the import or export of mechanosensitive transcription factors, such as YAP/TAZ and MKL1[47,57,144], through additional mechanisms (Fig. 2). Lamin A/C has also been shown to sequester transcription factors, such as retinoblastoma protein[145,146] and Fos[44], at the nuclear periphery and thereby control their activity within the nucleus. Through these mechanisms, the nuclear lamina may further modulate gene expression and cell behaviour.

Whereas short-term force application has been shown to rapidly induce transcription[28,43], long-term force application (12 h) can result in a global increase in heterochromatin and transcriptional repression[4], suggesting that there may be a different response to force application that depends on the duration of stimulation. Future studies will also need to consider differences in the response across cell types, as certain cell types may have an increased susceptibility to chromatin stretching that results from differences in lamin A/C expression[61]. Lastly, although it appears that chromatin stretching can rapidly increase gene activation and PolII recruitment (Fig. 2), prolonged mechanical stimulation probably activates mechanoresponsive feedback mechanisms that further influence gene expression, nuclear organization and nucleo-cytoskeletal force transmission. Notably, mechanical force application to isolated nuclei through nesprins results in lamin-A/C recruitment and emerin phosphorylation, causing nuclear stiffening[26]. Thus, biochemical signalling pathways activated by mechanoresponsive genes could result in similar feedback loops that alter the responsiveness of the cell to further mechanical forces.

Technologies to study nuclear mechanotransduction

One major challenge in the field of nuclear mechanotransduction is uncoupling changes in nuclear structure, organization and transcription that are directly due to force application to the nucleus from those that are secondary to changes in cytoplasmic mechanosensitive signalling pathways. Addressing this challenge requires (1) improvements in the temporal resolution of nuclear events to distinguish between immediate and downstream consequences; (2) enhanced detection of force-induced changes in chromatin organization and local transcription; (3) direct measurements of intranuclear and perinuclear forces; and (4) experimental approaches that can physically separate contributions of mechanotransduction on the nucleus and cytoplasm.

One method to study the force-induced relocation of genes within the nucleus, or the local stretching and unfolding of chromatin loops within a single chromosomal region, is to insert arrays of LacO sequences into specific genomic loci and then fluorescently label these sites with GFP–LacI[28] (Fig. 3). This reporter system enables the assessment of how effective chromatin stretching, measured by an increased distance between adjacent GFP–LacI loci, corresponds to changes in gene expression of the reporter gene, which can be quantified by fluorescence in situ hybridization of the RNA transcript. Recent developments in the labelling of specific genomic regions of endogenous genes using CRISPR–Cas9 and related systems could help to overcome the challenge of having to insert large LacO arrays or using bacterial artificial chromosome reporters, and may even enable multi-colour imaging by using dCas9 constructs from different bacterial species, each tagged with a different fluorophore[147,148] (Fig. 3). Measuring changes in the 4D nucleome could be further aided by the use of

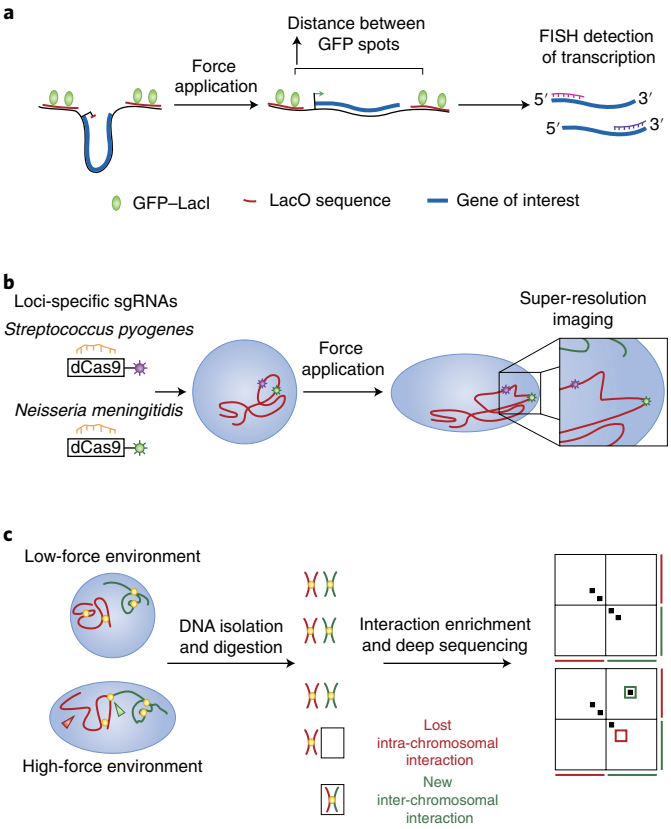

Fig. 3 | Technologies to study the effect of force transmission to the nucleus on genome organization and gene regulation. a, Schematic of a reporter transgene that measures chromatin stretching. The transgene is flanked by two fluorescently labelled regions of DNA. An increase in the distance between the fluorescent spots indicates effective chromatin stretching. Changes to the level of transcription of the transgene can be assessed by RNA fluorescence in situ hybridization (FISH), enabling analysis of the correlation between force-induced chromatin stretch and changes in transgene expression. **b**, Specific endogenous DNA loci can be fluorescently labelled using CRISPR–dCas9 from different species. Changes to the positioning and spacing between adjacent loci following force application can be determined with high resolution by fluorescence microscopy. **c**, Hi-C maps genome-wide chromatin interactions using deep sequencing, with changes to the interaction profile being displayed using heat maps. Interactions appear as hot spots off the diagonal.

super-resolution microscopy, which allows resolving of features that are 20–100 nm in intact cells[149] (Table 1). In addition to optical microscopy-based approaches, changes to the arrangement of chromosomes can be studied using sequence-based technology, such as Hi-C, which is based on chromosome conformation capture-based methodology[150] (Fig. 3). Hi-C can detect chromatin interactions across the entire genome, both within and between chromosomes, by covalently crosslinking protein–DNA complexes in their in situ configuration followed by deep sequencing. Whereas Hi-C is traditionally performed on large cell numbers (approximately 10^6 cells), approaches are currently under development that extent this technique to smaller cell numbers and even single cells[151]. Changes in the accessibility of DNA regions may provide additional information on force-induced changes in chromatin organization that could modulate transcriptional activity. One exciting approach is the assay for transposase-accessible chromatin using sequencing (ATAC-seq), which identifies accessible chromatin regions on the basis of the insertion of a hyperactive transposase and subsequent genome

Table 1 | Microscopy techniques: examples of super-resolution microscopy and their application to study nuclear processes and structures

Type of microscopy	Mechanism of action	Application to imaging nuclear structures
Stimulated emission depletion.	Enhances resolution by depleting fluorescence in specific regions of the sample while leaving a center focal spot active to emit fluorescence. This is achieved by generating a 'doughnut' around the focal spot using a second depletion laser beam.	γ-H2AX foci colocalizing with Ku foci[160]. Mobility of proteins being imported into the nucleus[161].
Spatially modulated illumination.	Spatially modulated illumination microscopy achieves higher spatial resolution by modulating the illuminating light along the optical axis, after which the sample is moved through a standing wave field at precise axial steps. This technique provides improved *z*-axis resolution for each of the fluorophores[162].	Chromatin compaction of specific loci[163]. Live-cell measurements of a Tet-operator repeat insert in U2OS cells[164].
Structured illumination microscopy.	Similar to spatially modulated illumination microscopy in that it generates a spatially modulated illumination pattern; however this occurs along the object plane (*x*, *y*) rather than the optical (*z*) plane[165]. Multiple images are acquired and then computationally combined to generate an image with twice the resolution than traditional wide-field microscopy[165].	RecA bundle formation and localization[166]. NPC colocalization with channels in the lamin network and peripheral heterochromatin[167].
Photo-activated localization microscopy and stochastic optical reconstruction microscopy.	Identify precise locations of individual fluorophores by using photoswitchable fluorophores to achieve optical isolation of the signal[168].	Volume of chromatin in different epigenetic states[169]. H2B localization in interphase cells[170].

fragmentation and sequencing[152]. Applying Hi-C and ATAC-seq analyses to cells in high- and low-force environments, or to cells before and after nuclear force application, should provide detailed information on how external forces alters the spatial interactome of chromatin, which could be further coupled with RNA-sequencing analyses to determine whether chromatin changes correspond to changes in gene transcription.

Molecular tension sensors can provide insights into the forces applied across specific cellular structures. Biophysical measurements of intact cells and isolated nuclei indicate that approximately 1–10 nN are required to induce substantial nuclear deformation[116,153,154]. The recent development of a nesprin tension biosensor has enabled the first measurements of forces transmitted across the LINC complex[25,155]. Using an artificial nesprin-2 giant construct containing a Förster resonance energy transfer (FRET)-based tension module, it was shown that force transmission changed with both myosin activity and cell elongation, and that the basal and apical sections of the nucleus are exposed to different forces[25]. Potential limitations of the current version of the tension sensor include a low signal-to-noise ratio, the insertion site of the FRET tension module, and a limit of the force range of about 6 pN[156,157], encouraging further work in this area.

Lastly, one way to circumvent the confounding cytoplasmic signalling events that arise from applying force at the cell surface is to study isolated nuclei or to use micromanipulation to apply force in close proximity to the nucleus[158,159]. Using magnetic beads bound to the cytoplasmic domain of nesprins allows studying the role of the LINC complex in nuclear mechanotransduction and targeting specific nesprin isoforms[26]. One limitation of using isolated nuclei is that the isolation procedure may perturb nuclear structure, as well as the chemical composition of the nuclear interior (for example, ion concentrations, ATP levels and molecular crowding), which could affect nuclear mechanics and other nuclear processes[42]. Furthermore, working with isolated nuclei limits experiments to studying factors that originate within the nucleus and excludes studying the import of cytoplasmic factors. Disrupting the LINC complex in intact cells allows exchange of biochemical molecules and can help to identify events that require force transmission to the nucleus and nuclear deformation[159]. However, external force application may still induce nuclear deformation through LINC-complex independent mechanisms.

Future perspective

The field of mechanobiology has substantially evolved and advanced in the past two decades, greatly increasing our knowledge of how mechanical cues govern cell behaviour. It is now well-recognized that nuclear envelope proteins have an important role in the cellular response to mechanical stimuli, and that forces are transmitted from the cell surface and cytoskeleton to the interior of the nucleus. Findings suggest that the nucleus can act as a cellular mechanosensor. Nonetheless, many questions remain, including to what extent the nucleus itself responds to mechanical forces, where such nuclear mechanotransduction processes occur, and whether these nuclear processes complement or act in parallel or downstream of cytoplasmic signalling pathways. To further untangle the strong interplay between the nucleus, cytoskeleton and cell surface will require an integrative approach that uses biophysical assays, genetic manipulation, high-throughput genomics and proteomics, and live-cell imaging with high spatial and temporal resolution. Furthermore, experimental approaches must be used that attempt to uncouple nuclear changes due to indirect mechanisms (that is, cytoplasmic signals that modulate chromatin organization and transcription) from force-induced, nucleus-intrinsic events, for example, by utilizing models in which nuclear force transmission is disrupted while other cytoplasmic mechanosensitive pathways remain intact. Unravelling the force-sensitive molecular regulatory networks controlled by the nucleus and the nuclear lamina will not only increase our understanding of cellular mechanotransduction, but may also encourage the development of novel therapeutical approaches to treat the currently incurable diseases that arise from impaired nuclear mechanics and mechanotransduction.

Received: 16 October 2017; Accepted: 9 January 2018;
Published online: 21 February 2018

References

1. Dewey, C. F. Jr, Bussolari, S. R., Gimbrone, M. A. Jr & Davies, P. F. The dynamic response of vascular endothelial cells to fluid shear stress. *J. Biomech. Eng.* **103**, 177–185 (1981).
2. Freeman, P. M., Natarajan, R. N., Kimura, J. H. & Andriacchi, T. P. Chondrocyte cells respond mechanically to compressive loads. *J. Orthop. Res.* **12**, 311–320 (1994).

3. Magid, A. & Law, D. J. Myofibrils bear most of the resting tension in frog skeletal muscle. *Science* **230**, 1280–1282 (1985).
4. Le, H. Q. et al. Mechanical regulation of transcription controls Polycomb-mediated gene silencing during lineage commitment. *Nat. Cell Biol.* **18**, 864–875 (2016).
5. Lecuit, T. & Lenne, P. F. Cell surface mechanics and the control of cell shape, tissue patterns and morphogenesis. *Nat. Rev. Mol. Cell Biol.* **8**, 633–644 (2007).
6. Barnes, J. M., Przybyla, L. & Weaver, V. M. Tissue mechanics regulate brain development, homeostasis and disease. *J. Cell Sci.* **130**, 71–82 (2017).
7. Matthews, B. D., Overby, D. R., Mannix, R. & Ingber, D. E. Cellular adaptation to mechanical stress: role of integrins, Rho, cytoskeletal tension and mechanosensitive ion channels. *J. Cell Sci.* **119**, 508–518 (2006).
8. Reidy, M. A. & Bowyer, D. E. Scanning electron microscopy of arteries. The morphology of aortic endothelium in haemodynamically stressed areas associated with branches. *Atherosclerosis* **26**, 181–194 (1977).
9. Tucker, J. B. & Meats, M. Microtubules and control of insect egg shape. *J. Cell Biol.* **71**, 207–217 (1976).
10. Ingber, D. E. Mechanobiology and diseases of mechanotransduction. *Ann. Med.* **35**, 564–577 (2003).
11. Jaalouk, D. E. & Lammerding, J. Mechanotransduction gone awry. *Nat. Rev. Mol. Cell Biol.* **10**, 63–73 (2009).
12. Iskratsch, T., Wolfenson, H. & Sheetz, M. P. Appreciating force and shape—the rise of mechanotransduction in cell biology. *Nat. Rev. Mol. Cell Biol.* **15**, 825–833 (2014).
13. Humphrey, J. D., Dufresne, E. R. & Schwartz, M. A. Mechanotransduction and extracellular matrix homeostasis. *Nat. Rev. Mol. Cell Biol.* **15**, 802–812 (2014).
14. Muehlich, S., Hermanns, C., Meier, M. A., Kircher, P. & Gudermann, T. Unravelling a new mechanism linking actin polymerization and gene transcription. *Nucleus* **7**, 121–125 (2016).
15. Panciera, T., Azzolin, L., Cordenonsi, M. & Piccolo, S. Mechanobiology of YAP and TAZ in physiology and disease. *Nat. Rev. Mol. Cell Biol.* **18**, 758–770 (2017).
16. Ross, T. D. et al. Integrins in mechanotransduction. *Curr. Opin. Cell Biol.* **25**, 613–618 (2013).
17. Sun, Z., Guo, S. S. & Fassler, R. Integrin-mediated mechanotransduction. *J. Cell Biol.* **215**, 445–456 (2016).
18. Murthy, S. E., Dubin, A. E. & Patapoutian, A. Piezos thrive under pressure: mechanically activated ion channels in health and disease. *Nat. Rev. Mol. Cell Biol.* **18**, 771–783 (2017).
19. Fedorchak, G. R., Kaminski, A. & Lammerding, J. Cellular mechanosensing: getting to the nucleus of it all. *Prog. Biophys. Mol. Biol.* **115**, 76–92 (2014).
20. Maniotis, A. J., Chen, C. S. & Ingber, D. E. Demonstration of mechanical connections between integrins, cytoskeletal filaments, and nucleoplasm that stabilize nuclear structure. *Proc. Natl Acad. Sci. USA* **94**, 894–854 (1997).
21. Chambliss, A. B. et al. The LINC-anchored actin cap connects the extracellular milieu to the nucleus for ultrafast mechanotransduction. *Sci. Rep.* **3**, 1087 (2013).
22. Wang, N., Tytell, J. D. & Ingber, D. E. Mechanotransduction at a distance: mechanically coupling the extracellular matrix with the nucleus. *Nat. Rev. Mol. Cell Biol.* **10**, 75–82 (2009).
23. Cho, S., Irianto, J. & Discher, D. E. Mechanosensing by the nucleus: from pathways to scaling relationships. *J. Cell Biol.* **216**, 305–315 (2017).
24. Miroshnikova, Y. A., Nava, M. M. & Wickstrom, S. A. Emerging roles of mechanical forces in chromatin regulation. *J. Cell Sci.* **130**, 2243–2250 (2017).
25. Arsenovic, P. T. et al. Nesprin-2G, a component of the nuclear LINC complex, is subject to myosin-dependent tension. *Biophys. J.* **110**, 34–43 (2016).
26. Guilluy, C. et al. Isolated nuclei adapt to force and reveal a mechanotransduction pathway in the nucleus. *Nat. Cell Biol.* **16**, 376–381 (2014).
27. Lombardi, M. L. et al. The interaction between nesprins and sun proteins at the nuclear envelope is critical for force transmission between the nucleus and cytoskeleton. *J. Biol. Chem.* **286**, 26743–26753 (2011).
28. Tajik, A. et al. Transcription upregulation via force-induced direct stretching of chromatin. *Nat. Mater.* **15**, 1287–1296 (2016).
29. Caille, N., Thoumine, O., Tardy, Y. & Meister, J. J. Contribution of the nucleus to the mechanical properties of endothelial cells. *J. Biomech.* **35**, 177–187 (2002).
30. Lammerding, J. Mechanics of the nucleus. *Compr. Physiol.* **1**, 783–807 (2011).
31. Dreger, M., Bengtsson, L., Schoneberg, T., Otto, H. & Hucho, F. Nuclear envelope proteomics: novel integral membrane proteins of the inner nuclear membrane. *Proc. Natl Acad. Sci. USA* **98**, 11943–11948 (2001).
32. Worman, H. J. & Schirmer, E. C. Nuclear membrane diversity: underlying tissue-specific pathologies in disease? *Curr. Opin. Cell Biol.* **34**, 101–112 (2015).
33. Jovanovic-Talisman, T. & Zilman, A. Protein transport by the nuclear pore complex: simple biophysics of a complex biomachine. *Biophys. J.* **113**, 6–14 (2017).
34. de Leeuw, R., Gruenbaum, Y. & Medalia, O. Nuclear lamins: thin filaments with major functions. *Trends Cell Biol.* **28**, 34–45 (2018).
35. Ho, C. Y. & Lammerding, J. Lamins at a glance. *J. Cell Sci.* **125**, 2087–2093 (2012).
36. Genschel, J. & Schmidt, H. H. Mutations in the LMNA gene encoding lamin A/C. *Hum. Mutat.* **16**, 451–459 (2000).
37. Bonne, G. et al. Mutations in the gene encoding lamin A/C cause autosomal dominant Emery–Dreifuss muscular dystrophy. *Nat. Genet.* **21**, 285–288 (1999).
38. Fatkin, D. et al. Missense mutations in the rod domain of the lamin A/C gene as causes of dilated cardiomyopathy and conduction-system disease. *N. Engl. J. Med.* **341**, 1715–1724 (1999).
39. Lammerding, J. et al. Lamins A and C but not lamin B1 regulate nuclear mechanics. *J. Biol. Chem.* **281**, 25768–25780 (2006).
40. Zwerger, M. et al. Altering lamina assembly reveals lamina-dependent and -independent functions for A-type lamins. *J. Cell Sci.* **128**, 3607–3620 (2015).
41. Broers, J. L. et al. Decreased mechanical stiffness in *LMNA*$^{-/-}$ cells is caused by defective nucleo-cytoskeletal integrity: implications for the development of laminopathies. *Hum. Mol. Genet.* **13**, 2567–2580 (2004).
42. Dahl, K. N., Kahn, S. M., Wilson, K. L. & Discher, D. E. The nuclear envelope lamina network has elasticity and a compressibility limit suggestive of a molecular shock absorber. *J. Cell Sci.* **117**, 4779–4786 (2004).
43. Lammerding, J. et al. Lamin A/C deficiency causes defective nuclear mechanics and mechanotransduction. *J. Clin. Invest.* **113**, 370–378 (2004).
44. Ivorra, C. et al. A mechanism of AP-1 suppression through interaction of c-Fos with lamin A/C. *Genes Dev.* **20**, 307–320 (2006).
45. Osmanagic-Myers, S., Dechat, T. & Foisner, R. Lamins at the crossroads of mechanosignaling. *Genes Dev.* **29**, 225–237 (2015).
46. Dorner, D. et al. Lamina-associated polypeptide 2α regulates cell cycle progression and differentiation via the retinoblastoma–E2F pathway. *J. Cell Biol.* **173**, 83–93 (2006).
47. Ho, C. Y., Jaalouk, D. E., Vartiainen, M. K. & Lammerding, J. Lamin A/C and emerin regulate MKL1–SRF activity by modulating actin dynamics. *Nature* **497**, 507–511 (2013).
48. Harr, J. C. et al. Directed targeting of chromatin to the nuclear lamina is mediated by chromatin state and A-type lamins. *J. Cell Biol.* **208**, 33–52 (2015).
49. Solovei, I. et al. LBR and lamin A/C sequentially tether peripheral heterochromatin and inversely regulate differentiation. *Cell* **152**, 584–598 (2013).
50. Harada, T. et al. Nuclear lamin stiffness is a barrier to 3D migration, but softness can limit survival. *J. Cell Biol.* **204**, 669–682 (2014).
51. Lee, J. S. et al. Nuclear lamin A/C deficiency induces defects in cell mechanics, polarization, and migration. *Biophys. J.* **93**, 2542–2552 (2007).
52. Davidson, P. M., Denais, C., Bakshi, M. C. & Lammerding, J. Nuclear deformability constitutes a rate-limiting step during cell migration in 3-D environments. *Cell. Mol. Bioeng.* **7**, 293–306 (2014).
53. Robijns, J. et al. In silico synchronization reveals regulators of nuclear ruptures in lamin A/C deficient model cells. *Sci. Rep.* **6**, 30325 (2016).
54. Vargas, J. D., Hatch, E. M., Anderson, D. J. & Hetzer, M. W. Transient nuclear envelope rupturing during interphase in human cancer cells. *Nucleus* **3**, 88–100 (2012).
55. Zwerger, M. et al. Myopathic lamin mutations impair nuclear stability in cells and tissue and disrupt nucleo-cytoskeletal coupling. *Hum. Mol. Genet.* **22**, 2335–2349 (2013).
56. Folker, E. S., Ostlund, C., Luxton, G. W., Worman, H. J. & Gundersen, G. G. Lamin A variants that cause striated muscle disease are defective in anchoring transmembrane actin-associated nuclear lines for nuclear movement. *Proc. Natl Acad. Sci. USA* **108**, 131–136 (2011).
57. Bertrand, A. T. et al. Cellular microenvironments reveal defective mechanosensing responses and elevated YAP signaling in LMNA-mutated muscle precursors. *J. Cell Sci.* **127**, 2873–2884 (2014).
58. Cupesi, M. et al. Attenuated hypertrophic response to pressure overload in a lamin A/C haploinsufficiency mouse. *J. Mol. Cell. Cardiol.* **48**, 1290–1297 (2010).
59. Buxboim, A. et al. Coordinated increase of nuclear tension and lamin-A with matrix stiffness out-competes lamin-B receptor which favors soft tissue phenotypes. *Mol. Biol. Cell* **28**, 3333–3348 (2017).
60. Ihalainen, T. O. et al. Differential basal-to-apical accessibility of lamin A/C epitopes in the nuclear lamina regulated by changes in cytoskeletal tension. *Nat. Mater.* **14**, 1252–1261 (2015).
61. Swift, J. et al. Nuclear lamin-A scales with tissue stiffness and enhances matrix-directed differentiation. *Science* **341**, 1240104 (2013).
62. Sullivan, T. et al. Loss of A-type lamin expression compromises nuclear envelope integrity leading to muscular dystrophy. *J. Cell Biol.* **147**, 913–920 (1999).

63. Kubben, N. et al. Post-natal myogenic and adipogenic developmental: defects and metabolic impairment upon loss of A-type lamins. *Nucleus* **2**, 195–207 (2011).
64. Alam, S. G. et al. The nucleus is an intracellular propagator of tensile forces in NIH 3T3 fibroblasts. *J. Cell Sci.* **128**, 1901–1911 (2015).
65. Crisp, M. & Burke, B. The nuclear envelope as an integrator of nuclear and cytoplasmic architecture. *FEBS Lett.* **582**, 2023–2032 (2008).
66. Chang, W., Worman, H. J. & Gundersen, G. G. Accessorizing and anchoring the LINC complex for multifunctionality. *J. Cell Biol.* **208**, 11–22 (2015).
67. Rajgor, D. & Shanahan, C. M. Nesprins: from the nuclear envelope and beyond. *Expert Rev. Mol. Med.* **15**, e5 (2013).
68. Wilson, M. H. & Holzbaur, E. L. Nesprins anchor kinesin-1 motors to the nucleus to drive nuclear distribution in muscle cells. *Development* **142**, 218–228 (2015).
69. Fridolfsson, H. N., Ly, N., Meyerzon, M. & Starr, D. A. UNC-83 coordinates kinesin-1 and dynein activities at the nuclear envelope during nuclear migration. *Dev. Biol.* **338**, 237–250 (2010).
70. Wilhelmsen, K. et al. Nesprin-3, a novel outer nuclear membrane protein, associates with the cytoskeletal linker protein plectin. *J. Cell Biol.* **171**, 799–810 (2005).
71. Roux, K. J. et al. Nesprin 4 is an outer nuclear membrane protein that can induce kinesin-mediated cell polarization. *Proc. Natl Acad. Sci. USA* **106**, 2194–2199 (2009).
72. Horn, H. F. LINC complex proteins in development and disease. *Curr. Top. Dev. Biol.* **109**, 287–321 (2014).
73. Elosegui-Artola, A. et al. Force triggers YAP nuclear entry by regulating transport across nuclear pores. *Cell* **171**, 1397–1410 (2017).
74. Thiam, H. R. et al. Perinuclear Arp2/3-driven actin polymerization enables nuclear deformation to facilitate cell migration through complex environments. *Nat. Commun.* **7**, 10997 (2016).
75. Banerjee, I. et al. Targeted ablation of nesprin 1 and nesprin 2 from murine myocardium results in cardiomyopathy, altered nuclear morphology and inhibition of the biomechanical gene response. *PLoS Genet.* **10**, e1004114 (2014).
76. Lottersberger, F., Karssemeijer, R. A., Dimitrova, N. & de Lange, T. 53BP1 and the LINC complex promote microtubule-dependent DSB mobility and DNA repair. *Cell* **163**, 880–893 (2015).
77. Makhija, E., Jokhun, D. S. & Shivashankar, G. V. Nuclear deformability and telomere dynamics are regulated by cell geometric constraints. *Proc. Natl Acad. Sci. USA* **113**, 32–40 (2016).
78. Keeling, M. C., Flores, L. R., Dodhy, A. H., Murray, E. R. & Gavara, N. Actomyosin and vimentin cytoskeletal networks regulate nuclear shape, mechanics and chromatin organization. *Sci. Rep.* **7**, 5219 (2017).
79. Hatch, E. M. & Hetzer, M. W. Nuclear envelope rupture is induced by actin-based nucleus confinement. *J. Cell Biol.* **215**, 27–36 (2016).
80. Yeung, T. et al. Effects of substrate stiffness on cell morphology, cytoskeletal structure, and adhesion. *Cell Motil. Cytoskelet.* **60**, 24–34 (2005).
81. Swift, J. & Discher, D. E. The nuclear lamina is mechano-responsive to ECM elasticity in mature tissue. *J. Cell Sci.* **127**, 3005–3015 (2014).
82. Staszewska, I., Fischer, I. & Wiche, G. Plectin isoform 1-dependent nuclear docking of desmin networks affects myonuclear architecture and expression of mechanotransducers. *Hum. Mol. Genet.* **24**, 7373–7389 (2015).
83. Konieczny, P. et al. Myofiber integrity depends on desmin network targeting to Z-disks and costameres via distinct plectin isoforms. *J. Cell Biol.* **181**, 667–681 (2008).
84. Stroud, M. J. et al. Nesprin 1α2 is essential for mouse postnatal viability and nuclear positioning in skeletal muscle. *J. Cell Biol.* **216**, 1915–1924 (2017).
85. Bone, C. R. & Starr, D. A. Nuclear migration events throughout development. *J. Cell Sci.* **129**, 1951–1961 (2016).
86. Collins, M. A. et al. Emery–Dreifuss muscular dystrophy-linked genes and centronuclear myopathy-linked genes regulate myonuclear movement by distinct mechanisms. *Mol. Biol. Cell* **28**, 2303–2317 (2017).
87. Roman, W. et al. Myofibril contraction and crosslinking drive nuclear movement to the periphery of skeletal muscle. *Nat. Cell Biol.* **19**, 1189–1201 (2017).
88. Zhang, Q. et al. Nesprin-1 and -2 are involved in the pathogenesis of Emery Dreifuss muscular dystrophy and are critical for nuclear envelope integrity. *Hum. Mol. Genet.* **16**, 2816–2833 (2007).
89. Puckelwartz, M. J. et al. Disruption of nesprin-1 produces an Emery Dreifuss muscular dystrophy-like phenotype in mice. *Hum. Mol. Genet.* **18**, 607–620 (2009).
90. Stroud, M. J., Banerjee, I., Veevers, J. & Chen, J. Linker of nucleoskeleton and cytoskeleton complex proteins in cardiac structure, function, and disease. *Circ. Res.* **114**, 538–548 (2014).
91. De Vos, W. H. et al. Repetitive disruptions of the nuclear envelope invoke temporary loss of cellular compartmentalization in laminopathies. *Hum. Mol. Genet.* **20**, 4175–4186 (2011).
92. Zuela, N., Zwerger, M., Levin, T., Medalia, O. & Gruenbaum, Y. Impaired mechanical response of an EDMD mutation leads to motility phenotypes that are repaired by loss of prenylation. *J. Cell Sci.* **129**, 1781–1791 (2016).
93. Gonzalez-Granado, J. M. et al. Nuclear envelope lamin-A couples actin dynamics with immunological synapse architecture and T cell activation. *Sci. Signal.* **7**, ra37 (2014).
94. Khatau, S. B. et al. The distinct roles of the nucleus and nucleus-cytoskeleton connections in three-dimensional cell migration. *Sci. Rep.* **2**, 488 (2012).
95. Chang, W., Antoku, S., Ostlund, C., Worman, H. J. & Gundersen, G. G. Linker of nucleoskeleton and cytoskeleton (LINC) complex-mediated actin-dependent nuclear positioning orients centrosomes in migrating myoblasts. *Nucleus* **6**, 77–88 (2015).
96. King, S. J. et al. Nesprin-1 and nesprin-2 regulate endothelial cell shape and migration. *Cytoskeleton* **71**, 423–434 (2014).
97. Horn, H. F. et al. The LINC complex is essential for hearing. *J. Clin. Invest.* **123**, 740–750 (2013).
98. Potter, C. et al. Multiple isoforms of nesprin1 are integral components of ciliary rootlets. *Curr. Biol.* **27**, 2014–2022 (2017).
99. Stewart, R. M. et al. Nuclear–cytoskeletal linkages facilitate cross talk between the nucleus and intercellular adhesions. *J. Cell Biol.* **209**, 403–418 (2015).
100. Zhang, X. et al. SUN1/2 and syne/nesprin-1/2 complexes connect centrosome to the nucleus during neurogenesis and neuronal migration in mice. *Neuron* **64**, 173–187 (2009).
101. Khatau, S. B. et al. A perinuclear actin cap regulates nuclear shape. *Proc. Natl Acad. Sci. USA* **106**, 19017–19022 (2009).
102. Driscoll, T. P., Cosgrove, B. D., Heo, S. J., Shurden, Z. E. & Mauck, R. L. Cytoskeletal to nuclear strain transfer regulates YAP signaling in mesenchymal stem cells. *Biophys. J.* **108**, 2783–2793 (2015).
103. Ramdas, N. M. & Shivashankar, G. V. Cytoskeletal control of nuclear morphology and chromatin organization. *J. Mol. Biol.* **427**, 695–706 (2015).
104. Geyer, P. K., Vitalini, M. W. & Wallrath, L. L. Nuclear organization: taking a position on gene expression. *Curr. Opin. Cell Biol.* **23**, 354–359 (2011).
105. Chen, H. et al. Functional organization of the human 4D Nucleome. *Proc. Natl Acad. Sci. USA* **112**, 8002–8007 (2015).
106. Misteli, T. Beyond the sequence: cellular organization of genome function. *Cell* **128**, 787–800 (2007).
107. Sexton, T., Schober, H., Fraser, P. & Gasser, S. M. Gene regulation through nuclear organization. *Nat. Struct. Mol. Biol.* **14**, 1049–1055 (2007).
108. Zullo, J. M. et al. DNA sequence-dependent compartmentalization and silencing of chromatin at the nuclear lamina. *Cell* **149**, 1474–1487 (2012).
109. Wang, Y., Nagarajan, M., Uhler, C. & Shivashankar, G. V. Orientation and repositioning of chromosomes correlate with cell geometry-dependent gene expression. *Mol. Biol. Cell* **28**, 1997–2009 (2017).
110. Spagnol, S. T. & Dahl, K. N. Spatially resolved quantification of chromatin condensation through differential local rheology in cell nuclei fluorescence lifetime imaging. *PLoS ONE* **11**, e0146244 (2016).
111. Booth-Gauthier, E. A., Alcoser, T. A., Yang, G. & Dahl, K. N. Force-induced changes in subnuclear movement and rheology. *Biophys. J.* **103**, 2423–2431 (2012).
112. Poh, Y. C. et al. Dynamic force-induced direct dissociation of protein complexes in a nuclear body in living cells. *Nat. Commun.* **3**, 866 (2012).
113. Spagnol, S. T., Armiger, T. J. & Dahl, K. N. Mechanobiology of chromatin and the nuclear interior. *Cell. Mol. Bioeng.* **9**, 268–276 (2016).
114. Chalut, K. J. et al. Chromatin decondensation and nuclear softening accompany Nanog downregulation in embryonic stem cells. *Biophys. J.* **103**, 2060–2070 (2012).
115. Dahl, K. N., Engler, A. J., Pajerowski, J. D. & Discher, D. E. Power-law rheology of isolated nuclei with deformation mapping of nuclear substructures. *Biophys. J.* **89**, 2855–2864 (2005).
116. Stephens, A. D., Banigan, E. J., Adam, S. A., Goldman, R. D. & Marko, J. F. Chromatin and lamin A determine two different mechanical response regimes of the cell nucleus. *Mol. Biol. Cell* **28**, 1984–1996 (2017).
117. Stephens, A. D. et al. Chromatin histone modifications and rigidity affect nuclear morphology independent of lamins. *Mol. Biol. Cell* **29**, 220–233 (2018).
118. Cui, Y. & Bustamante, C. Pulling a single chromatin fiber reveals the forces that maintain its higher-order structure. *Proc. Natl Acad. Sci. USA* **97**, 127–132 (2000).
119. Bennett, R. R. et al. Elastic-fluid model for DNA damage and mutation from nuclear fluid segregation due to cell migration. *Biophys. J.* **112**, 2271–2279 (2017).
120. Irianto, J. et al. DNA damage follows repair factor depletion and portends genome variation in cancer cells after pore migration. *Curr. Biol.* **27**, 210–223 (2017).
121. Buxboim, A. et al. Matrix elasticity regulates lamin-A, C phosphorylation and turnover with feedback to actomyosin. *Curr. Biol.* **24**, 1909–1917 (2014).

122. Tifft, K. E., Bradbury, K. A. & Wilson, K. L. Tyrosine phosphorylation of nuclear-membrane protein emerin by Src, Abl and other kinases. *J. Cell Sci.* **122**, 3780–3790 (2009).
123. Enyedi, B., Jelcic, M. & Niethammer, P. The cell nucleus serves as a mechanotransducer of tissue damage-induced inflammation. *Cell* **165**, 1160–1170 (2016).
124. Enyedi, B. & Niethammer, P. Nuclear membrane stretch and its role in mechanotransduction. *Nucleus* **8**, 156–161 (2017).
125. Heald, R. & Cohen-Fix, O. Morphology and function of membrane-bound organelles. *Curr. Opin. Cell Biol.* **26**, 79–86 (2014).
126. Shibata, Y. et al. Mechanisms determining the morphology of the peripheral ER. *Cell* **143**, 774–788 (2010).
127. Isermann, P. & Lammerding, J. Consequences of a tight squeeze: nuclear envelope rupture and repair. *Nucleus* **8**, 268–274 (2017).
128. Denais, C. M. et al. Nuclear envelope rupture and repair during cancer cell migration. *Science* **352**, 353–358 (2016).
129. Raab, M. et al. ESCRT III repairs nuclear envelope ruptures during cell migration to limit DNA damage and cell death. *Science* **352**, 359–362 (2016).
130. Takaki, T. et al. Actomyosin drives cancer cell nuclear dysmorphia and threatens genome stability. *Nat. Commun.* **8**, 16013 (2017).
131. Lammerding, J. & Wolf, K. Nuclear envelope rupture: actin fibers are putting the squeeze on the nucleus. *J. Cell Biol.* **215**, 5–8 (2016).
132. Le Berre, M., Aubertin, J. & Piel, M. Fine control of nuclear confinement identifies a threshold deformation leading to lamina rupture and induction of specific genes. *Integr. Biol.* **4**, 1406–1414 (2012).
133. Sun, L., Wu, J., Du, F., Chen, X. & Chen, Z. J. Cyclic GMP–AMP synthase is a cytosolic DNA sensor that activates the type I interferon pathway. *Science* **339**, 786–791 (2013).
134. Gluck, S. et al. Innate immune sensing of cytosolic chromatin fragments through cGAS promotes senescence. *Nat. Cell Biol.* **19**, 1061–1070 (2017).
135. Harding, S. M. et al. Mitotic progression following DNA damage enables pattern recognition within micronuclei. *Nature* **548**, 466–470 (2017).
136. Mackenzie, K. J. et al. cGAS surveillance of micronuclei links genome instability to innate immunity. *Nature* **548**, 461–465 (2017).
137. Dou, Z. et al. Cytoplasmic chromatin triggers inflammation in senescence and cancer. *Nature* **550**, 402–406 (2017).
138. Chug, H., Trakhanov, S., Hulsmann, B. B., Pleiner, T. & Gorlich, D. Crystal structure of the metazoan Nup62•Nup58•Nup54 nucleoporin complex. *Science* **350**, 106–110 (2015).
139. Stuwe, T. et al. Architecture of the fungal nuclear pore inner ring complex. *Science* **350**, 56–64 (2015).
140. Solmaz, S. R., Blobel, G. & Melcak, I. Ring cycle for dilating and constricting the nuclear pore. *Proc. Natl Acad. Sci. USA* **110**, 5858–5863 (2013).
141. Liu, Q. et al. Functional association of Sun1 with nuclear pore complexes. *J. Cell Biol.* **178**, 785–798 (2007).
142. Jahed, Z., Soheilypour, M., Peyro, M. & Mofrad, M. R. The LINC and NPC relationship—it's complicated! *J. Cell Sci.* **129**, 3219–3229 (2016).
143. Fahrenkrog, B. & Aebi, U. The nuclear pore complex: nucleocytoplasmic transport and beyond. *Nat. Rev. Mol. Cell Biol.* **4**, 757–766 (2003).
144. Dupont, S. et al. Role of YAP/TAZ in mechanotransduction. *Nature* **474**, 179–183 (2011).
145. Dorner, D., Gotzmann, J. & Foisner, R. Nucleoplasmic lamins and their interaction partners, LAP2α, Rb, and BAF, in transcriptional regulation. *FEBS J.* **274**, 1362–1373 (2007).
146. Markiewicz, E., Dechat, T., Foisner, R., Quinlan, R. A. & Hutchison, C. J. Lamin A/C binding protein LAP2α is required for nuclear anchorage of retinoblastoma protein. *Mol. Biol. Cell* **13**, 4401–4413 (2002).
147. Ma, H. et al. Multicolor CRISPR labeling of chromosomal loci in human cells. *Proc. Natl Acad. Sci. USA* **112**, 3002–3007 (2015).
148. Shao, S. et al. Long-term dual-color tracking of genomic loci by modified sgRNAs of the CRISPR/Cas9 system. *Nucleic Acids Res.* **44**, e86 (2016).
149. Donnert, G. et al. Macromolecular-scale resolution in biological fluorescence microscopy. *Proc. Natl Acad. Sci. USA* **103**, 11440–11445 (2006).
150. Belton, J. M. et al. Hi-C: a comprehensive technique to capture the conformation of genomes. *Methods* **58**, 268–276 (2012).
151. Nagano, T. et al. Single-cell Hi-C reveals cell-to-cell variability in chromosome structure. *Nature* **502**, 59–64 (2013).
152. Buenrostro, J. D., Wu, B., Chang, H. Y. & Greenleaf, W. J. ATAC-seq: a method for assaying chromatin accessibility genome-wide. *Curr. Protoc. Mol. Biol.* **109**, 21.29.1–21.29.9 (2015).
153. Neelam, S. et al. Direct force probe reveals the mechanics of nuclear homeostasis in the mammalian cell. *Proc. Natl Acad. Sci. USA* **112**, 5720–5725 (2015).
154. Krause, M., Te Riet, J. & Wolf, K. Probing the compressibility of tumor cell nuclei by combined atomic force-confocal microscopy. *Phys. Biol.* **10**, 065002 (2013).
155. Arsenovic, P. T., Bathula, K. & Conway, D. E. A protocol for using Förster resonance energy transfer (FRET)-force biosensors to measure mechanical forces across the nuclear LINC complex. *J. Vis. Exp.* **122**, e54902 (2017).
156. Grashoff, C. et al. Measuring mechanical tension across vinculin reveals regulation of focal adhesion dynamics. *Nature* **466**, 263–266 (2010).
157. Meng, F., Suchyna, T. M., Lazakovitch, E., Gronostajski, R. M. & Sachs, F. Real time FRET based detection of mechanical stress in cytoskeletal and extracellular matrix proteins. *Cell. Mol. Bioeng.* **4**, 148–159 (2011).
158. Fedorchak, G. & Lammerding, J. Cell Microharpooning to study nucleo-cytoskeletal coupling. *Methods Mol. Biol.* **1411**, 241–254 (2016).
159. Lombardi, M. L., Zwerger, M. & Lammerding, J. Biophysical assays to probe the mechanical properties of the interphase cell nucleus: substrate strain application and microneedle manipulation. *J. Vis. Exp.* **55**, e3087 (2011).
160. Britton, S., Coates, J. & Jackson, S. P. A new method for high-resolution imaging of Ku foci to decipher mechanisms of DNA double-strand break repair. *J. Cell Biol.* **202**, 579–595 (2013).
161. Bianchini, P., Cardarelli, F., Di Luca, M., Diaspro, A. & Bizzarri, R. Nanoscale protein diffusion by STED-based pair correlation analysis. *PLoS ONE* **9**, e99619 (2014).
162. Failla, A. V., Spoeri, U., Albrecht, B., Kroll, A. & Cremer, C. Nanosizing of fluorescent objects by spatially modulated illumination microscopy. *Appl. Opt.* **41**, 7275–7283 (2002).
163. Hildenbrand, G. et al. Nano-sizing of specific gene domains in intact human cell nuclei by spatially modulated illumination light microscopy. *Biophys. J.* **88**, 4312–4318 (2005).
164. Reymann, J. et al. High-precision structural analysis of subnuclear complexes in fixed and live cells via spatially modulated illumination (SMI) microscopy. *Chromosome Res.* **16**, 367–382 (2008).
165. Cremer, C., Szczurek, A., Schock, F., Gourram, A. & Birk, U. Super-resolution microscopy approaches to nuclear nanostructure imaging. *Methods* **123**, 11–32 (2017).
166. Lesterlin, C., Ball, G., Schermelleh, L. & Sherratt, D. J. RecA bundles mediate homology pairing between distant sisters during DNA break repair. *Nature* **506**, 249–253 (2014).
167. Schermelleh, L. et al. Subdiffraction multicolor imaging of the nuclear periphery with 3D structured illumination microscopy. *Science* **320**, 1332–1336 (2008).
168. Henriques, R., Griffiths, C., Hesper Rego, E. & Mhlanga, M. M. PALM and STORM: unlocking live-cell super-resolution. *Biopolymers* **95**, 322–331 (2011).
169. Boettiger, A. N. et al. Super-resolution imaging reveals distinct chromatin folding for different epigenetic states. *Nature* **529**, 418–422 (2016).
170. Ricci, M. A., Manzo, C., Garcia-Parajo, M. F., Lakadamyali, M. & Cosma, M. P. Chromatin fibers are formed by heterogeneous groups of nucleosomes in vivo. *Cell* **160**, 1145–1158 (2015).

Acknowledgements

We apologize to all authors whose work could not be cited due to space constraints. This work was supported by awards from the National Institutes of Health (R01 HL082792 and U54 CA210184), the Department of Defense Breast Cancer Research Program (Breakthrough Award BC150580), the National Science Foundation (CAREER Award CBET-1254846 and MCB-1715606) and a Fleming Postdoctoral Fellowship to T.J.K.

Competing interests

The authors declare no competing interests.

Additional information

Reprints and permissions information is available at www.nature.com/reprints.

Correspondence and requests for materials should be addressed to J.L.

Publisher's note: Springer Nature remains neutral with regard to jurisdictional claims in published maps and institutional affiliations.

DOI: 10.1002/JLB.3HI1217-488R

JLB JOURNAL OF LEUKOCYTE BIOLOGY

HIGHLIGHTED ARTICLE

Frontline Science: Elevated nuclear lamin A is permissive for granulocyte transendothelial migration but not for motility through collagen I barriers

Sandeep Kumar Yadav[1] | Sara W. Feigelson[1] | Francesco Roncato[1] | Merav Antman-Passig[2] | Orit Shefi[2] | Jan Lammerding[3] | Ronen Alon[1]

[1]Department of Immunology, The Weizmann Institute of Science, Rehovot, Israel

[2]Faculty of Engineering, Bar Ilan Institute of Nanotechnologies and Advanced Materials, Bar Ilan University, Ramat Gan, Israel

[3]Nancy E. and Peter C. Meinig School of Biomedical Engineering, Weill Institute for Cell and Molecular Biology, Cornell University, Ithaca, New York, USA

Correspondence
Ronen Alon, Ph.D., Department of Immunology, The Weizmann Institute of Science, Rehovot, 76100, Israel.
Email: ronen.alon@weizmann.ac.il

Abstract

Transendothelial migration (TEM) of lymphocytes and neutrophils is associated with the ability of their deformable nuclei to displace endothelial cytoskeletal barriers. Lamin A is a key intermediate filament component of the nuclear lamina that is downregulated during granulopoiesis. When elevated, lamin A restricts nuclear squeezing through rigid confinements. To determine if the low lamin A expression by leukocyte nuclei is critical for their exceptional squeezing ability through endothelial barriers, we overexpressed this protein in granulocyte-like differentiated HL-60 cells. A 10-fold higher lamin A expression did not interfere with chemokinetic motility of these granulocytes on immobilized CXCL1. Furthermore, these lamin A high leukocytes exhibited normal chemotaxis toward CXCL1 determined in large pore transwell barriers, but poorly squeezed through 3 μm pores toward identical CXCL1 gradients. Strikingly, however, these leukocytes successfully completed paracellular TEM across inflamed endothelial monolayers under shear flow, albeit with a small delay in nuclear squeezing into their sub-endothelial pseudopodia. In contrast, CXCR2 mediated granulocyte motility *through* collagen I barriers was dramatically delayed by lamin A overexpression due to a failure of lamin A high nuclei to translocate into the pseudopodia of the granulocytes. Collectively, our data predict that leukocytes maintain a low lamin A content in their nuclear lamina in order to optimize squeezing through extracellular collagen barriers but can tolerate high lamin A content when crossing the highly adaptable barriers presented by the endothelial cytoskeleton.

KEYWORDS
chemokines, chemotaxis, granulocytes, inflammation, motility

1 | INTRODUCTION

The nucleus is the largest cellular organelle and is mechanically stabilized by a constitutive network of laminar proteins.[1] Nucleus deformation is the rate-limiting step for cells to pass through constrictions that are smaller than the nucleus size.[1–5] The mechanical stability of the nucleus, particularly for large deformations, is dictated by lamins, intermediate filaments proteins that form a network underlying the inner nuclear membrane.[4,6,7] Lamin A and its spliced variant lamin C impart the nucleus with its mechanical stability whereas the lamin B1 and B2 intermediate filaments are ubiquitously expressed but appear to be less important in mechanical stability of nuclei.[8] The nuclei of both circulating T cells and neutrophils are soft due to a low content of lamin A/C and B in their lamina.[9] Furthermore, in contrast to epithelial and mesenchymal cells and solid tumors, which usually keep their stiff nuclei at their rear, motile leukocytes translocate their soft nucleus to their leading edge (pseudopodia) irrespective of the barriers they cross.[10] However, the relationship between lamin composition, nuclear stiffness and nucleus location, and the impact of each of these parameters on the squeezing ability of leukocytes and other cells remains obscure.

Abbreviations: 2D, two-dimensional; 3D, three-dimensional; dHL-60, differentiated HL-60 cells; HDMVEC, human dermal micro-vascular endothelial cells; OE, overexpressing; TEM, transendothelial migration

Received: 11 December 2017 | Revised: 15 February 2018 | Accepted: 16 February 2018

It has been traditionally argued that leukocyte squeezing through endothelial barriers and extracellular barriers composed of collagen fibers involves passage through sub-micron wide gaps. Recent reports suggest, however, that leukocyte TEM involves a considerable widening of paracellular endothelial junctions as well as transcellular endothelial channels by the squeezing leukocyte.[10,11] This leukocyte driven widening involves large displacement of endothelial stress fibers rather than active endothelial contractility.[10,11] Our real-time imaging of nuclei in transmigrating leukocytes also suggested that the endothelial gap widening by squeezing leukocytes is driven by nuclear lobes, which are either preexistent or de novo formed by the deformable nuclei of T cells.[10] This recent analysis of nuclear squeezing dynamics also raised the possibility that nuclear deformation determines both the gap size generated by squeezing leukocytes during TEM and the dynamics of nuclear squeezing.[10] Leukocyte nuclei appear to function as mechanical "drillers" that displace and collapse different actin assemblies within the endothelial cytoskeleton.[10] Nevertheless, a direct molecular demonstration that nuclear deformation and mechanical stiffness determine leukocyte passage through endothelial barriers and control gap sizes has been missing.

To address these standing questions, we have used a model system based on differentiated HL-60, human promyelocytic leukemia cells, which upon in vitro differentiation give rise to either granulocyte-like leukocytes or macrophages.[12] Whereas genetic manipulation of freshly isolated neutrophils is difficult and can result in side effects caused by the procedures required for ectopic gene expression, HL-60 cells can be readily transfected or transduced with target vectors prior to their differentiation into short-lived granulocyte-like cells. This line has therefore been widely used for structural and functional assays of leukocytes.[12–15] Forced expression of lamin A in a similar HL-60 system, differentiated using all-trans-retinoic acid stimulation for 5 days, impaired nuclear lobulation during differentiation and inhibited serum triggered leukocyte perfusion through narrow channels and migration through rigid pores.[16] We used a similar system of DMSO differentiated HL-60 to generate granulocyte-like cells with 10-fold higher expression of lamin A. Having validated that the ability of these cells to transit through rigid micron-scale constrictions is severely compromised, we further investigated the ability of these leukocytes to squeeze through inflamed endothelial monolayers as well as through distinct fibrous barriers. Our results indicate that granulocytes overexpressing lamin A successfully adhered to and squeezed through confluent inflamed endothelial cell monolayers and successfully completed TEM in response to chemotactic signals, displacing the endothelial cytoskeleton and translocating their body underneath the monolayer, albeit with slightly delayed rates and creating larger pores in the endothelial layer. On the other hand, these lamin A enriched cells exhibited major defects in their ability to migrate through collagen I barriers in response to similar chemotactic signals. Our results suggest that chemokine-guided leukocyte squeezing through different cytoskeletal and extracellular matrix barriers is restricted to different extents by a given alteration in the stiffness of the leukocyte nuclear lamina.

2 | MATERIALS AND METHODS

2.1 | Reagents and antibodies

Human CXCL1 was purchased from Peprotech (Rocky Hill, NJ, USA). PE-anti-human CD11a, PE-anti-human/mouse CD11b (M1/70), PE-anti-human CD29, and PE-anti-human CXCR2 antibodies were purchased from Ebioscience-Thermo Fisher Scientific (Waltham, MA, USA). HECA-452 was purchased from BD Bioscience Pharmingen (Franklin Lakes, New Jersey, USA). Anti CD18 mAb (TS1/18) was a kind gift from D. Staunton (ICOS, Bothell, WA, USA). Anti-lamin A/C mAb was purchased from Santa Cruz Biotechnology (Dallas, Texas, USA). Rabbit polyclonal anti-human Lamin B1 was a kind gift from E. Gomes (University of Lisbon). Alexa 647 anti VE-cadherin mAb was purchased from Biolegend (San Diego, CA). R-Phycoerythrin AffiniPure F(ab')2 fragment goat anti-rat IgM (μ chain specific) and goat anti-mouse IgG (H+L) antibodies were purchased from Jackson ImmunoResearch Laboratories (West Grove, PA, USA). BSA (fraction V), Hoechst, HEPES, $CaCl_2$, $MgCl_2$, and HBSS were purchased from Sigma–Aldrich (St. Louis, MO, USA).

2.2 | Cell culture

The CXCR2-HL-60 cell variant line was described elsewhere.[17] Both parental HL-60[15,16,31] and the CXCR2-HL-60 variants were grown in RPMI-1640 medium supplemented with 20 mM HEPES, 10% fetal calf serum, L-glutamine, and Pen-Strep-Amphotericin. Cells were maintained at less than 1×10^6 cells/ml and differentiated into granulocyte-like cells (dHL-60) by culturing for 7 days in culture medium supplemented with 1.3% (v/v) DMSO. Granulocyte-like appearance was confirmed by upregulation of CD11a and CD11b (Supplementary Fig. 1A, B). HDMVECs (C-12211; PromoCell, Heidelberg, Germany) were grown in PromoCell EC medium MV (C-22020), according to manufacturer's protocol and were used at passages 2–3.

2.3 | Retroviral transduction

Stably modified lamin A overexpressing (Lamin A-OE) CXCR2-HL-60 cells were generated by retroviral transduction with a bicistronic vector pRetroX-PrelaminA-IRES-ZsGreen1 as described.[16] A ZsGreen1 retroviral vector was used to generate the mock control cells. Retroviruses were produced by transfecting Phoenix cells using Lipofectamine® 2000 reagent following manufacturer's protocol. Retrovirus containing supernatant was collected at 48 h post transfection and used fresh to infect CXCR2-HL-60 cells in the presence of 4 mg/ml polybrene (Sigma). Cells were either sorted and maintained at >90% purity or taken as a mixture of lamin A-ZsGreen1 expressing and non-expressing cells for differentiation into granulocyte like cells using DMSO.

2.4 | Flow cytometry

For analysis of integrin or chemokine surface expression, cells were incubated with primary fluorescence-labeled mAb (CD11a,

CD29, CD11b: 10 μg/ml) or unlabeled mAb (CXCR2, CD18, HECA-452: 10 μg/ml) followed by secondary antibodies (1:100, Jackson Immunoresearch) for 20 min at 4°C per incubation. For intracellular stainings, cells were fixed in chilled 80% methanol for 5 min, followed by 3 washes and permeabilization with tween (0.1%, PBS, 20 min at room temperature). Cells were incubated with anti-CD16/CD32 (10 μg/ml diluted in 10% goat serum) for 20 min at room temperature for blockage of Fc receptors. Cells were then incubated with primary antibody (anti-Lamin A/C or mIgG isotype control) diluted in 10% goat serum for 30 min at room temperature, washed, and stained with phycoerythrin-labeled goat anti-mouse secondary antibodies (1:100) for 30 min at room temperature in the dark. Antibody stainings and washes were carried out in fluorescence-activated cell sorting (FACS) buffer (Ca^{2+} and Mg^{2+} free PBS (PBS-/-), 1% BSA, 5 mM EDTA, and 0.01% sodium azide). Stained cell suspensions were washed and resuspended in PBS+/+ prior to analysis by CytoFlex flow cytometer (Beckman Coulter). Data were acquired with CytExpert software (Beckman Coulter) and post-acquisition analysis was performed using FlowJo software (Tree Star).

2.5 | Cell proliferation assay

A total of 250,000 cells/ml were plated (Day 0) in a 10 cm culture plate. Cell count was determined every 24 h over the course of 4 d by forward and side scattering and by ZsGreen1 fluorescence in a Cytoflex Flow Cytometer (Beckman Coulter Life Sciences, USA).

2.6 | Analysis of leukocyte migration under shear flow

Primary HDMVECs were plated at confluence on either plastic or glass bottom 60 mm petri dishes coated with 2 μg/ml fibronectin (cat. # F0895; Sigma–Aldrich, USA). A day later, cells were stimulated for 3 h with IL-1β (2 ng/ml). Endothelial cell coated plates were assembled in a flow chamber and washed extensively with the binding medium HBSS (HBSS containing 2 mg/ml BSA and 10 mM HEPES, pH 7.4, supplemented with 1 mM $CaCl_2$ and 1 mM $MgCl_2$). Neutrophil-like cells were perfused over the monolayer in binding medium for 40 s at 1.5 dyn/cm^2, and were then subjected to a shear stress of 5 dyn/cm^2 for 10 min. Images were acquired at an interval of 15 sec using IX83, Olympus microscope equipped with 20 × or 60 × phase contrast objectives. Cells were tracked individually using ImageJ and categorized in at least 3 fields of view (~50 cells per field) as previously described.[18,19]

For analysis of migratory categories, leukocytes accumulated during the accumulation phase (40 s) were individually tracked throughout the assay by time-lapse microscopy and categorized as fractions of leukocytes originally accumulated at the end of this accumulation phase. Crawling leukocytes were defined as cells moving a distance of at least 30 μm from their initial point of arrest. Transmigrating leukocytes were defined as either arrested or crawling cells which translocated their entire body through the endothelial monolayer. To monitor nuclear translocation and shape changes during TEM, cells were labeled with Hoechst 33342 as described[10] shortly before their introduction into the flow chamber. The location of pseudopodia sent by individual transmigrating dHL-60 cells and their respective nuclei were manually determined from time-lapse recordings (images were captures at 15 s intervals). Gap size generated by transmigrating Hoechst labeled dHL-60 cells was determined as described by the displacement of a non-blocking Alexa 647 anti-VE-cadherin mAb[10] (incubated at 2 μg/ml, 10 min prior to the beginning of the TEM assay). Since the majority of the gaps were oval, an average of both the long and short axes was calculated for each gap generated by transmigrating granulocyte-like dHL-60 cells.

2.7 | Transwell migration assay

Differentiated HL-60 cells were washed with PBS(-/-) containing 5 mM EDTA, resuspended at a density of 2×10^6 cells/ml in binding medium HBSS (described above), and seeded in the upper chamber of 24-well transwells with 3 or 5 μm pore sizes (BD Biosciences, San Jose, CA, USA). The bottom chambers were filled with the corresponding media supplemented with and without CXCL1 (50 ng/ml) and incubated at 37°C in 5% CO_2 for 30 min. The transwell inserts were removed, the cells recovered from the bottom chambers were collected, and their numbers were determined by FACS analysis using the CytoFlex flow cytometer (Beckman Coulter).

2.8 | Nuclear shape analysis and location

Hoechst 33342 labeled granulocyte-like HL-60 cells were allowed to settle for 15 min at 37°C on poly-L-Lysine (PLL) coated glass surface prepared by incubating PLL (0.01% w/v in ddH_2O) for 30 min at 37°C. Images were acquired using a 20× objective (IX83, Olympus, Shinjuku, Tokyo, Japan). Nuclear circularity index was determined using ImageJ. Similarly, nuclear circularity index was determined for Hoechst labeled granulocyte like HL-60 cells migrating over immobilized CXCL1. Thirty consecutive frames were captured for each granulocyte at 15 s intervals, and the circularity index values in each frame were averaged for each cell. Nuclear location in each of these cells was manually determined. The nuclear locations of polarized and motile granulocytes were classified manually using CellSens Dimension Desktop software (Olympus) as either anterior and posterior based on whether the nuclei remained confined to either the leading or trailing edges, respectively for at least half of the total assay period.

2.9 | Chemokine mediated two-dimensional and three-dimensional cell motility assays

Ibidi chamber slides (μ-Slide VI 0.4, Ibidi) were coated with 50 ng/ml CXCL1. Granulocyte-like dHL-60 cells were washed and resuspended in binding solution, injected into the Ibidi chamber, and allowed to settle for 10 min at 37°C, and images were acquired with a 20× or 60× objective (IX83, Olympus). Velocity calculations were performed using ImageJ and trajectory analysis was performed using Imaris 9.0.0 (Bitplane, Belfast, UK) software. For three-dimensional (3D) migration assays, granulocyte-like dHL-60 cells were washed and resuspended in cold matrigel solution (BD-356234, stock solution

mixed with binding medium at 1:1 ratio) or in cold collagen I solution (rat tail, Corning, 3.2 mg/ml in binding medium) and injected into the Ibidi chamber at 4°C. The cells were sedimented at 50 × *g* for 3 min and incubated under the matrigel or collagen I solutions at 37°C for 30 min to allow collagen polymerization. Images were acquired with a 20× or 60× objective (IX83, Olympus) for 30 min at intervals of 60 s. Nuclear location and granulocyte velocities were determined with ImageJ software.

2.10 | Confocal reflectance microscopy

Collagen I and matrigel solutions were prepared as described above, plated in 35 mm petri dishes and incubated for 30 min at 37°C in a humidified incubator. Gels were imaged using a Leica TCS SP5 confocal microscope by a 63×, 0.9 NA water immersion lens. Samples were illuminated with 488 nm Argon laser light and the meta channel of the microscope was set to detect wavelengths between 474 and 494 nm to allow reflectance mode.[20]

2.11 | Scanning electron microscopy of collagen matrices

Samples were fixed using 2.4% paraformaldehyde/2.5% glutaraldehyde in 0.1 M sodium cacodylate buffer for 1 h at room temperature. After fixation, samples were rinsed repeatedly with PBS-/- (without Ca^{2+} or Mg^{2+}, pH 7.4) and then treated with guanidine-HCl/tannic acid (4:5) solution (2%) for 1 h at room temperature. Samples were rinsed repeatedly with PBS-/- and then dehydrated in a graded series of 50, 70, 80, 90, and 100% ethanol/water (v/v) for 10 min each. The residual ethanol was then removed using a series of 50, 75, and 100% (×3) Freon solutions in ethanol for 10 min each. Finally, the samples were air dried for few seconds. The dried samples were mounted on aluminum stubs, sputter coated with carbon, and viewed with the scanning electron microscopy (FEI Quanta 250 FEG, OR, USA).

2.12 | Statistical analysis

All the data are reported as the sample mean ± SD or SEM, as indicated, and means of different groups were compared pairwise using two-tailed, unpaired Student's *t*-test. The difference between 2 datasets was considered significant for *p* values below 0.05.

3 | RESULTS

3.1 | Lamin A overexpression in granulocyte-like cells does not affect their chemokinesis but restricts migration through small, rigid pores

Primary neutrophils as well as granulocyte-like differentiated HL-60 cells (dHL-60) downregulate expression of the nuclear lamina proteins lamin A and C during differentiation.[9] In our experiments, we used a variant of HL-60 that stably expresses CXCR2 levels comparable to those in primary neutrophils[21] in order to facilitate migration of these leukocytes across CXCL1-producing inflamed endothelial cell monolayers. This introduced CXCR2 expression was critical for the ability of these cells to cross IL-1β-stimulated human dermal micro-vascular endothelial cells, a well-studied low permeability endothelial barrier, which supports robust neutrophil accumulation and TEM under physiological shear flow[10,19] (Fig. 1A and data not shown). To overexpress lamin A in these HL-60 variants, we infected them with an IRES containing retroviral vector co-encoding the pre lamin A precursor and a ZsGreen1 reporter as previously described.[16] ZsGreen1 expressing cells were found to have 10-fold higher levels of lamin A than control CXCR2-HL-60 cells, when differentiated with DMSO into granulocyte-like cells (Fig. 1B). Importantly, lamin A overexpression in these granulocyte-like leukocytes did not impair their proliferation rates, nor alter Lamin B1 expression, CXCR2 levels, or change the levels of major integrin members or the expression of E-selectin carbohydrate ligands (Fig. 1C-H and Supplemenatry Fig. 1C, D). Lamin A overexpression also did not affect chemokinetic motility of the differentiated granulocyte-like CXCR2-HL-60 cells (henceforth referred to as CXCR2-dHL-60) measured on a two-dimensional (2D) surface coated with the CXCR2 chemokine CXCL1 (Fig. 1I). The lamin A overexpressing granulocyte-like dHL-60 cells also normally crossed through 5 μm pore transwells toward a CXCL1 gradient, comparable to non-modified control cells (Fig. 2A). However, when compared for their ability to squeeze toward identical CXCL1 gradients through transwells containing 3 μm pores, which are substantially smaller than their nuclear diameter, only a minute fraction of lamin A-OE CXCR2-dHL-60 successfully passed through these smaller pores, whereas control CXCR2-dHL-60 cells showed efficient migration through these pores, albeit less than in the larger pores (Fig. 2A). Notably, lamin A overexpression did not change the nuclear shape of these differentiated HL-60 cells as assessed by the average circularity of the nuclei in these granulocyte-like cells settled on a poly-L-lysine substrate (Fig. 2B,C). Given that lamin A overexpression had only a moderate or no effect on nuclear circularity (Fig. 2B-D), we conclude that the impaired migration of lamin A overexpressing CXCR2-dHL-60 cells through 3 μm pores is caused by the increased nuclear stiffness due to higher lamin levels, and not an increase in nuclear circularity. These migration results are consistent with previous findings in dHL-60 granulocyte-like cells obtained by all-trans-retinoic acid treatment.[16]

To further validate that the ZsGreen1 reporter on its own is inert in our various assays, the ZsGreen1 gene alone was introduced into CXCR2-dHL-60 cells by an identical viral vector, and both ZsGreen1 expressing and non-expressing CXCR2-dHL-60 cells were compared for their ability to cross rigid transwell pores and transmigrate across inflamed endothelial barriers. As expected, the ZsGreen1 expressing granulocyte-like CXCR2-dHL-60 normally crossed through small rigid pores toward CXCL1 gradients (Supplementary Fig. 1E). Thus, high-level expression of the ZsGreen1 reporter, on its own, does not alter the mechanical properties and squeezing capacity of CXCR2-dHL-60 cells. This observation also suggested that the ZsGreen1 negative granulocyte-like CXCR2-dHL-60 cells are practically identical to ZsGreen1 expressing granulocyte-like CXCR2-dHL-60 cells with

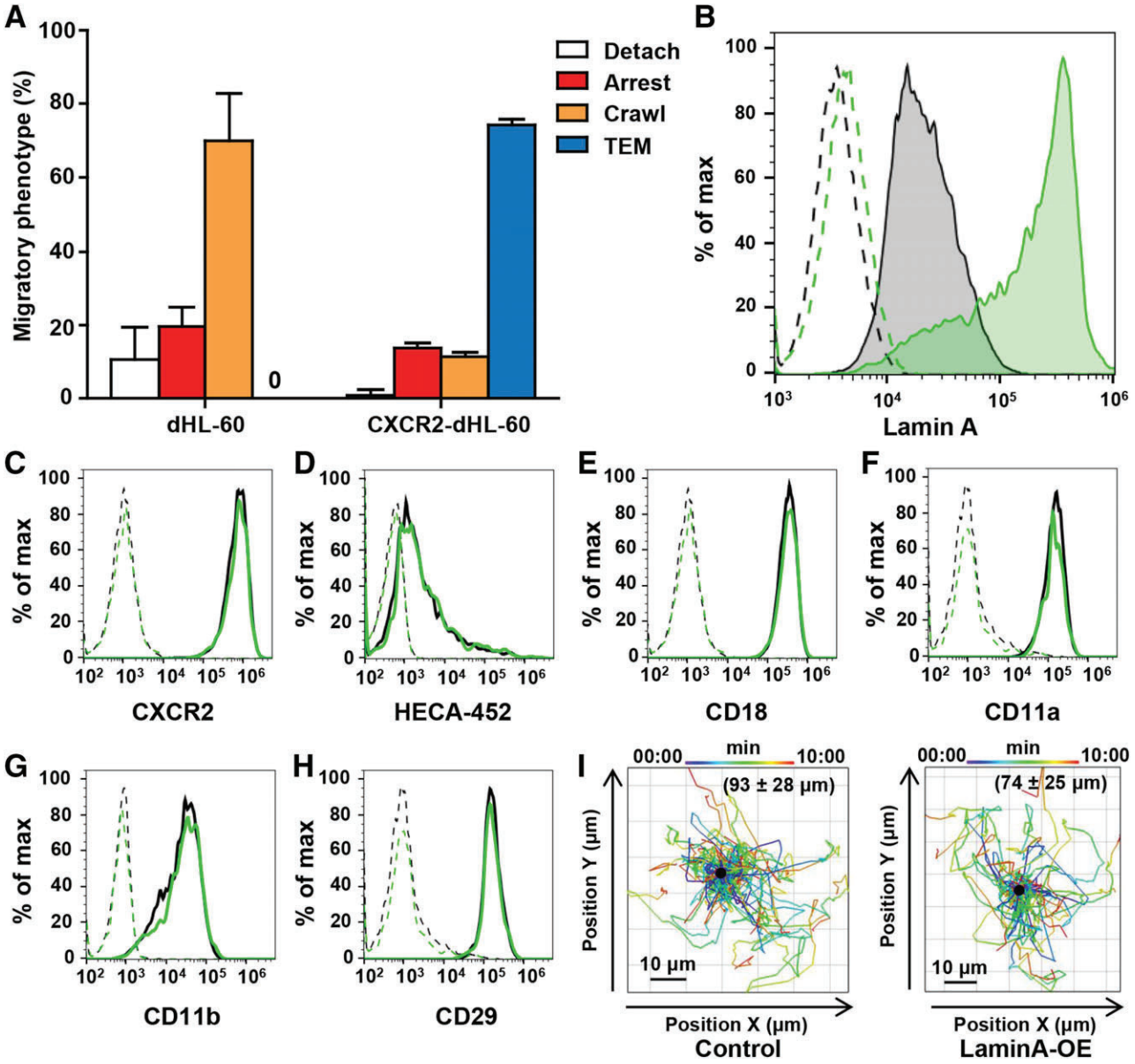

FIGURE 1 **Lamin A overexpression in CXCR2 expressing granulocyte-like dHL-60 cells does not affect the surface expression of receptors involved in trans-endothelial migration and does not alter CXCL1 driven chemokinesis.** (A) Adhesive and migratory phenotypes of granulocyte-like DMSO differentiated HL-60 (dHL-60) variants deficient in CXCR2 or stably expressing CXCR2 crossing inflamed endothelial monolayers under shear flow. The 2 groups of dHL-60 cells were perfused over monolayers of confluent HDMVECs which had been stimulated with IL-1β for 3 h to induce E-selectin, integrin ligands, and multiple CXCR2 and CCR2 chemokines. (B) Intracellular FACS staining of lamins A/C in permeabilized CXCR2 dHL-60 cells stably expressing the pRetroX-PrelaminA-IRES-ZsGreen1 construct (green) or control CXCR2 dHL-60 cells (black). Dashed line depicts cell staining with an isotype matched control mAb. (C–H) FACS analyzed surface staining of CXCR2, the E-selectin carbohydrate ligand carrying the HECA-452 epitope, and the integrin subunits CD18, CD11a, CD11b, and CD29 on sham (black) vs. ZsGreen1-lamin A/C overexpressing (green) dHL-60 cells. Cells were labeled as described in the Materials and Methods section with either PE conjugated anti-human mAbs or with unlabeled primary antibodies followed by a PE or APC conjugated secondary Ab. (I) Migration tracks of control and lamin A overexpressing dHL-60 cells settled on immobilized CXCL1 analyzed with Imaris 9.0.0 software. The migration tracks are plotted with a common origin (central black dot) and the color code depicts the start and end time points of each track. The average total distance mean ± SD travelled by individual granulocyte-like cells within the indicated experimental groups interacting with immobilized CXCL1 is depicted in parenthesis

respect to their mechanical nuclear properties. Hence, in all the rest of the experiments, we assessed the motility and squeezing of the granulocyte-like CXCR2-dHL-60 cells co-expressing high ZsGreen1 and high lamin A levels to those of similarly co-cultured and co-differentiated granulocyte-like CXCR2-dHL-60 cells which did not overexpress lamin A.

3.2 | Lamin A overexpression in granulocyte-like cells is permissive for protrusion and TEM but slows down nuclear squeezing through endothelial junctions

To further elucidate the effect of lamin A overexpression on dHL-60 migration across endothelial barriers, we next determined the

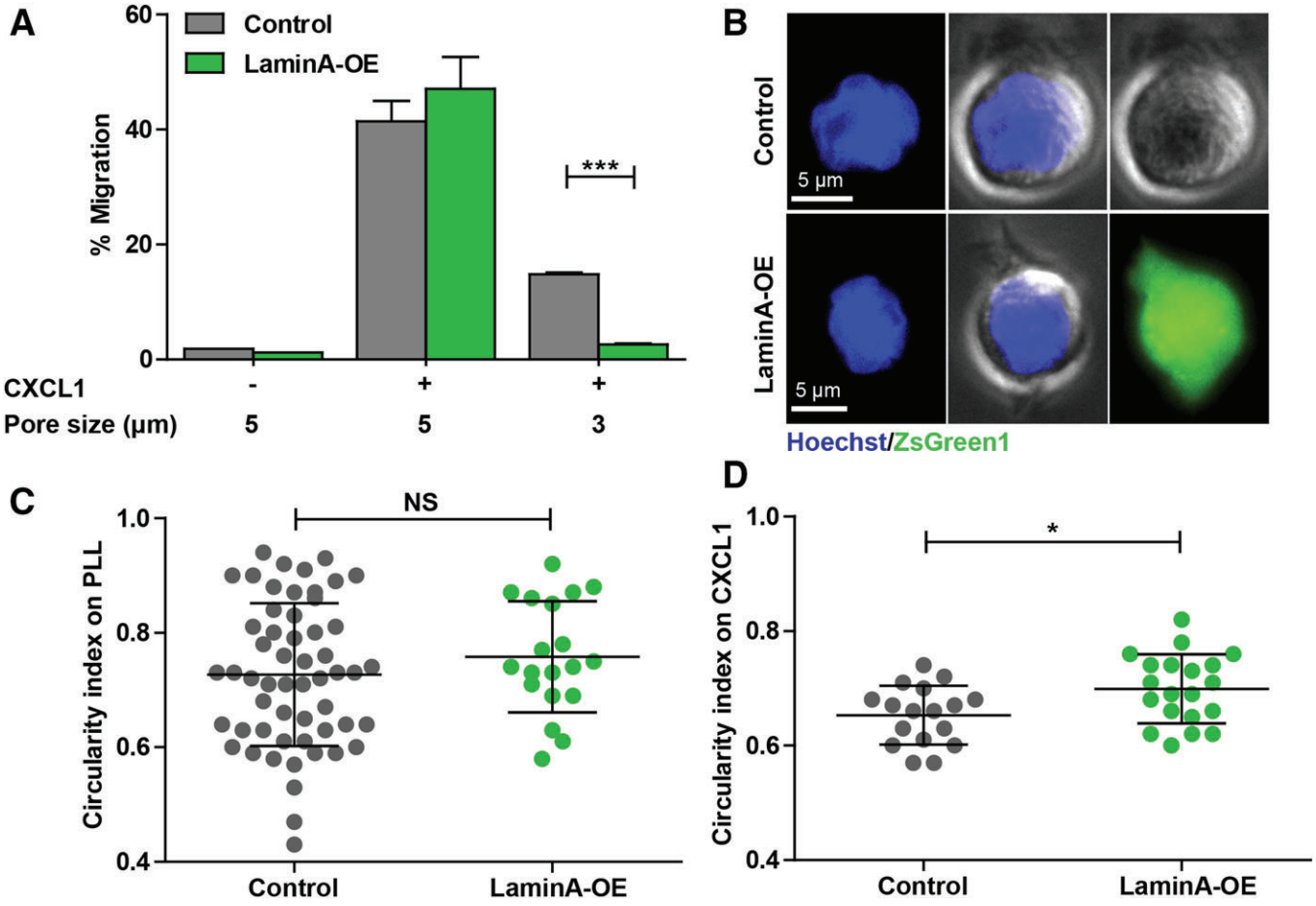

FIGURE 2 **Lamin A overexpression in granulocyte-like HL-60 cells restricts chemotaxis via small rigid pores.** (A) Chemotaxis of control and lamin A overexpressing (Lamin A-OE) granulocyte-like CXCR2 expressing dHL-60 cells towards a CXCL1 gradient across transwell membranes with either 3 or 5 micron pore sizes. Cells were collected 30 min after introduction to the upper wells. The assays were performed in triplicate. Results are representative of 2 independent experiments. (B) Representative images of Hoechst labeled CXCR2 control (black) and ZsGreen1-lamin A overexpressing (green, Lamin A OE cells) dHL-60 cells settled on a PLL coated surface. (C and D) Scatter plots of nuclear circularity index determined for Hoechst labeled control and lamin A overexpressing dHL-60 cells attached to PLL coated surface (C) or immobilized CXCL1 (D). For more details, refer to the Materials and Methods section. The experiments in C and D are each representative of 3. Error bars represent mean ± SD. $^*P < 0.02$

adhesive and migratory capacities of ZsGreen1-Lamin A overexpressing granulocyte-like CXCR2-dHL-60 (green cells) to CXCR2-dHL-60 cells which did not express the ZsGreen1-lamin A construct. When both populations were perfused under shear flow on low permeability confluent monolayers of HDMVECs stimulated by IL-1β,[10] lamin A overexpressing dHL-60 cells normally resisted detachment by continuously applied shear forces (Fig. 3A). Both groups of dHL-60 cells arrested nearby the endothelial junctions eventually transmigrated through while exhibiting negligible lateral crawling on the apical endothelial surfaces (Fig. 3A). Surprisingly, although lamin A overexpressing granulocyte-like dHL-60 cells failed to squeeze through 3 μm diameter rigid pores (Fig. 2A), comparable fractions of lamin A overexpressing and control CXCR2-dHL-60 transmigrated through IL-1β inflamed HDMVECs (Fig. 3A, TEM category). Nevertheless, kinetic analysis of the TEM of these leukocytes revealed a statistically significant delay of the lamin A overexpressing cells compared to the control cells (Fig. 3B,C). In order to further elucidate at a single cell level the basis for this delay in successful TEM, we analyzed the kinetics of leukocyte protrusion through the endothelial monolayer, as well as the overall time spent by either individual control or high lamin A expressing dHL-60 cells subsequent to this initial protrusion underneath the endothelial monolayer until the completion of TEM. While the rate of protrusion and extension of a basolateral pseudopodium (leading edge) underneath the endothelial monolayer was indistinguishable between control and lamin A overexpressing CXCR2-dHL-60 cells (Fig. 3D,E), the lamin A overexpressing CXCR2-dHL-60 cells had an over 30% increase in the average period required for TEM completion compared with control CXCR2-dHL-60 cells (Fig. 3F). Notably, the periods required for TEM completion of individual granulocytes was highly variable for both lamin A low and high CXCR2-dHL-60 cells, reflecting the multiple barriers, these leukocytes had to overcome to successfully cross the inflamed endothelial monolayers.

Further comparison of Hoechst labeled control and lamin A high CXCR2-dHL-60 cells indicated that the main step delayed for the lamin A overexpressing CXCR2-dHL-60 cells was the time it took for the nuclei of these cells to completely pass through the endothelial barrier (Fig. 4A,B and Video 1). In contrast, the rate of retraction of the uropod of these cells was comparable (data not shown). These results

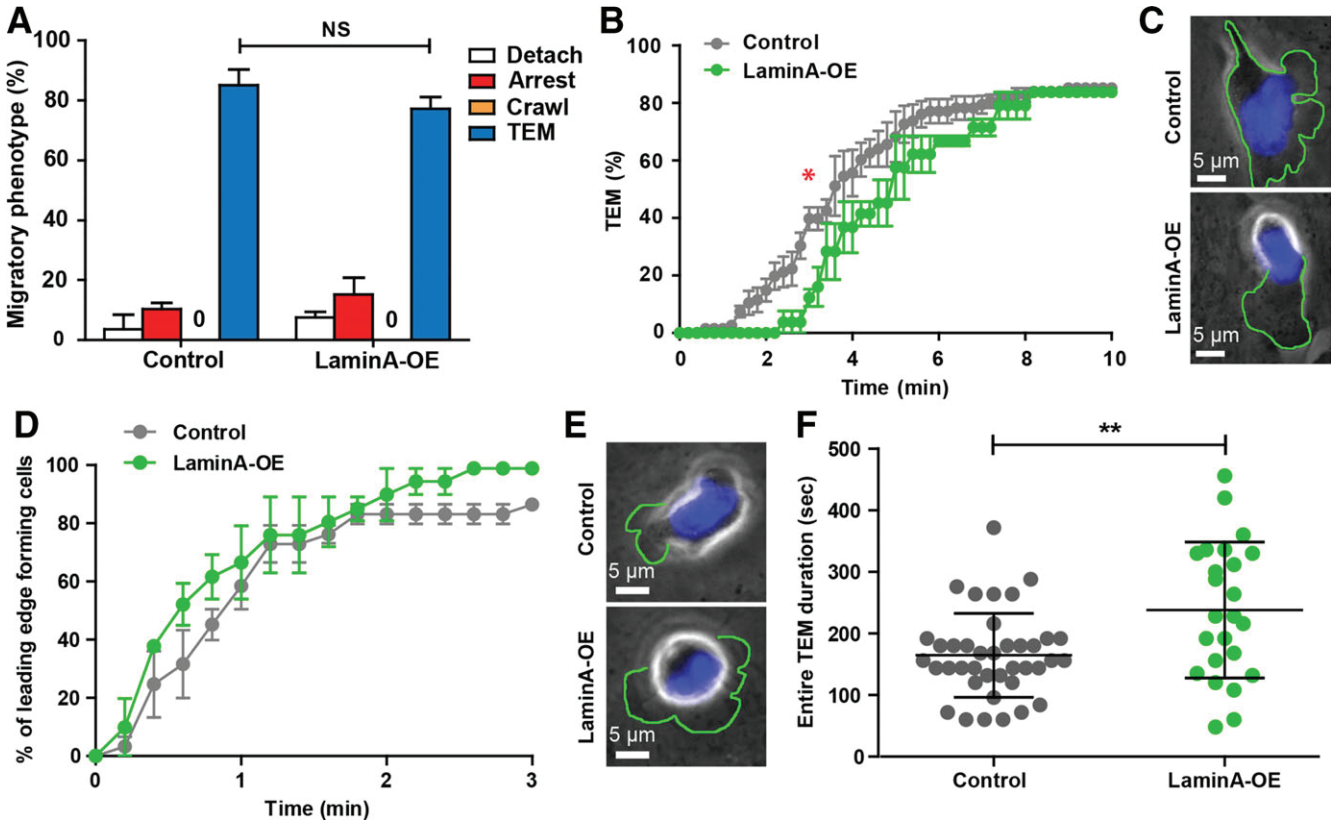

FIGURE 3 **Lamin A overexpression in granulocyte-like HL-60 cells is permissive for TEM across an inflamed IL-1β stimulated human dermal micro-vascular endothelial cells (HDMVEC) monolayer.** (A) Migratory phenotypes of control and lamin A overexpressing (Lamin A-OE) granulocyte-like differentiated CXCR2 expressing HL-60 cells interacting with HDMVECs stimulated for 3 h with IL-1β under shear flow. Values represent the mean ± SD of 3 fields in each experimental group. The experiment shown is representative of 3. (B) The percentage of granulocyte-like CXCR2 dHL-60 cells that completed transmigration across the inflamed HDMVEC monolayer at the indicated time points following the accumulation phase. Values represent the mean ± SEM of 3 fields in each experiment. The experiment shown is representative of 3. $^{*}p < 0.02$ for $t = 3$ min. (C) Images of a representative Hoechst-labeled sham (control) and lamin A overexpressing (Lamin A-OE) granulocyte-like dHL-60 cell during paracellular TEM taken 3 min after the end of the accumulation phase. The green outline depicts the basolateral leading edge of the transmigrating dHL-60 cell. (D) The percentage of dHL-60 cells that projected a protrusive sub-endothelial leading edge underneath the monolayer at the indicated time points prior to nucleus crossing. (E) Images of a representative Hoechst-labeled sham (control) and lamin A overexpressing (Lamin A-OE) dHL-60 cell taken 15 s after the end of the accumulation phase. The green outline depicts the basolateral leading edge generated during the early stage of TEM. (F) TEM kinetics of individual control vs. lamin A overexpressing (Lamin A-OE) granulocyte-like CXCR2 dHL-60 cells that crossed the inflamed HDMVEC monolayer measured from the first detectable protrusion of a sub-endothelial leading edge to the final detachment of the dHL-60 uropod from the apical endothelial aspect. Values were determined in multiple fields taken from 3 independent experiments. Error bars represent mean ± SD. $^{**}P < 0.002$

collectively suggest that the nuclei of granulocytes overexpressing lamin A are delayed in their insertion into the otherwise normal basolateral pseudopodia generated by these granulocytes in response to chemotactic CXCR2 signals. Thus, their ability to lift the endothelial cells engaged by their basolateral pseudopodia and open gaps between neighboring endothelial cells is impaired, resulting in considerably larger sub-endothelial pseudopodia (Fig. 4A and Video 1).

We have recently shown that leukocyte nuclear squeezing through transcellular routes of TEM is associated with pore widening to about 5 μm in diameter.[10] We, therefore, asked if granulocyte-like cells that overexpress lamin A and are delayed in their squeezing through endothelial gaps exceed this upper limit of endothelial gaps. To address this question, we probed gap formation by VE-cadherin displacement by our different granulocyte-like CXCR2-dHL-60 cells. Remarkably, the average gap size generated by lamin A overexpressing CXCR2-dHl-60 cells was 20% larger than the average gap diameter generated by control CXCR2-dHL-60 cells (Fig. 4C) consistent with the higher circularity of the nuclei of lamin A overexpressing CXCR2-dHL-60 cells polarized on immobilized CXCL1 (Fig. 2D). These larger openings created in the endothelial layer may explain why lamin A overexpressing CXCR2-dHL-60 cells have similar TEM efficiency as control cells, despite their rounder and less deformable nuclei. Notably, both lamin A overexpressing and control CXCR2-dHL-60 cells readily displaced the stress fibers of the individual endothelial cells they squeezed between, without rupturing these fibers (data not shown).

3.3 | Lamin A overexpression in granulocyte-like cells restricts chemokine driven motility through and crossing of collagen I barriers

Extravasating leukocytes must cross additional extracellular matrix barriers upon exiting blood vessels and crossing the basement

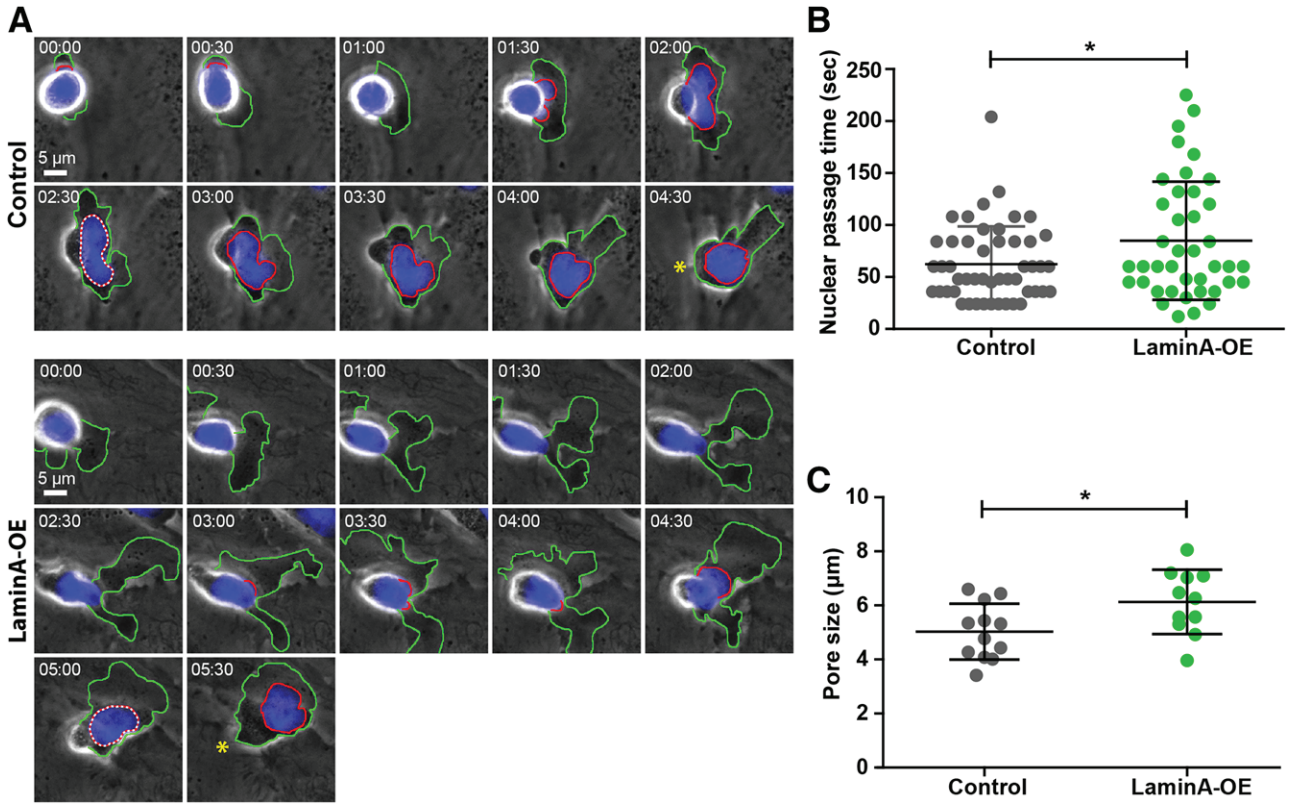

FIGURE 4 **Lamin A overexpressing granulocyte-like dHL-60 cells exhibit slower nuclear squeezing and generate larger endothelial gaps during paracellular TEM.** (A) Images taken from Supplemental Video 1 recording a representative Hoechst-labeled sham (control) and lamin A overexpressing (Lamin A-OE) granulocyte-like CXCR2 dHL-60 cell squeezing through paracellular EC junctions. The green outline depicts the basolateral leading edge of the transmigrating dHL-60 cell and the red outline depicts the nuclear lobes inserted underneath the endothelial monolayer. The red circumference of the nucleus is highlighted in white dots at the first time point at which the entire nucleus of each of the transmigrating dHL-60 cells has completed its passage underneath the endothelial monolayer. The yellow asterisks denote the leukocyte uropods at the time of TEM completion. Time intervals are depicted in each image. Scale bar = 5 μm. (B) Nuclear passage duration in individual control and lamin A overexpressing (Lamin A-OE) CXCR2 dHL-60 cells transmigrating across inflamed HDMVECs monolayers. Values represent cells from multiple fields taken from 3 independent experiments. Error bars represent mean ± SD. $^*p < 0.03$. (C) The diameter of endothelial gaps generated by crossing granulocyte-like CXCR2 dHL-60 (control vs. Lamin A-OE) cells determined as described in Materials and Methods. Values for cells from multiple fields were collected in 3 independent experiments. Error bars represent the mean ± SD. $^*P < 0.03$

membrane deposited by both the endothelial cells and their neighboring pericytes.[22] To mimic the barriers encountered by leukocytes during interstitial motility, we designed a new readout, which combines chemokine driven leukocyte motility on a rigid 2D surface with a mechanical barrier exerted by a 3D matrix composed of distinct collagen containing fibrous barriers. To this end, both lamin A overexpressing and control CXCR2-dHL-60 cells were settled on a glass slide coated with CXCL1 in the presence of medium alone or medium supplemented with either 50% matrigel, which was allowed to undergo in situ polymerization for 20–30 min at 37°C, or medium supplemented with collagen I allowed to undergo identical in situ polymerization (Fig. 5A). Matrigel is an extract derived from mice harboring tumors, and is rich in laminin and collagen IV, and is therefore sometimes used as a surrogate basement membrane.[23] While both collagen I and matrigel are commonly used models of cell invasion, they have distinct biomechanical properties. Matrigel is characterized by small pore sizes and high deformability, while collagen I matrices at comparable collagen concentrations have larger pore sizes but are less deformable.[23] Comparison of these 2 types of barriers using confocal reflective microscopy revealed that the collagen I barrier is composed of thick fibers as opposed to the matrigel (Fig. 5B). Scanning electron microscopy analysis of these matrices[24] further supported the notion that the collagen I matrix is much denser than the matrigel matrix (Supplementary Fig. 2).

We next compared both the nucleus location and the motility of either control or lamin A overexpressing CXCR2-dHL-60 cells settled on CXCL1 in the presence of these different media (Fig. 6A–D). Notably, in aqueous media, dHL-60 with high lamin A content underwent normal polarization on CXCL1 coated 2D surfaces (Fig. 6A, Video 2), the nuclei of both granulocytes were readily translocated into their leading edges (Fig. 6C, and Video 2), and both granulocytes locomoted at comparable velocities on this 2D substrate (Fig. 6D and Video 2). As expected, the granulocyte-like CXCR2-dHL-60 cells locomoted more slowly on immobilized CXCL1 when embedded inside the matrigel relative to when the same cells were settled on the immobilized CXCL1 in medium only (Fig. 6B, D and Video 3). Nevertheless, in the presence of the matrigel, lamin A overexpression modestly affected nuclear translocation into the leading edge of migrating granulocytes (Fig. 6C

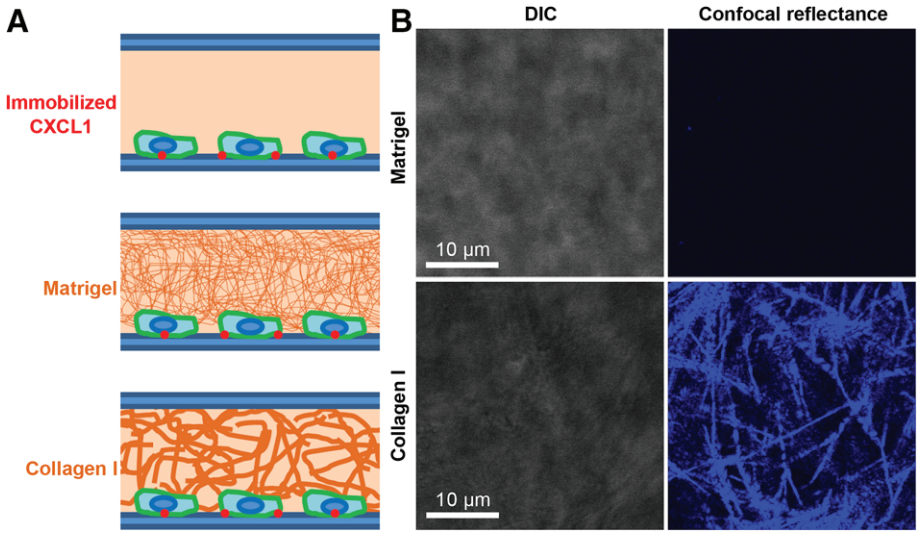

FIGURE 5 **A setup for leukocyte motility on a chemokine-coated surface in the presence of distinct 3D collagenous barriers.** (A) A scheme depicting the experimental model used to assess leukocyte crossing of distinct collagenous barriers. Leukocytes suspended in cold matrigel or collagen I solutions were sedimented for 3 min and incubated under the distinct collagen solutions for 30 min at 37°C to allow collagen polymerization. Leukocyte motility was recorded for 30 additional minutes. (B) Representative confocal reflectance images of matrigel (50% solution) and collagen 1 matrices (3.2 mg/ml) which underwent polymerization for 30 min at 37°C. Scale bars = 10 μm

and Video 3) and reduced granulocyte motility by only ~20% (Fig. 6D). These results indicate that the stiffer nuclei of lamin A overexpressing granulocyte-like CXCR2-dHL-60 cells only marginally restrict the 2D chemokinetic motility when the cells are embedded inside a soft matrigel barrier and do not restrict the nuclear translocation and motility of these cells in aqueous medium. Since none of the lamin A high granulocyte-like CXCR2-dHL-60 cells were arrested by the matrigel barrier, and the majority of their nuclei readily translocated into the leading edge of motile leukocytes (Fig. 6B–D, Video 3), these results indicate that when the porous barrier is sufficiently deformable, most lamin A overexpressing, stiff leukocyte nuclei can override the low resistance imposed by such a barrier.

To evaluate the contrasting scenario of a less deformable extracellular matrix network, we assessed the impact of leukocyte nuclear stiffness on squeezing through a distinct porous barrier that closely resembles the collagen I rich interstitial tissue encountered by leukocytes once they enter peripheral tissues.[25] We therefore compared the ability of lamin A overexpressing and control CXCR2-dHL-60 cells settled on immobilized CXCL1 and embedded in a matrix of pure collagen I to cross this barrier. Notably, the vast majority of lamin A high granulocyte-like CXCR2-dHL-60 cells failed to translocate their nuclei to their protrusive leading edges in spite of their normal ability to extend filopodia-like protrusions (Fig. 7A, B and Video 4). Consequently, lamin A overexpressing cells showed a substantially reduced motility when embedded in the collagen I matrix compared with control granulocyte-like CXCR2-dHL-60 cells (Fig. 7C), and their ability to successfully move through the collagen, although inherently variable, was significantly impaired (Fig. 7D). Interestingly, polymerized collagen I did not slow down the motility of normal granulocyte-like CXCR2 dHL-60 cells more than did the matrigel barrier (i.e., a mean velocity of ±6.1 in collagen I compared to a mean velocity of ±6.6 in matrigel), indicating that it imposed a major barrier selectively on the migration of lamin A overexpressing granulocyte-like cells, which have stiffer nuclei,[16] whereas control ganulocyte-like cells with their highly deformable nuclei can still easily penetrate the collagen I matrix. The dramatically slower motility of these granulocytes through the collagen I gel and retarded nuclear translocation to the leading edge of these leukocytes was not the result, however, of augmented integrin mediated adhesiveness of the lamin A overexpressing CXCR2-dHL-60 cells to the collagen I fibers because the motility of these granulocytes was not affected by exclusion of Mg^{++} (data not shown). Thus, integrin-independent CXCR2 mediated granulocyte motility through collagen I barriers is dramatically delayed by lamin A overexpression due to a failure of the stiffer, lamin A high nuclei to translocate into the pseudopodia of granulocytes crossing this poorly deformable barrier.

4 | DISCUSSION

The lamin cortex of all mammalian nuclei is a thin, elastic shell encoded by 3 functionally nonredundant genes, *LMNA*, encoding lamins A/C, and *LMNB1* and *LMNB2*, encoding lamin B1 and lamin B2, respectively.[26] Lamins exist in dynamic equilibrium between the nucleoplasm and the lamina network.[27] The ratio between the *LMNA* gene products lamin A and its shorter spliced variant lamin C and the other lamins is proportionally related to nuclear stiffness in both mesenchymal and hematopoietic cells.[28] In addition to their roles in structure and nuclear stability, the various lamins are also involved in transcription, chromatin organization, and DNA replication and their mutations are associated with multiple pathologies.[29,30] Nevertheless, the lamin A overexpression in our model HL-60 cell system did not affect the expression of the canonical surface markers associated with this differentiation or of key functional receptors involved in leukocyte TEM and motility such as integrins and myeloid GPCRs. Furthermore, lamin A overexpression did not affect the migratory properties of dHL-60 cells

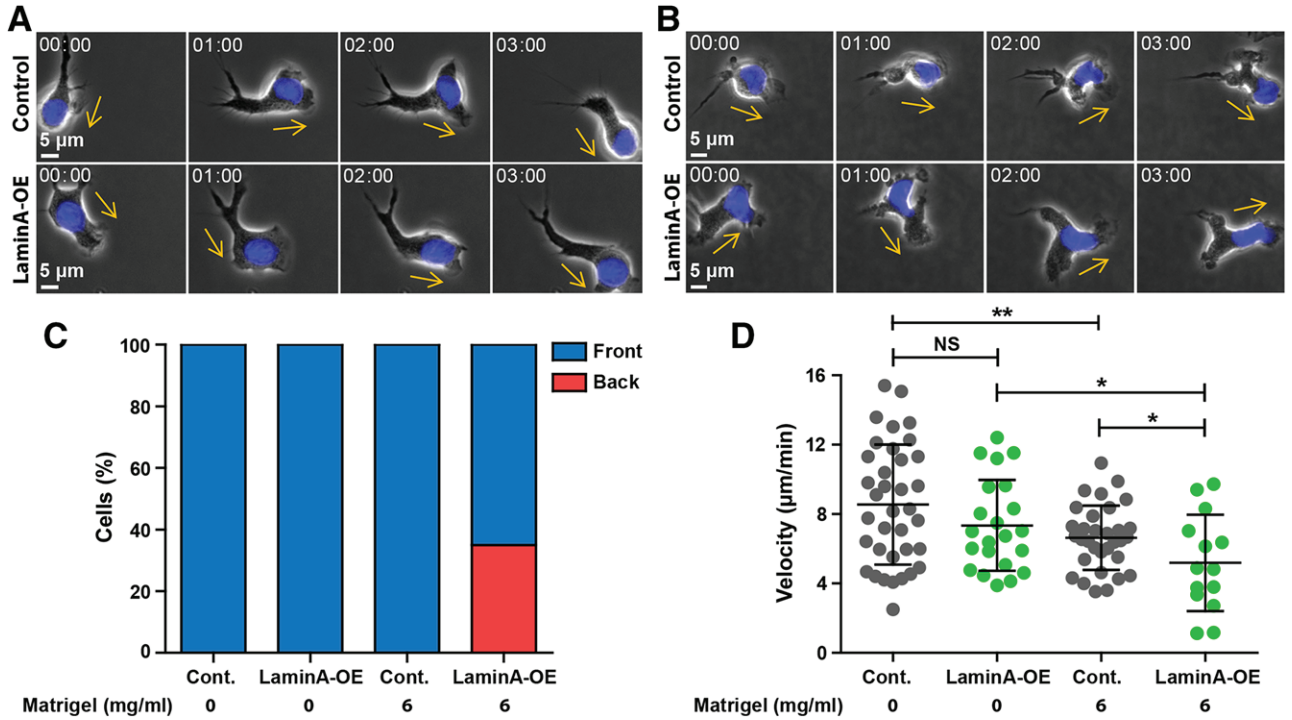

FIGURE 6 **Lamin A overexpression in granulocyte-like cells does not affect their chemokine driven motility through a permissive matrigel barrier**. Images from Supplemental Videos 2 and 3 depicting representative control (A) vs. lamin A overexpressing (Lamin A-OE; B) Hoechst-labeled granulocyte-like dHL-60 cells migrating on immobilized CXCL1 either in aqueous medium (left) or when embedded inside a polymerized matrigel matrix (right). Time codes are depicted and scale bars = 5 μm. (C) Nuclear locations in control (Cont.) and lamin A (LaminA-OE) overexpressing Hoechst labeled granulocyte like dHL-60 cells migrating over immobilized CXCL1 either in medium or embedded in polymerized matrigel (50% solution). Results were determined for 40–50 cells from 3 independent experiments. (D) The velocities of individual control (Cont.) and lamin A overexpressing (Lamin A-OE) granulocyte-like dHL-60 cells migrating over immobilized CXCL1 alone or when embedded in the polymerized matrigel. Values represent cells from multiple fields taken from 3 independent experiments. Error bars represent mean ± SD. $^{*}P < 0.05$; $^{**}P < 0.007$

under different conditions, such as chemokine driven motility on 2D surfaces or chemotaxis through large rigid pores, suggesting that their differentiation and major cytoskeletal machineries were not functionally affected by lamin A overexpression.

Circulating leukocytes express very low lamin A levels, which keep their nuclei soft and thereby presumably allowing these cells to readily squeeze through vascular barriers.[1] Strikingly, however, our granulocyte-like cells genetically manipulated to express 10-fold higher levels of lamin A could still readily cross the low permeability endothelial barriers used in our in vitro TEM setups. These results suggest that leukocytes with stiff nuclei can open up sufficiently large gaps in between neighboring endothelial cells, orders of magnitude larger than the gaps these cells normally maintain to squeeze their nuclei through these openings and lift these endothelial cells microns above the basement membrane they normally deposit.[31] Thus, while lamin A overexpressing cells take slightly longer to transmigrate through an endothelial cell monolayer, they eventually successfully transmigrate through this barrier, and this is accomplished by opening larger gaps in between neighboring endothelial cells that allow transit of the more rigid nuclei in the lamin A overexpressing cells.

Our data indicate that the size of endothelial gaps generated by squeezing leukocytes is probably dictated by the dimension of the leukocyte nuclei more than by the resistance of the endothelial cytoskeleton to leukocyte squeezing. The endothelial cells were traditionally proposed to facilitate gap enlargement via myosin driven contraction, yet we and other groups have recently ruled out this alternative mechanism for endothelial gap formation.[10,11,32] Our new results further suggest that endothelial gap formation is simultaneously regulated by both the leukocyte nuclei and by the endothelial cytoskeleton. In addition to restricting gap widening by squeezing leukocytes, the endothelial cytoskeleton restricts the ability of the endothelial cell to be lifted above the slide by the squeezed leukocyte nucleus. Our results indicate that even the dramatic stiffening introduced to the nuclear lamina of granulocytes by lamin A overexpression only moderately affects this endothelial lifting, without which the leukocyte cannot complete its squeezing through endothelial monolayers.

The nuclear stiffening introduced by lamin A overexpression in our model granulocyte-like HL-60 cells exerted dramatic effects on the ability of these cells to squeeze and migrate through 3D collagen I matrices in response to chemokinetic CXCL1 signals. At the same time, lamin A high granulocytes successfully crossed the much softer matrigel barriers in response to identical chemokinetic CXCL1 signals. Notably, these cells also normally translocated their stiff nuclei to their lamellipodia and protrusions, further indicating that nucleus stiffening and lamin A overexpression, on their own, do not alter the position of the nucleus in migrating leukocytes. Rather, the translocation of the nucleus in motile leukocytes to the leukocyte lamellipodia is

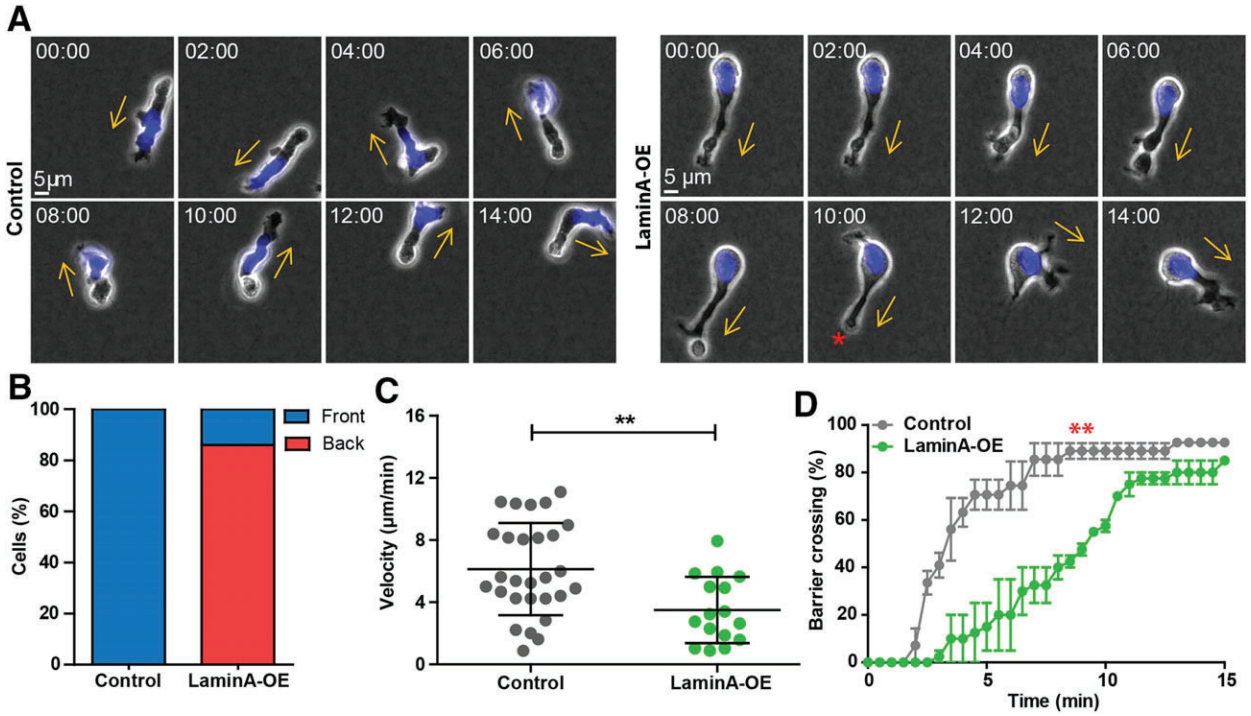

FIGURE 7 **Lamin A overexpression in granulocyte-like cells restricts nucleus squeezing and chemokine driven motility through a dense collagen I barrier**. (A) Images from Supplemental Video 4 depicting representative control vs. lamin A overexpressing (Lamin A-OE) Hoechst-labeled granulocyte-like dHL-60 cells migrating on immobilized CXCL1 while being embedded inside a polymerized collagen I matrix (B). Time codes are depicted for each image. Scale bar = 5 μm. Yellow arrows depict the direction of granulocyte motility over the chemokine coated 2D surface. The red asterisk indicates a retracting leading edge. (B) Nuclear locations in control and lamin A overexpressing (Lamin A-OE) Hoechst labeled granulocyte like dHL-60 cells migrating over immobilized CXCL1 through the collagen I barrier. Results were determined for 40–50 cells from 3 independent experiments. (C) Scatter plot of velocities of individual control and lamin A/C overexpressing (Lamin A-OE) granulocyte-like dHL-60 cells migrating through polymerized collagen I matrices. Values were collected from 3 independent experiments. Error bars represent mean ± SD. $^{**}p < 0.004$. (D) Kinetics of collagen I barrier crossing of individual control and lamin A overexpressing (Lamin A-OE) granulocyte-like dHL-60 cells. The numbers of cells within each experimental group that successfully crossed a 20 μm long barrier of collagen I as a function of time. Values represent the mean ± SEM of 3 fields. $^{**}P < 0.01$ for $t = 9$ mins. The experiment shown is a representative of 3

determined both by its relative stiffness and the relative mechanical resistance of the external environment surrounding the motile leukocyte. Why then did the same nuclear stiffening introduced by lamin A overexpression not affect granulocyte squeezing through matrigels? Whereas the components of matrigel are chemically similar to the major components of endothelial basement membranes, polymerized matrigel is mechanically softer than polymerized collagen I.[33,34] Our structural analysis of 3D matrigel and 3D collagen I gels also indicates the presence of thick collagen fibers in the collagen I gels and absence in polymerized matrigels. This is attributed to the molecular differences between fiber-forming collagen I as opposed to the network assembly of collagen IV together with laminin within matrigels. The 3D collagen I barriers constructed by us in the present work appear to better mimic the physiologically relevant barrier leukocytes encounter during their interstitial motility in tissues. An open question of interest is the crossing ability of leukocytes with stiff nuclei through endothelial basement membrane barriers given that some basement membranes are discontinuous around post capillary venules at some sites of inflammation.[35,36]

One of the most surprising results of our study is the efficient squeezing of the lamin A high nuclei across endothelial junctions and underneath endothelial monolayers. This reflects the remarkable ability of the endothelial barrier to adapt its cytoskeleton to stiff lamin A high nuclei. This adaptive nature of the endothelial cytoskeleton sharply contrasts the mechanical resistance of collagen I fibers to the squeezing of identically stiff nuclei.[37] We thus predict, that unlike these fibers, both the endothelial actin filaments and microtubules that construct the main mechanical barriers of the endothelial cytoskeleton can likely bend, get displaced, and undergo remodeling when crossed by either soft (i.e., lamin A low) or stiff (i.e., lamin A high) nuclei. The endothelial resistance to nuclear squeezing is low, likely because of the high elasticity of the endothelial stress fibers and the fast turnover of the short actin filaments interlaced in between these actin bundles.[10,32] Our results also elude to the possibility that the pulling and pushing forces normally exerted by the leukocyte actomyosins are sufficiently high to propel even the stiffer nucleus of lamin A overexpressing leukocytes into the leukocyte pseudopodia and thereby override the low mechanical resistance imposed by the endothelial cytoskeleton. These actomyosin derived forces are also strong enough to squeeze the stiff lamin A enriched nuclei through thin and porous barriers, such as those imposed by matrigels. Similar forces are, on the other hand, insufficient to override the indefinitely high mechanical resistance imposed on the same nuclei by rigid pores and by the high resistance imposed by stiff collagen I fibers.

In summary, our results highlight the permissive nature of the endothelial cytoskeleton, which is highly dynamic and can actively remodel and rapidly change its fine structure, compared to extracellular matrices, which are relatively passive materials. The remarkable adaptive nature of endothelial cytoskeletal barriers to nuclear squeezing warrants future in vivo analysis of the relative abilities of other leukocytes with variable content of nuclear lamin A and stiffness to squeeze through distinct vascular beds and their different basement membranes. Such future studies should provide additional insights as to why most leukocytes maintain a low lamin A content of their nuclei, while most other cells, including leukocyte precursors in the bone marrow and subsets of activated lymphocytes, benefit from high lamin A content of their nuclei.[28,38,39]

ACKNOWLEDGMENTS

We thank Dr. Ann Richmond (Vanderbilt University, Nashville, Tennessee) for providing the CXCR2 expressing HL-60 line. R.A. is the Incumbent of the Linda Jacobs Chair in Immune and Stem Cell Research. R.A. is supported by the Israel Science Foundation, the Flight Attendant Medical Research Institute Foundation (FAMRI), USA, the Minerva Foundation, Germany as well as a research grant from Carol A. Milett. J.L. is supported by awards from the National Institutes of Health [R01 HL082792 and U54 CA210184], the Department of Defense Breast Cancer Research Program [Breakthrough Award BC150580], and the National Science Foundation [CAREER Award CBET-1254846 and MCB-1715606].

AUTHORSHIP

S.K.Y. performed most of the experiments, analyzed data, and assisted in manuscript preparation and writing; S.W.F. assisted in FACS analyses and manuscript writing; F.R. performed some of the real time fluorescence microscopy experiments. J.L. provided reagents, expertise, and assisted in the interpretation of results and editing of the manuscript. R.A. designed and supervised experiments and wrote the manuscript.

DISCLOSURE

The authors declare no conflict of interest.

REFERENCES

1. Friedl P, Wolf K, Lammerding J. Nuclear mechanics during cell migration. *Curr Opin Cell Biol*. 2011;23:55–64.
2. Khatau SB, Bloom RJ, Bajpai S, et al. The distinct roles of the nucleus and nucleus-cytoskeleton connections in three-dimensional cell migration. *Sci Rep*. 2012;2:488.
3. Davidson PM, Denais C, Bakshi MC, Lammerding J. Nuclear deformability constitutes a rate-limiting step during cell migration in 3-D environments. *Cell Mol Bioeng*. 2014;7:293–306.
4. Denais C, Lammerding J. Nuclear mechanics in cancer. *Adv Exp Med Biol*. 2014;773:435–470.
5. Thiam HR, Vargas P, Carpi N, et al. Perinuclear Arp2/3-driven actin polymerization enables nuclear deformation to facilitate cell migration through complex environments. *Nat Commun*. 2016;7:10997.
6. Fruleux A, Hawkins RJ. Physical role for the nucleus in cell migration. *J Phys Condens Matter*. 2016;28:363002.
7. Stephens AD, Banigan EJ, Adam SA, Goldman RD, Marko JF. Chromatin and lamin A determine two different mechanical response regimes of the cell nucleus. *Mol Biol Cell*. 2017;28:1984–1996.
8. Lammerding J, Fong LG, Ji JY, et al. Lamins A and C but not lamin B1 regulate nuclear mechanics. *J Biol Chem*. 2006;281:25768–25780.
9. Olins AL, Zwerger M, Herrmann H, et al. The human granulocyte nucleus: unusual nuclear envelope and heterochromatin composition. *Eur J Cell Biol*. 2008;87:279–290.
10. Barzilai S, Yadav SK, Morrell S, et al. Leukocytes breach endothelial barriers by insertion of nuclear lobes and disassembly of endothelial actin filaments. *Cell Rep*. 2017;18:685–699.
11. Heemskerk N, Schimmel L, Oort C, et al, (2016) F-actin-rich contractile endothelial pores prevent vascular leakage during leukocyte diapedesis through local RhoA signalling. *Nat Commun*. 2016; 7:10493.
12. Collins SJ. The HL-60 promyelocytic leukemia cell line: proliferation, differentiation, and cellular oncogene expression. *Blood*. 1987;70:1233–1244.
13. Xu J, Wang F, Van Keymeulen A, et al. Divergent signals and cytoskeletal assemblies regulate self-organizing polarity in neutrophils. *Cell*. 2003;114:201–214.
14. Xu J, Wang F, Van Keymeulen A, Rentel M, Bourne HR. Neutrophil microtubules suppress polarity and enhance directional migration. *Proc Natl Acad Sci USA*. 2005;102:6884–6889.
15. Gera N, Swanson KD, Jin T. beta-Arrestin 1-dependent regulation of Rap2 is required for fMLP-stimulated chemotaxis in neutrophil-like HL-60 cells. *J Leukoc Biol*. 2017;101:239–251.
16. Rowat AC, Jaalouk DE, Zwerger M, et al. Nuclear envelope composition determines the ability of neutrophil-type cells to passage through micron-scale constrictions. *J Biol Chem*. 2013;288:8610–8618.
17. Sai J, Walker G, Wikswo J, Richmond A. The IL sequence in the LLKIL motif in CXCR2 is required for full ligand-induced activation of Erk, Akt, and chemotaxis in HL60 cells. *J Biol Chem*. 2006;281:35931–35941.
18. Shulman Z, Alon R. Real-time analysis of integrin-dependent transendothelial migration and integrin-independent interstitial motility of leukocytes. *Methods Mol Biol*. 2012;757:31–45.
19. Shulman Z, Cohen SJ, Roediger B, et al. Transendothelial migration of lymphocytes mediated by intraendothelial vesicle stores rather than by extracellular chemokine depots. *Nat Immunol*. 2012;13: 67–76.
20. Antman-Passig M, Levy S, Gartenberg C, Schori H, Shefi O. Mechanically oriented 3D collagen hydrogel for directing neurite growth. *Tissue Eng Part A*. 2017;23:403–414.
21. Liu Y, Sai J, Richmond A, Wikswo JP. Microfluidic switching system for analyzing chemotaxis responses of wortmannin-inhibited HL-60 cells. *Biomed Microdevices*. 2008;10:499–507.
22. Nourshargh S, Alon R. Leukocyte migration into inflamed tissues. *Immunity*. 2014;41:694–707.
23. Sodek KL, Brown TJ, Ringuette MJ. Collagen I but not Matrigel matrices provide an MMP-dependent barrier to ovarian cancer cell penetration. *BMC Cancer*. 2008;8:223.
24. Anguiano M, Castilla C, Maska M, et al. Characterization of three-dimensional cancer cell migration in mixed collagen-Matrigel scaffolds using microfluidics and image analysis. *PLoS One*. 2017; 12:e0171417.
25. Sorokin L. The impact of the extracellular matrix on inflammation. *Nat Rev Immunol*. 2010;10:712–723.

26. Funkhouser CM, Sknepnek R, Shimi T, Goldman AE, Goldman RD, Olvera de la Cruz M. Mechanical model of blebbing in nuclear lamin meshworks. *Proc Natl Acad Sci USA*. 2013;110:3248–3253.
27. Pajerowski JD, Dahl KN, Zhong FL, Sammak PJ, Discher DE. Physical plasticity of the nucleus in stem cell differentiation. *Proc Natl Acad Sci USA*. 2007;104:15619–15624.
28. Shin JW, Spinler KR, Swift J, Chasis JA, Mohandas N, Discher DE. Lamins regulate cell trafficking and lineage maturation of adult human hematopoietic cells. *Proc Natl Acad Sci USA*. 2013;110:18892–18897.
29. Bell ES, Lammerding J. Causes and consequences of nuclear envelope alterations in tumour progression. *Eur J Cell Biol*. 2016;95:449–464.
30. Tran JR, Chen H, Zheng X, Zheng Y. Lamin in inflammation and aging. *Curr Opin Cell Biol*. 2016;40:124–130.
31. Stoler-Barak L, Barzilai S, Zauberman A, Alon R. Transendothelial migration of effector T cells across inflamed endothelial barriers does not require heparan sulfate proteoglycans. *Int Immunol*. 2014;26:315–324.
32. Alon R, van Buul JD. Leukocyte breaching of endothelial barriers: the actin link. *Trends Immunol*. 2017;38:606–615.
33. Engbring JA, Kleinman HK. The basement membrane matrix in malignancy. *J Pathol*. 2003;200:465–470.
34. Kalluri R. Basement membranes: structure, assembly and role in tumour angiogenesis. *Nat Rev Cancer*. 2003;3:422–433.
35. Wang S, Voisin MB, Larbi KY, et al. Venular basement membranes contain specific matrix protein low expression regions that act as exit points for emigrating neutrophils. *J Exp Med*. 2006;203:1519–1532.
36. Voisin MB, Probstl D, Nourshargh S. Venular basement membranes ubiquitously express matrix protein low-expression regions: characterization in multiple tissues and remodeling during inflammation. *Am J Pathol*. 2010;176:482–495.
37. Yang YL, Kaufman LJ. Rheology and confocal reflectance microscopy as probes of mechanical properties and structure during collagen and collagen/hyaluronan self-assembly. *Biophys J*. 2009;96:1566–1585.
38. Gonzalez-Granado JM, Silvestre-Roig C, Rocha-Perugini V, et al. Nuclear envelope lamin-A couples actin dynamics with immunological synapse architecture and T cell activation. *Sci Signal*. 2014;7:ra37.
39. Rocha-Perugini V, Gonzalez-Granado JM. Nuclear envelope lamin-A as a coordinator of T cell activation. *Nucleus*. 2014;5:396–401.

SUPPORTING INFORMATION

Additional information may be found online in the supporting information tab for this article.

How to cite this article: Yadav SK, Feigelson SW, Roncato F, et al. Elevated nuclear lamin A is permissive for granulocyte transendothelial migration but not for motility through collagen I barriers. *J Leukoc Biol*. 2018;104:239–251. https://doi.org/10.1002/JLB.3HI1217-488R

Trends in Cancer

CellPress
REVIEWS

Special Issue: Physical Sciences in Oncology

Opinion

Beyond` Tissue Stiffness and Bioadhesivity: Advanced Biomaterials to Model Tumor Microenvironments and Drug Resistance

Ankur Singh,[1,2,3,*] Ilana Brito,[1] and Jan Lammerding[1,4]

Resistance to chemotherapy and pathway-targeted therapies poses a major problem in cancer research. While the fields of tumor biology and experimental therapeutics have already benefited from *ex vivo* preclinical tissue models, these models have yet to address the reasons for malignant transformations and the emergence of chemoresistance. With the increasing number of *ex vivo* models poised to incorporate physiological biophysical properties, along with the advent of genomic sequencing information, there are now unprecedented opportunities to better understand tumorigenesis and to design therapeutic approaches to overcome resistance. Here we discuss that new preclinical *ex vivo* models should consider – in addition to common biophysical parameters such as matrix stiffness and bioadhesivity – a more comprehensive milieu of tissue signaling, nuclear mechanics, immune response, and the gut microbiome.

Highlights

Matrix stiffness influences the phenotype and epigenetics of tumor cells and influences chemoresistance across solid, palpable, and liquid tumors.

Biomaterials that independently modulate matrix stiffness from composition and architecture reveal that, in normal mammary epithelial cells, increasing matrix stiffness alone induces malignant phenotypes.

Healthy and malignant cells migrating through narrow confinements undergo nuclear deformation, which can result in transient loss of nuclear envelope integrity, herniation of chromatin across the nuclear envelope, DNA damage, and redistribution of mobile nuclear proteins.

An immune-privileged microenvironment could selectively impair the recognition of tumor antigens by cytotoxic T cells.

A commensal microbiota promotes the efficacy of cancer therapies.

Chemoresistance and Changes in Biophysical Factors

Therapeutic resistance in cancer often arises through genetic mutations that enhance drug metabolism, inactivate apoptotic pathways, and activate prosurvival signals [1–3]. The underlying genetic mutations are accompanied and sometimes preceded by changes in the biochemical and biophysical properties of the surrounding tissue. The biophysical factors, such as bioadhesivity, porosity, confinement, and stiffness, have been extensively studied as the response of individual cells to these factors and are vital for cellular functioning and tissue development. Cells cope with biophysical stimuli through integrated mechanosignaling by physically interconnected proteins starting from extracellular matrix (ECM) adhesion molecules (integrins), focal adhesion plaques, actin fibers, and structural components of the cells' nuclei, among others. The mechanotransduction response includes the activation of mechanosensitive transcription factors and downstream genes as well as the rearrangement of cellular structure and organization to adjust to the physical environment [4,5]. Mutations in cellular proteins and alterations in the cellular microenvironment aberrantly engage mechanosignaling networks in cancer cells, either by perturbing the mechanical input or by altering the signaling network itself, which can promote cell growth, invasion, migration, and probably chemoresistance. For example, integrin signaling has been shown to increase epidermal growth factor secretion and receptor tyrosine-protein kinase erbB-2 (ERBB2) clustering in breast cancer cells, resulting in resistance to the ERBB2 inhibitor trastuzumab [6]. Increased tumor and stroma stiffness has also become a hallmark of cancer, as evident from the use of palpation for detection of breast tumors and cancerous lymph nodes in the case of lymphomas. Increased tissue stiffness in the liver, pancreas, prostate, and lung has also been shown to be a positive indicator of disease progression in the corresponding cancers [7–10]. Nevertheless, how chemoresistance and changes in biophysical and biochemical factors relate to one another is poorly understood.

[1]Nancy E. and Peter C. Meinig School of Biomedical Engineering, Cornell University, Ithaca, NY, USA
[2]Sibley School of Mechanical and Aerospace Engineering, Cornell University, Ithaca, NY, USA
[3]Caryl and Israel Englander Institute for Precision Medicine, New York Presbyterian Hospital–Weill Cornell Medicine, New York, NY, USA
[4]Weill Institute for Cell and Molecular Biology, Cornell University, Ithaca, NY, USA

*Correspondence:
as2833@cornell.edu (A. Singh).

While genomic studies have benefitted from direct patient sample analysis, exploring the role that the stiffness of the microenvironment plays in cellular function has become possible only through the use of atomic force microscopy (AFM), microindenters, and engineered tissues. *Ex vivo* preclinical models that recapitulate the tumor microenvironment have been critical in improving our understanding of tumorigenic growth and resistance. In the case of mammary tumors, changes in tissue stiffness are associated with increased deposition and crosslinking of collagen type I, and the stiffness can increase from 100–400 Pa up to 1–5 kPa when comparing normal and cancerous mammary tissue [9,11]. It is now well accepted that matrix stiffness perturbs epithelial morphogenesis by clustering integrins to enhance extracellular signal-regulated kinase (ERK) activation and increase Rho-associated protein kinase (ROCK)-generated contractility and focal adhesions. Integrin signaling and stiffness are involved not only in chemoresistance in solid tumors but also in palpable lymphoid malignancies, as shown by us [12], as well as in liquid tumors [13]. Recent work from Shin and Mooney demonstrated that matrix softening leads to resistance against standard chemotherapy in myeloid leukemias [13]. More recently, matrix softness was shown to influence the histone methylation and epigenetics of tumor-repopulating cells [10], which exhibit high chemoresistance to conventional chemotherapeutic drug treatment. To better understand the role of tissue stiffness in cancer, we refer the reader to excellent recent reviews [11,14]. Nonetheless, these *ex vivo* models have yet to successfully address the reasons for the emergence of tumor resistance. This is because most *ex vivo* tissues focus on bioadhesive signaling and stiffness. Although extensively investigated, cell adhesion- and stiffness-mediated drug resistance is not the only factor that contributes to chemoresistance *in vivo*. Here we discuss that, in addition to matrix stiffness, cellular, biochemical, and biophysical parameters such as stress relaxation, adhesion, spatiotemporal protein signaling, and porosity/confinement need to be considered. For *ex vivo* models, it will thus be important to incorporate these various biophysical parameters, ideally in a modular fashion to maximize control of cell fate and the drivers of oncogenic transformations. We propose several new areas of technological advancement needed for the building of better *ex vivo* cancer models to understand tumor resistance. These topics cover the integration of biomaterials-based engineering with emerging forefronts of tissue mechanics, nuclear mechanics, the immune response, and the gut microbiome.

Integrating Independent Control of Biomechanical and Spatiotemporal Signaling of Tumors

The plasticity of cancer cells to evolve different drug-resistant phenotypes is encoded by the organization and spatiotemporal dynamics of signal transduction networks. This plasticity allows them to adapt to challenging microenvironments, remodel them in their own favor, and withstand highly toxic therapeutic assaults. A recent review discusses the rich molecular signaling dynamics and their impact on cancer cell proliferation, survival, invasiveness, and drug resistance [15]. Most prior studies in cancer 3D modeling used hydrogels or scaffolds as hydrated networks of motif-containing bulk proteins or their peptidomeric forms. These peptides are either short peptides that represent adhesive binding motifs (e.g., fibronectin- or vitronectin-derived RGD) or hydrogel crosslinking peptides that are matrix metalloproteinase (MMP) degradable and allow matrix remodeling. While numerous studies have shown the utility of these hydrogels in spread, mesenchymal-like cells, we have engineered modular hydrogels to show that integrin ligands and matrix degradability can serve as prosurvival signals in B and T cell lymphomas, modulating their 3D aggregation and response to therapeutics [12]. Using RGD-presenting hydrogels and complementary studies in patient-derived xenograft mouse models, we have further shown that integrin $\alpha v\beta 3$ acts as a membrane receptor for thyroid hormones to mediate angiogenesis in malignant T cells [16]. This particular study led us to discover a novel mechanism for the endocrine modulation of T cell lymphoma pathophysiology.

However, the flow of information between tumor cells and the surrounding ECM is bidirectional and functions in a spatiotemporal manner. The adhesion process involves dynamic interactions occurring over multiple time and length scales, from seconds for nanoscale integrin receptor–ECM ligand binding to days and weeks for meso/macroscale ECM remodeling and cancerous tissue organization. Similar to the dynamic nature of cell–ECM interactions, the engineering of materials to elicit desired tumor cell responses will require precise and independent, multidimensional control over matrix spatiotemporal bioligand presentation, structural porosity, and the mechanical properties of the materials (Figure 1A, Key Figure). Recent biomaterials designs now allow spatiotemporal control, as reported by several research groups across various cell–tissue models [17–21]. Nonetheless, current hydrogels have yet to demonstrate that the same biomaterials can provide independent control over all of the bioadhesivity, spatiotemporal signaling, stiffness, and porosity of the material. In a major advance, chemical strategies that allow external manipulation of ligand presentation in real time were recently developed. A new class of hydrogels was reported that used an addition–fragmentation-chain transfer chemistry and permitted repeated exchange of biochemical ligands in a non-destructive manner [22]. Such advances afford powerful designer tools in material engineering to study cancer cell processes.

Another emerging trend is the understanding of stress relaxation *in vivo* and *ex vivo* and is increasingly becoming a crucial parameter for biomaterials design. Using bead displacement methods, Legant and colleagues showed deformations of 20–30% peak principal strain in the hydrogel surrounding the cell [78]. In 2D culture of cells on acrylamide gels, strains of 3–4% (ratio of traction to elastic modulus) are typically observed [23]. The ability of *ex vivo* scaffolds to either store (purely elastic) or dissipate (viscoelastic) forces generated by cells in contact with these surfaces can influence a cell's interaction with its surrounding [24] and we believe they may in turn regulate spread, growth, migration, and possibly chemoresistance. Stem cell growth and differentiation are enhanced in hydrogels with fast stress relaxation characteristics, as reported recently by Chaudhuri and colleagues [24]. Most non-degradable, synthetic hydrogels are purely elastic, whereas many naturally derived matrices and tissues are viscoelastic (Figure 1B), can be degraded/remodeled by cells, and often exhibit partial stress relaxation when a constant strain of 15% is applied [24]. For example, collagen and fibronectin matrices exhibit a decrease in the storage or elastic modulus over time when a constant strain is applied. This is likely to occur from the unbinding of weak hydrophobic and electrostatic interactions that hold the fibers in a network [25,26]. The elasticity of these materials is also nonlinear. On reconstituted natural matrices, the resistance to cellular traction forces is expected to relax over time due to flow and remodeling of the matrix, dissipating the energy that cell-generated forces impart into the material. Substrates with stress relaxation enhance cell spreading at a low initial elasticity, which is mediated through β1 integrin, actin polymerization, and actomyosin contractility and is associated with increased Yes-associated protein (YAP) nuclear localization and proliferation [26,27]. This suggests that increased stress relaxation can compensate for matrices with a lower stiffness. Since several mechanosignaling network components are involved, we suspect that changes in stress relaxation and the resulting cellular response could be key to chemoresistance. Therefore, it is imperative that advanced tissue models for cancer (and also for regenerative medicine) research should consider stress relaxation beyond, and independent of, stiffness and bioadhesivity. Some of the questions to be considered are: can stress relaxation potentially program tumor cells into a more resistant phenotype? Ccan stress relaxation crosstalk with genetic mutations? What is the role of time-dependent viscoelastic properties in tumorigenesis and the infiltration of immune cells? What categories of tumors depend on stress relaxation? These questions can be answered by using engineered biomaterials that incorporate stress relaxation behaviors

CellPress REVIEWS

Key Figure

Ex Vivo Cancer Tissues with Multidimensional Control of Biophysical and Biochemical Properties

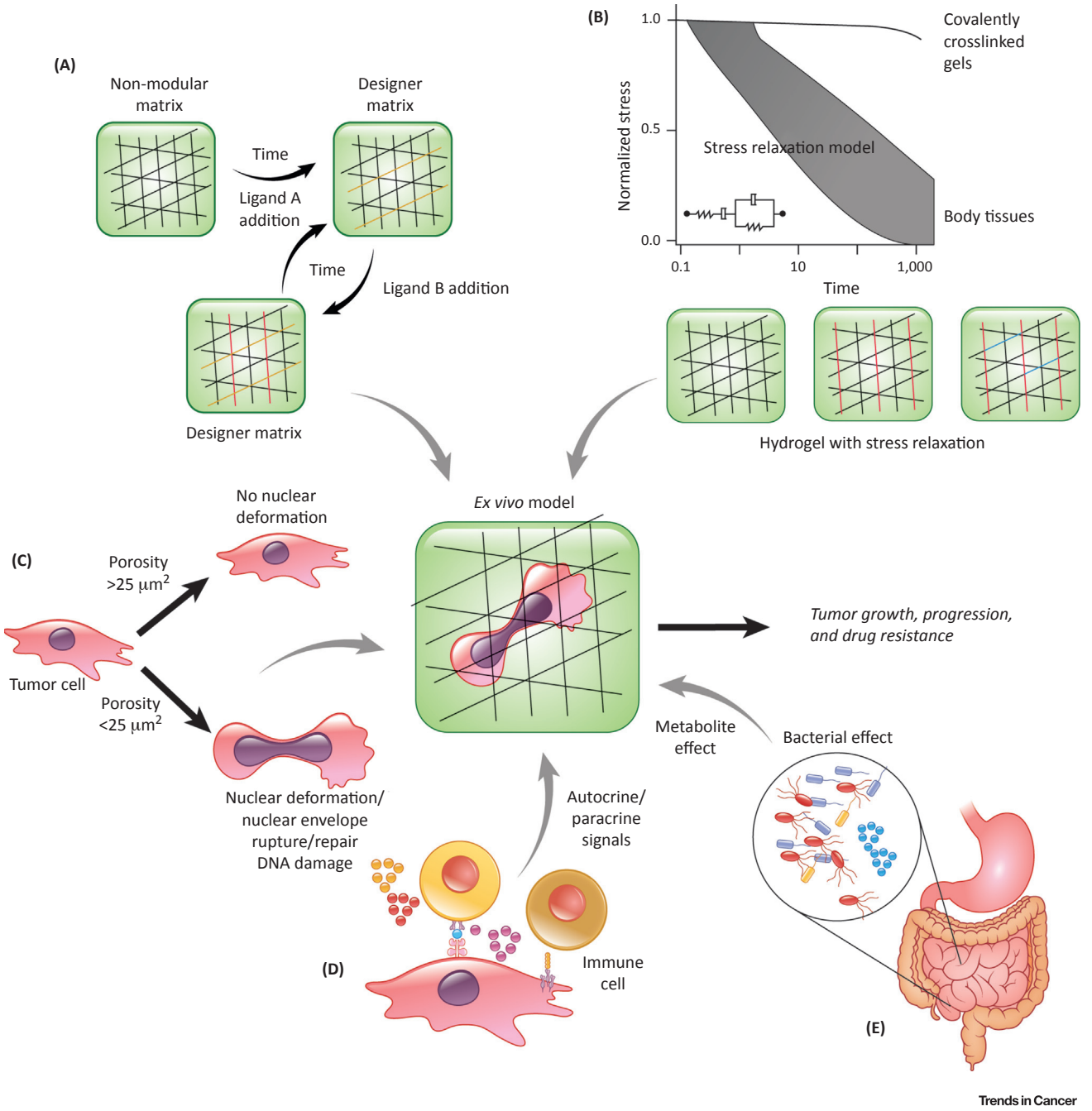

Figure 1. The schematic depicts the integration of new strategies into existing tumor tissue models. (A) Time-dependent, controlled, reversible exchange of biochemical ligands. (B) Stress relaxation, which models the viscoelastic behavior of tissues compared with current, covalently crosslinked matrices. Simple covalently crosslinked hydrogels (black-lined network) with stress relaxation can be designed by including ionic bridges (red lines) and chemical spacers (e.g., polyethylene glycol; blue lines). (C) 3D niche porosity to model the nuclear deformability of cancer cells. (D,E) Integrating the cell–cell and autocrine/paracrine effect of the immune system and the gut microbiome.

and comparing them with purely elastic materials. The challenge will be in developing such materials where stress relaxation, bioadhesivity, porosity, stiffness, and topography are independently tunable.

Designing 3D Niche Porosity to Accommodate Nuclear Deformability of Cells

In vivo cells often have to transit through narrow constrictions smaller than their nuclear diameter during migration; for example, when passing through interstitial spaces or endothelial layers during intra- and extravasation. This concept applies to all migrating cells, including immune cells, fibroblasts, invasive cancer cells, and possibly even tissue stem cells. Recent work suggests that the biophysical properties of the nucleus can play a crucial rate-limiting role during cell migration in 3D environments: For pores substantially smaller than the nuclear cross-section, migration efficiency decreases, and cells eventually stall completely when the pore size reaches the 'nuclear migration limit' [28]. The ability of cells to pass through such confined spaces is mostly determined by nuclear size, deformability, and cytoskeletal contractility, which are affected by nuclear and cytoskeletal composition and organization [28–31]. As these parameters can vary widely between cell types, porosity and confinement should be key considerations in engineered microenvironments. Although most engineered niches have considered the porosity of the scaffold from the crosslinking density perspective, better material designs are needed to account for nuclear deformability, as some applications may favor designs that prevent (specific) cells from entering while other designs may benefit from having large enough pores to allow cells to enter the material. In addition to limiting the motility of cells, moving a large cell nucleus through small pores can have other biological consequences. Migrating through such tight spaces places substantial physical stress on the nucleus, which can result in transient loss of nuclear envelope integrity, herniation of chromatin across the nuclear envelope, DNA damage, and redistribution of mobile nuclear proteins *in vitro* and *in vivo* [32–34]. Recent *in vitro* work by the Discher group further supports the concept that migration through tight spaces results in increased genomic stability [34,35], but direct observations of migration-induced DNA damage *in vivo* and resulting genomic instability remains outstanding. Nuclear deformation may also alter chromatin organization and gene expression, which could further modulate tumor progression and resistance to therapy. Nuclear envelope rupture and migration-induced DNA damage may emerge as a potential novel therapeutic approach to specifically target metastatic cells. Supporting this idea, combined inhibition of nuclear envelope repair and DNA damage repair resulted in significant death of cancer cells during migration through confined environments [32]. Finally, our recent work further links nuclear envelope rupture in micronuclei and an inflammatory response, explaining how chromosomal instability drives metastasis through a cytosolic DNA response [36].

Given the importance of cell migration in many biomedical applications, ranging from tissue engineering to prosthetic device coating and cancer therapy, these recent findings highlight the importance of considering pore sizes and the nuclear deformability of the relevant cells in the design process of biomaterials-based scaffolds. In general, when designing new biomaterials-based *ex vivo* tissue-engineered models for development, wound healing, tumors, and even the coating of prosthetic devices, one should consider tissue scaffold pore sizes of $<25\ \mu m^2$ in cross-section (Figure 1C). These considerations will vary with regard to tumor type and patient-specific attributes. Infiltrating immune cells, such as leukocytes, neutrophils, and dendritic cells, can squeeze through much smaller pores, down to around 1–2 μm^2. We suggest that the scaffold pore size is an important design parameter, especially since small pores could not only slow migrating cells but also induce nuclear rupture and deformation. We suspect that nuclear rupture and deformation can contribute to DNA damage and genomic instability, promoting

drug resistance through genomic rearrangements or mutations that increase cell proliferation and/or abnormal signaling. Nevertheless, a generalized approach in determining pore size is not feasible because of wide differences in the biophysical characteristics of tumor cells. Applications for different cells will require different considerations for pore size, and the degradability of the material must also be considered, as many cells can remodel the ECM, for example, by secretion of MMPs.

Integrating the Immune System and the Effect of the Gut Microbiome

In addition to changes in cell and tissue stiffness, other hallmarks of cancer include chronic inflammation and altered immune responses [37]. While modeling of the tumor immune interaction in engineered tissues is important, another point of view is that tumor-infiltrating immune cells differentiate into phenotypes that support each step of the metastatic cascade and thus are novel targets for therapy. *In vivo* tumor-infiltrating T cells (including regulatory T cells), B cells, immunosuppressive myeloid-derived suppressor cells (MDSCs), and macrophages continuously interact with tumor cells through direct cell contact or by the secretion of a milieu of proinflammatory cytokines and chemokines. This immune-privileged microenvironment could selectively impair the recognition of tumor antigens by cytotoxic T cells and also protect residual tumor cells against cytotoxic destruction [38–41]. Immune cell populations, like T cells and natural killer cells, can control metastases of cancer cells by either restricting them to the primary tumor niche or promoting migration away from the primary tumor site [42,43]. Even macrophages, the cells of the innate immune system, adapt to the tumor microenvironment and polarize to the M1 extreme and secrete high levels of interleukins (e.g., interleukin-8 and -10) and granulocyte colony-stimulating factor, which suppress immunity [44]. The secretion of cytokines is dependent on tumor subtype.

The introduction of these immune components and recapitulation of the immune–cancer interaction complex in an *ex vivo* engineered system is ideal but non-trivial (Figure 1D). One of the main challenges is that immune cells, when cultured *ex vivo*, undergo rapid apoptosis over time unless rescued by antiapoptotic signals and replenished with a fresh supply of immune cells [45]. Newer approaches that recapitulate the continuous replenishment of immune cells *in vivo* can be achieved by integrating microfluidic platforms [46] with engineered tissues, where immune cells could be added to the feeding lymphatic or vascular networks. Simple encapsulation of immune cells in collagen or Matrigel is suboptimal, as these biomaterials may not provide the necessary survival signals and functional immune cells. Alternatively, advanced biomaterials-based scaffolds that support immune cell growth [47–51] could be integrated with the existing tumor niches and other on-chip approaches [52]. The development of such tissues can further be applied to study the efficacy of immunotherapy and the effect of immunomodulatory drugs on immune cells.

In addition to immune cells, tumor progression and the efficacy of antitumor therapies are now known to be affected by the microbiome. For example, *Fusobacterium nucleatem*, among other bacteria, is enriched in colorectal cancer patients' microbiomes [53,54] and *Helicobacter pylori* has been shown to be abundant in patients with non-cardia gastric cancers [55]. These interactions can be local, as *Clostridium*, *Bifidobacterium*, and *Salmonella* (reviewed in [56]) have been shown to grow in the tumor microenvironment and elicit immune reactions that can assist in tumor suppression. Similarly, in the colon, microbial biofilms have been implicated in the progression of colon cancer [57]. Direct impacts of the microbiome may also be systemic. Recently, the production of a microbe-derived carcinogen, deoxycholic acid, was shown to directly contribute to liver cancer [58]. Although the mechanisms that causally link microbes and tumorigenicity have not been established [59], several mechanisms have been proposed,

including metabolic signaling to promote proliferation or angiogenesis pathways [60]. Microbes may also produce reactive oxygen species, which may in turn contribute to DNA damage and, ultimately, tumor resistance. Manipulating these systems *in vivo* can be technically challenging due to the complexity of the communities and the difficulty of working with germ-free or monocolonized mice. An outstanding question is how to best integrate the effects of the microbiome into current *in vitro* engineered model systems for cancer and tumor resistance to create a more efficient cancer ecosystem (Figure 1E).

The longest-standing evidence for a link between the microbiome and cancer is in relation to colon cancer. *In vitro* models of colon cancer utilize organoid models, which are extremely useful for testing drug delivery, genetic manipulation, and the incorporation of biopsied tissue. Bacteria can be administered in these models by injecting them directly into the organoid cavity [61], but integration of biofilms into the organoid model of colon cancer remains to be done. An alternative to organoids for intestinal cancer models are 3D scaffold models of intestinal tissue. Several studies have been completed with co-culture of organisms on these scaffolds [62,63], but these experiments are limited in scope to a handful of organisms and are constrained by the difficulties of co-culturing intestinal cells with organisms that are normally found in an anaerobic environment. There are additional engineering challenges in introducing the range of biologically relevant cell types, which would both enhance mucous production and maintain barrier integrity. More attention is warranted in the areas of understanding the microscale interactions of these organisms and cancer cells and the shear stress caused by the laminar flow of intestinal contents, peristalsis, and large-scale mechanical reflexes and cellular apoptosis.

The mechanistic effects of the microbiome in colon cancer may be direct (e.g., signaling and small-molecule delivery directly to intestinal stem cells, affecting their proliferation) or indirect, via immune system function. The most striking example of this relates the microbiome and the efficacy of cancer immunotherapies in rodent models of colon cancer and melanoma [64,65]. It is currently thought that that the microbiome alters the function of the immune system, specifically through changes in immune cell composition, maturation, and the inflammatory milieu. Several questions remain: do *in vitro* models of cancer lacking microbes adequately recapitulate *in vivo* malignancies or must we include microbes? Are there effects on tumors or the immune system that are specific to certain microbes or microbiome compositions? Are microbiome-mediated effects on cancer progression direct or predominantly mediated through the immune system? Can microbiome-mediated effects on cancer progression be modeled by simply introducing metabolites, cellular lysate, or supernatant to tumor cell culture or do we need to co-culture bacterial cells via *ex vivo* gut reactors integrated with immune and cancer tissues to elicit real-time feedback? Additionally, this feedback is likely to impact the composition of the microbiome as well as its function. The promise of the integration of complex microbial communities is that it will permit bidirectional analysis of microbiome effects on cancerous cells and the effects of tumorigenic cells on those bacteria. Single-cell analysis of individual bacteria [66] will provide information on selective pressures exerted on bacteria in the tumor microenvironment; metagenomic and strain-level analyses of microbial communities [67] co-cultured with tumor cells can be used to examine the function of these cells, including information on the metabolites they produce that might in turn influence tumorigenic progression and the formation of resistance. *In vitro* systems may prove fruitful in testing the effects of these different communities on immune or cancer tissue.

Last, because we know that the tumor microenvironment is permissive to bacterial colonization, can we study the effects of tumor-targeting synthetic bacteria *in vitro*? Din and colleagues

engineered a side-trap array microfluidic platform to co-culture human cervical cancer HeLa cells with *Salmonella typhimurium* [68]. Ingber and colleagues have also reported a simple biomimetic 'human gut-on-a-chip' microdevice that recapitulates epithelium polarization and villus-like folds and can be used for co-culture of a normal intestinal microbe (*Lactobacillus rhamnosus* GG) for extended periods of time (>1 week) without compromising epithelial cell viability [69]. Yissachar *et al*. [70] have taken an alternative approach whereby segments of intestinal tissue are excised and cultured *in vitro*, linking intestinal inputs and outputs directly to cultured immune and neuronal cells. This system may prove valuable in linking microbiome outputs to other *in vitro* models of tumor progression. The next challenge will be in determining how to integrate the diversity of the microbiome so that we can study its effect on overall tumor progression, tumor resistance, and drug targeting while modulating other aspects of the tumor microenvironment crosstalk (Figure 2).

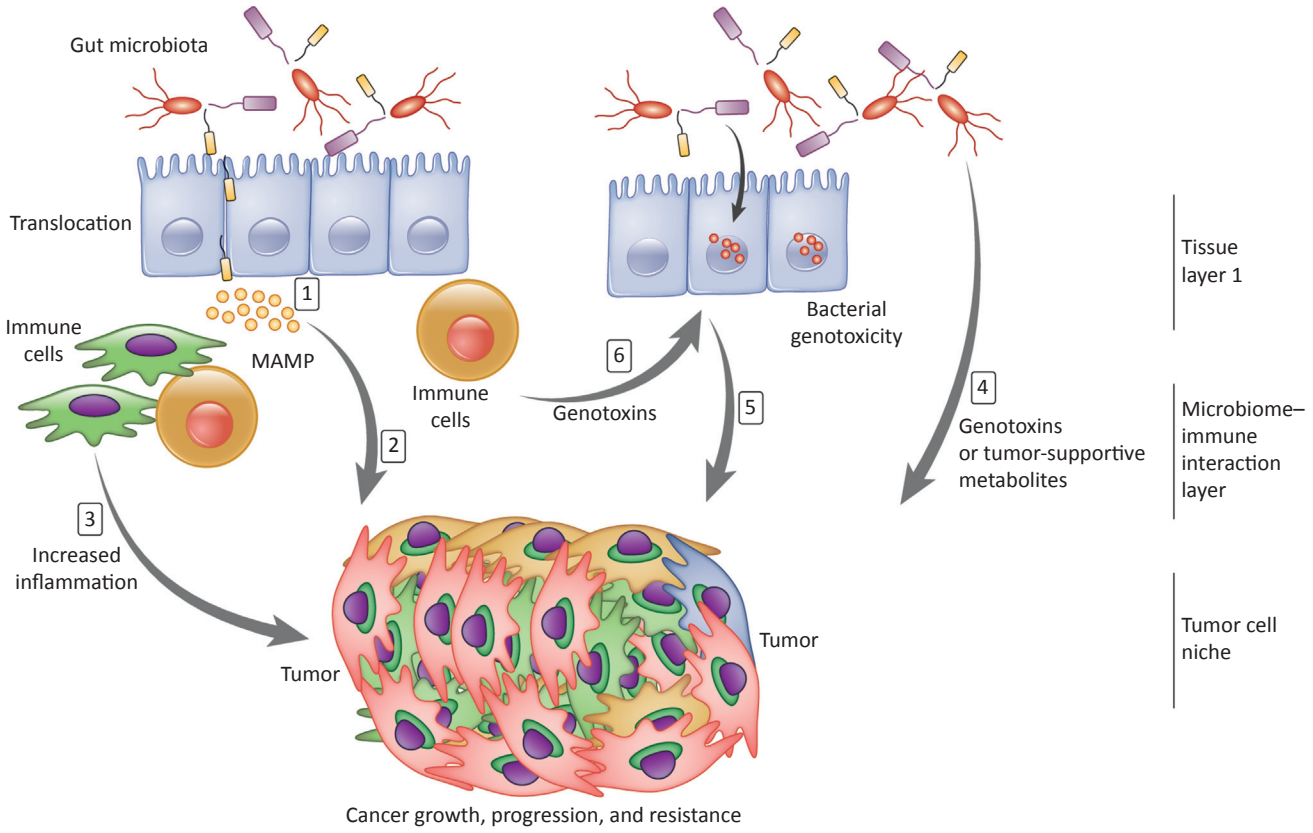

Figure 2. *Ex Vivo* Cancer Models with Possible Microbiome–Tumor Interactions. The figure shows an example of a three-layer *ex vivo* model. (1) Alterations in gut microbiota may result in increased bacterial translocation. (2) Increased abundance of microorganism-associated molecular patterns (MAMPs) directly influences tumor cells through local or distant mediators. (3) MAMPs stimulate Toll-like receptors on immune and other niche cells, leading to an increased tumor-supportive milieu of cytokines (e.g., interleukins) and growth factors. (4) The microbiota mediates tumor suppression through the generation of short-chain fatty acids and biological activation of cancer-preventing phytochemicals. (5) Bacterial genotoxins, after being delivered to the nuclei of host cells, actively induce DNA damage in organs that are in direct contact with the microbiome, such as the gastrointestinal tract. Other genotoxic components include reactive oxygen species, reactive nitrogen species released from inflammatory cells, and hydrogen sulfide from the microbiota. (6) Gut-mediated metabolites may result in: (i) activation of genotoxins such as acetaldehyde; (ii) activation of the metabolism of hormones; or (iii) alterations in the metabolism of bile acids.

Concluding Remarks

Engineered microenvironments have already emerged as important and useful tools to study tumor cells *in vitro*. A key advantage of *ex vivo* models is that the number of features (and correspondingly, the number of variables in the system) is constrained so that the effects of specific factors can be more clearly delineated. Although the most comprehensive models may not necessarily be the best model for a particular application, there remains a need to address unresolved questions of cellular, molecular, and microenvironment complexity (see Outstanding Questions). In addition to conventional bioadhesive matrices, decellularized matrices and glycosaminoglycans (GAGs) offer alternative choices for fine-tuning the 'right' characteristics in the model in terms of both pore size and matrix relaxation. Most previous *ex vivo* models have focused on stiffness and biochemical ligand presentation as the predominant design parameters and tumor invasion as the primary readouts. We propose that additional parameters should be considered in the design of such models, including viscoelastic properties, physical pore sizes, and the microbiome. Additional aspects of tumor microenvironments could include cancer-associated fibroblasts, stromal cells, immune cells, the role of fluid flow, matrix heterogeneity, and interactions with the vascular and lymphatic circulations [71–73]. In addition, genomic and epigenetic evolution of cancer cells should be considered as key drivers of therapy resistance, and the effect of the physical microenvironment on these processes should be investigated in more detail. We believe that careful modeling of *ex vivo* niches will result in improved understanding of epigenetic, metabolic, and signaling patterns in cancer, therefore leading to the development of new therapeutics [16,74–77]. Modular approaches that enable independent tuning of individual biophysical and biochemical parameters will facilitate more systematic studies. Technical advances that permit co-culture of bacteria with cancer cells can not only lead to better understanding of the tumor–microbiome interaction but also drive new directions to systemically deliver an antitumor toxin using synthetically engineered bacteria. Finally, newer *ex vivo* models that recapitulate complete selective aspects of the tumor immune microenvironment interactome are needed to maximize our effort towards a tumor microenvironment-driven precision medicine strategy and evaluate synergies between combination therapies to overcome resistance. Such innovative approaches will increase the 'predictive power' of preclinical inhibitors, provide potential biomarkers for correlative studies in new inhibitor clinical trials, and provide clues towards mechanisms that induce resistance to therapeutic inhibitors by more faithfully representing patient biological features and creating clinically relevant treatment regimens.

Outstanding Questions

How do chemoresistance and changes in biophysical and biochemical factors relate to one another?

Can stress relaxation potentially program tumor cells into a more resistant phenotype? Can stress relaxation crosstalk with genetic mutations? What categories of tumors depend on stress relaxation?

What is the role of time-dependent viscoelastic properties in tumorigenesis and infiltration of immune cells?

How can we engineer *ex vivo* models with cell-specific consideration of pore size?

Is it sufficient to leave out the microbes from *in vitro* models of cancer? Are there effects of specific microbes or is it mainly the triggers they provide to the immune system?

Can microbiome-mediated effects on cancer progression be modeled by simply introducing metabolites, cellular lysate, or supernatant to tumor cell culture or do we need to co-culture bacterial cells via *ex vivo* gut reactors integrated with immune and cancer tissues to elicit real-time feedback?

How can we best integrate the effects of the microbiome into current *in vitro*-engineered model systems of cancer and tumor resistance to create a more efficient cancer ecosystem?

Acknowledgments

The authors acknowledge financial support from the National Institutes of Health (NIH) (1 R01 AI132738-01A1, A.S.; 1 R33 CA212968-01, A.S.; U54 CA210184, J.L.; R01 HL082792, J.L.), Department of Defense Career Development Award (W81XWH-17-1-0215, A.S.), the US Department of Defense Breast Cancer Research Program (Breakthrough Award BC150580, J.L.), and the National Science Foundation (NSF) CAREER Awards (DMR-1554275, A.S.; CBET-1254846, J.L.). The authors also acknowledge financial support from the Sloan Foundation Research Fellowship (I.B.) and the NSF (MCB-1650122, I.B.). This work was supported by the Office of the Assistant Secretary of Defense for Health Affairs, through the Peer Reviewed Cancer Research Program, under Award No. W81XWH-17-1-0215 (A.S.). Opinions, interpretations, conclusions, and recommendations are those of the author and are not necessarily endorsed by the Department of Defense, the NIH, the NSF, or other funding agency.

References

1. Holohan, C. *et al.* (2013) Cancer drug resistance: an evolving paradigm. *Nat. Rev. Cancer* 13, 714–726
2. Correia, A.L. and Bissell, M.J. (2012) The tumor microenvironment is a dominant force in multidrug resistance. *Drug Resist. Updat.* 15, 39–49
3. Holzel, M. *et al.* (2013) Plasticity of tumour and immune cells: a source of heterogeneity and a cause for therapy resistance? *Nat. Rev. Cancer* 13, 365–376
4. Case, L.B. and Waterman, C.M. (2015) Integration of actin dynamics and cell adhesion by a three-dimensional, mechanosensitive molecular clutch. *Nat. Cell Biol.* 17, 955–963

5. Kanchanawong, P. *et al.* (2010) Nanoscale architecture of integrin-based cell adhesions. *Nature* 468, 580–584
6. Wang, S.E. *et al.* (2009) Transforming growth factor beta induces clustering of HER2 and integrins by activating Src-focal adhesion kinase and receptor association to the cytoskeleton. *Cancer Res.* 69, 475–482
7. Acerbi, I. *et al.* (2015) Human breast cancer invasion and aggression correlates with ECM stiffening and immune cell infiltration. *Integr. Biol. (Camb.)* 7, 1120–1134
8. Apoorva, F.N.U. *et al.* (2017) Lymph node stiffness-mimicking hydrogels regulate human B-cell lymphoma growth and cell surface receptor expression in a molecular subtype-specific manner. *J. Biomed. Mater. Res. A* 105, 1833–1844
9. Paszek, M.J. *et al.* (2005) Tensional homeostasis and the malignant phenotype. *Cancer Cell* 8, 241–254
10. Tan, Y. *et al.* (2014) Matrix softness regulates plasticity of tumour-repopulating cells via H3K9 demethylation and Sox2 expression. *Nat. Commun.* 5, 4619
11. Butcher, D.T. *et al.* (2009) A tense situation: forcing tumour progression. *Nat. Rev. Cancer* 9, 108–122
12. Tian, Y.F. *et al.* (2015) Integrin-specific hydrogels as adaptable tumor organoids for malignant B and T cells. *Biomaterials* 73, 110–119
13. Shin, J.W. and Mooney, D.W. (2016) Extracellular matrix stiffness causes systematic variations in proliferation and chemosensitivity in myeloid leukemias. *Proc. Natl. Acad. Sci. U. S. A.* 113, 12126–12131
14. Pickup, M.W. *et al.* (2014) The extracellular matrix modulates the hallmarks of cancer. *EMBO Rep.* 15, 1243–1253
15. Kolch, W. *et al.* (2015) The dynamic control of signal transduction networks in cancer cells. *Nat. Rev. Cancer* 15, 515–527
16. Cayrol, F. *et al.* (2015) Integrin αvβ3 acting as membrane receptor for thyroid hormones mediates angiogenesis in malignant T cells. *Blood* 125, 841–851
17. McKinnon, D.D. *et al.* (2014) Biophysically defined and cytocompatible covalently adaptable networks as viscoelastic 3D cell culture systems. *Adv. Mater.* 26, 865–872
18. Alge, D.L. *et al.* (2013) Synthetically tractable click hydrogels for three-dimensional cell culture formed using tetrazine–norbornene chemistry. *Biomacromolecules* 14, 949–953
19. DeForest, C.A. and Anseth, K.S. (2011) Cytocompatible click-based hydrogels with dynamically tunable properties through orthogonal photoconjugation and photocleavage reactions. *Nat. Chem.* 3, 925–931
20. Chaudhuri, O. *et al.* (2014) Extracellular matrix stiffness and composition jointly regulate the induction of malignant phenotypes in mammary epithelium. *Nat. Mater.* 13, 970–978
21. Lee, T.T. *et al.* (2015) Light-triggered *in vivo* activation of adhesive peptides regulates cell adhesion, inflammation and vascularization of biomaterials. *Nat. Mater.* 14, 352–360
22. Gandavarapu, N.R. *et al.* (2014) Photo-click living strategy for controlled, reversible exchange of biochemical ligands. *Adv. Mater.* 26, 2521–2526
23. Discher, D.E. *et al.* (2005) Tissue cells feel and respond to the stiffness of their substrate. *Science* 310, 1139–1143
24. Chaudhuri, O. *et al.* (2016) Hydrogels with tunable stress relaxation regulate stem cell fate and activity. *Nat. Mater.* 15, 326–334
25. Munster, S. *et al.* (2013) Strain history dependence of the nonlinear stress response of fibrin and collagen networks. *Proc. Natl. Acad. Sci. U. S. A.* 110, 12197–12202
26. Nam, S. *et al.* (2016) Strain-enhanced stress relaxation impacts nonlinear elasticity in collagen gels. *Proc. Natl. Acad. Sci. U. S. A.* 113, 5492–54927
27. Chaudhuri, O. *et al.* (2015) Substrate stress relaxation regulates cell spreading. *Nat. Commun.* 6, 6364
28. Wolf, K. *et al.* (2013) Physical limits of cell migration: control by ECM space and nuclear deformation and tuning by proteolysis and traction force. *J. Cell Biol.* 210, 1069–1084
29. Harada, T. *et al.* (2014) Nuclear lamin stiffness is a barrier to 3D migration, but softness can limit survival. *J. Cell Biol.* 204, 669–682
30. Davidson, P.M. *et al.* (2014) Nuclear deformability constitutes a rate-limiting step during cell migration in 3-D environments. *Cell. Mol. Bioeng.* 7, 293–306
31. Lautscham, L.A. *et al.* (2015) Migration in confined 3D environments is determined by a combination of adhesiveness, nuclear volume, contractility, and cell stiffness. *Biophys. J.* 109, 900–913
32. Denais, C.M. *et al.* (2016) Nuclear envelope rupture and repair during cancer cell migration. *Science* 352, 353–358
33. Raab, M. *et al.* (2016) ESCRT III repairs nuclear envelope ruptures during cell migration to limit DNA damage and cell death. *Science* 352, 359–362
34. Irianto, J. *et al.* (2017) DNA damage follows repair factor depletion and portends genome variation in cancer cells after pore migration. *Curr. Biol.* 27, 210–223
35. Pfeifer, C.R. *et al.* (2017) Genome variation across cancers scales with tissue stiffness – an invasion–mutation mechanism and implications for immune cell infiltration. *Curr. Opin. Syst. Biol.* 2, 103–114
36. Bakhoum, S.F. *et al.* (2018) Chromosomal instability drives metastasis through a cytosolic DNA response. *Nature* 553, 467–472
37. Kitamura, T. *et al.* (2015) Immune cell promotion of metastasis. *Nat. Rev. Immunol.* 15, 73–86
38. Gilbert, L.A. and Hemann, M.T. (2010) DNA damage-mediated induction of a chemoresistant niche. *Cell* 143, 355–366
39. Gilbert, L.A. and Hemann, M.T. (2011) Chemotherapeutic resistance: surviving stressful situations. *Cancer Res.* 71, 5062–5066
40. Shree, T. *et al.* (2011) Macrophages and cathepsin proteases blunt chemotherapeutic response in breast cancer. *Genes Dev.* 25, 2465–2479
41. Nakasone, E.S. *et al.* (2012) Imaging tumor–stroma interactions during chemotherapy reveals contributions of the microenvironment to resistance. *Cancer Cell* 21, 488–503
42. Bidwell, B.N. *et al.* (2012) Silencing of Irf7 pathways in breast cancer cells promotes bone metastasis through immune escape. *Nat. Med.* 18, 1224–1231
43. Fridlender, Z.G. *et al.* (2015) Promoting metastasis: neutrophils and T cells join forces. *Cell Res.* 25, 765–766
44. Wang, R. *et al.* (2011) Increased IL-10 mRNA expression in tumor-associated macrophage correlated with late stage of lung cancer. *J. Exp. Clin. Cancer Res.* 30, 62
45. Singh, A. (2017) Biomaterials innovation for next generation *ex vivo* immune tissue engineering. *Biomaterials* 130, 104–110
46. Shin, Y. *et al.* (2012) Microfluidic assay for simultaneous culture of multiple cell types on surfaces or within hydrogels. *Nat. Protoc.* 7, 1247–1259
47. Purwada, A. *et al.* (2015) *Ex vivo* engineered immune organoids for controlled germinal center reactions. *Biomaterials* 63, 24–34
48. Purwada, A. *et al.* (2017) Modular immune organoids with integrin ligand specificity differentially regulate *ex vivo* B cell activation. *ACS Biomater. Sci. Eng.* 3, 214–225
49. Purwada, A. and Singh, A. (2017) Immuno-engineered organoids for regulating the kinetics of B cell development and antibody production. *Nat. Protoc.* 12, 168–182
50. Fan, Y. *et al.* (2015) Bioengineering thymus organoids to restore thymic function and induce donor-specific immune tolerance to allografts. *Mol. Ther.* 23, 1262–1277
51. Hun, M. *et al.* (2017) Native thymic extracellular matrix improves *in vivo* thymic organoid T cell output, and drives *in vitro* thymic epithelial cell differentiation. *Biomaterials* 118, 1–15
52. Bhatia, S.N. and Ingber, D.E. (2014) Microfluidic organs-on-chips. *Nat. Biotechnol.* 32, 760–772
53. Kostic, A.D. *et al.* (2013) *Fusobacterium nucleatum* potentiates intestinal tumorigenesis and modulates the tumor-immune microenvironment. *Cell Host Microbe* 14, 207–215

54. Castellarin, M. *et al.* (2012) *Fusobacterium nucleatum* infection is prevalent in human colorectal carcinoma. *Genome Res.* 22, 299–306
55. Fuccio, L. *et al.* (2010) Gastric cancer, *Helicobacter pylori* infection and other risk factors. *World J. Gastrointest. Oncol.* 2, 342–347
56. Pawelek, J.M. *et al.* (2003) Bacteria as tumour-targeting vectors. *Lancet Oncol.* 4, 548–556
57. Johnson, C.H. *et al.* (2015) Metabolism links bacterial biofilms and colon carcinogenesis. *Cell Metab.* 21, 891–897
58. Yoshimoto, S. *et al.* (2013) Obesity-induced gut microbial metabolite promotes liver cancer through senescence secretome. *Nature* 499, 97–101
59. Thomas, R.M. and Jobin, C. (2015) The microbiome and cancer: is the 'oncobiome' mirage real? *Trends Cancer* 1, 24–35
60. Lax, A.J. and Thomas, W. (2002) How bacteria could cause cancer: one step at a time. *Trends Microbiol.* 10, 293–299
61. Bartfeld, S. *et al.* (2015) *In vitro* expansion of human gastric epithelial stem cells and their responses to bacterial infection. *Gastroenterology* 148, 126–136 e6
62. Shah, P. *et al.* (2016) A microfluidics-based *in vitro* model of the gastrointestinal human–microbe interface. *Nat. Commun.* 7, 11535
63. Kim, H.J. *et al.* (2016) Contributions of microbiome and mechanical deformation to intestinal bacterial overgrowth and inflammation in a human gut-on-a-chip. *Proc. Natl. Acad. Sci. U. S. A.* 113, E7–E15
64. Sivan, A. *et al.* (2015) Commensal *Bifidobacterium* promotes antitumor immunity and facilitates anti-PD-L1 efficacy. *Science* 350, 1084–1089
65. Vetizou, M. *et al.* (2015) Anticancer immunotherapy by CTLA-4 blockade relies on the gut microbiota. *Science* 350, 1079–1084
66. Xu, L. *et al.* (2016) Virtual microfluidics for digital quantification and single-cell sequencing. *Nat. Methods* 13, 759–762
67. Brito, I.L. and Alm, E.J. (2016) Tracking strains in the microbiome: insights from metagenomics and models. *Front. Microbiol.* 7, 712
68. Din, M.O. *et al.* (2016) Synchronized cycles of bacterial lysis for *in vivo* delivery. *Nature* 536, 81–85
69. Kim, H.J. *et al.* (2012) Human gut-on-a-chip inhabited by microbial flora that experiences intestinal peristalsis-like motions and flow. *Lab Chip* 12, 2165–2174
70. Yissachar, N. *et al.* (2017) An intestinal organ culture system uncovers a role for the nervous system in microbe–immune crosstalk. *Cell* 168, 1135–1148 e12
71. Calvo, F. *et al.* (2013) Mechanotransduction and YAP-dependent matrix remodelling is required for the generation and maintenance of cancer-associated fibroblasts. *Nat. Cell Biol.* 15, 637–646
72. Seo, B.R. *et al.* (2015) Obesity-dependent changes in interstitial ECM mechanics promote breast tumorigenesis. *Sci. Transl. Med.* 7, 301ra130
73. Polacheck, W.J. *et al.* (2014) Mechanotransduction of fluid stresses governs 3D cell migration. *Proc. Natl. Acad. Sci. U. S. A.* 111, 2447–2452
74. Huang, L. *et al.* (2015) Ductal pancreatic cancer modeling and drug screening using human pluripotent stem cell- and patient-derived tumor organoids. *Nat. Med.* 21, 1364–1371
75. Beguelin, W. *et al.* (2017) EZH2 enables germinal centre formation through epigenetic silencing of CDKN1A and an Rb-E2F1 feedback loop. *Nat. Commun.* 8, 877
76. Stephenson, R. and Singh, A. (2017) Drug discovery and therapeutic delivery for the treatment of B and T cell tumors. *Adv. Drug Deliv. Rev.* 114, 285–300
77. Jarde, T. *et al.* (2016) Wnt and Neuregulin1/ErbB signalling extends 3D culture of hormone responsive mammary organoids. *Nat. Commun.* 7, 13207
78. Legant, W.R. *et al.* (2010) Measurement of mechanical tractions exerted by cells in three-dimensional matrices. *Nat. Methods* 7, 969–971

PLOS ONE

RESEARCH ARTICLE

Automated analysis of cell migration and nuclear envelope rupture in confined environments

Joshua J. Elacqua, Alexandra L. McGregor, Jan Lammerding*

Meinig School of Biomedical Engineering, Weill Institute for Cell and Molecular Biology, Cornell University, Ithaca, NY, United States of America

* jan.lammerding@cornell.edu

OPEN ACCESS

Citation: Elacqua JJ, McGregor AL, Lammerding J (2018) Automated analysis of cell migration and nuclear envelope rupture in confined environments. PLoS ONE 13(4): e0195664. https://doi.org/10.1371/journal.pone.0195664

Editor: Ramani Ramchandran, Medical College of Wisconsin, UNITED STATES

Received: October 31, 2017

Accepted: March 27, 2018

Published: April 12, 2018

Data Availability Statement: All relevant data are within the paper and its Supporting Information files.

Funding: This work was supported by awards from the National Institutes of Health [R01 HL082792 (National Heart, Lung, and Blood Institute) and U54 CA210184 (National Cancer Institute), to J.L.]; the Department of Defense Breast Cancer Research Program (Congressionally Directed Medical Research Program) [Breakthrough Award BC150580, to J.L.], the National Science Foundation [CAREER Award CBET-1254846, to J.

Abstract

Recent *in vitro* and *in vivo* studies have highlighted the importance of the cell nucleus in governing migration through confined environments. Microfluidic devices that mimic the narrow interstitial spaces of tissues have emerged as important tools to study cellular dynamics during confined migration, including the consequences of nuclear deformation and nuclear envelope rupture. However, while image acquisition can be automated on motorized microscopes, the analysis of the corresponding time-lapse sequences for nuclear transit through the pores and events such as nuclear envelope rupture currently requires manual analysis. In addition to being highly time-consuming, such manual analysis is susceptible to person-to-person variability. Studies that compare large numbers of cell types and conditions therefore require automated image analysis to achieve sufficiently high throughput. Here, we present an automated image analysis program to register microfluidic constrictions and perform image segmentation to detect individual cell nuclei. The MATLAB program tracks nuclear migration over time and records constriction-transit events, transit times, transit success rates, and nuclear envelope rupture. Such automation reduces the time required to analyze migration experiments from weeks to hours, and removes the variability that arises from different human analysts. Comparison with manual analysis confirmed that both constriction transit and nuclear envelope rupture were detected correctly and reliably, and the automated analysis results closely matched a manual analysis gold standard. Applying the program to specific biological examples, we demonstrate its ability to detect differences in nuclear transit time between cells with different levels of the nuclear envelope proteins lamin A/C, which govern nuclear deformability, and to detect an increase in nuclear envelope rupture duration in cells in which CHMP7, a protein involved in nuclear envelope repair, had been depleted. The program thus presents a versatile tool for the study of confined migration and its effect on the cell nucleus.

L.; GRFP Award DGE-1144153 to A.L.M.]; and the Cornell University College of Engineering [Engineering Learning Initiatives Grant, to J.E.]. This work was performed in part at the Cornell NanoScale Facility, a member of the National Nanotechnology Coordinated Infrastructure (NNCI), which is supported by the National Science Foundation (Grant ECCS-1542081). The funders had no role in study design, data collection and analysis, decision to publish, or preparation of the manuscript.

Competing interests: The authors have declared that no competing interests exist.

Introduction

Cell migration is necessary for a number of important physiological processes including immune response, wound healing, and cancer metastasis. Cell migration is particularly important in the context of cancer metastasis, which is responsible for the vast majority of cancer-related deaths, including over 90% of breast cancer deaths [1]. For cancer cells to metastasize, they must first migrate away from the site of the primary tumor (invasion), enter blood or lymphatic vessels (intravasation) through which they are transported to distant parts of the body, and then exit the vessels (extravasation) and migrate to new sites, where they may grow into secondary tumors [1, 2]. The migration behavior of cancer cells is a good indicator of patient prognosis, as more migratory cells form metastases at higher rates. Preventing or reducing cancer cell migration could significantly improve cancer patient outcomes, and present a key step in reducing metastasis-related mortality.

During the processes of tissue invasion and intra- and extravasation, cancer cells have to squeeze through small spaces between other cells and within the extracellular matrix (ECM). Recent findings point to an important role of the cell nucleus in the migration of cells through such confined environments [3]. Deformation of the nucleus, which is the largest and stiffest cellular organelle, determines the ability of cells to pass through constrictions smaller than the nuclear cross-section [3–5]. Cells with less deformable nuclei take longer to pass through microscopic pores than cells with more deformable nuclei [6–8]. One of the primary determinants of nuclear deformability is the expression of lamins A and C, intermediate filament proteins that form a dense protein network (nuclear lamina) underneath the inner nuclear membrane [9, 10]. Intriguingly, expression of lamin A/C is decreased in many cancers [11–15], which could contribute to increased metastatic potential of tumor cells by facilitating both invasion and intra- and extravasation.

In addition to modulating transit efficiency through confined environments, migration through tight spaces places substantial physical stresses on the nucleus, which can lead to a transient loss of nuclear envelope (NE) integrity during interphase, referred to as NE rupture [16, 17]. NE rupture, which allows uncontrolled exchange of cytoplasmic and nuclear proteins, along with protrusion of chromatin into the cytoplasm, could result in increased genomic instability and promote cancer progression [18]. Cells can restore NE integrity using components of the endosomal sorting complexes required for transport-III (ESCRT-III) machinery [16, 17]. Inhibiting NE repair, when combined with inhibition of DNA damage repair pathways, results in substantially increased cell death after NE rupture [16, 17], pointing to potential treatment approaches to specifically target metastatic cancer cells.

These findings have motivated a rapidly growing interest in studying nuclear deformation and NE rupture, particularly during confined migration [10, 18–22]. Microfluidic devices with precisely defined constrictions that mimic interstitial spaces *in vivo* have emerged as powerful tools to study the role of nuclear deformation and NE rupture in cell migration [7, 16, 17, 20, 23–28]. Although the walls of such devices are more rigid than the *in vivo* spaces through which cells migrate, confined migration and NE rupture results obtained in these microfluidic devices closely match those obtained in collagen matrices and from intravital imaging studies [16, 17], and the devices enable time-lapse imaging of single-cell migration under precisely defined conditions. In such experiments, nuclei are often identified by fluorescently labeled DNA (e.g., staining with Hoechst 33342) or histones (e.g., expression of H2B-tdTomato). NE rupture events can be detected by monitoring the intracellular localization of a green fluorescent protein containing a nuclear localization sequence (NLS-GFP) [16, 17, 29]. NLS-GFP is normally contained within the nucleus but spills into the cytoplasm during NE rupture and is gradually re-imported into the nucleus upon NE repair (Fig 1). Time-lapse experiments using

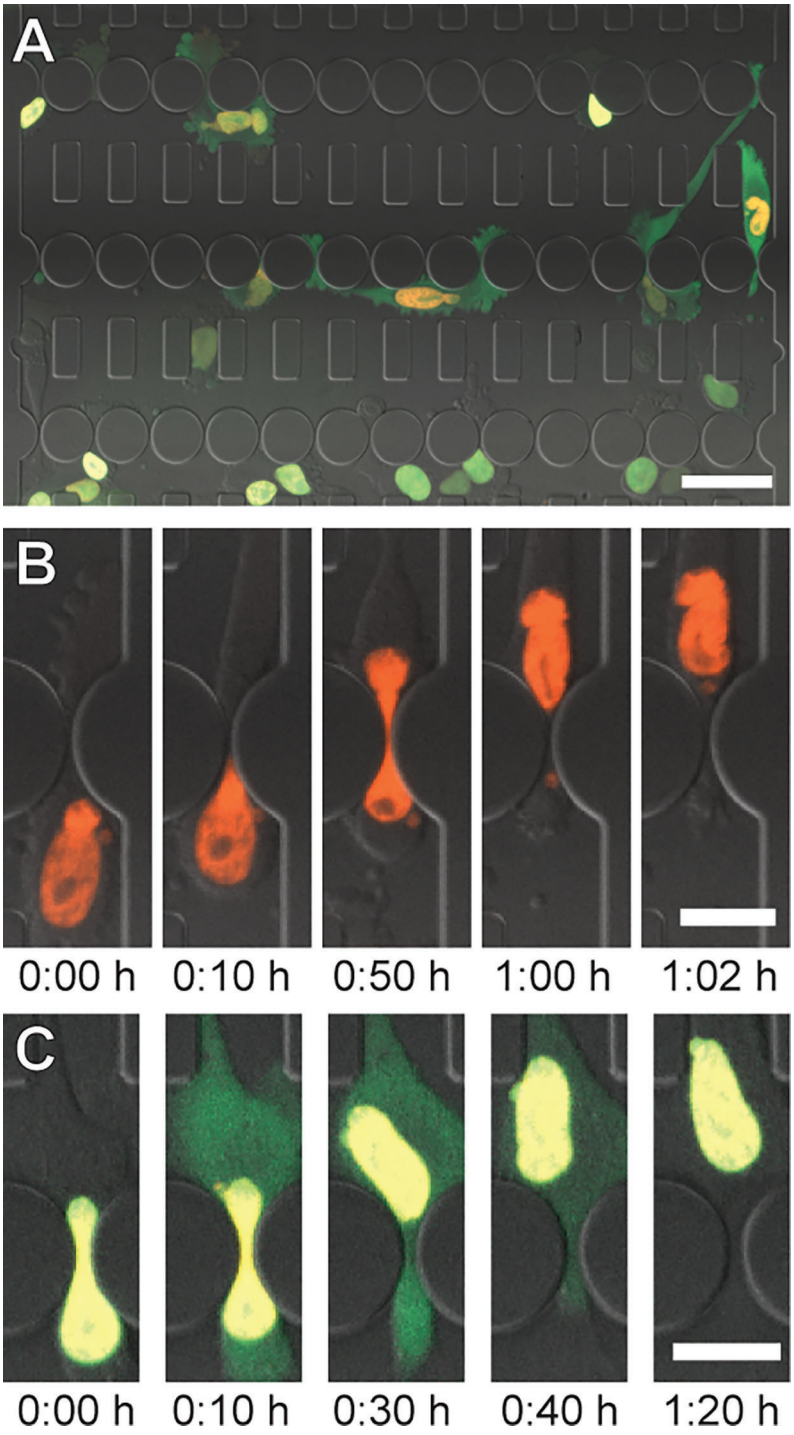

Fig 1. Cell migration through microfluidic constrictions. (**A**) Cells expressing NLS-GFP and H2B-tdTomato migrating through a microfluidic device. Scale bar: 50 μm. (**B**) Time series of a nucleus squeezing through a constriction. Scale: bar 20 μm. (**C**) Time series of a NE rupture event. NLS-GFP leaks into the cytoplasm upon NE rupture and is reimported into the nucleus as the NE is repaired. Scale bar: 20 μm.

https://doi.org/10.1371/journal.pone.0195664.g001

cancer cells typically cover 6 to 24 hours, with multi-color (fluorescence and transmitted light) images acquired every 2 to 10 minutes, resulting in large (>40 GB per experiment), multi-dimensional data sets that take several days to weeks to manually analyze. Such low throughput

image analysis provides a substantial challenge when studying large sets of experimental conditions. Furthermore, manual analysis by different observers can add substantial variability to the experimental data.

To address these issues, we developed a MATLAB program to perform the image analysis in an automated, reproducible, and robust process. The program is capable of tracking individual cells/nuclei as they migrate through microfluidic constriction channels and compute transit times for individual constrictions. While primarily intended to study cell migration in confined environments, the program can also be used to study cells migrating on unconfined 2-D substrates. The progam can also reliably detect NE rupture events and their duration. The program automatically recognizes dividing cells, resulting in increased robustness and accuracy comparable to expert manual analysis, but with substantially increased efficiency.

Automated analysis algorithm

Overview

Automated image analysis begins by locating the constrictions in the first image (Fig 2). The image is then processed to reduce noise and to detect fluorescently labeled nuclei. For each subsequent image in the sequence, image stabilization is performed to account for small shifts in the field of view during image acquisition. Each image is then subject to the same processing as above to reduce noise and detect nuclei. Identified nuclei are tracked from the previous image to the current one. All nuclei are then observed for incidences of constriction passage and NE rupture. After the full sequence has been analyzed, the tracking results are exported to a spreadsheet and presented to the user for manual validation (Fig 2). The program was implemented in MATLAB 2016a and runs on all MATLAB supported platforms, version 2016a and newer. It can be downloaded at the following URL: https://github.com/Lammerding/MATLAB-CellTracking.

Locating constrictions

Constriction location is performed by identifying the round pillars in the microfluidic devices that form the three rows of constrictions (Fig 1A and S1 Fig). This is accomplished by applying

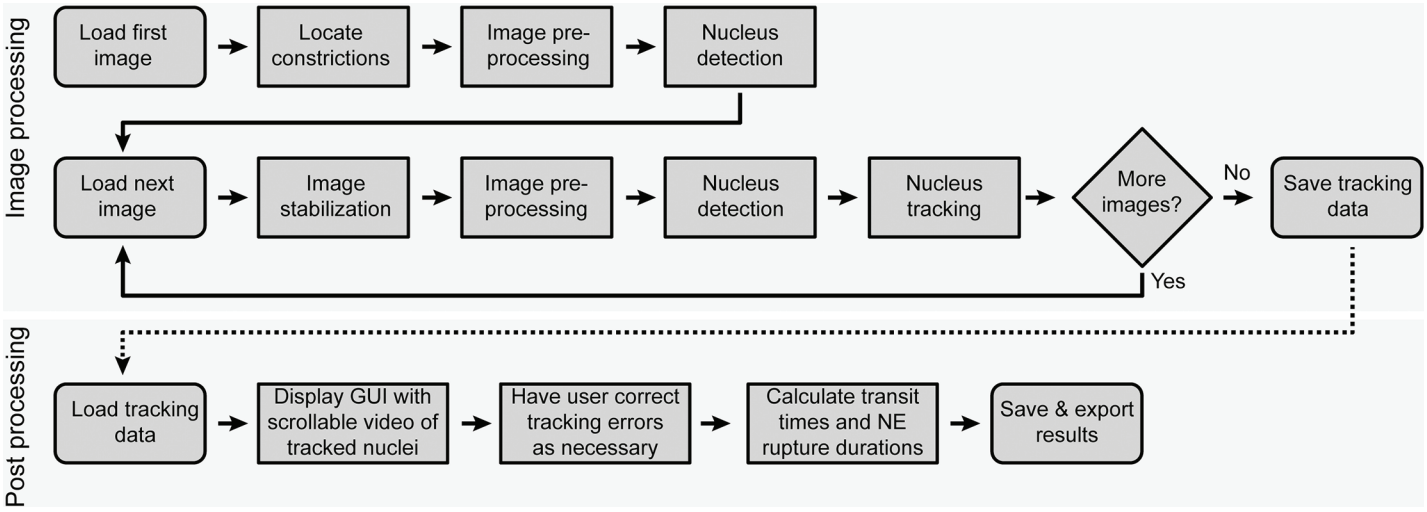

Fig 2. Flowchart of automated analysis steps. Steps the program takes when analyzing an image sequence are detailed, including image processing (top) and post-processing (bottom).

https://doi.org/10.1371/journal.pone.0195664.g002

a circular Hough transform (a technique that identifies circles in an image) to a transmitted light image of the device. All images are then rotated to align the rows of constrictions horizontally. Virtual boundaries are defined at a specific distance above and below the constriction centerline to determine nucleus entry and exit for each row of constrictions. (S1 Fig). This approach can be adjusted for devices with different designs.

Image pre-processing and stabilization. To reduce the noise in the fluorescence images and enhance the contrast between the nuclear signals and the background, a 10 × 10 pixel Gaussian filter is applied to the images of the fluorescence channels. Image stabilization is then performed via normalized 2D cross-correlation between an image and its predecessor. The obtained spatial offset values are applied to the transmitted light as well as the fluorescence image channels.

Nucleus detection

Nuclei are identified by binarizing images with a locally adaptive threshold based on their H2B-tdTomato signal and applying connected component analysis. Local thresholding, while more computationally expensive, provides better results than global thresholding, especially for unevenly illuminated images. To separate touching nuclei into distinct objects, further segmentation is necessary. Since nuclei are generally oval-shaped, the program uses watershed segmentation based of the distance transform of the identified nuclei. Watershedding segments an image based on "watershed lines", which separate the image into different "catchment basins". Figuratively, the image is treated like a topographic map, with image intensities representing the height. This means image areas containing low pixel intensity values are grouped together and separated from other groups if there are high pixel intensity values between them (the "watersheds"). The resulting regions are converted into binary images and further processed to distinguish single nuclei, which form a single catchment basin, from multiple touching nuclei, which form multiple basins separated by a watershed line. Additional imaging process steps are applied to prevent over-segmentation. A visual guide to this algorithm is provided in S2 Fig. Nuclei inside of constrictions are excluded from this segmentation since they take on a dumbbell shape (Fig 1B, 0:50 h) and otherwise may be incorrectly split into two objects. After image segmentation, identified objects are deleted if their properties, such as size and circularity, suggest that they are not nuclei (Fig 3A and 3B).

Nucleus tracking

After nuclei have been identified, they are tracked over time by recording their centroid position at each time point. The following error function is applied to every possible pairing of a

Fig 3. Examples of nuclear identification and tracking. (**A**) Merged image of the transmitted light and tdTomato channels. Nuclei (red) can be seen in the migration device. Scale bar: 50 μm. (**B**) Binarized version of red channel of image A. Each nucleus is identified as a separate object (white). (**C**) Example of tracking results. Nuclei (red) have been identified, and their centroid positions during migration are shown as yellow tracks. For clarity, tracks displayed here are limited to data for only the last six hours.

https://doi.org/10.1371/journal.pone.0195664.g003

nucleus in one image and a nucleus in the following image:

$$E = distance^2 + 2 * |\Delta fluorescent\ intensity| + 2 * |\Delta area|$$

This error function is related to the likelihood that two objects are the same nucleus and is based on the square of the distance between the centroids of the two objects. Since comparing only the distances between objects produces inaccurate results when multiple nuclei are in close proximity, the error function also includes the change in each object's area and its average H2B-tdTomato fluorescent intensity. These values are expected to remain relatively constant over time for individual nuclei, but vary between different nuclei. The object from the previous time point and the object in the current time point that together have the lowest error function value are paired with one another and marked as unavailable for other pairings. Pairs can only be made if the centroids of the objects are within 40 μm of one another, which is the maximum distance a cell typically travels within the chosen time interval. If necessary, the user can later correct this during the manual validation and editing stage, but we found that such instances are rare. Object pairing and marking availability status continues until no further object pairings are available. Upon completion, time-resolved data for each identified nucleus include centroid position, bounding box, area, and fluorescence intensity, which can be displayed for each nucleus (Fig 3C) and used for further analysis.

Detection of cell transit through constrictions

The passage of nuclei through constrictions is evaluated as follows: if the top of a nucleus' bounding box is above the lower boundary of a constriction and the bottom of the nucleus' bounding box is below the upper boundary of the constriction, the nucleus is considered to be attempting to pass through the constriction (Part A in S3 Fig). When an attempting nucleus moves completely above the upper bounding box, it is recorded as having successfully passed the constriction (Part B in S3 Fig). A nucleus that is attempting to traverse a constriction but then moves back out of the boundary of the constriction is recorded as failing to pass through the constriction (Part C in S3 Fig). Nuclei that only briefly (1 time point) attempt to enter a constriction are excluded from the analysis. Such instances can occur when a cell moves parallel to the row of constrictions and a part of the nucleus crosses the boundary of the constriction, without the cell attempting to pass through the constriction.

NE rupture detection

NE rupture is detected by monitoring the inverse ratio of the nuclear NLS-GFP signal to the H2B-tdTomato signal. Since the total amount of NLS-GFP per cell stays approximately constant over time, and NLS-GFP spills into the cytoplasm during NE rupture, the average NLS-GFP nuclear intensity decreases during NE rupture. In contrast, the H2B-tdTomato signal remains nearly constant, allowing for normalization to the H2B-tdTomato signal. The normalization accounts for variations due to photobleaching and other image acquisition effects. The ratio of average H2B-tdTomato signal to average nuclear NLS-GFP signal [*H2B/NLS*] is measured for each nucleus at every time point. If the difference in ratio between two consecutive time points [*Δ(H2B/NLS)*] exceeds 20% of the previous time point's ratio, or if the *H2B/NLS* ratio increases continuously over the course of at least 5 consecutive time points, then NE rupture is determined to have begun (Fig 4A, red arrow). As the NE is repaired, NLS-GFP re-enters the nucleus, and *Δ(H2B/NLS)* becomes negative. The NE rupture event is completed when the *H2B/NLS* ratio returns close to its pre-rupture value and *Δ(H2B/NLS)* returns to zero (Fig 4C and 4D).

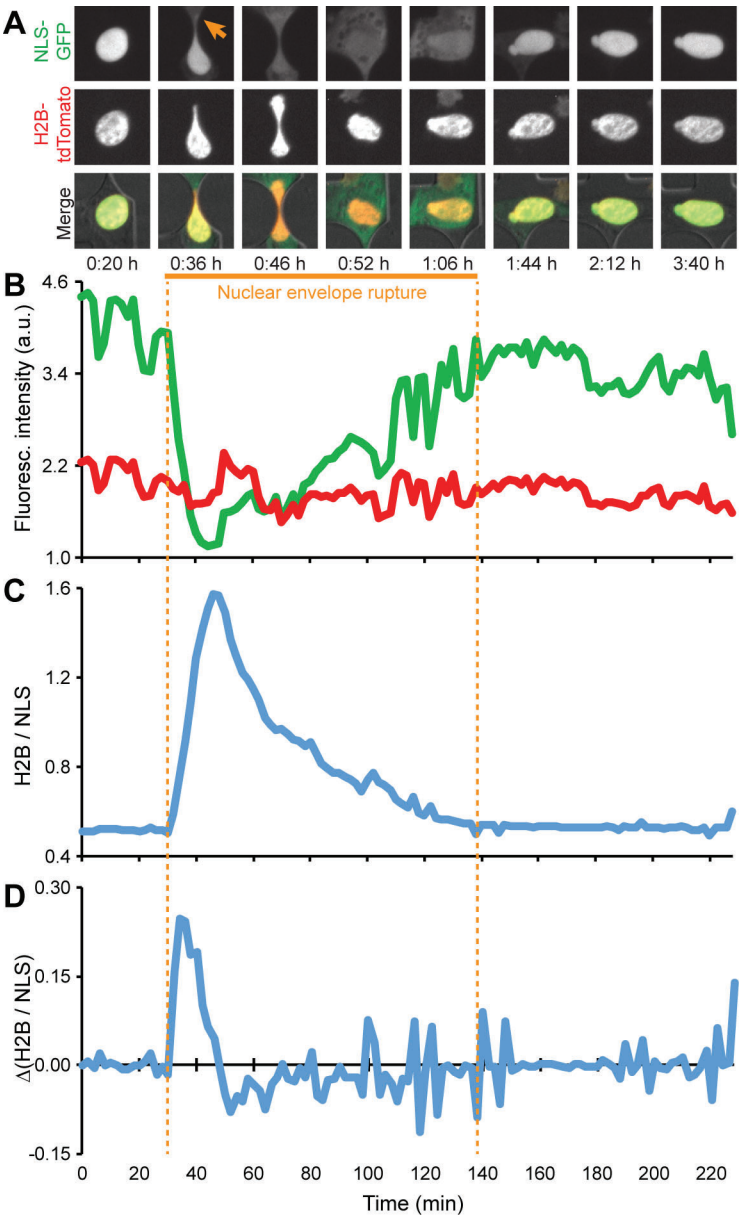

Fig 4. Detection of NE rupture. (**A**) During NE rupture (arrow), NLS-GFP (green) spreads throughout the cytoplasm, causing the nuclear NLS-GFP signal to lose intensity. In contrast, the H2B-tdTomato signal (red) remains approximately constant. (**B**) Normalizing these two signals against one another (H2B/ NLS) significantly reduces the effects of noise and allows for more accurate NE rupture detection. (**C**) Steep increases in the H2B/NLS ratio, which correspond to high values of Δ(H2B/NLS), plotted in (**D**), indicate the start of a NE rupture event. The data shown here are for a representative cell.

https://doi.org/10.1371/journal.pone.0195664.g004

Since NE breakdown also occurs during mitosis, it is important to distinguish loss of nuclear NLS-GFP signals between mitotic cells and those exhibiting interphase NE rupture to avoid false positive detection of NE rupture. Mitosis and NE rupture both begin with NLS-GFP spreading into the cytoplasm and are initially indistinguishable from one another. However, during mitosis, two daughter nuclei form from one initial nucleus. Thus, if a nucleus is detected as undergoing NE rupture, and a new nucleus appears in its vicinity in the next time point, the event is reclassified as mitosis, and not NE rupture (S4 Fig).

Manual verification

Automated data analysis can occasionally misidentify events; therefore, a video for manual verification is generated for every image sequence analyzed. The video is displayed on a graphical user interface, and the user can manually select individual nuclei and events to make corrections as necessary. Recorded data is exported to a file after manual validation.

Automated analysis results

Comparison of automated and manual analysis

To assess the accuracy of the program, we acquired two image sequences of BT-549 breast cancer cells migrating through a microfluidic device with 2-μm wide constrictions. The two image sequences were manually analyzed by four trained observers, recording constriction entry and exit times for each nucleus. One image sequence (S1 Video) was used to "train" the automated image analysis program to define the boundaries that mark entry and exit of the nucleus into/out of the constrictions. The program analyzed the video for six conditions, with constriction boundary lines placed either 5, 6, 7, 8, 9, or 10 μm from the constriction centerline. Comparing the program's results with the manual results revealed that placing the boundaries 7 μm above and below the center produced the best agreement with the manual analysis.

The other image sequence (S2 Video) was then used to "test" the program and the 7-μm constriction boundaries (Fig 5). Results of the automated image analysis for each nuclear transit event were compared to a manual analysis gold-standard, defined as the average result from four expert reviewers who assess nuclear transit times based on the visible deformation of the nucleus as it enters and exists the constriction. Comparison of the constriction transit times of individual cells determined by the program and four expert observers showed excellent agreement between the program and the manual gold-standard (Fig 5A). Similarly, the average constriction transit times computed by the program for each of the image sequences closely matched the data of the manual observers. Importantly, the program and all four observers correctly identified that cells that overexpress lamin A (Image sequence 1), and which have less deformable nuclei, had significantly longer transit times ($p < 0.05$) than mock-modified control cells (Image sequence 2) (Fig 5B).

Out of the 50 verified constriction transit events present and analyzed in the two image sequences, 46 were identified by the program prior to manual verification/correction, resulting in a "miss" rate of 8%. We recorded similar "miss" rates in six separate, independent image sequences analyzed by the program (data not shown). The four expert analysts had a combined "miss" rate of 10%, identifying an average of 45 events out of the total 50 transit events in the two image sequences. Therefore, even prior to manual verification, the program misses a similar or even lower number of nuclear constriction transit events than the expert analysts. The events missed by the program can be quickly and easily added to the programmatic analysis during the manual verification stage.

In addition to the identification of true nuclear transit events, person-to-person variability also applies to the transit times measured for each event. For any given transit event, the transit times recorded by the four manual analysts varied by greater than 2 image frames on average, ranging from 0 (complete agreement) to a maximum of 6 image frames. In all but one case (identified by the asterisk in Fig 5A) the program determined a transit time within the range of the manual measurements for that event. The single exception occurred in a cell that moved back and forth as it struggled to pass through the constriction, and the event could be identified as either one long attempt (as assessed by the expert analysts) or two shorter attempts (the first of which a failed attempt, followed by a successful attempt), as assessed by the program.

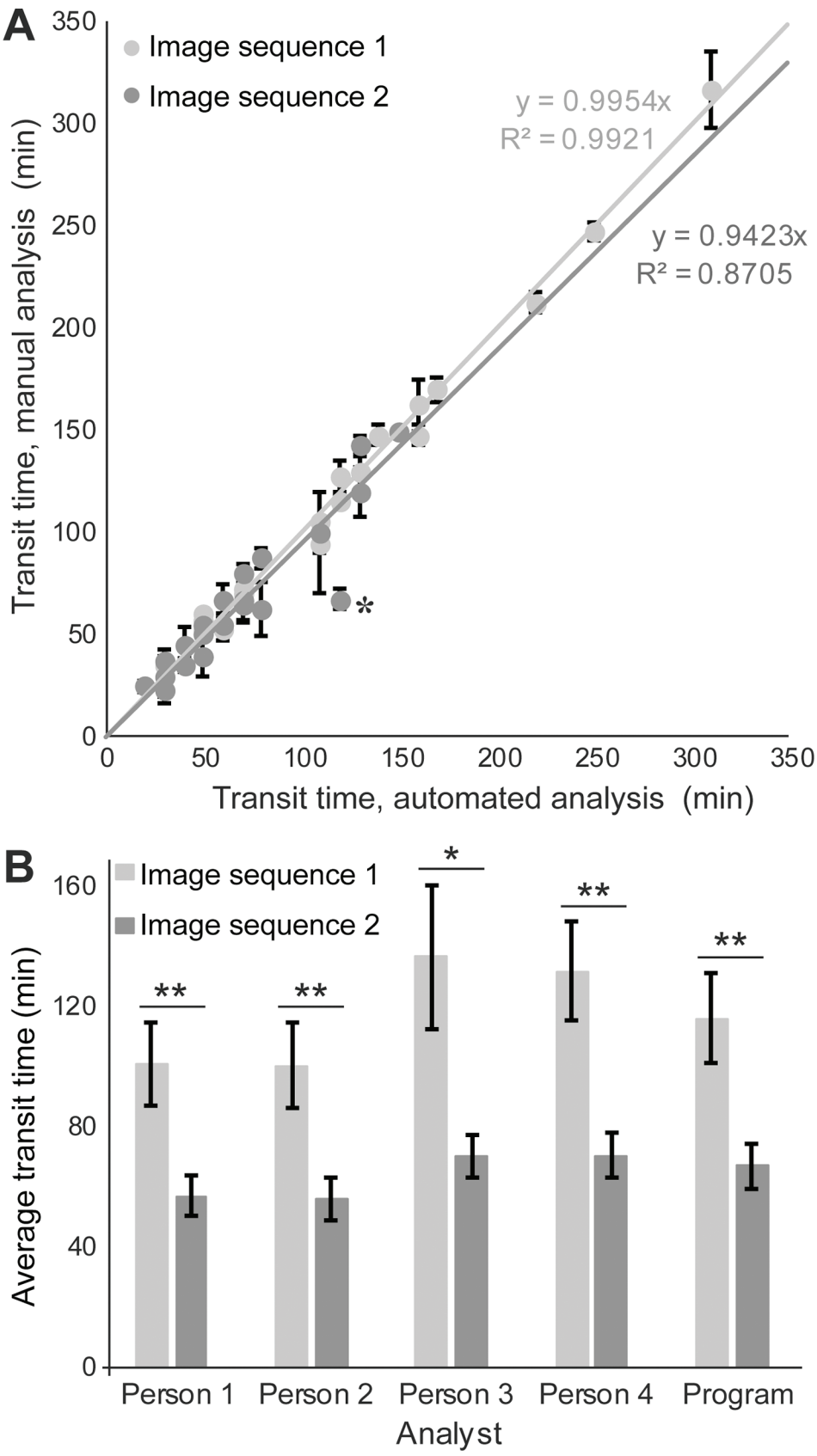
A
Image sequence 1
Image sequence 2
y = 0.9954x
R² = 0.9921
y = 0.9423x
R² = 0.8705
Transit time, manual analysis (min)
Transit time, automated analysis (min)
0
50
100
150
200
250
300
350
*
B
Image sequence 1
Image sequence 2
Average transit time (min)
0
40
80
120
160
**
**
*
**
**
Person 1
Person 2
Person 3
Person 4
Program
Analyst

Fig 5. Verification of automated image analysis by comparison to manual analysis. (**A**) Automated analysis results plotted against manual analysis results (mean ± s.e.m. from four observers) for individual cells in two separate image sequences, each of which corresponds to a single section of a microfluidic device. For perfect agreement, the regression line plotted through these points would have a slope of one. Only one automated-analysis result substantially deviated from the manual reference, indicated by an asterisk. The manual analysis determined the nucleus to make two attempts to pass through the constriction, failing the first but succeeding the second time. The program identified this as a single, longer attempt. (**B**) Constriction transit times (mean ± s.e.m.) determined by four manual analysts and the automated analysis for the cells in the same two image sequences analyzed for panel A. Cells are BT-549 breast cancer and are either overexpressing lamin A (Image sequence 1) or an empty vector (Image sequence 2). Overexpression of lamin A results in less deformable nuclei and longer transit times through narrow constrictions (*, $p < 0.05$; **, $p < 0.001$ as calculated by ANOVA followed by Tukey's multiple comparison test; $n = 23–26$ and 20–24 (depending on the analyst), respectively).

https://doi.org/10.1371/journal.pone.0195664.g005

Detection of differences in constriction transit times

To assess whether the program could detect differences in constriction transit times in cell lines other than those used for the 'training' and 'test' data, we performed experiments with A549 human lung carcinoma cells treated with siRNA against lamin A/C or a non-target control (S5 Fig). A previous study found that lamin A/C depletion in A549 cells results in increased transit efficiency through small pores [6]. In another study, lamin A/C-deficient mouse embryo fibroblasts had significantly shorted transit times for passage through small constrictions than wild-type controls [7]. Consistent with the previous reports, the automated image analysis of our experiments found that lamin A/C-depleted cells passed faster through 1- and 2-μm wide constrictions than the non-target controls ($p < 0.05$). In contrast, both groups had comparable transit times ($p = 0.34$) when passing through 15-μm wide control channels that do not require nuclear deformation (Fig 6A).

Detection of differences in NE rupture durations

The program's ability to detect NE rupture events was verified through manual inspection of analyzed image sequences. To ensure that automated NE rupture detection is both precise and robust at identifying the durations of NE rupture/repair, we performed experiments with HT-1080 human fibrosarcoma cells treated with siRNA against the ESCRT-III family protein charged multivesicular body protein 7 (CHMP7) (S6 Fig). Since ESCRT-III proteins and CHMP7 are crucial for NE repair [16, 17, 29, 30], depletion of CHMP7 is expected to result in increased NE rupture duration. Automated image analysis confirmed that CHMP7-depleted HT-1080 cells experienced significantly longer NE rupture durations than the non-target controls ($p < 0.01$) (Fig 6B). CHMP7-depleted and non-target control cells showed similar H2B-tdTomato/NLS-GFP ratio values prior to NE rupture ($p > 0.9$) and 2 hours after rupture ($p = 0.28$), while CHMP7-depleted cells were slower to return to this baseline following NE rupture (Fig 6C).

Discussion

We have developed and validated a MATLAB program for the automated and robust analysis of nuclear activity as cells migrate through microfluidic devices. This automation reduces the amount of time required to analyze an image sequence from multiple days/weeks to ~5 hours for a time-lapse experiment with 24 positions/experimental conditions and over 100 time points per position. Furthermore, the automated analysis removes person-to-person variability in the obtained results. The results produced by the program are in close agreement with expert manual analysis. The program is suitable for a broad range of applications that use microfluidic devices to study the migration of cells through confined environments, including analysis of transit times through pores of different size, or incidence of NE rupture. Previously,

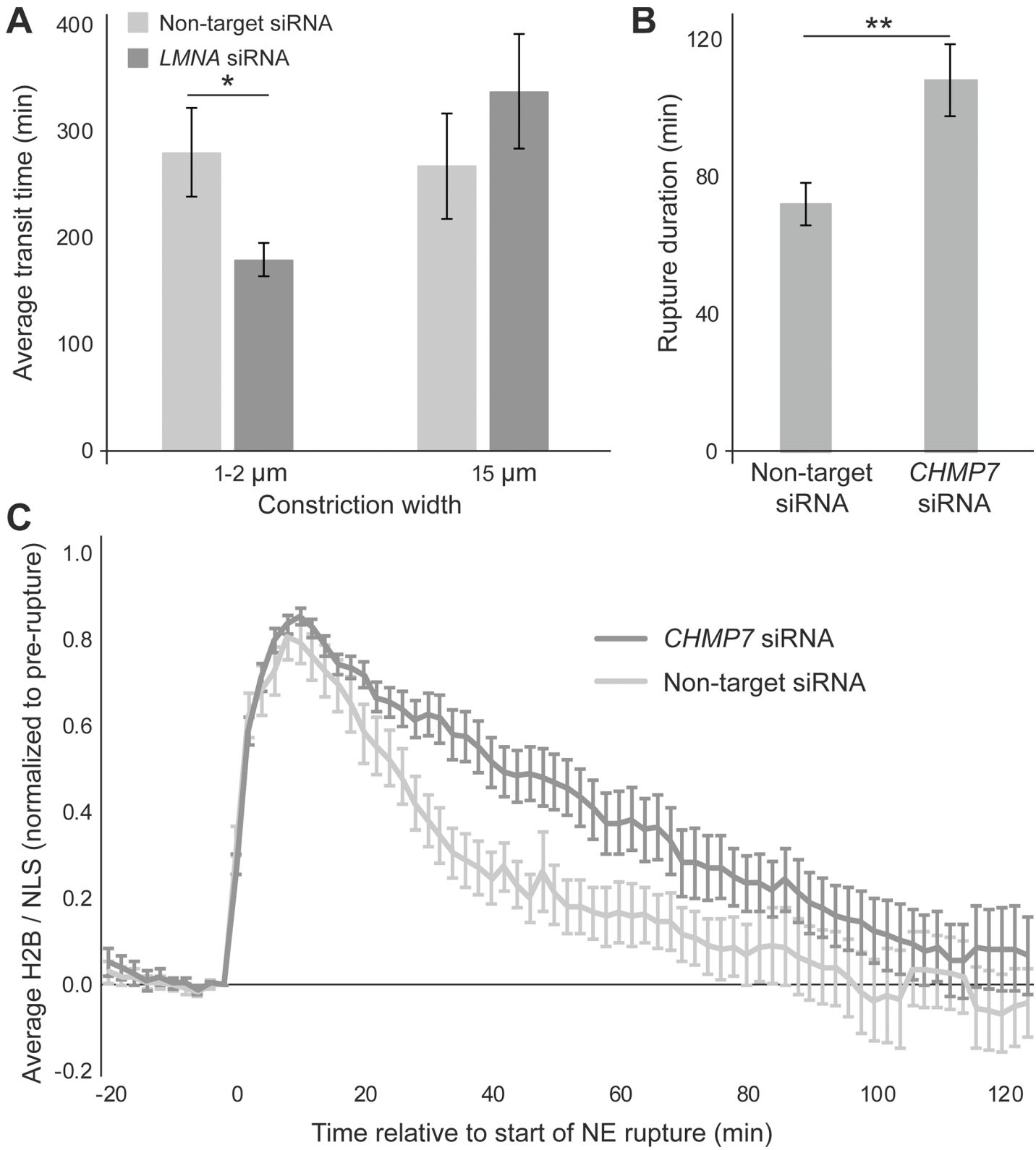

Fig 6. Application of automated image analysis program. (**A**) A549 cells depleted for lamin A/C ($n = 40$ cells across 4 microfluidic device sections) pass faster through small constrictions than non-target controls ($n = 26$ cells across 4 device sections). Transit times through larger openings were not statistically different (*, $p < 0.05$ as calculated by t-test; $n = 21, 14$, respectively). (**B**) HT-1080 cells depleted for CHMP7 ($n = 65$ cells across 3 device sections) took longer to repair their NE and restore nucleo-cytoplasmic compartmentalization than non-target controls (**, $p < 0.01$ as calculated by Mann-Whitney t-test; $n = 48$ cells across 3 device sections). (**C**) Dynamics of NE rupture and repair visualized by the ratio of nuclear H2B-tdTomato/NLS-GFP fluorescence for the CHMP7-depleted and non-target control cells. The

H2B/NLS signal is expressed relative to its value at $t = 0$, i.e., immediately prior to rupture, and normalized to reach a peak value of 1 for each nucleus. CHMP7-depletion results in slower return to baseline, indicating delay in NE repair. Error bars represent mean ± s.e.m.

https://doi.org/10.1371/journal.pone.0195664.g006

collecting data on a large number of cell lines, patient samples, or treatment conditions would have been impractical due to the substantial amount of time required to analyze the image sequences.

While the results presented here are based on a specific microfluidic migration device design, the modular nature of the program can be easily adapted to different design geometries, making it useful for a broad user base. Notably, the implemented automatic alignment and recognition of constrictions is independent of the constriction size and position. Similarly, fluorophores other than H2B-tdTomato and NLS-GFP can be used for the identification of nuclei and NE rupture, respectively.

The automated analysis is precise and robust enough to reach reliable conclusions concerning a population of cells' constriction transit times and NE rupture durations with only minimal user supervision. Furthermore, the program can generate and collect data that would be challenging to obtain through manual analysis. For example, the ability to collect pixel intensity values in specific areas of interest allows the program to monitor the intensity of fluorescence in every nucleus over time. This allows the actual time course of NE repair to be observed, recorded, and compared across populations of cells. In contrast, while manual analysis can record the duration of NE rupture events, it lacks the accuracy required to analyze the extent of repair at earlier time points.

This nucleus tracking program is currently used only to monitor constriction transit times and NE rupture events, but could readily be expanded to a broader array of applications. For example, measurements of nuclear migration persistence, i.e., the tendency of the nucleus to move in a constant direction, could be recorded, since nucleus centroids are determined for each time point. Such an analysis would be extremely tedious and highly time-consuming if done manually. The automated analysis could also be expanded to include cell death detection, for example, based on the permanent loss of NLS-GFP intensity and unmatched nuclei after cell death. Automated cell death analysis could be useful for screening of drugs that target metastatic cancer cells. Under the conditions used in the current experiments, only few cells died during imaging, and these cases appeared to be the result of confined migration and continuous NE rupture, rather than phototoxicity, consistent with previous reports [13, 16]. Additionally, the object identification and tracking elements of the program could be applied to any other set of time-lapse images, for example, to cells migrating on 2-D substrates or contact-printed micropatterns.

Materials and methods

Creating microfluidic devices

Microfluidic devices were created from a silicon wafer mold fabricated by 2-layer SU-8 photolithography as described previously [20]. Polydimethylsiloxane (PDMS) was created by mixing Sylgard 184 Silicone Elastomer Base and Silicone Elastomer Curing Agent in a 10:1 ratio as per the manufacturer's instructions (Corning). A vacuum chamber was then used to remove air bubbles, and the PDMS was poured into the silicon mold and baked for 2 hours at 65˚C to solidify. After removal from the mold, the PDMS was cut to size, and biopsy needles were used to cut out device reservoirs and perfusion channel inlets/outlets.

Devices and glass slides were then washed with deionized water and isopropyl alcohol, dried, and plasma cleaned for five minutes. Covalent bonding of the devices to the slides then

occurred by gentle pressing of the device onto the slide and placing the slide on a hot plate at 95˚C for 5 minutes. Slide-bound devices were then brought to a tissue-culture hood, and rinsed with 70% ethanol followed by deionized water. Device reservoirs were filled with 20 μg/mL of fibronectin in PBS (for A549 and BT-549 cells) or 0.05 mg/mL of collagen in 0.02 M acetic acid (HT-1080 cells). Devices were kept in a sealed Petri dish at 4˚C overnight to allow binding of the protein to the glass slide and PDMS.

Cell culture

The human lung carcinoma cell line A549 (ATCC) was cultured in F-12K media (Gibco) supplemented with 10% fetal bovine serum (FBS, VWR) and 1% penicillin and streptomycin (pen/strep, Gibco). The human fibrosarcoma cell line HT-1080 (ATCC) was cultured in DMEM supplemented with 10% FBS and 1% pen/strep. BT-549 breast cancer cells (ATCC) were cultured in RPMI media supplemented with 10% FBS and 1% pen/strep. All cells were cultured at 37˚C and 5% CO_2.

Generation of fluorescently labelled cell lines

Cell lines were stably modified with a retroviral vector to express both the NE rupture reporter NLS-GFP, and histone marker H2B-tdTomato (pQCXIP-NLS-copGFP-P2A-H2B-tdTomato-IRES-puro, System Biosciences). The retroviral vector was generated in two steps. LifeAct-GFP was digested out of the pQCXIP-LifeAct-GFP-P2A-H2B-tdTomato vector, and NLS-copGFP was ligated into the vector. NLS-copGFP was obtained from a lentiviral vector (pCDH-CMV-NLS-copGFP-EF1-blastiS) via digestion. The product was then amplified via touchdown PCR, introducing the NotI and AgeI restriction sites, using the following forward and reverse primers, respectively: 5′-CAAGCGGCCGCACCATGACTGCTCCAAAGAAGAAGCG-3′ and 5'-GCAACCGGTGCGAGATCCGGTGGAGCCGG-3'. Retroviral particles were produced via 293-GPG cell transfection with the plasmid and Lipofectamine 2000 (Invitrogen) following the manufacturer's protocol. Retrovirus-containing supernatants were collected once every 24 hours for 5 days following transfection and strained through a 0.22 μm filter. Cells were seeded into 6-well plates to reach 50–60% confluency on the day of infection, and were transduced with viral stock in the presence of 8 μg/mL polybrene (Sigma-Aldrich) every 24 hours for three days. On the fourth day, the viral solution was replaced with fresh culture medium, and cells were cultured for three days before selection with puromycin. After selection, cells were sorted on a BD FACSARIA FUSION fluorescence activated cell sorter (Cornell University Biotechnology Resource Center), and used for experiments or frozen down.

siRNA mediated depletion of lamin A/C and CHMP7

Lamin A/C depletion in A549 cells and CHMP7 depletion in HT-1080 cells was accomplished using DharmaFECT (Dharmacon) and target-specific siRNA according to the manufacturer's protocol, with final siRNA concentrations of 2.5 nM (*LMNA*) and 100 nM (*CHMP7*). SmartPool siRNA oligonucleotides, containing four target sequences in one mix to reduce off-target effects, were purchased from Dharmacon (GE Healthcare): human LMNA (ON-TARGET plus SMART pool, L-004978-00), human CHMP7 (ON-TARGETplus SMARTpool, L-015514-01), and non-targeting control siRNA (ON-TARGETplus non-targeting pool, D-001810-10).

Generation of cell lines overexpressing lamin A

BT-549 cells were stably modified to express NLS-RFP using a pCDH lentiviral construct (Systems Biosciences). After selection with blasticidin (InvivoGen), cells were modified with a retroviral

bicistronic constructs expressing lamin A or a mock control as described previously [31]. Cells were then sorted for RFP- and GFP-expressing cells before being used in experiments.

Seeding cells into microfluidic devices

Cells were trypsynized, centrifuged, counted and resuspended in media to a concentration of 5,000 cells/μL. A cell suspension containing 30,000 cells was added to the inlet port of each device. Device reservoirs were then filled with media and kept in an incubator overnight to allow cell attachment to the fibronectin- or collagen-coated devices. In the morning media was removed, and one reservoir was filled with plain media while the other was simultaneously filled with FBS-supplemented media, creating a chemotactic gradient to promote cell migration across the constrictions. Devices were then returned to the incubator until the start of imaging. Just prior to imaging, media was again removed from the devices. The FBS gradient was established in the same manner as before, but with Fluorobrite (Gibco) imaging media containing 25 mM 4-(2-hydroxyethyl)-1-piperazineethanesulfonic acid (HEPES, Gibco) to keep the cells at physiologic pH in the absence of 5% CO_2 during time-lapse imaging. Cover slips were placed over the devices to prevent evaporation of media.

A detailed schematic of the microfluidic device used, including reservoirs, cell seeding ports, and constrictions, can be found elsewhere [20]. The constriction design we used here is the rightmost one presented in Fig 1G of that reference. Designs for the device are available at: http://lammerding.wicmb.cornell.edu/migration-device-design/

Imaging

Migration devices were imaged on an inverted Zeiss Observer Z1 microscope with a temperature-controlled stage set to 37˚C at 20× magnification (NA 0.8 air objective) and a CoolSNAP EZ CCD camera (Photometrics). Zen software (Zeiss) was used to automate image acquisition, taking images of specific sections of the migration device every 2 min (HT-1080) or 10 min (A549 and BT-549). Images of the migration device and cells were acquired with differential interference contrast (DIC); fluorescence microscopy was used to capture the NLS-GFP signal (excitation with 450–490 nm light, collection of emission at 500–550 nm; exposure time of 75 ms), and the H2B-tdTomato signal (excitation by 550–580 nm light, collection of 590–650 nm light; exposure time of 400 ms). All images were saved in the Carl Zeiss Image (*.czi) format.

Western blotting

To quantify protein depletion, Western blots were performed with cell lysates. Parallel prepared samples of the siRNA treated cells were lysed at the time of imaging in high salt radioimmunoprecipitation assay (HS RIPA) buffer. Lysates were vortexed for five minutes to shear DNA, heated to 93˚C for two minutes, and centrifuged to pellet DNA. Protein concentrations were determined by Bradford assay. Equal amounts of protein (15 μg) for each sample were loaded into a NuPAGE 10% Bis-Tris gel (Gibco). Gels ran in 3-(N-morpholino)propanesulfonic acid (MOPS) buffer at 100 V until the ladder bands began to separate, and then at 175 V until completion. Proteins were then transferred to a polyvinylidene difluoride (PVDF, Millipore) membrane at 16 V for one hour. Gels were stained with Coomassie to observe quality of protein loading. After transfer, the membrane was blocked for at least one hour at room temperature in 5% milk. Primary antibodies (anti-lamin A/C, Santa Cruz, sc-6215, dilution 1:2000; anti-CHMP7, Sigma, HPA036119, dilution 1:200; anti-actin, Santa Cruz, sc-1615 HRP, dilution 1:2000) were added and left on overnight at 4˚C. Secondary antibodies (donkey anti-rabbit 800 cw and donkey anti-mouse 680 RD, Licor) were incubated for one hour at room temperature prior to imaging on a LI-COR Odyssey CLx.

Image analysis

Image sequences were analyzed using the custom-written MATLAB program. To allow the program to read the images in the .czi format, the Bio-Formats package was downloaded from the Open Microscopy Environment's webpage and added to the MATLAB search path. Constriction passage times as well as NE rupture events were recorded for all cells. Data was automatically exported into a comma-separated values (*.csv) file for use with Microsoft Excel. To verify the accuracy of the program, results for selected image sequences were compared to results from manual analysis using Zen software.

Statistical analysis

Statistical analysis was performed on GraphPad's Prism software. Distributions of constriction transit times and NE rupture durations were tested for normality, and their means were compared using the appropriate statistical tests. Two-tailed t-tests with Welch's correction for unequal variances were used to compare two normally distributed means. The Mann-Whitney test was used to compare two means if either was not normally distributed. One-way analysis of variance (ANOVA) followed by Tukey's multiple comparison test was used to compare the constriction transit times determined by the program with those determined through manual analysis. In the comparison between manual and automated image analysis, three data points were excluded due to large discrepancies in the manual analysis between the four observers. Two-tailed t-tests with the Bonferroni correction were used to compare the normalized fluorescent intensities during NE rupture events.

Supporting information

S1 Fig. Automated detection of microfluidic constrictions. (**A**) Image of a microfluidic device section prior to rotation. The rows of constrictions are angled upwards. (**B**) The results of a circular Hough transform have been superimposed onto the original image (red). These circles represent the columns that form the constrictions and their centers are used to determine the angle of rotation. (**C**) Image of the microfluidic device rotated so that the rows of constrictions are horizontal. (**D**) A circular Hough transform is applied to the rotated image (red). Now the locations of the circles' centers can be used to place boundaries for entering and exiting a constriction (blue).
(TIF)

S2 Fig. Example of watershed segmentation. 1) An image of migrating nuclei is binarized based on the H2B-tdTomato signal. Since the two nuclei shown are touching, they become a single object in the binary image. **2)** The binary image is inverted so that the distance transform, which measures the distance from any given pixel to the nearest non-zero (white) pixel, works as needed. **3)** The distance transform is applied. Inside of the nuclei, values are higher (closer to white in the image) the farther they are from the nucleus' nearest edge. **4)** The image from the distance transform is inverted so that the watershed segmentation works as needed. Now the center of a nucleus is a minimum (closer to black in the image). **5a)** A watershed transform is applied. The black lines represent watershed lines, cutting through local maxima to separate all of the image's local minima or catchment basins (each of which is shown as a different shade of gray). **6a)** The watershed lines are used to segment the original binary image. Over-segmentation has occurred since the top nucleus has been erroneously split into three separate objects. **5b)** An h-minima transform is applied to the inversion of the distance transform. Local minima that are too shallow are removed from the image to prevent over-segmentation from occurring. **6b)** A watershed transform is applied. Since negligible minima

were removed from the image there are now only two catchment basins. **7b)** The watershed line is used to segment the original binary image. Application of the h-minima transform during this process prevented over-segmentation from occurring. Use of the watershed segmentation successfully separated two touching nuclei into distinct objects.
(TIF)

S3 Fig. Examples on constriction transit identification. A) The two nuclei depicted are identified as attempting to pass through the constrictions by the program. This is because the leading (top) edges of their bounding boxes (shown in blue) are above the lower constriction boundary (both constriction boundaries depicted as dashed green lines), but their bounding box trailing (lower) edges are still below the upper constriction boundary. **B)** Movement of the nucleus as shown here would result in the program recording a successful constriction passage since the trailing edge of the nucleus' bounding box eventually crosses the upper constriction boundary. **C)** Movement of the nucleus as shown here would result in the program recording a failed constriction passage since the leading edge of the nucleus' bounding box recedes below the lower constriction boundary.
(TIF)

S4 Fig. Detection of mitotic cells to reduce misclassification of nuclear envelope rupture and incorrect nucleus matching. (A) Example of incorrectly labeled nuclear envelope rupture (box with the letter R) and unmatched nucleus appearing in the fourth frame (magenta box) when a mitotic cell divides into two daughter cells. (B) Results obtained with the automated mitosis detection feature of the program. The nucleus outlined in cyan is now recorded as undergoing division (signified by the letter D). The nuclei outlined in magenta and gray are recorded as daughters of the cyan-outlined nucleus. Proper distinction between mitosis and nuclear envelope rupture is necessary to prevent recording of false positive nuclear envelope rupture data.
(TIF)

S5 Fig. Depletion of lamin A/C by siRNA. (**A**) Western blot of the A549 cells used in four independent migration experiments. Visual inspection reveals lower lamin A/C expression in the cells that received the knockdown (KD) as compared to the cells that received the non-targeting siRNA (NT). (**B**) Quantification of lamin A levels, normalized to actin loading control. (**C**) Quantification of lamin C levels, normalized to actin loading control. *, $p < 0.05$
(TIF)

S6 Fig. Depletion of CHMP7 by siRNA. Western blot of the HT1080 cells used in three independent migration experiments. Visual inspection confirms lower CHMP7 expression in the cells that received the knockdown (KD) as compared to the cells that received the non-targeting siRNA (NT). (**B**) Quantification of CHMP7 levels, normalized to actin loading control. ***, $p < 0.001$.
(TIF)

S1 Video. Video of migrating nuclei corresponding to Image Sequence 1 of Fig 5. Video of BT-549 cells migrating through a microfluidic device with 2-μm wide constrictions, corresponding to Image Sequence 1 in Fig 5. Cells were modified to express NLS-GFP and overexpress lamin A, resulting in more rigid nuclei and impaired transit through the constrictions. This video was used as the "training" data for the program.
(AVI)

S2 Video. Video of migrating nuclei corresponding to Image Sequence 2 of Fig 5. Video of BT-549 cells migrating through a microfluidic device with 2-μm wide constrictions,

corresponding to Image Sequence 2 in Fig 5. Cells were modified to express NLS-GFP and a mock control vector. This video was used as the "test" data for the program.
(AVI)

Acknowledgments

The authors thank Emily Bell, Gregory Fedorchak, Philipp Isermann, Jay Jun, Jineet Patel, and Pragya Shah for their manual image analysis and helpful discussion. The authors thank João Filipe Henriques for contributing a small section of MATLAB code that helped with manual interaction with a video.

Author Contributions

Conceptualization: Joshua J. Elacqua, Alexandra L. McGregor, Jan Lammerding.

Data curation: Joshua J. Elacqua.

Formal analysis: Joshua J. Elacqua, Jan Lammerding.

Funding acquisition: Jan Lammerding.

Investigation: Joshua J. Elacqua, Alexandra L. McGregor.

Methodology: Joshua J. Elacqua, Alexandra L. McGregor, Jan Lammerding.

Project administration: Jan Lammerding.

Software: Joshua J. Elacqua.

Supervision: Alexandra L. McGregor, Jan Lammerding.

Validation: Joshua J. Elacqua, Alexandra L. McGregor.

Visualization: Joshua J. Elacqua, Alexandra L. McGregor.

Writing – original draft: Joshua J. Elacqua.

Writing – review & editing: Joshua J. Elacqua, Alexandra L. McGregor, Jan Lammerding.

References

1. Chaffer CL, Weinberg RA. A perspective on cancer cell metastasis. Science. 2011; 331(6024):1559–64. Epub 2011/03/26. https://doi.org/10.1126/science.1203543 PMID: 21436443.
2. Poste G, Fidler IJ. The pathogenesis of cancer metastasis. Nature. 1980; 283(5743):139–46. Epub 1980/01/10. PMID: 6985715.
3. Krause M, Wolf K. Cancer cell migration in 3D tissue: negotiating space by proteolysis and nuclear deformability. Cell adhesion & migration. 2015; 9(5):357–66. Epub 2015/08/25. https://doi.org/10.1080/19336918.2015.1061173 PMID: 26301444; PubMed Central PMCID: PMC4955366.
4. Wolf K, Te Lindert M, Krause M, Alexander S, Te Riet J, Willis AL, et al. Physical limits of cell migration: control by ECM space and nuclear deformation and tuning by proteolysis and traction force. The Journal of cell biology. 2013; 201(7):1069–84. Epub 2013/06/27. https://doi.org/10.1083/jcb.201210152 PMID: 23798731; PubMed Central PMCID: PMC3691458.
5. Friedl P, Wolf K, Lammerding J. Nuclear mechanics during cell migration. Current opinion in cell biology. 2011; 23(1):55–64. Epub 2010/11/27. https://doi.org/10.1016/j.ceb.2010.10.015 PMID: 21109415; PubMed Central PMCID: PMC3073574.
6. Harada T, Swift J, Irianto J, Shin JW, Spinler KR, Athirasala A, et al. Nuclear lamin stiffness is a barrier to 3D migration, but softness can limit survival. The Journal of cell biology. 2014; 204(5):669–82. Epub 2014/02/26. https://doi.org/10.1083/jcb.201308029 PMID: 24567359; PubMed Central PMCID: PMC3941057.
7. Davidson PM, Denais C, Bakshi MC, Lammerding J. Nuclear deformability constitutes a rate-limiting step during cell migration in 3-D environments. Cellular and molecular bioengineering. 2014; 7(3):293–

306. Epub 2014/12/02. https://doi.org/10.1007/s12195-014-0342-y PMID: 25436017; PubMed Central PMCID: PMC4243304.

8. Rowat AC, Jaalouk DE, Zwerger M, Ung WL, Eydelnant IA, Olins DE, et al. Nuclear envelope composition determines the ability of neutrophil-type cells to passage through micron-scale constrictions. The Journal of biological chemistry. 2013; 288(12):8610–8. Epub 2013/01/29. https://doi.org/10.1074/jbc.M112.441535 PMID: 23355469; PubMed Central PMCID: PMC3605679.

9. Lammerding J, Fong LG, Ji JY, Reue K, Stewart CL, Young SG, et al. Lamins A and C but not lamin B1 regulate nuclear mechanics. The Journal of biological chemistry. 2006; 281(35):25768–80. Epub 2006/07/11. https://doi.org/10.1074/jbc.M513511200 PMID: 16825190.

10. Stephens AD, Banigan EJ, Adam SA, Goldman RD, Marko JF. Chromatin and lamin A determine two different mechanical response regimes of the cell nucleus. Molecular biology of the cell. 2017; 28(14):1984–96. Epub 2017/01/07. https://doi.org/10.1091/mbc.E16-09-0653 PMID: 28057760; PubMed Central PMCID: PMC5541848.

11. Capo-chichi CD, Cai KQ, Smedberg J, Ganjei-Azar P, Godwin AK, Xu XX. Loss of A-type lamin expression compromises nuclear envelope integrity in breast cancer. Chinese journal of cancer. 2011; 30(6):415–25. Epub 2011/06/02. https://doi.org/10.5732/cjc.010.10566 PMID: 21627864; PubMed Central PMCID: PMC3941915.

12. Bell ES, Lammerding J. Causes and consequences of nuclear envelope alterations in tumour progression. European journal of cell biology. 2016; 95(11):449–64. Epub 2016/07/12. https://doi.org/10.1016/j.ejcb.2016.06.007 PMID: 27397692; PubMed Central PMCID: PMC5110382.

13. Irianto J, Pfeifer CR, Ivanovska IL, Swift J, Discher DE. Nuclear lamins in cancer. Cellular and molecular bioengineering. 2016; 9(2):258–67. Epub 2016/08/30. https://doi.org/10.1007/s12195-016-0437-8 PMID: 27570565; PubMed Central PMCID: PMC4999255.

14. Wazir U, Ahmed MH, Bridger JM, Harvey A, Jiang WG, Sharma AK, et al. The clinicopathological significance of lamin A/C, lamin B1 and lamin B receptor mRNA expression in human breast cancer. Cellular & molecular biology letters. 2013; 18(4):595–611. Epub 2013/12/03. https://doi.org/10.2478/s11658-013-0109-9 PMID: 24293108.

15. Matsumoto A, Hieda M, Yokoyama Y, Nishioka Y, Yoshidome K, Tsujimoto M, et al. Global loss of a nuclear lamina component, lamin A/C, and LINC complex components SUN1, SUN2, and nesprin-2 in breast cancer. Cancer medicine. 2015; 4(10):1547–57. Epub 2015/07/16. https://doi.org/10.1002/cam4.495 PMID: 26175118; PubMed Central PMCID: PMC4618625.

16. Denais CM, Gilbert RM, Isermann P, McGregor AL, te Lindert M, Weigelin B, et al. Nuclear envelope rupture and repair during cancer cell migration. Science. 2016; 352(6283):353–8. Epub 2016/03/26. https://doi.org/10.1126/science.aad7297 PMID: 27013428; PubMed Central PMCID: PMC4833568.

17. Raab M, Gentili M, de Belly H, Thiam HR, Vargas P, Jimenez AJ, et al. ESCRT III repairs nuclear envelope ruptures during cell migration to limit DNA damage and cell death. Science. 2016; 352(6283):359–62. Epub 2016/03/26. https://doi.org/10.1126/science.aad7611 PMID: 27013426

18. Shah P, Wolf K, Lammerding J. Bursting the Bubble—Nuclear Envelope Rupture as a Path to Genomic Instability? Trends in cell biology. 2017; 27(8):546–55. Epub 2017/03/14. https://doi.org/10.1016/j.tcb.2017.02.008 PMID: 28285738; PubMed Central PMCID: PMC5524594.

19. Lim S, Quinton RJ, Ganem NJ. Nuclear envelope rupture drives genome instability in cancer. Molecular biology of the cell. 2016; 27(21):3210–3. Epub 2016/11/02. https://doi.org/10.1091/mbc.E16-02-0098 PMID: 27799497; PubMed Central PMCID: PMC5170854.

20. Davidson PM, Sliz J, Isermann P, Denais C, Lammerding J. Design of a microfluidic device to quantify dynamic intra-nuclear deformation during cell migration through confining environments. Integrative biology: quantitative biosciences from nano to macro. 2015; 7(12):1534–46. Epub 2015/11/10. https://doi.org/10.1039/c5ib00200a PMID: 26549481; PubMed Central PMCID: PMC4666765.

21. Takaki T, Montagner M, Serres MP, Le Berre M, Russell M, Collinson L, et al. Actomyosin drives cancer cell nuclear dysmorphia and threatens genome stability. Nature communications. 2017; 8:16013. Epub 2017/07/25. https://doi.org/10.1038/ncomms16013 PMID: 28737169; PubMed Central PMCID: PMC5527285.

22. McGregor AL, Hsia CR, Lammerding J. Squish and squeeze-the nucleus as a physical barrier during migration in confined environments. Current opinion in cell biology. 2016; 40:32–40. Epub 2016/02/20. https://doi.org/10.1016/j.ceb.2016.01.011 PMID: 26895141; PubMed Central PMCID: PMC4887392.

23. Thomas DG, Yenepalli A, Denais CM, Rape A, Beach JR, Wang YL, et al. Non-muscle myosin IIB is critical for nuclear translocation during 3D invasion. The Journal of cell biology. 2015; 210(4):583–94. Epub 2015/08/12. https://doi.org/10.1083/jcb.201502039 PMID: 26261182; PubMed Central PMCID: PMC4539979.

24. Skau CT, Fischer RS, Gurel P, Thiam HR, Tubbs A, Baird MA, et al. FMN2 Makes Perinuclear Actin to Protect Nuclei during Confined Migration and Promote Metastasis. Cell. 2016; 167(6):1571–85 e18.

Epub 2016/11/15. https://doi.org/10.1016/j.cell.2016.10.023 PMID: 27839864; PubMed Central PMCID: PMC5135586.

25. Malboubi M, Jayo A, Parsons M, Charras G. An open access microfluidic device for the study of the physical limits of cancer cell deformation during migration in confined environments. Microelectronic engineering. 2015; 144:42–5. Epub 2015/09/29. https://doi.org/10.1016/j.mee.2015.02.022 PMID: 26412914; PubMed Central PMCID: PMC4567073.

26. Lautscham LA, Kammerer C, Lange JR, Kolb T, Mark C, Schilling A, et al. Migration in Confined 3D Environments Is Determined by a Combination of Adhesiveness, Nuclear Volume, Contractility, and Cell Stiffness. Biophysical journal. 2015; 109(5):900–13. Epub 2015/09/04. https://doi.org/10.1016/j.bpj.2015.07.025 PMID: 26331248; PubMed Central PMCID: PMC4564685.

27. Mekhdjian AH, Kai F, Rubashkin MG, Prahl LS, Przybyla LM, McGregor AL, et al. Integrin-mediated traction force enhances paxillin molecular associations and adhesion dynamics that increase the invasiveness of tumor cells into a three-dimensional extracellular matrix. Molecular biology of the cell. 2017; 28(11):1467–88. Epub 2017/04/07. https://doi.org/10.1091/mbc.E16-09-0654 PMID: 28381423; PubMed Central PMCID: PMC5449147.

28. Fu Y, Chin LK, Bourouina T, Liu AQ, VanDongen AM. Nuclear deformation during breast cancer cell transmigration. Lab on a chip. 2012; 12(19):3774–8. Epub 2012/08/07. https://doi.org/10.1039/c2lc40477j PMID: 22864314.

29. Robijns J, Molenberghs F, Sieprath T, Corne TD, Verschuuren M, De Vos WH. In silico synchronization reveals regulators of nuclear ruptures in lamin A/C deficient model cells. Scientific reports. 2016; 6:30325. Epub 2016/07/28. https://doi.org/10.1038/srep30325 PMID: 27461848; PubMed Central PMCID: PMC4962089.

30. Isermann P, Lammerding J. Consequences of a tight squeeze: Nuclear envelope rupture and repair. Nucleus. 2017; 8(3):268–74. Epub 2017/03/14. https://doi.org/10.1080/19491034.2017.1292191 PMID: 28287898; PubMed Central PMCID: PMC5499899.

31. Zwerger M, Jaalouk DE, Lombardi ML, Isermann P, Mauermann M, Dialynas G, et al. Myopathic lamin mutations impair nuclear stability in cells and tissue and disrupt nucleo-cytoskeletal coupling. Human molecular genetics. 2013; 22(12):2335–49. Epub 2013/02/22. https://doi.org/10.1093/hmg/ddt079 PMID: 23427149; PubMed Central PMCID: PMC3658163.

Chapter 10

Assembly and Use of a Microfluidic Device to Study Cell Migration in Confined Environments

Jeremy Keys, Aaron Windsor, and Jan Lammerding

Abstract

Cells migrating in tissues must often pass through physical barriers in their surroundings in the form of fibrous extracellular matrix or other cells. To improve our understanding of how cells move in such confined microenvironments, we have designed a microfluidic device in which cells migrate through a series of three-dimensional polydimethylsiloxane (PDMS) constrictions with precisely controlled geometries that mimic physiological pore sizes. The migration device offers an experimental platform that combines a well-defined three-dimensional (3D) environment with a setup well suited for imaging confined cell migration at high spatial and temporal resolution. In this protocol, we describe the fabrication and use of these devices using standard soft lithography techniques and light microscopy. Analysis of live-cell time-lapse series of cells with fluorescently labeled nuclear and/or cytoskeletal structures migrating in the devices can reveal new insights into the molecular processes required for confined migration, including the role of the linker of nucleoskeleton and cytoskeleton (LINC) complex, which has been implicated in 3D migration.

Key words Cell migration, Confined environments, Microfluidics, Nucleus, LINC complex, Microscopy, Live-cell imaging

1 Introduction

Cell migration represents a crucial step in a variety of biological processes, including cancer metastasis, inflammation, and wound healing. In the in vivo tissue environment, interstitial spaces, extracellular matrix networks, and other cells constitute a confined environment for migrating cells. Dense fibrous tissue matrix and layers of endothelial cells form narrow constrictions, which measure 0.1–30 μm in diameter [1, 2]. To move through such tight spaces, cells must produce significant intracellular forces to compress their nucleus, as it is typically the largest and stiffest organelle [3–5]. Prior work has suggested that the linker of nucleus and cytoskeleton (LINC) complex facilitates the transmission of forces from contractile actomyosin fibers to the nucleus during confined migration [6–10]. Consequently, depletion of LINC complex proteins such as Nesprin-2 and Nesprin-3 reduces migration speed through

Gregg G. Gundersen and Howard J. Worman (eds.), *The LINC Complex: Methods and Protocols*, Methods in Molecular Biology, vol. 1840, https://doi.org/10.1007/978-1-4939-8691-0_10,

confining environments and impairs the cell's ability to deform its nucleus [6–9]. Since the dimensionality of the cell environment modulates migratory behavior, the study of cell migration in vitro requires model systems that faithfully reproduce the 3D confinements of biological tissue (Fig. 1A, B) [11]. Additionally, to elucidate the dynamic nuclear and cytoskeletal processes that mediate nuclear translocation in confined spaces, these model systems must also enable the detailed observation of cells by time-lapse microscopy by confocal or wide-field microscopy.

Many tools have been developed for the study of confined migration in vitro [12, 13]. One popular group of devices are transwell invasion assays, such as the Boyden chamber. However, these systems have a limited ability to directly observe cells during migration, as cells in these chambers migrate perpendicular to the imaging plane. Another approach for studying confined migration are extracellular matrix scaffolds (e.g., collagen or Matrigel). These scaffolds are generated through random self-assembly of matrix fibers, which produces an environment that closely mimics biological tissue but provides only limited control over the size of individual pores. In recent years, microfluidic devices have been developed using soft

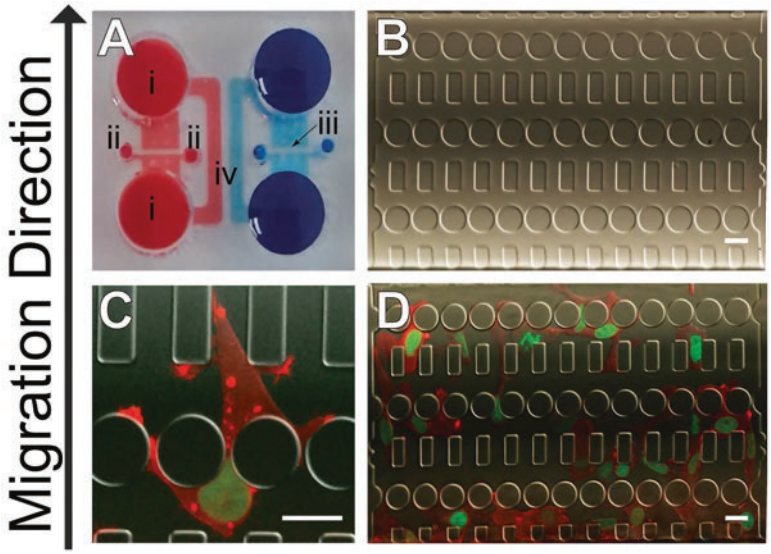

Fig. 1 Overview of the migration device. (**A**) Top-down view of migration device, with food coloring added to enhance details. Cell culture media is added into the media reservoirs (i). Cells are seeded into the devices through seeding ports (ii) that lead to the 5-μm-tall area with the constrictions (iii). Larger bypass channels (iv) allow rapid equilibration of media reservoir levels to prevent flow through constrictions, facilitating formation of a chemotactic gradient by diffusion if serum or growth factors are added to one of the reservoirs. (**B**) Image of the 5-μm-tall area of the device with 2-μm-wide constrictions without cells present. Scale bar 25 μm. (**C**, **D**) Images of constriction area containing MDA-MB-231 breast cancer cells expressing an mCherry-actin chromobody and an mNeonGreen-H2B histone label. Panel (**C**) depicts a cell as it starts to pass through a constriction. Scale bar 25 μm

lithography techniques to reproduce the physical confinements of the in vivo tissue environment [12, 14, 15]. These devices feature channels of defined geometries through which the cells must migrate, either spontaneously or following a chemotactic gradient. These microfluidic platforms are quite versatile as they provide the user with flexibility in the design and layout of constrictions.

In this protocol, we describe the design and use of a polydimethylsiloxane (PDMS) microfluidic device with a series of tight constrictions located between two larger chambers (Fig. 1B, C) [14]. Cells are seeded in one of the chambers and then migrate through a section 5 μm in height containing constrictions between 1 and 2 μm in width, formed by 30 μm wide circular pillars (Fig. 1). Additionally, there is a set of 15-μm-wide constrictions, which cells can migrate through without deforming their nucleus and which serve as an important control to assess effects independent of nuclear confinement. Unlike other microfluidic devices, in which cells often move through long, continuously confining channels, the confinement in the device described here is limited to a very short segment, i.e., cells move through a single, tight constriction, enter a less confined region, and then encounter the next constriction. This design seeks to reproduce the varied, discontinuous sequence of pores and confinement which cells are subjected to during in vivo migration, such as matrix fibers or endothelial cell layers [1, 16]. These devices have already aided in our initial studies of dynamic processes that occur during confined migration, such as the rupture of the cell nucleus and the essential role of perinuclear myosin IIB in moving the nucleus through narrow constrictions [7, 17].

To produce these devices, SU-8 microfluidic features are formed onto a silicon wafer through photolithography. Next, a PDMS replica is cast from the SU-8 features; the PDMS is cut into individual devices, bound to a glass slide, functionalized with extracellular matrix (ECM) solution, and seeded with cells. Following a period of incubation to allow cells to enter the constrictions, analysis of cell migration can be performed by live-cell imaging or standard immunofluorescence techniques. This protocol will outline the procedures necessary for both producing these devices and using them for the study of confined migration (Fig. 2). The protocol assumes basic familiarity with SU-8 and PDMS soft lithography. For users new to soft lithography, we recommend Qin et al. as a good starting point [18].

2 Materials

2.1 Photolithography

1. CZ silicon wafer, 4 in. diameter, type N, 525 μm thick, <1-0-0> orientation (Silicon Quest International).
2. Chrome photomask on a quartz substrate, 5″ × 5″ × 0.090″ (Telic, Valencia, CA).

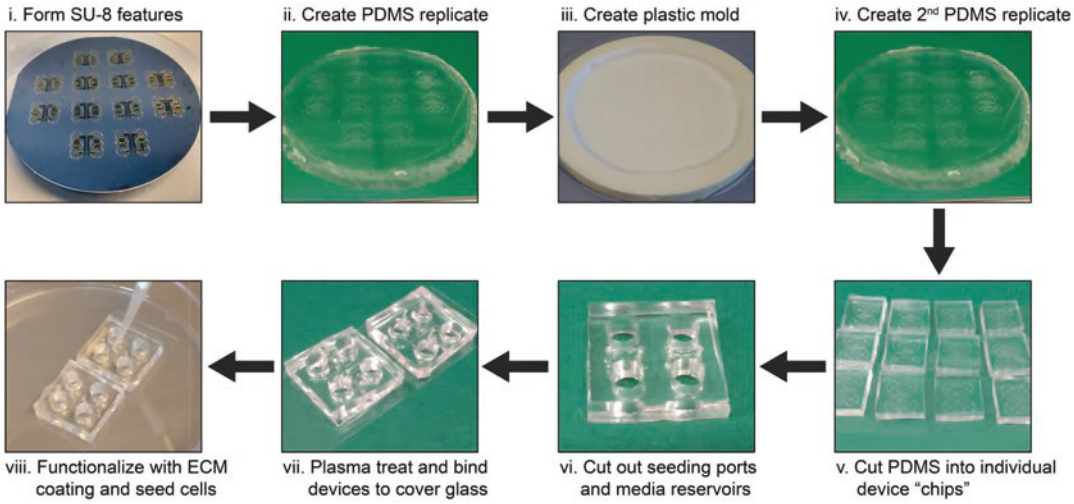

Fig. 2 Overview of migration device fabrication. (i) SU-8 microfluidic features are developed onto a silicon wafer through photolithography. (ii) A PDMS replicate of these features is formed using a two-part elastomer curing-base mixture. (iii) Optionally (but recommended), a secondary plastic mold can be cast from the initial PDMS replicate, which will be used to form additional PDMS devices. (iv) Using a similar process to step *ii*, a PDMS replicate is formed from the secondary plastic mold. (v) The PDMS replicate is cut into 12 device "chips." Each "chip" contains two independent microfluidic devices, each with the features shown in Fig. 1. (vi) Media reservoirs (labeled i in Fig. 1A) and seeding ports (labeled ii in Fig. 1A) are cut out using biopsy punches. (vii) Devices are cleaned with IPA and DI water, treated using a plasma cleaner, and then covalently bound to glass slides. (viii) Devices are functionalized with extracellular matrix proteins prior to adding cells through the seeding ports (labeled ii in Fig. 1A) and filling reservoirs with cell media. At this point, devices may be incubated until ready for analysis using live-cell imaging or immunofluorescence

3. Heidelberg DWL 2000 mask writer (Heidelberg Instruments, Heidelberg, Germany).
4. Long-pass filter for near-UV light (PL-360LP from Omega Optical or equivalent).
5. AutoCAD software (Autodesk, Mill Valley, CA) or equivalent.
6. Mask aligner system (ABM, San Jose, CA).
7. Molecular vapor deposition system (SPTS Technologies, Newport, RI).
8. Kapton polyimide film (DuPont, Wilmington, DE).
9. Oven suitable for temperatures up to 150 °C.
10. CEE Model 100 spin coater, or equivalent (Brewer Sciences, Rolla, MO).
11. SU-8 2005 photoresist (MicroChem, Newton, MA).
12. SU-8100 photoresist (MicroChem, Newton, MA).
13. SU-8 developer (MicroChem, Newton, MA).
14. Semiconductor grade acetone.

15. Cleanroom swab (Texwipe TX761 Alpha Swab with long handle, or equivalent).
16. CMOS grade isopropyl alcohol (IPA).
17. Deionized (DI) water.
18. >95% (1*H*,1*H*,2*H*,2*H*-perfluorooctyl)trichlorosilane (FOTS) (Gelest Inc., Morrisville, PA).

2.2 Casting of Migration Devices in PDMS

1. 150 mm petri dish.
2. Sylgard 184 silicone elastomer base and curing agent (Dow Corning, Midland, MI).
3. Stirring rod for mixing elastomer base and curing components.
4. Vacuum pump (Oerlikon Trivac D2.5E).
5. Vacuum desiccator (Catalog# Fisher 08-594-16C).
6. Oven suitable for temperatures of 65 °C (e.g., VWR Gravity Convection Oven, Catalog# 414005-108, or equivalent).

2.3 Mounting and Seeding of Devices

1. Biopsy punches (1.2 and 5 mm).
2. 24 mm × 60 mm Number 1.5 Micro Cover Glass (VWR, Radnor, PA, Catalog# 48393-251) stored overnight in 0.2 M hydrochloric acid.
3. Isopropyl alcohol (IPA).
4. DI water.
5. 70% ethanol.
6. Oxygen plasma cleaner (Harrick Plasma, Catalog# PDC-001).
7. Type I collagen (50 μg/mL in 0.02 M glacial acetic acid) or fibronectin (5 μg/mL in PBS) solution.
8. Dulbecco's phosphate-buffered saline (DPBS), no calcium, no magnesium (Thermo Fisher, Waltham, MA, Catalog# 14200-075 or equivalent).
9. Cells of interest (*see* **Note 1**).
10. Cell culture media appropriate for cells of interest.
11. Pipettes and tips for loading devices (20 and 200 μL pipettes work well).

2.4 Microscopy and Analysis

1. Inverted fluorescence microscope. Microscope should have objective with 20× magnification and fluorescence excitation/emission filters for GFP and/or other fluorophores of interest.
2. Stage-top incubation chamber for microscope to maintain temperature at 37 °C. Humidity control is optional, as microfluidic devices can be sealed.
3. Microscope-mounted CCD or CMOS camera for image acquisition.

4. Image acquisition software, such as ZEN BLUE (Zeiss), Micromanager, or others.
5. ImageJ, FIJI, MATLAB, or other software for image analysis.

3 Methods

3.1 Photolithography

All photolithography steps should be performed in a dedicated clean-room facility under standard clean-room conditions, with protective equipment and sufficient ventilation underneath a fume hood. The development of SU-8 microfluidic features onto a silicon wafer is described below:

1. Generate a design for the mask using CAD software and the downloaded CAD files. The device design and geometry are described in detail in Davidson et al. [14]. The CAD files for the device can be downloaded at http://lammerding.wicmb.cornell.edu/.
2. Using a Heidelberg DWL 2000 Mask Writer, develop the chrome photomask based on the CAD design layout. This photomask will be used to expose the design features in SU-8 photoresist onto the silicon wafer using near-ultraviolet (UV) light.
3. Clean silicon wafer using standard metal oxide semiconductor (MOS) cleaning procedures (*see* **Note 2**), and bake overnight at 90 °C to dehydrate.
4. Coat wafer with ~2 mL of SU-8 2005 (MicroChem), and spin down using a spin coater (CEE Model 100 spin coater, or equivalent) at 3000 RPM for 30 s (*see* **Note 3**) to obtain a 5-μm-thick layer, which will be used for the design of the first layer with the 5-μm-tall features.
5. Allow the SU-8 to relax for 10 min at room temperature (RT). Then remove 5 mm of excess SU-8 from the edge of the wafer perimeter using a clean-room swab soaked in acetone.
6. Bake the wafer on a hot plate from RT to 65 °C at a rate of 2.0 °C/min, hold at 65 °C for 10 min, then remove from plate, and allow to cool back to RT (*see* **Note 4**).
7. Expose the wafer to near-UV light at 365 nm using an ABM contact aligner with a long-pass filter for 40 s (*see* **Note 5**).
8. An hour after exposure, bake the wafer on a hot plate from RT to 95 °C at a rate of 2.0 °C/min, hold at 95 °C for 1 min, and then leave to cool back to RT.
9. Place wafer in SU-8 developer overnight to remove unexposed SU-8.

10. Rinse wafer with fresh SU-8 developer, then rinse with isopropyl alcohol and deionized water two times each to clean.
11. Bake wafer in an oven from RT to 150 °C for 20 min. Then shut off oven, and allow wafer to cool to RT. This step is a "hard-bake" step, which solidifies the first SU-8 layer and prevents unwanted merging with the second layer.
12. Dehydrate wafer overnight by baking at 90 °C.
13. Cover the alignment marks on the wafer for the 5 μm layer using Kapton tape (*see* **Note 6**).
14. For a thickness of 200 μm, coat wafer with ~2 mL SU-8100, and spin at 1500 RPM for 60 s (*see* **Note 7**).
15. Allow the SU-8 to relax for 10 min, and then remove 5 mm of excess SU-8 from the edge of the wafer perimeter using a clean-room swab soaked in acetone.
16. Bake the wafer on a hot plate with a lid (any cover is sufficient; we use a Pyrex petri dish cover) from RT to 55 °C at a rate of 2.0 °C/min for 14 h, then increase to 60 °C at a rate of 2.0 °C/min for 14 h, and then leave to cool back to RT.
17. Score the edges of the Kapton tape with a razor and gently remove from the wafer.
18. Expose the wafer on the contact aligner with a long-pass filter for 1 min, six times with 1 min of rest in between (*see* **Note 8**).
19. Twenty minutes after exposure, bake the wafer on a hot plate with a lid. Increase the temperature from RT to 95 °C at a rate of 1.5 °C/min, hold at 95 °C for 1 min, and then leave to cool back to RT.
20. Leave wafers in SU-8 developer overnight.
21. Rinse wafer with fresh SU-8 developer, followed by a wash with isopropyl alcohol and deionized water, two times each.
22. Bake wafers from RT to 60 °C for 2 h in an oven on an aluminum plate to remove moisture, and leave to cool in the oven to RT.
23. Coat wafers with FOTS using a molecular vapor deposition (MVD) tool.
24. Wafers can now be removed from the clean room and used for casting into PDMS (Fig. 2ii, iv).

3.2 Casting of Migration Devices in PDMS

From this point on, all components should be handled with nitrile gloves to minimize the risk of contamination of devices. All steps may be performed on a lab bench, until devices are assembled, sprayed with ethanol, and moved into a cell culture hood.

1. Place the silicon wafer with SU-8 features facing upward into a 150 mm petri dish (or use secondary plastic mold; *see* **Note 9**).

2. Add PDMS base and curing agents into a standard plastic cup at a 10:1 ratio (typically 50 g of base and 5 g of curing agent is sufficient for a set of 12 device chips), and stir vigorously for 5 min to fully combine. The stirring of these components will cause many air bubbles to form in the mixture, and these must be removed through degassing prior to curing of the PDMS.
3. Place PDMS mixture into a vacuum desiccator at 30 psi for 20 min to eliminate bubbles and accelerate degassing of the polymer.
4. Pour PDMS mixture over wafer (or secondary device mold), and allow 5–10 min to set at room temperature.
5. Using a very light stream of pressurized air, blow directly over the surface of the PDMS in order to eliminate all remaining bubbles. After this step, PDMS should be completely clear.
6. Preheat an oven to 65 °C, and then bake PDMS mixture in oven for at least 2 h (*see* **Note 10**).
7. Remove mold from oven and allow PDMS to cool to room temperature (*see* **Note 11**).
8. Using a razor, cut around edges of PDMS mold, ensuring that there is sufficient space in between the cut-edge and device features.
9. Carefully peel PDMS out of the mold, ensuring that PDMS does not tear during removal. The molded PDMS will contain 12 device "chips," each of which contains 2 migration devices (Fig. 1A).
10. Using a razor, cut PDMS into 12 device chip segments (Fig. 2v).
11. Place PDMS devices onto clean packing tape, feature-side down, to protect devices from dust during storage.
12. Store devices at room temperature, or proceed immediately to mounting onto glass slides for use with cells.

3.3 Mounting and Seeding of Devices

1. Prior to mounting, store glass slides overnight in 0.2 M hydrochloric acid (*see* **Note 12**).
2. Remove a device chip from packing tape and immediately prepare for cleaning.
3. Cut out holes for seeding ports and media reservoir into PDMS using biopsy punches (Fig. 1A, i and ii). Location of holes is marked on PDMS as part of the mask design. Media reservoirs are cut out using a 5 mm punch, while the seeding inlets should be cut out with a 1.2 mm punch (*see* **Note 13**).
4. Hold device with forceps, and rinse with isopropyl alcohol (IPA), followed by deionized water. Repeat once (*see* **Note 14**).

5. Using pressurized air, dry device thoroughly, and then place inside of plasma cleaner, feature-side up.
6. Repeat washing and drying steps on cover glass slides, and place inside of plasma cleaner alongside device (*see* **Note 15**).
7. Close plasma cleaner and turn on pump and power switches. Wait a few minutes to allow the plasma cleaner to warm up, and then turn on the RF level (which regulates the intensity of plasma within the chamber) to high.
8. Plasma treat the PDMS devices and glass cover slides for 5 min, adjusting the air intake in order to keep the plasma active (a bright pink color) throughout the treatment procedure (*see* **Note 16**).
9. Turn off the plasma cleaner and release the air pressure very slowly.
10. Remove the treated glass slide and PDMS device from the plasma cleaner, and place the device onto the glass slide, feature-side down (*see* **Note 17**).
11. Using your thumb, press the device down firmly onto the glass slide. Press around the device to ensure that the whole device is firmly bonded to the glass cover slide (*see* **Note 18**).
12. To improve adhesion of the PDMS to the glass, place the bonded device onto a hot plate at 95 °C for 5 min (*see* **Note 19**).
13. Remove the device from the hot plate, and allow the device to cool for a few minutes, before spraying the outside of the device completely with ethanol and moving the device into a cell culture hood.
14. Fill the media reservoirs with ethanol, and allow the device to incubate for 10 min at RT for sterilization.
15. Remove ethanol from the device, and rinse the media reservoirs three times with PBS for 5 min each. Each device will hold between 150 and 200 μL of fluid.
16. At this stage, the inside surfaces of the device can be functionalized with various biologically relevant coating, depending on the cell line to be used and the experimental goals. We use fibronectin or collagen coatings for most cell lines. To functionalize the inside of the device, fill devices with protein solution through seeding ports (Fig. 1A, ii), and allow the coatings several hours to set to the device surface (*see* **Note 20**, Table 1).
17. Remove coating solution, and rinse the inside of the device three times using 180 μL of cell culture media applied to one of the reservoirs, allowing 5 min of incubation between each rinse.
18. Prepare cells for seeding into devices (*see* **Note 21**, Table 1).
19. Completely aspirate all media from devices, ensuring that bypass channels and device features are clear.

Table 1
Optimal cell seeding densities and concentrations of ECM coating to prepare migration devices

Cell line	Cells seeded per device	ECM coating	ECM incubation
HT1080	80,000 cells seeded minimum 2 h before imaging	50 μg/mL corning 354,236 rat tail collagen type I diluted in 0.02 M acetic acid	4 °C overnight or longer
MDA-MB-231 on collagen	50,000 seeded minimum 2 h before imaging	50 μg/mL corning 354,236 rat tail collagen type I diluted in 0.02 M acetic acid	4 °C overnight or longer
MDA-MB-231 on fibronectin	30,000 seeded 24 h before imaging	5 μg/mL Millipore FC010 human plasma fibronectin diluted in PBS	4 °C overnight or longer, or 4 h at 37 °C
Human fibroblasts	30,000 seeded 24 h before imaging	3 μg/mL Millipore FC010 human plasma fibronectin diluted in PBS	4 °C overnight

20. Pipette 6 μL of cell suspension into the seeding port on the same side of the device as the bypass channel (Fig. 1A). Seed cells into the right port on left device and left port on right device (*see* **Note 22**).
21. Check seeding of the cells underneath a bright-field microscope. The cells should be distributed evenly across the front of the device constriction channels (Fig. 3A). If the cells are biased toward one end of the constrictions (Fig. 3B), aspirate cells from the device, and repeat seeding process.
22. Slowly add 180 μL of cell culture media into the media reservoir at the end of the device opposite from where cells were seeded (Fig. 1A, into top reservoirs). When media is added to one reservoir, it will flow through the constrictions and bypass channels to fill the reservoir on the opposite side. By adding media on the reservoir on the end of the device opposite the seeding channels, this prevents the inflow of media from pulling cells off of the glass and potentially pushing them prematurely into the constrictions.
23. Check cell seeding under microscope after this step to ensure that addition of media did not move cells from their original, uniformly seeded position.
24. Place the device with cells into a 37 °C cell culture incubator, and incubate until ready to image.

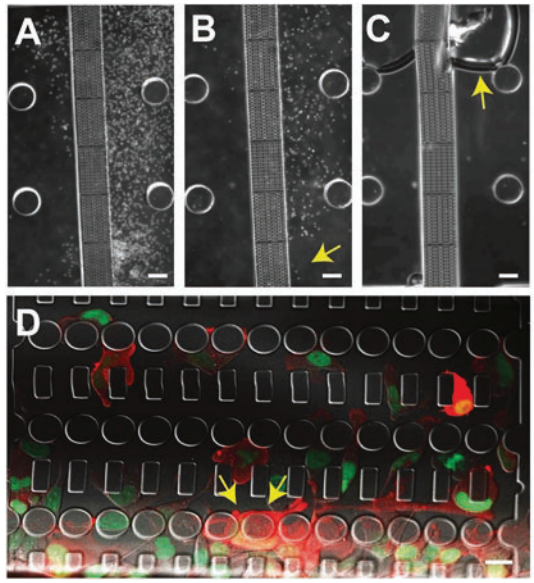

Fig. 3 Recognizing potential issues with device loading and bonding. (**A**) Properly loaded cells with even distribution across the device. Scale bar 200 μm. (**B**) Uneven loading of cells in front of constrictions; bottom constriction section has no cells at entrance (arrow). Scale bar 200 μm. (**C**) Air bubbles in cell media formed within the device, blocking entry into the constriction channels. Scale bar 200 μm. (**D**) Cells migrating underneath constriction pillars (arrows), indicating insufficient bonding of PDMS pillars to glass. Scale bar 25 μm

3.4 Time-Lapse Imaging and Analysis of Cell Migration

Time-lapse imaging of cells requires a microscope with an incubation chamber to maintain optimal cell culture conditions (i.e., adequate temperature, CO_2 concentration, humidity) throughout the imaging process (*see* **Note 23**). When using fluorescence microscopy, the experiments may require some troubleshooting to determine suitable excitation intensity, imaging intervals, exposure times, and imaging duration to avoid phototoxicity caused by repeated imaging throughout the experiment. Here, we will briefly outline our analysis protocol for studying nuclear transit in confined migration, after a time series of migrating cells within these devices has been collected. Alternatively, cells can also be fixed within migration devices and processed with standard immunofluorescence staining techniques for further analysis of nuclear and cytoskeletal elements involved in nuclear translocation (*see* **Note 24**):

1. Place the migration device in the microscope incubation chamber, and bring the cells into focus. We find that a single region of constrictions is best visualized under 20× magnification to measure transit times, but higher magnification may be required to capture subcellular dynamics.
2. Let the microscope with mounted migration device thermally equilibrate for 15–30 min to avoid drift of focus.
3. Set up image acquisition software to capture region of interest within the device at regular time intervals (minimum of one frame

every 10 min, more frequent imaging may be necessary for faster migrating cells). Each device has six regions to capture, representing areas with different constriction sizes (three with 1 × 5 μm² constrictions, two with 2 × 5 μm² constrictions, and one with 15 × 5 μm² constrictions), and each chip contains two devices.

4. Acquire time-lapse image series of all regions of interest overnight (*see* **Note 25**).
5. Using ImageJ, or an equivalent image analysis software, define the nuclear perimeter of each cell throughout the time series of images. If using cells modified to express fluorescently labeled proteins within the nucleus, you may define the nuclear perimeter using an intensity threshold (*see* Fig. 4). For cells expressing fluorescent nuclear markers, such as histone H2B-GFP, we have developed a MATLAB automated image analysis program for cell tracking and transit time analysis [19].
6. For each cell attempting to pass through a constriction, define the time point at which the cell has "committed" to enter the constriction. This can be done by noting when the front of the nucleus crosses an imaginary line parallel to the center of the constriction (*see* Fig. 4, **Note 26**). Similarly, define the time point at which the nucleus has exited the constriction, either when the rear of the nucleus crosses a second imaginary line toward the rear of the constriction (successful pass; *see* Fig. 4) or when the nucleus backs out of the constriction, i.e., the front of

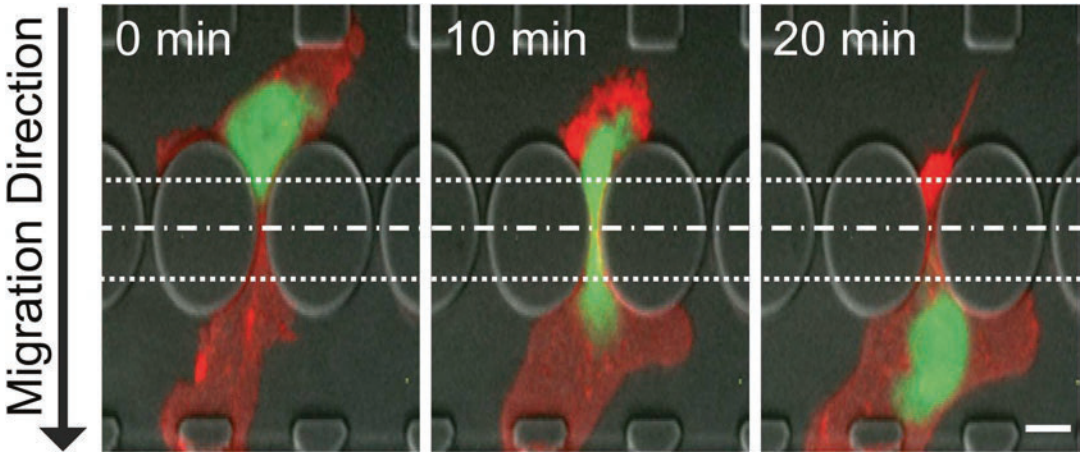

Fig. 4 Analysis of nuclear transit time through constriction. Nuclear transit time is defined as the time for a cell to completely translocate its nucleus through a single constriction. The most robust metric for this measurement is the time from when the nucleus "commits" to enter a constriction (i.e., crossing an imaginary dashed line, located 7 μm outside the constriction center, top dashed line) and begins to deform, to when it has fully passed the constriction (i.e., the trailing edge of the nucleus has passed an imaginary line 7 μm past the constriction center, bottom dashed line). This analysis can be performed manually or using automated particle tracking programs. The example shows an MDA-MB-231 breast cancer cell expressing an mCherry-actin chromobody and an mNeonGreen-H2B histone label. Scale bar 10 μm

the nucleus is no longer inside the region between the imaginary lines (unsuccessful attempt). For successful passes, the "transit time" is defined as the time between the entry and exit point.

7. Repeat this process for cells in the 15-μm-wide channels. This measurement is crucial when comparing different cell lines or treatment conditions, which may affect the overall motility of cells, regardless of nuclear confinement (*see* **Note 27**).
8. Normalize the transit time of cells moving through the 1- and 2-μm-wide constrictions to the average transit time of cells under the same condition (genotype, treatment) moving through the 15-μm-wide channels. This is considered the "normalized transit time" and describes the effect of the nuclear confinement on the migration efficiency.
9. Compare normalized transit times between different constriction sizes (e.g., 1 μm vs. 2-μm-wide constrictions), genotype, and treatment (e.g., LINC complex disruption vs. mock control) for analysis of migration times throughout the device.

4 Notes

1. Most migratory cell lines should work well in these devices. We have had success with HT1080 fibrosarcoma cells, mouse embryonic fibroblasts, differentiated HL60 neutrophil-like cells, MDA-MB-231 metastatic breast cancer cells, and a variety of other invasive breast cancer cell lines.
2. MOS cleaning is a 10 min base dip in one part NH_4OH, one part H_2O_2, and six parts water for 10 min, DI water rinse, and an acid dip in one part HCl, one part H_2O_2, and six parts water for another 10 min with a final DI water rinse.
3. It is important to slowly ramp up and ramp down from the 3000 RPM top speed to ensure even spreading of the SU-8. The spin protocol we have found to be successful is ramped up to 500 RPM at 100 RPM/s for 10 s, increaseed to 3000 RPM at 300 RPM/s for 30 s, and then ramped down to 100 RPM at 100 RPM/s for 30 s before stopping.
4. This preexposure baking step removes excess solvents, improves the photoresistive profile of the SU-8, and prevents adhesion to the contact mask.
5. ABM Contact Aligner dose with long-pass filter: 8.8 mW/cm^2 at 365 nm wavelength and 12.9 mW/cm^2 at 405 nm wavelength. Long-pass filter is a PL-360LP from Omega Optical or equivalent.
6. Tape may be forgone by using a clean-room wipe with acetone to remove the freshly spun SU-8 from the alignment marks.

7. Same as in **Note 2**: ramp up to 500 RPM at 100 RPM/s for 10 s, increase to 1500 RPM at 300 RPM/s for 30 s, and ramp down to 100 RPM at 100 RPM/s for 15 s before stopping.
8. It may be possible to use shorter exposure times, but 1 min exposure is typically sufficient to achieve good SU-8 feature sizes. The UV lamp intensity can decrease over its lifetime, and therefore the optimal exposure time for this step may vary. Over- or underexposure will affect the dimensions of the SU-8 features and of the final PDMS device. Thus, constriction dimensions should be validated for new devices. This can be done by imaging the SU-8 features, or by filling the assembled PDMS devices with fluorescently labeled dextran or other fluorescent solution and acquiring confocal image stacks of the constriction channels.
9. In order to protect the silicon wafer and delicate SU-8 features from damage during regular device production, we recommend that the first set of PDMS cast migration devices is used to produce a secondary plastic mold. This plastic mold should then be used for subsequent reproduction of migration devices. Detailed notes on producing a secondary plastic mold can be found in Desai et al. [20].
10. Ensure that the mold sits completely flat in the oven to prevent PDMS from tilting during curing. Tilted devices can still be used; however the devices will vary in thickness and therefore will not be able to hold the same volume of cell media.
11. When using a secondary plastic mold to make devices, the PDMS can be immediately removed following baking. When using the silicon wafer as your device mold, be sure to allow the device to cool completely before proceeding to avoid damaging SU-8 features.
12. 0.2 M hydrochloric acid (HCl) solution should be replaced on a weekly basis. Over time, HCl will evaporate, and devices will not properly adhere to glass slides.
13. During this step, be very careful with the placement of the punch-outs. The 1.2 mm punch sits between the bypass channel and the constrictions; interference with either will likely affect your results. It is also advised that you punch through the PDMS with the feature-side up to prevent poorly located cutouts.
14. When rinsing device, hold device upward, above your hands, and pour IPA and water downward onto device. Otherwise, runoff of material from gloves may fall onto the device and prevent adhesion between PDMS and the glass slide.
15. During drying of cover glass with pressurized air, hold glass firmly, and slowly increase air pressure, blowing parallel to the length of the glass to prevent bending and breaking of the glass.

16. This will activate the surface of the PDMS, allowing better adhesion between the device features and the glass slide. Pay close attention, and adjust air intake to keep plasma bright pink throughout cleaning, as we have found that poor device adhesion often results from poor plasma cleaning technique.
17. At this stage, ensure that you do not touch the surface of the glass slide nor the device-side surface of the PDMS. Additionally, check orientation of the device constrictions, and place very carefully, as you will not be able to adjust the orientation after it contacts the glass. Orientation of devices is entirely up to the user, but if mounting multiple devices on a single glass slide, analysis is generally easier if all cells are migrating in the same direction. Generally, we align the devices so that the cells will migrate "upward" (i.e., in the *y*-direction) while observing under a microscope.
18. This step may take some trial and error; if the PDMS device is not pressed sufficiently firmly against the glass, some device features may not fully adhere to the glass. In this case, cells can migrate underneath the PDMS pillars (Fig. 3D). If the PDMS device is pressed too hard against the glass, the features may collapse, preventing cells from migrating through the device. We have found that gently pressing around the device perimeter, evenly rolling one finger across the whole device with very light pressure, works best.
19. At this step, the device can be inspected underneath a bright-field microscope to see if the PDMS features are fully adhered. There will be a notably different color coming through regions of the device that are not bonded to the glass.
20. When coating, check the inside of the device for pockets of air bubbles, which may form during addition of protein solutions into the device. These air bubbles can form around constrictions, which can prevent the protein from coating these features. To eliminate the bubbles, vigorously pipette protein solution through the device. Optimal seeding densities of cells and concentrations of ECM solutions that we have determined are found in Table 1.
21. The exact number of cells to be seeded will be dependent on the specific cell line and may require optimization depending on what cell density is desired for the experiments. We have found that seeding 30,000 MDA-MB-231 cells per device works well for live-imaging experiments. In order to concentrate this number of cells into 6 μL of cell suspension, cells should be suspended in media at a concentration of 5 million cells per mL.
22. Cells must be seeded slowly and steadily with the pipette. Pushing the cells into the device too quickly may lead to the

cells spreading unevenly across the device (Fig. 3B). Additionally, when seeding cells, do not dispense the pipette past the first point of resistance; injection of air behind the cells results in the formation of bubbles within the device and can hinder cell migration (Fig. 3C).

23. If necessary, HEPES or other buffers may be added to cell culture media to maintain pH balance, particularly for longer duration studies. To prevent evaporation of cell media, devices should be sealed with cover glass laid across the media reservoirs before moving to microscope. In experiments that run longer than 12 h, it may be necessary to change cell culture media on a regular basis (typically every 24 h).
24. Fixation and staining of cells can be performed using standard immunofluorescence protocols; however it is recommended that longer times are used for each incubation and washing step to ensure that reagents have sufficient time to distribute completely throughout the microfluidic device. For immunofluorescence studies, cells should be seeded at lower densities, as large numbers of cells can block up the entry to the constriction channels, preventing staining reagents from reaching some cells within the devices. Alternatively, experiments can be performed with devices without covalently attaching the PDMS to the glass slides (i.e., without plasma treatment). In this case, the PDMS can be removed after fixing the cells inside the devices, and staining can be performed on cells adhering to the glass slide. The fixation step may require some optimization to identify conditions that promote cells to preferentially adhere to the glass cover slide and not the PDMS features.
25. Total imaging time is up to the user and depends on the cell line being used. For most cell lines, imaging overnight (12–14 h) is sufficient to yield a good number of cells passing through constrictions (10–30 cells per region of interest). For longer studies, it may be necessary to periodically replace cell media to keep cells healthy.
26. We have found that the most consistent measurement for a "point of commitment," i.e., when a cell is attempting to pass through a constriction, is an imaginary line drawn 7 μm away from the centerline of the constrictions, toward the entry side (Fig. 4). Another imaginary line can be drawn on the opposite side center line to define when the nucleus has fully passed through the constriction. It is also necessary to check image sequences for signs of potential issues with the constrictions, which would result in exclusion of the affected cells. For example, if it appears that some part of the nucleus or the cell body passes underneath the device pillars during migration, instead of in between the pillars that form the constriction, this indi-

cates that the PDMS pillars were not sufficiently bonded to the glass and the nucleus is not fully confined.

27. As in **Note 26**, it is also important to establish criteria for exclusion of particular cells migrating through the 15 μm channels. For example, when determining the migration speed or nuclear transit time of cells in the 15-μm-wide channels, it may be necessary to exclude cells that spontaneously switch their migration direction, as this would affect the results.

Acknowledgments

This work was supported by awards from the National Institutes of Health [R01 HL082792 and U54 CA210184], the Department of Defense Breast Cancer Research Program [Breakthrough Award BC150580], and the National Science Foundation [CAREER Award CBET-1254846].

References

1. Weigelin B, Bakker GJ, Friedl P (2012) Intravital third harmonic generation microscopy of collective melanoma cell invasion. Intravital 1(1):32–43
2. Doerschuk CM, Beyers N, Coxson HO, Wiggs B, Hogg JC (1993) Comparison of neutrophil and capillary diameters and their relation to neutrophil sequestration in the lung. J Appl Physiol 74:3040–3045
3. McGregor AL, Hsia C, Lammerding J (2016) Squish and squeeze—the nucleus as a physical barrier during migration in confined environments. Curr Opin Cell Biol 40:32–40
4. Caille N, Thoumine O, Tardy Y, Meister JJ (2002) Contribution of the nucleus to the mechanical properties of endothelial cells. J Biomech 35(2):177–187
5. Davidson PM, Lammerding J (2014) Broken nuclei-lamins, nuclear mechanics, and disease. Trends Cell Biol 24(4):247–256
6. Petrie R, Koo H, Yamada K (2014) Generation of compartmentalized pressure by a nuclear piston governs cell motility in a 3D matrix. Science 342(6200):1062–1065
7. Thomas DG, Yenepalli A, Denais CM, Rape A, Beach JR, Wang Y-L, Schiemann WP, Baskaran H, Lammerding J, Egelhoff TT (2015) Non-muscle myosin IIB is critical for nuclear translocation during 3D invasion. J Cell Biol 210:583–594
8. Jayo A, Malboubi M, Antoku S, Chang W, Ortiz-Zapater E, Groen C, Pfisterer K, Tootle T, Charras G, Gundersen G, Parsons M (2016) Fascin regulates nuclear movement and deformation in migrating cells. Dev Cell 38(4):371–383
9. Khatau S, Bloom R, Bajpai S, Razafsky D, Zang S, Giri A, Wu P, Marchand J, Celedon A, Hale C, Sun S, Hodzic D, Wirtz D (2012) The distinct roles of the nucleus and nucleus-cytoskeleton connections in three-dimensional cell migration. Sci Rep 2:488
10. Bone C, Chang Y, Cain N, Murphy S, Starr D (2016) Nuclei migrate through constricted spaces using microtubule motors and actin networks in *C. elegans* hypodermal cells. Development 143(22):4193–4202
11. Doyle AD, Petrie RJ, Kutys ML, Yamada KM (2013) Dimensions in cell migration. Curr Opin Cell Biol 25(5):642–649
12. Lautenschlager F, Piel M (2012) Microfabricated devices for cell biology: all for one and one for all. Curr Opin Cell Biol 25(1):116–124
13. Kramer N, Walzl A, Unger C, Rosner M, Krupitza G, Hengstschlager M, Dolznig H (2013) In vitro cell migration and invasion assays. Mutat Res 752(1):10–24
14. Davidson PM, Sliz J, Isermann P, Denais CM, Lammerding J (2015) Design of a microfluidic device to quantify dynamic intranuclear deformation during cell migration through confining environments. Integr Biol 7:1534–1546
15. Tong Z, Balzer EM, Dallas MR, Hung WC, Stebe KJ, Konstantopolous K (2012) Chemotaxis of cell populations through con-

fined spaces at single-cell resolution. PLoS One 7:1–10

16. Wolf K, te Lindert M, Krause M, Alexander S, te Riet J, Willis LA, Hoffman RM, Figdor CG, Weiss SJ, Friedl P (2013) Physical limits of cell migration: control ECM space and nuclear deformation and tuning by proteolysis and traction force. J Cell Biol 201:1069–1084
17. Denais CM, Gilbert RM, Isermann P, McGregor AL, te Lindert M, Weigelin B, Davidson PM, Friedl P, Wolf K, Lammerding J (2016) Nuclear envelope rupture and repair during cancer cell migration. Science 352(6283):353–358
18. Qin D, Xia Y, Whitesides GM (2010) Soft lithography for micro- and nanoscale patterning. Nat Protoc 5(3):491–503
19. Elacqua JJ, McGregor AL, Lammerding J (2018) Automated analysis of cell migration and nuclear envelope rupture in confined environments. PLoS One 13(4):e0195664
20. Desai SP, Freeman DM, Voldman J (2009) Plastic masters-rigid templates for soft lithography. Lab Chip 9:1631–1637

Local, transient tensile stress on the nuclear membrane causes membrane rupture

Qiao Zhang[a], Andrew C. Tamashunas[a], Ashutosh Agrawal[b], Mehdi Torbati[b], Aditya Katiyar[c], Richard B. Dickinson[a], Jan Lammerding[d], and Tanmay P. Lele[a,*]

[a]Department of Chemical Engineering and [c]Department of Mechanical and Aerospace Engineering, University of Florida, Gainesville, FL 32611; [b]Department of Mechanical Engineering, University of Houston, Houston, TX 77204; [d]Weill Institute for Cell and Molecular Biology and Meinig School of Biomedical Engineering, Cornell University, Ithaca, NY 14853

ABSTRACT **Cancer cell migration through narrow constrictions generates compressive stresses on the nucleus that deform it and cause rupture of nuclear membranes. Nuclear membrane rupture allows uncontrolled exchange between nuclear and cytoplasmic contents. Local tensile stresses can also cause nuclear deformations, but whether such deformations are accompanied by nuclear membrane rupture is unknown. Here we used a direct force probe to locally deform the nucleus by applying a transient tensile stress to the nuclear membrane. We found that a transient (~0.2 s) deformation (~1% projected area strain) in normal mammary epithelial cells (MCF-10A cells) was sufficient to cause rupture of the nuclear membrane. Nuclear membrane rupture scaled with the magnitude of nuclear deformation and the magnitude of applied tensile stress. Comparison of diffusive fluxes of nuclear probes between wild-type and lamin-depleted MCF-10A cells revealed that lamin A/C, but not lamin B2, protects the nuclear membranes against rupture from tensile stress. Our results suggest that transient nuclear deformations typically caused by local tensile stresses are sufficient to cause nuclear membrane rupture.**

Monitoring Editor
Valerie Marie Weaver
University of California, San Francisco

Received: Sep 28, 2018
Revised: Dec 3, 2018
Accepted: Dec 14, 2018

INTRODUCTION

Cell migration through narrow constrictions causes nuclear deformations (Wolf *et al.*, 2013; Irianto *et al.*, 2017). These deformations can be accompanied by local rupture of the nuclear membrane (Denais *et al.*, 2016; Raab *et al.*, 2016). Exposing nuclear contents to the cytoplasm causes DNA damage (Denais *et al.*, 2016; Irianto *et al.*, 2017) that may contribute to cancer progression. In these situations, increased intranuclear pressure resulting from compressive cytoskeletal forces is thought to cause the formation of micron-sized membrane blebs that separate from the lamina and eventually rupture (Denais *et al.*, 2016; Hatch and Hetzer, 2016; Lammerding and Wolf, 2016). Such spontaneous membrane rupture occurs not only during cell migration in confined spaces but also in cultured cancer cells, likely due to actin confinement (Hatch and Hetzer, 2016).

Local tensile stresses can also cause nuclear deformations (Maniotis *et al.*, 1997; Lammerding *et al.*, 2006; Wang *et al.*, 2009; Chancellor *et al.*, 2010; Wu *et al.*, 2014; Alam *et al.*, 2015; Tajik *et al.*, 2016; Lele *et al.*, 2018). For example, extracellular stresses applied to integrin receptors on the cell membrane can be propagated to the nucleus through the cytoskeleton, causing local nuclear deformations, rotations, and translations (Maniotis *et al.*, 1997; Wang *et al.*, 2009; Tajik *et al.*, 2016). Tensile stresses on the nuclear surface are also generated during cell migration, which can cause nuclear translations (Wu *et al.*, 2014). Also, local cell membrane protrusions proximal to the nuclear surface have been shown to cause local nuclear deformations (Alam *et al.*, 2015). Such tensile stresses are transmitted to the nuclear surface through molecular connections between nesprin proteins embedded in the outer nuclear envelope, which bind to the cellular cytoskeleton (Luxton and Starr, 2014; Uhler and Shivashankar, 2017; Kirby and Lammerding, 2018; Lee and Burke, 2018). Because nesprins are embedded in the cell membrane and bind to SUN proteins that are also in the inner nuclear

This article was published online ahead of print in MBoC in Press (http://www.molbiolcell.org/cgi/doi/10.1091/mbc.E18-09-0604) on December 19, 2018.

*Address correspondence to: Tanmay P. Lele (tlele@che.ufl.edu).

Abbreviations used: cGAS, cyclic GMP-AMP synthase; DBS, donor bovine serum; EGF, epidermal growth factor; FEM, finite element method; GFP, green fluorescent protein; INM, inner nuclear membrane; LINC, linker of nucleoskeleton and cytoskeleton; LMNA, lamin A/C; LMNB2, lamin B2; MEF, mouse embryonic fibroblast; NLS, nuclear localization sequence; ONM, outer nuclear membrane; RT-qPCR, reverse transcription quantitative PCR; SUN, Sad1 and UNC.

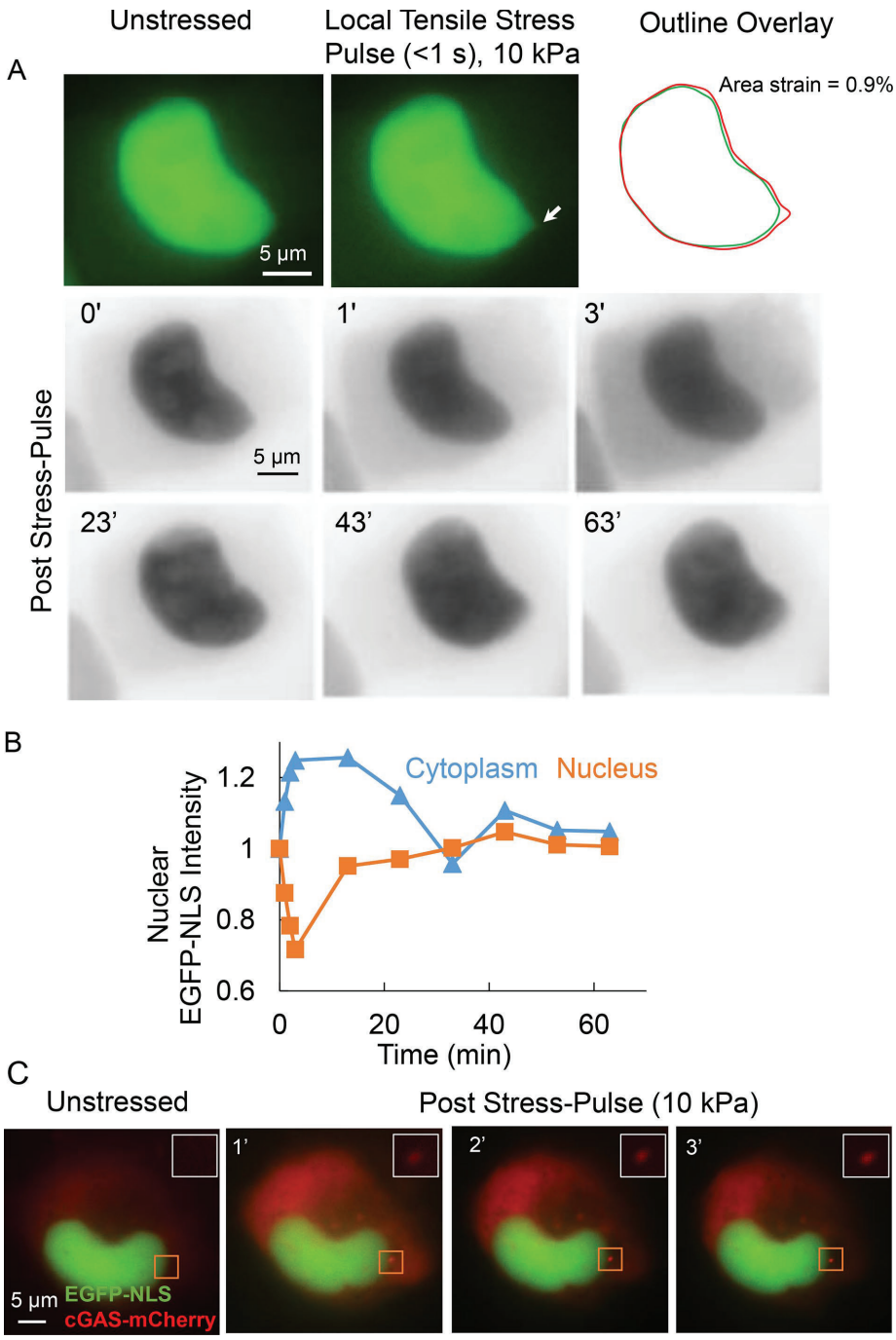

FIGURE 1: Local tensile stress applied to the nucleus in adherent cells can rupture the nuclear membranes. (A) Top: images show a representative MCF-10A nucleus expressing EGFP-NLS before application of stress (unstressed) and at the point of maximum deformation due to a local stress pulse of 10 kPa and duration of <1 s. The arrow indicates the location where the micropipette tip was attached to the nucleus. The outline overlay compares the outlines of the unstressed and deformed nucleus (right). Bottom: inverted time lapse fluorescent images of the nucleus probed above along with cytoplasm. The images show that the cytoplasmic intensity increases and the nuclear intensity decreases—the corresponding quantification of cytoplasmic and nuclear intensities (normalized to the corresponding initial intensity; stress pulse applied at time = 0) is shown in B—over the first several seconds, which indicates membrane rupture. Over longer times (~30 min), both cytoplasmic and nuclear intensity are restored to levels before rupture indicating the nuclear membranes are repaired over time. (C) Images show cGAS-mCherry stably expressing MDA-MB-231 cell nucleus transfected with EGFP-NLS. Local tensile stress of 10 kPa (at the site indicated by rectangular box) causes the accumulation of cGAS cytoplasmic DNA binding protein near the site of stress application.

membrane, it is possible that tensile stresses exerted on these proteins may cause rupture of the nuclear membranes. However, whether such deformations are accompanied by nuclear membrane rupture has not yet been examined.

Here, we applied local tensile stress on the nuclear membranes in living adherent cells using a direct force probe (Neelam *et al.*, 2015; Zhang *et al.*, 2018) and examined nuclear membrane integrity with previously established nuclear membrane rupture reporters (Denais *et al.*, 2016). Our results suggest that transient nuclear deformations typically caused by local tensile stresses are indeed sufficient to cause nuclear membrane rupture.

RESULTS

Using the direct force probe, we applied stress directly to the nuclear surface in an adherent living cell. The method involves suction-sealing a narrow micropipette to the nuclear surface.The suction pressure in the micropipette is known precisely (Neelam *et al.*, 2015; Zhang *et al.*, 2018). Moving the micropipette away from the nucleus deforms the nucleus locally. Eventually, the micropipette detaches when the restoring forces in the nucleus equal the applied suction pressure across the small nuclear membrane section. Using this method, we applied a short (<1 s; see Supplemental Movie 1) force pulse of 2 nN over a circular area (diameter 0.5 μm) of the nucleus of a normal mammary epithelial cell (MCF-10A cell) expressing an EGFP-NLS nuclear rupture reporter. This force corresponds to a (nearly normal) stress of 10 kPa. The nucleus transiently deformed at the force application site; the deformation resulted in a loss of nuclear membrane integrity (nuclear membrane rupture), as evidenced by the leakage of EGFP-NLS into the cytoplasm, resulting in a transient loss of nuclear EGFP-NLS fluorescence and a corresponding increase in the cytoplasmic EGFP-NLS signal (Figure 1, A, and corresponding intensities in B). By ~60 min after the end of the force pulse, the nuclear and cytoplasmic EGFP-NLS intensities recovered back to preforce levels, indicating membrane repair and reimport of the EGFP-NLS reporter (Figure 1, A and B). These results confirm that the initial decrease in EGFP-NLS corresponded to an actual rupture event. For additional confirmation, we modified cells to express cGAS-mCherry, a cytoplasmic DNA-binding protein that accumulates at the site of nuclear envelope rupture where the

genomic DNA is exposed to the cytoplasm (Denais *et al.*, 2016). The rapid accumulation of cGAS-mCherry at the force application site indicated that the nuclear membrane rupture was local (Figure 1C; see inserts for an enlarged view).

We tested whether the direct force probe causes consistent and reproducible rupture by analyzing the time-dependent decay in the nuclear EGFP-NLS intensity after the force pulse over several cells. Data pooled from several probed cells showed a consistent decrease in the nuclear intensity upon application of the stress pulse, an increase in cytoplasmic intensity, and a relatively small change in control cells (Figure 2A, control cells are unstressed, and in the same image as the stressed cell, which helps control for photobleaching effects). We quantified the extent of nuclear deformation by overlaying images of the nucleus before and at maximum deformation using the method in Neelam *et al.* (2015) (see *Materials and Methods*). A stress pulse of 10 kPa corresponded to an average area strain of 0.8% ± 0.1%. These data suggest that local tensile stresses, resulting in transient nuclear deformations of the degree typically caused by local tensile stresses (Maniotis *et al.*, 1997; Lammerding *et al.*, 2005; Lammerding and Lee, 2009; Alam *et al.*, 2015; Tajik *et al.*, 2016), consistently rupture the nuclear membranes of MCF-10A cells.

To test the hypothesis that the extent of rupture depends on the magnitude of tensile stress applied by the direct force probe, we repeated these experiments over a range of applied nuclear membrane stresses. Figure 2B shows pooled data for dynamic decrease in nuclear EGFP-NLS intensity at different stress levels. There was a measurable decrease in the nuclear EGFP-NLS intensity in the nucleus at stresses as low as 2 kPa. The maximum loss of nuclear EGFP-NLS intensity (measured as the intensity at 120 s after the stress pulse, i.e., long enough for the nuclear EGFP-NLS intensity to fully decay) scaled with the magnitude of the nuclear membrane stress applied (Figure 2C). Histograms of EGFP-NLS intensity at 120 s also show a clear trend toward higher means at larger stress values with only a minor effect on the probability of rupture (Supplemental Figure S1A). We confirmed a similar dependence of nuclear membrane rupture on applied membrane stress in mouse embryonic fibroblasts (MEFs) (Supplemental Figure S2), indicating that the findings are not specific to a single cell line or species.

The underlying nuclear lamina may protect the nuclear membranes from rupture under tensile stress (Denais *et al.*, 2016; Hatch and Hetzer, 2016). We therefore depleted nuclear lamins and examined the effect on nuclear membrane rupture. Depletion of lamin A/C by siRNA (small interfering RNA) (Supplemental Figure S3) resulted in a higher loss of nuclear EGFP-NLS (Figure 3A), whereas depletion of lamin B2 had no significant effect (Figure 3B). This was surprising, as previous studies with nuclear compression found that lamin B2 has a protective role in nuclear membrane rupture (Hatch *et al.*, 2013; Bakhoum *et al.*, 2018). Given that loss of of lamin A/C softens the nucleus (Broers *et al.*, 2004; Lammerding *et al.*, 2004; Pajerowski *et al.*, 2007; Schäpe *et al.*, 2009; Swift *et al.*, 2013; Davidson *et al.*, 2015; Stephens *et al.*, 2017), we examined the effect of lamin depletion on nuclear deformation under transiently applied local nuclear membrane stress. Lamin B2 depletion had no effect on nuclear deformation (Supplemental Figure S4), consistent with previous studies (Lammerding *et al.*, 2006), and correspondingly had no effect on rupture (Figure 3D), whereas lamin A/C depletion resulted in larger nuclear deformation (and a larger extent of membrane rupture) (Figure 3C). The loss in nuclear EGFP-NLS intensity after rupture scaled with the stress levels and with the extent of maximum nuclear deformation under stress for both MCF-10A cells and MEFs (Figure 3E).

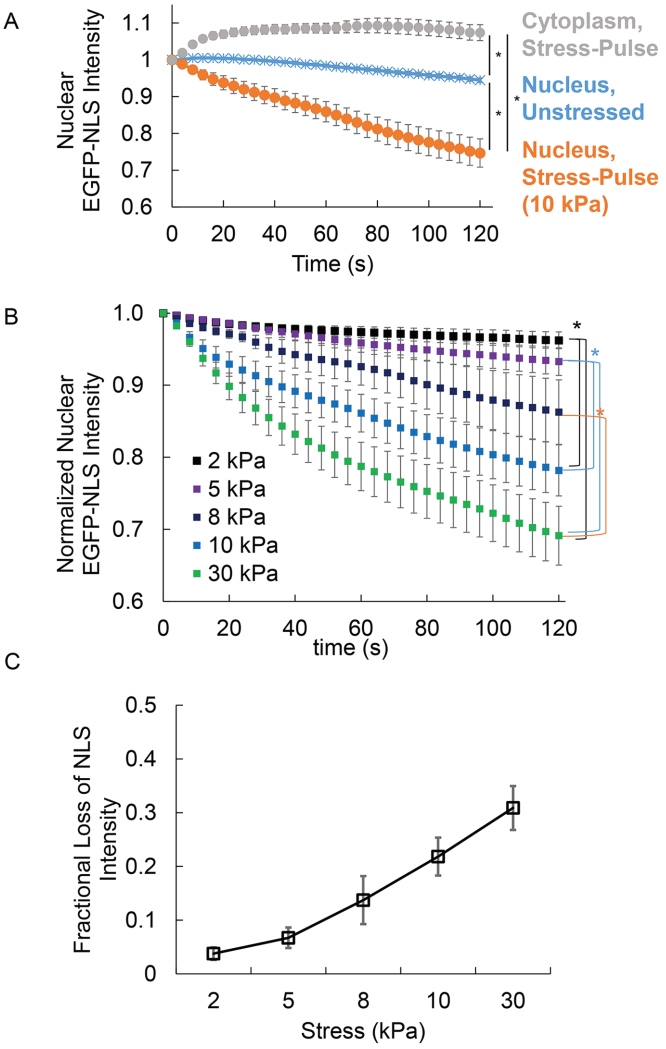

FIGURE 2: The extent of rupture of nuclear membranes scales with the magnitude of tensile stress. (A) The plot shows pooled measurements of cytoplasmic and nuclear EGFP-NLS fluorescence intensities (normalized to the initial intensity) at 120 s after a stress pulse was applied to the MCF-10A nucleus (gray and orange circles, respectively), along with EGFP-NLS fluorescence intensities in nuclei (blue; normalized to the initial intensity), which were present in the same field of view as the stressed nucleus, but which were not subjected to stress. The decrease in the fluorescence intensity of unstressed nuclei is due to photobeaching during image capture. The fluorescence intensity of stressed nuclei decreases consistently after application of the stress pulse. Data were pooled from 23 nuclei. The stress applied was 10 kPa. Error bars are SEM. Statistical differences were detected with two-way analysis of variance (ANOVA) (* represents $p < 0.05$). (B) Plot shows pooled mean values of normalized EGFP-NLS intensity from at least 20 nuclei per stress magnitude. Normalization involved correcting for effects of photobleaching by dividing stressed nuclear EGFP-NLS intensities with EGFP-NLS intensities in the unstressed control nucleus in the same field of view for each cell probed (see *Materials and Methods* for details on normalization). Rupture behavior is seen to change with the magnitude of the stress applied. Error bars are SEM ($N \geq 20$). Statistical differences were detected with two-way ANOVA with Bonferroni correction (* represents $p < 0.05$/number of comparison). (C) Plot shows the fractional loss of nuclear EGFP-NLS intensity quantified from the data in B at 120 s after the stress pulse (see *Materials and Methods* for calculation). The data show that the extent of NLS loss is larger at a higher magnitude of stress. Error bars are SEM ($N \geq 20$).

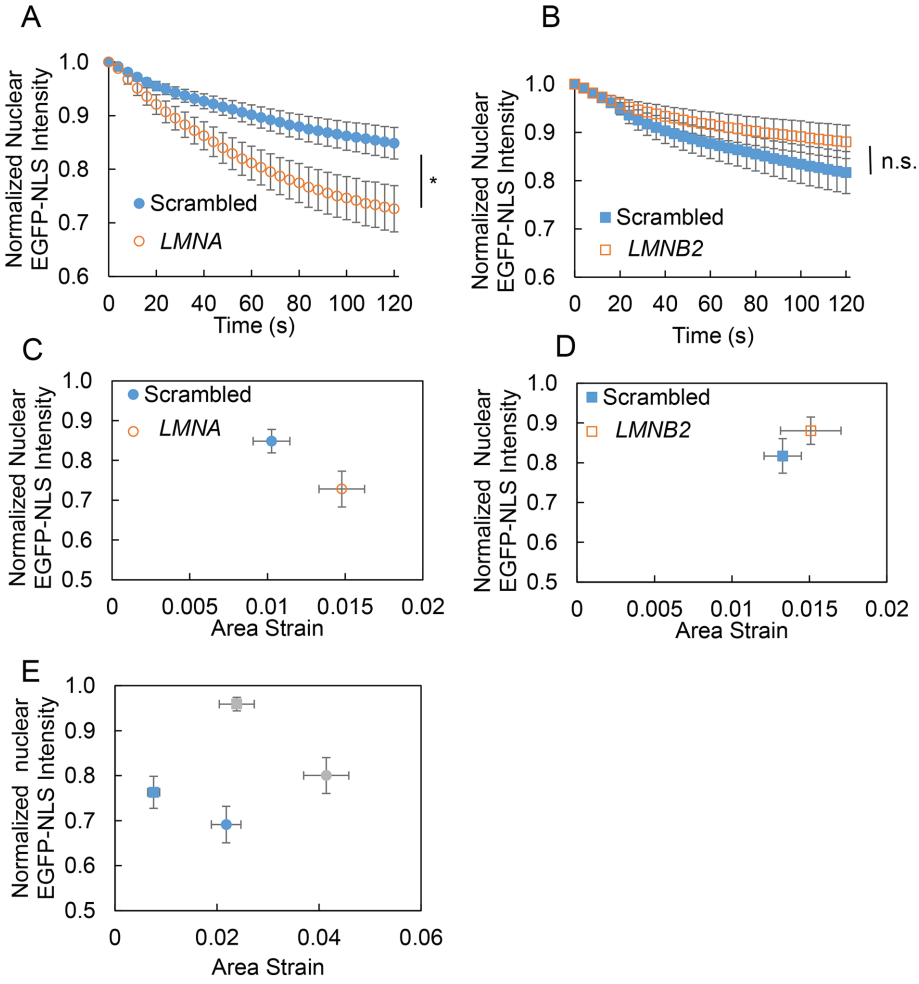

FIGURE 3: Effect of lamin depletion on nuclear membrane rupture caused by local tensile stress. Plots show pooled mean normalized nuclear EGFP-NLS intensity after a 10 kPa stress pulse was applied to the nucleus in MCF-10A cells transfected with (A) nontargeting siRNA (scrambled) and siRNA targeting LMNA and (B) siRNA targeting LMNB2 ($N \geq 22$ for each condition). Statistical differences were detected with ANOVA (* represents $p < 0.05$). (C, D) Plots show the normalized nuclear EGFP-NLS intensity at 120 s after a 10 kPa stress pulse vs. the maximum nuclear deformation (quantified as area strain) in MCF-10A cells transfected with (C) nontargeting siRNA or siRNA targeting LMNA and (D) nontargeting siRNA or siRNA targeting LMNB2. Error bars are SEM ($N \geq 21$). The EGFP-NLS intensity at the pseudosteady state of 120 s postrupture appears to correlate with the maximum deformation. (E) Plot shows the normalized nuclear EGFP-NLS intensity at 120 s poststress pulse vs. the maximum nuclear deformation (quantified as area strain) in MCF-10A cells (blue symbols; square corresponds to 10 kPa, and circle corresponds to 30 kPa), and MEFs (gray symbols; square corresponds to 10 kPa, and circle corresponds to 30 kPa). Error bars are SEM ($N \geq 17$). For a given cell type, the pseudosteady fluorescence intensity of EGFP-NLS at 120 s postrupture scales inversely with the extent of deformation.

To estimate the size of the membrane defect during nuclear rupture, we used the quantitative kinetic data on the decrease of EGFP-NLS in the nucleus, combined with finite element modeling (FEM) of the diffusion of EGFP-NLS, through a small circular hole in the surface of the three-dimensional nucleus separating the nucleus and the cytoplasm (Figure 4A shows a two-dimensional projection of the three-dimensional nucleus and cell). Notably, the calculations estimate an "effective size," as it is possible that more than one smaller hole is created in the membranes, below the resolution limit of the light microscope. In this calculation, three-dimensional cell and nuclear geometric parameters were chosen based on our previously published measurements with MCF-10A cells (Neelam *et al.*, 2016) (Table 1), and the diffusion coefficient of EGFP-NLS has been previously reported in both the cytoplasm and the nucleus (Wu *et al.*, 2009) (Table 1). EGFP-NLS is reimported from the cytoplasm into the nucleus, and this reimport rate depends on the cytoplasmic concentration, the number of nuclear pores, and the efficiency of the nuclear transport mechanism (the latter are not easily measurable for a given cell). To avoid the complications of nuclear reimport, we modeled only the initial rates of loss of EGFP-NLS when the cytoplasmic intensity and hence the reimport rate are negligible. The FEM calculations yield the initial rate of NLS loss as a function of hole diameter (Figure 4B). Comparison between experimental and simulation data (Figure 4, B and C) allowed us to estimate the force-dependent effective hole size (Table 2). Our model indicates that these hole diameters are ~100 nm (ranging from ~96 nm at lower stresses to ~465 nm at higher stresses), in agreement with similar pore sizes used by others (Deviri *et al.*, 2017) and a previous estimate based on superresolution imaging (Denais *et al.*, 2016).

DISCUSSION

Both compressive and tensile stress can cause nuclear deformation. Compressive stresses can cause rupture of the nuclear membrane, thereby exposing nuclear contents to the cytoplasm. Whether tensile stress–induced deformations similarly cause nuclear membrane rupture is currently unknown. Here we used the direct force probe to apply tensile stresses directly to the nuclear surface. Our results provide the first evidence that a tensile stress applied locally and transiently on the nuclear surface that elicits elastic nuclear deformation is sufficient to cause transient nuclear membrane rupture. The extent of nuclear deformation required for rupture under tensile stresses is relatively modest (<1% projected area strain) and is typical of what has been reported for nuclear deformations under tensile stress (Maniotis *et al.*, 1997; Lammerding *et al.*, 2005; Lammerding and Lee, 2009; Alam *et al.*, 2015; Tajik *et al.*, 2016).

Because the nuclear membrane is not a single membrane but consists of an outer and inner membrane fused to each other at several thousand nuclear pores, its mechanical rupture under stress is expected to be different from the well-studied situation of rupture of a single free-standing membrane. In addition, proteins that localize in the membrane mechanically couple the two membranes; these include SUN1/2 proteins embedded in the inner nuclear membrane that bind to nesprins embedded in the outer nuclear membrane. Also, proteins in the inner nuclear membrane (such as emerin and farnesylated lamins) tether the inner nuclear membrane to the underlying nuclear lamina and chromatin providing

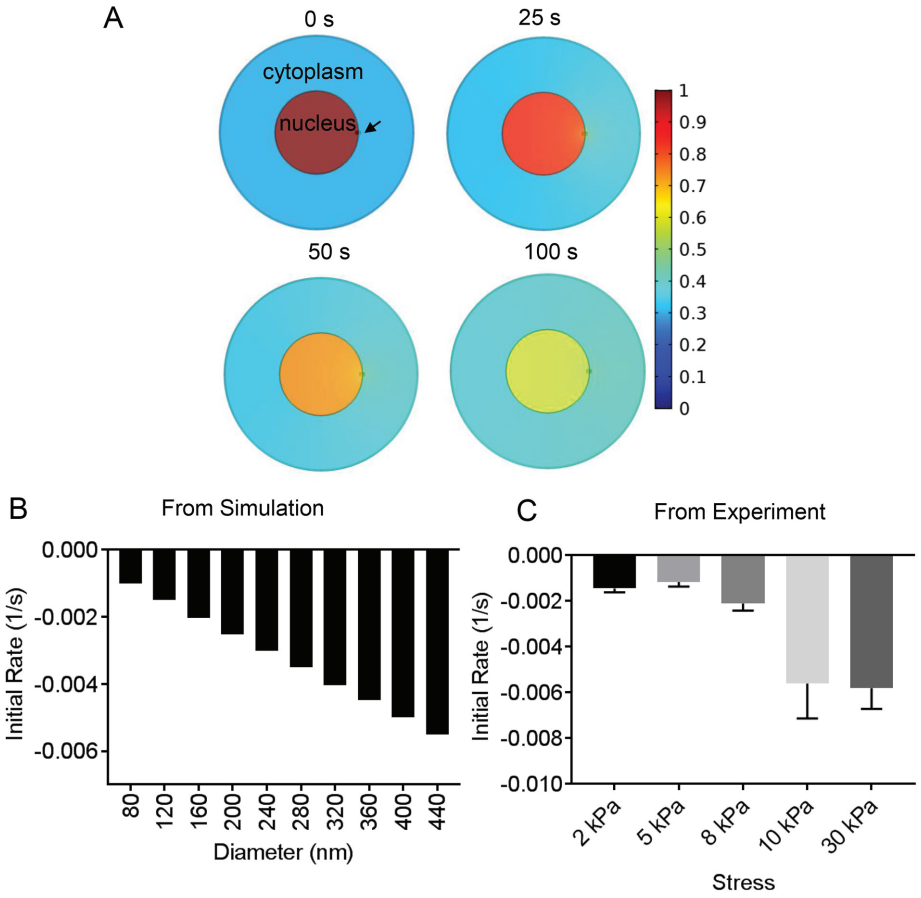

FIGURE 4: Experimental estimation of the hole size. (A) X-Y views of a finite element calculation of nuclear EGFP-NLS diffusion from a hole in the nucleus (marked by an arrow). The nucleus and cell are modeled as flat cylinders with geometrical parameters taken from experimental measurements in Neelam *et al.* (2016) and nuclear and cytoplasmic diffusion coefficients from Wu *et al.* (2009) (see Table 1). (B) Initial rate of EGFP-NLS diffusion from the nucleus into the cytoplasm through the nuclear hole as a function of hole size calculated from the finite element model in A (for details of how the initial rate was calculated from data, see *Materials and Methods*). (C) Plot shows experimental measurements of initial rate of nuclear EGFP-NLS decrease in the nucleus at different stress levels. Error bars are SEM $N \geq 22$ for each stress.

structural support (Foisner, 2001; Dahl *et al.*, 2008; Isermann and Lammerding, 2013; Chang *et al.*, 2015). The direct force probe allowed us to quantitatively compare rupture behavior between wild-type and lamin-depleted cells and also across cell types. Such comparisons are possible because the applied tensile stress is the same across these different conditions. We note here that although the applied stress is tensile (pulling), the mechanical response of nuclear components may be more complex, including possibly simultaneous compression of some elements and bending and expansion of others.

Depletion of lamin A/C, but not lamin B2, increased the loss in EGFP-NLS nuclear intensity under stress. The probability of rupture was not significantly altered upon depletion of lamin A/C (Supplemental Figure S1B), suggesting that the larger loss of intensity corresponded to a larger effective hole size. The hole size, estimated by comparison with the finite element calculations, was ~433 nm for lamin A/C depletion (228 nm for the scrambled control) and ~198 nm for lamin B2 depletion (223 nm for the scrambled control). This suggests that lamin A/C, but not lamin B2, plays a protective role in preventing rupture under tensile stresses.

The fact that the deformation scales with the applied stress (as we have previously reported [Neelam *et al.*, 2015]) indicates that the rupture process itself does not cause detachment from the micropipette. If the small patch of nuclear membranes in contact with the pipette tip was being torn away from the nucleus due to pipette motion, then the pipette would detach when this rupture occurred, and nuclear deformation would be independent of the suction pressure. Further, applying suction alone to the nuclear membrane without pulling on it did not change the EGFP-NLS intensity in the nucleus (Supplemental Figure S6), arguing against the possibility that the applied suction pressure damages or opens nuclear pores.

Here we have reported nuclear deformation in terms of the projected area strain. The local strains near the pipette tip are likely higher than the projected area strain. It is desirable to measure the actual membrane area strain caused by application of the tensile stresses (the critical lipid membrane strain for rupture is of the order of 2% [Staykova *et al.*, 2011]), but it is difficult to accurately quantify this strain in our live cell imaging experiments because the nuclear shape itself is changing locally (which involves translation of the membranes in addition to membrane strain).

In single-lipid bilayers, hole formation is determined by the energetic interplay between the surface tension in the bilayer and the line tension energy, which develops as a result of extreme bending of lipids at the pore interface (Gonzalez-Rodriguez *et al.*, 2012; Akimov *et al.*, 2017a,b). For such a system, there is a critical radius on the order of a few nanometers (Akimov *et al.*, 2017a,b). If the holes in single bilayers exceed this critical radius, they are unstable and expand continually. If the holes are smaller than the critical radius, they spontaneously close. However, our experiments suggest that the holes are much larger (100 nm) and are stable over several seconds. The mechanism underlying this stability is not clear.

The fact that the leakage through nuclear holes would require rupture of both the nuclear membranes leads us to speculate that stable holes may be due to the creation of a donut-shaped hole

	Nucleus	Cell		Nucleus	Cytoplasm
Height (μm)	4.2	4.2	Diffusion coefficient (μm²/s)	19	14
Radius (μm)	8.6	20	Initial intensity	1	0.3

TABLE 1: Parameters used for finite element analysis in Figure 4.

Simulation		Experimental		
Initial rate (/s) × 1000	Hole size (nm)	Stress (kPa)	Initial rate (/s) × 1000	Hole size (nm)
–1.00	80	2	–1.46 ± 0.17	116 ± 14
–1.27	100	5	–1.21 ± 0.22	96 ± 17
–1.50	120	8	–1.96 ± 0.36	156 ± 27
–1.76	140	10	–5.62 ± 1.52	450 ± 119
–2.02	160	30	–5.82 ± 0.91	465 ± 72
–5.50	440			
–5.76	460			

Left column: initial rates of decrease in EGFP-NLS concentration in the nucleus calculated from the finite element analysis in Figure 4, for different hole sizes (diameter). The magnitude of the rate increases for increasing hole size as expected. Right column: initial rates (i.e., immediately after the stress pulse) estimated from experimental plots of EGFP-NLS intensity in the nucleus with time. Comparison with simulations was used to estimate the hole size, which is shown in the rightmost column.

TABLE 2: Comparison between experimental and simulation data.

between the ONM and the INM. After the initial rapid formation of the hole (<1 s), the hole may reach an equilibrium size over several seconds after hole formation. We explored this speculative picture by modeling the geometry of such donut holes by minimizing the bending energy. This approach is similar to the one we adopted previously to explain the separation of bilayers in the nuclear envelope (Torbati *et al.*, 2016). It relies on the fact that a lipid bilayer is a two-dimensional elastic sheet, which is fluid in-plane, allowing lipids to diffuse freely, but resists out-of-plane bending deformations. We computed the equilibrium shapes of a donut hole for a prescribed membrane tension and appropriate boundary conditions (described under *Materials and Methods*). The calculation in Supplemental Figure S5A, top, shows a prediction of ~60 nm three-dimensional donut-shaped holes corresponding to a membrane tension of ~0.05 mN/m, which is comparable to our previous calculation of the resting tension in the nuclear membranes that explains the separation between these membranes (Torbati *et al.*, 2016). At a lower resting tension of ~0.01 mN/m, the hole diameter is predicted to be ~240 nm (Supplemental Figure S5A, bottom). One possibility is that the lower stress pulses (Table 2) do not significantly perturb the resting tension in the nuclear membranes, whereas the higher-force pulses result in a larger loss of the resting tension, resulting in bigger hole sizes.

The above model is limited in that it accounts for only the initiation of pore formation and not the subsequent recruitment of membrane repair machinery, such as the ESCRT proteins, that occurs over minutes (Denais *et al.*, 2016). These proteins can also apply physical forces onto the membranes (Chiaruttini *et al.*, 2015), changing the geometry of the membranes and participating in resealing the hole. Further, hole establishment may be a process that is far from equilibrium and may be far more complex due to the many interactions among membrane-embedded proteins, the nuclear lamina, and the cellular cytoskeleton (Lele *et al.*, 2018).

Our experimental results show that the direct force probe can be an effective tool to engineer ruptures in the nuclear membranes in adherent cells. The application of precise and known levels of stress to the nucleus allows comparisons of rupture behavior across cell types and across different types of perturbations to nuclear membranes. This probe could be valuable in understanding whether and how membrane components, such as LINC complex proteins that span the nuclear membranes, nuclear membrane composition, and membrane-embedded proteins, could contribute to nuclear membrane integrity under tensile forces.

MATERIALS AND METHODS

Cell culture

All cell types were maintained at 37°C in a humidified 5% CO_2 environment. MCF-10A cells were cultured in DMEM/F12 supplemented with 20 ng/ml EGF, 0.5 mg/ml hydrocortisone, 100 ng/ml cholera toxin, 100 µg/ml insulin, and 5% horse serum (Debnath *et al.*, 2003). Human breast cancer cells (MDA-MB-231) and MEF cells were cultured in 4.5 g/l glucose DMEM supplemented with 10% DBS and 1% penicillin-streptomycin.

Plasmid transfection

Transient transfection of plasmids into cells was performed with Lipofectamine 3000 reagent (Life Technologies/Invitrogen, Carlsbad, CA) in OPTI-MEM media (Life Technologies/Invitrogen, Carlsbad, CA). EGFP-NLS was a kind gift of Alexander Ishov at the University of Florida (Negorev *et al.*, 2001). Transfected cells were trypsinized and plated onto fibronectin-coated glass-bottomed dishes for micromanipulation and microscopy. The construction of cGAS-mCherry (pCDH-CMV-cGASE225A/D227A-mCherry2-EF1-blastiS) was described previously (Civril *et al.*, 2013).

Immunostaining

Cells were fixed in 4% paraformaldehyde for 10 min, washed with phosphate-bufferered saline, and then permeabilized and blocked with 0.1% Triton X-100 in 1% bovine serum albumin solution for 45 min. The primary antibodies used in this study included rabbit anti–lamin B2 (Abcam; used at 1:500) and mouse anti–lamin A (Abcam; used at 1:1000). Cells were incubated with the primary antibody at 4°C overnight and secondary antibodies at room temperature for 1 h. Secondary antibodies used included goat anti-mouse Alexa Fluor 647 (Invitrogen; 1:500) and goat anti-rabbit Alexa Fluor 594 (Invitrogen; 1:500).

Micromanipulation

Micromanipulation was performed using an Eppendorf InjectMan micromanipulator system as described previously (Neelam *et al.*, 2015; Zhang *et al.*, 2018). In brief, a Femtotip micropipette tip (Eppendorf; 0.5-µm tip diameter) was mounted and connected to the Eppendorf microinjection system (InjectMan) by a tube. The cell membrane was penetrated with the micropipette tip, and the tip was brought next to the nuclear surface. The tube was then disconnected and opened to the atmosphere, which creates a known negative pressure that seals the micropipette tip to the ONM with a specified suction pressure (Neelam *et al.*, 2015; Zhang *et al.*, 2018). Nuclear

deformation occurred when the pipette was translated away from the nucleus. When the resistance to nuclear motion and deformation balanced the applied suction force, there was a subsequent release from the tip (this process occured in less than a second, resulting in a short-stress pulse). The resisting stress on the ONM then is the suction stress at this point of detachment (calculated as suction pressure × area of tip). We have previously shown that the extent of nuclear motion and deformation depends on the suction force and is not due to nonspecific adhesion between the pipette tip and the membrane. Also, we have calculated negligible pressure drop due to flow through nuclear pores, such that the stress on the ONM is, for practical purposes, identical to the suction pressure (Neelam *et al.*, 2015; Zhang *et al.*, 2018). Time-lapse imaging was performed on a Nikon TE2000-inverted microscope with a 60× oil immersion objective and CCD camera (CoolSNAP; Photometrics, Tucson, AZ). Cells were maintained at 37°C at a 5% CO_2 level throughout imaging.

siRNA transfection

The siGENOME SMARTpool siRNA targeting LMNA and LMNB2 (Dharmacon) were used to deplete lamin A and lamin B2 proteins, respectively. The efficiency of siRNA depletion was confirmed by comparing the fluorescence intensity (confocal images, taken with the same imaging settings between scrambled group and transfected group) and the relative expression mRNA levels quantified with RT-qPCR (Supplemental Figure S3D). To perform RT-qPCR, whole cells were lysed 72 h posttransfection using the SingleShot Probes One-Step Kit (Bio-Rad). Lysates were then combined with complete RT-qPCR mix per the manufacturer's protocol and predesigned fluorogenic probes targeting LMNA, LMNB2, or GAPDH (loading control; Bio-Rad). Reactions were processed on a CFX96 Real-Time PCR Detection System (Bio-Rad) using the following thermocycler conditions: 10 min at 50°C, 3 min at 95°C, followed by 40 cycles of 15 s at 95°C and 30 s at 60°C. All results were analyzed using the 2-ΔΔCt method and normalized against GAPDH expression and a scrambled siRNA negative control (Livak and Schmittgen, 2001).

Analysis

The NLS intensity of forced nuclei was normalized by the intensity of reference unforced nuclei in the same image to account for photobleaching effects as follows:

$$I_{t,n} = \frac{I_t/I_{t=0}}{I_{t,u}/I_{t=0,u}} \tag{1}$$

where $I_{t,n}$ is the normalized intensity at time t, I_t is the fluorescence intensity of the stressed nucleus, and $I_{t,u}$ is the fluorescence intensity of the unstressed nucleus quantified from images. The fractional loss of NLS intensity was calculated as $1-I_{t\,=\,120,\,n}$ corresponding to $t = 120$ s. The initial rate of loss of NLS intensity in the nucleus was estimated by fitting the normalized intensity data for the first 20 s with a fifth-order polynomial and then calculating the derivative by differentiating the polynomial and calculating the maximum rate. The area strain calculation was previously described in Neelam *et al.* (2015). Briefly, the nucleus at its maximum deformation was overlaid onto its unstressed shape and the nonoverlapping area was calculated. The area strain was calculated as the nonoverlapping area divided by the unstressed nuclear area.

Modeling

Finite element calculations of diffusion from a hole in the surface of the flat cylindrical nucleus into the flat cylindrical cytoplasm were performed in COMSOL. Zero flux boundary conditions were imposed everywhere else except at the hole, where continuity of concentration and mass flux was imposed. The predicted concentration in the nucleus was numerically averaged over the nuclear volume and normalized to the initial concentration. Initial rates were calculated from the time-dependent concentration profile in MATLAB by first fitting a polynomial to the time-dependent curve and differentiating this polynomial to calculate the initial rate. Next, hole size was varied, and initial rate dependence on hole size was calculated.

For mechanical calculations, the geometry of the membranes was modeled around a single donut-shaped pore as two-dimensional elastic sheets with the Helfrich–Canham relation:

$$W = kH^2 + \bar{k}K \tag{2}$$

where H is the mean curvature, K is the Gaussian curvature, and $\left(k, \bar{k}\right)$ are the bending moduli. The membranes were assumed to possess axisymmetry and reflection symmetry about the equatorial plane and hence, the geometry of only a single bilayer was simulated. The system is defined by the arclength s, the radial distance from the axis of revolution $r(s)$, the elevation from a base plane $z(s)$, and the angle which the tangent makes with the radial vector $\psi(s)$ (see Supplemental Figure S5B). These parameters satisfy the geometric relation:

$$r'(s) = \cos\psi \tag{3}$$

$$z'(s) = \sin\psi \tag{4}$$

$$\psi' = 2H - \sin\psi/r \tag{5}$$

Here, ()′ is the partial derivative with respect to the arclength. These equations were integrated along with the force equilibrium equation, commonly referred to as the shape equation:

$$k\Delta H + 2kH\left(2H^2 - K\right) - 2kH^3 = 2\lambda H \tag{6}$$

to compute the hole geometry. Here, λ is the surface tension and Δ is the surface Laplacian, and the transmembrane pressure was assumed to be zero. The integration was carried out with the following boundary conditions prescribed at the two ends of the simulated domain. The inner boundary is defined at the point where the membrane meets the equatorial plane at the hole site. Here we require $z = 0$, $\psi = \pi/2$, and $rH\text{^}' = 0$. The last boundary condition imposes zero transverse shear, a condition that arises from reflection symmetry present in the geometry and allows the membranes to slide freely at the equatorial plane.The far boundary is assumed to lie at a distance of 200 nm from the center of the hole, midway between two typical adjacent holes (Belgareh and Doye, 1997; D'Angelo *et al.*, 2006; Dultz and Ellenberg, 2010). Here we require $\Psi = 0$ and $\lambda = \lambda_0$, where λ_0 is the prescribed resting tension in the membranes. In addition, we assume that no membrane is lost during the process of hole creation and expansion. We therefore simulate different hole diameters with a conserved membrane area. We implemented this constraint by switching from the independent variable from the arclength (s) to the surface area (a) and use the geometric relation $da = 2\pi rs\ ds$ to obtain the modified set of equations (Agrawal and Steigmann, 2009). We used the MATLAB solver BVP4C to perform numerical integration and computed the membrane geometry for different resting tensions.

ACKNOWLEDGMENTS

This work was supported by awards from the National Institutes of Health (R01 EB014869 [T.P.L.], R01 HL082792 [J.L.], and U54 CA210184 [J.L.]) and the Department of Defense Breast Cancer

Research Program (Breakthrough Award BC150580 [J.L.]). R.B.D.'s contribution is based on work supported by (while serving at) the National Science Foundation. We thank Guanrui Li for his assistance in imaging acquisition and data analysis.

REFERENCES

Agrawal A, Steigmann D (2009). Boundary-value problems in the theory of lipid membranes. Continuum Mech Thermodyn 21, 57–82.

Akimov SA, Volynsky PE, Galimzyanov TR, Kuzmin PI, Pavlov KV, Batishchev OV (2017a). Pore formation in lipid membrane I: Continuous reversible trajectory from intact bilayer through hydrophobic defect to transversal pore. Sci Rep 7, 12152.

Akimov SA, Volynsky PE, Galimzyanov TR, Kuzmin PI, Pavlov KV, Batishchev OV (2017b). Pore formation in lipid membrane II: Energy landscape under external stress. Sci Rep 7, 12509.

Alam SG, Lovett D, Kim DI, Roux K, Dickinson RB, Lele TP (2015). The nucleus is an intracellular propagator of tensile forces in NIH 3T3 fibroblasts. J Cell Sci 128, 1901–1911.

Bakhoum SF, Ngo B, Laughney AM, Cavallo JA, Murphy CJ, Ly P, Shah P, Sriram RK, Watkins TBK, Taunk NK, *et al.* (2018). Chromosomal instability drives metastasis through a cytosolic DNA response. Nature 553, 467–472.

Belgareh N, Doye V (1997). Dynamics of nuclear pore distribution in nucleoporin mutant yeast cells. J Cell Biol 136, 747–759.

Broers JL, Peeters EA, Kuijpers HJ, Endert J, Bouten CV, Oomens CW, Baaijens FP, Ramaekers FC (2004). Decreased mechanical stiffness in LMNA-/- cells is caused by defective nucleo-cytoskeletal integrity: implications for the development of laminopathies. Hum Mol Genet 13, 2567–2580.

Chancellor TJ, Lee J, Thodeti CK, Lele T (2010). Actomyosin tension exerted on the nucleus through nesprin-1 connections influences endothelial cell adhesion, migration, and cyclic strain-induced reorientation. Biophys J 99, 115–123.

Chang W, Worman HJ, Gundersen GG (2015). Accessorizing and anchoring the LINC complex for multifunctionality. J Cell Biol 208, 11–22.

Chiaruttini N, Redondo-Morata L, Colom A, Humbert F, Lenz M, Scheuring S, Roux A (2015). Relaxation of loaded ESCRT-III spiral springs drives membrane deformation. Cell 163, 866–879.

Civril F, Deimling T, de Oliveira Mann CC, Ablasser A, Moldt M, Witte G, Hornung V, Hopfner KP (2013). Structural mechanism of cytosolic DNA sensing by cGAS. Nature 498, 332–337.

Dahl KN, Ribeiro AJ, Lammerding J (2008). Nuclear shape, mechanics, and mechanotransduction. Circ Res 102, 1307–1318.

D'Angelo MA, Anderson DJ, Richard E, Hetzer MW (2006). Nuclear pores form de novo from both sides of the nuclear envelope. Science 312, 440–443.

Davidson PM, Sliz J, Isermann P, Denais C, Lammerding J (2015). Design of a microfluidic device to quantify dynamic intra-nuclear deformation during cell migration through confining environments. Integr Biol (Camb) 7, 1534–1546.

Debnath J, Muthuswamy SK, Brugge JS (2003). Morphogenesis and oncogenesis of MCF-10A mammary epithelial acini grown in three-dimensional basement membrane cultures. Methods 30, 256–268.

Denais CM, Gilbert RM, Isermann P, McGregor AL, te Lindert M, Weigelin B, Davidson PM, Friedl P, Wolf K, Lammerding J (2016). Nuclear envelope rupture and repair during cancer cell migration. Science 352, 353–358.

Deviri D, Discher DE, Safran SA (2017). Rupture dynamics and chromatin herniation in deformed nuclei. Biophys J 113, 1060–1071.

Dultz E, Ellenberg J (2010). Live imaging of single nuclear pores reveals unique assembly kinetics and mechanism in interphase. J Cell Biol 191, 15–22.

Foisner R (2001). Inner nuclear membrane proteins and the nuclear lamina. J Cell Sci 114, 3791–3792.

Gonzalez-Rodriguez D, Maddugoda MP, Stefani C, Janel S, Lafont F, Cuvelier D, Lemichez E, Brochard-Wyart F (2012). Cellular dewetting: opening of macroapertures in endothelial cells. Phys Rev Lett 108, 218105.

Hatch EM, Fischer AH, Deerinck TJ, Hetzer MW (2013). Catastrophic nuclear envelope collapse in cancer cell micronuclei. Cell 154, 47–60.

Hatch EM, Hetzer MW (2016). Nuclear envelope rupture is induced by actin-based nucleus confinement. J Cell Biol 215, 27–36.

Irianto J, Xia Y, Pfeifer CR, Athirasala A, Ji J, Alvey C, Tewari M, Bennett RR, Harding SM, Liu AJ, *et al.* (2017). DNA damage follows repair factor depletion and portends genome variation in cancer cells after pore migration. Curr Biol 27, 210–223.

Isermann P, Lammerding J (2013). Nuclear mechanics and mechanotransduction in health and disease. Curr Biol 23, R1113–R1121.

Kirby TJ, Lammerding J (2018). Emerging views of the nucleus as a cellular mechanosensor. Nat Cell Biol 20, 373–381.

Lammerding J, Fong LG, Ji JY, Reue K, Stewart CL, Young SG, Lee RT (2006). Lamins A and C but not lamin B1 regulate nuclear mechanics. J Biol Chem 281, 25768–25780.

Lammerding J, Hsiao J, Schulze PC, Kozlov S, Stewart CL, Lee RT (2005). Abnormal nuclear shape and impaired mechanotransduction in emerin-deficient cells. J Cell Biol 170, 781–791.

Lammerding J, Lee RT (2009). Mechanical properties of interphase nuclei probed by cellular strain application. Methods Mol Biol 464, 13–26.

Lammerding J, Schulze PC, Takahashi T, Kozlov S, Sullivan T, Kamm RD, Stewart CL, Lee RT (2004). Lamin A/C deficiency causes defective nuclear mechanics and mechanotransduction. J Clin Invest 113, 370–378.

Lammerding J, Wolf K (2016). Nuclear envelope rupture: actin fibers are putting the squeeze on the nucleus. J Cell Biol 215, 5–8.

Lee YL, Burke B (2018). LINC complexes and nuclear positioning. Semin Cell Dev Biol 82, 67–76.

Lele TP, Dickinson RB, Gundersen GG (2018). Mechanical principles of nuclear shaping and positioning. J Cell Biol 217, 3330.

Livak KJ, Schmittgen TD (2001). Analysis of relative gene expression data using real-time quantitative PCR and the 2(-Delta Delta C(T)) Method. Methods 25, 402–408.

Luxton GW, Starr DA (2014). KASHing up with the nucleus: novel functional roles of KASH proteins at the cytoplasmic surface of the nucleus. Curr Opin Cell Biol 28, 69–75.

Maniotis AJ, Chen CS, Ingber DE (1997). Demonstration of mechanical connections between integrins, cytoskeletal filaments, and nucleoplasm that stabilize nuclear structure. Proc Natl Acad Sci USA 94, 849–854.

Neelam S, Chancellor TJ, Li Y, Nickerson JA, Roux KJ, Dickinson RB, Lele TP (2015). Direct force probe reveals the mechanics of nuclear homeostasis in the mammalian cell. Proc Natl Acad Sci USA 112, 5720–5725.

Neelam S, Hayes PR, Zhang Q, Dickinson RB, Lele TP (2016). Vertical uniformity of cells and nuclei in epithelial monolayers. Sci Rep 6, 19689.

Negorev D, Ishov AM, Maul GG (2001). Evidence for separate ND10-binding and homo-oligomerization domains of Sp100. J Cell Sci 114, 59–68.

Pajerowski JD, Dahl KN, Zhong FL, Sammak PJ, Discher DE (2007). Physical plasticity of the nucleus in stem cell differentiation. Proc Natl Acad Sci USA 104, 15619–15624.

Raab M, Gentili M, de Belly H, Thiam HR, Vargas P, Jimenez AJ, Lautenschlaeger F, Voituriez R, Lennon-Duménil AM, Manel N, Piel M (2016). ESCRT III repairs nuclear envelope ruptures during cell migration to limit DNA damage and cell death. Science 352, 359–362.

Schäpe J, Prausse S, Radmacher M, Stick R (2009). Influence of lamin A on the mechanical properties of amphibian oocyte nuclei measured by atomic force microscopy. Biophys J 96, 4319–4325.

Staykova M, Holmes DP, Read C, Stone HA (2011). Mechanics of surface area regulation in cells examined with confined lipid membranes. Proc Natl Acad Sci USA 108, 9084–9088.

Stephens AD, Banigan EJ, Adam SA, Goldman RD, Marko JF (2017). Chromatin and lamin A determine two different mechanical response regimes of the cell nucleus. Mol Biol Cell 28, 1984–1996.

Swift J, Ivanovska IL, Buxboim A, Harada T, Dingal PC, Pinter J, Pajerowski JD, Spinler KR, Shin JW, Tewari M, *et al.* (2013). Nuclear lamin-A scales with tissue stiffness and enhances matrix-directed differentiation. Science 341, 1240104.

Tajik A, Zhang Y, Wei F, Sun J, Jia Q, Zhou W, Singh R, Khanna N, Belmont AS, Wang N (2016). Transcription upregulation via force-induced direct stretching of chromatin. Nat Mater 15, 1287–1296.

Torbati M, Lele TP, Agrawal A (2016). Ultradonut topology of the nuclear envelope. Proc Natl Acad Sci USA 113, 11094–11099.

Uhler C, Shivashankar GV (2017). Regulation of genome organization and gene expression by nuclear mechanotransduction. Nat Rev Mol Cell Biol 18, 717–727.

Wang N, Tytell JD, Ingber DE (2009). Mechanotransduction at a distance: mechanically coupling the extracellular matrix with the nucleus. Nat Rev Mol Cell Biol 10, 75–82.

Wolf K, Te Lindert M, Krause M, Alexander S, Te Riet J, Willis AL, Hoffman RM, Figdor CG, Weiss SJ, Friedl P (2013). Physical limits of cell migration: control by ECM space and nuclear deformation and tuning by proteolysis and traction force. J Cell Biol 201, 1069–1084.

Wu J, Corbett AH, Berland KM (2009). The intracellular mobility of nuclear import receptors and NLS cargoes. Biophys J 96, 3840–3849.

Wu J, Kent IA, Shekhar N, Chancellor TJ, Mendonca A, Dickinson RB, Lele TP (2014). Actomyosin pulls to advance the nucleus in a migrating tissue cell. Biophys J 106, 7–15.

Zhang Q, Tamashunas AC, Lele TP (2018). A direct force probe for measuring mechanical integration between the nucleus and the cytoskeleton. J Vis Exp 2018, e58038.

Annual Review of Biomedical Engineering

The Driving Force: Nuclear Mechanotransduction in Cellular Function, Fate, and Disease

Melanie Maurer and Jan Lammerding

Meinig School of Biomedical Engineering and Weill Institute for Cell and Molecular Biology, Cornell University, Ithaca, New York 14853, USA; email: mem529@cornell.edu, jan.lammerding@cornell.edu

Annu. Rev. Biomed. Eng. 2019. 21:443–68

The *Annual Review of Biomedical Engineering* is online at bioeng.annualreviews.org

https://doi.org/10.1146/annurev-bioeng-060418-052139

Keywords

mechanotransduction, nuclear mechanics, stem cells, LINC complex, lamin, laminopathies

Abstract

Cellular behavior is continuously affected by microenvironmental forces through the process of mechanotransduction, in which mechanical stimuli are rapidly converted to biochemical responses. Mounting evidence suggests that the nucleus itself is a mechanoresponsive element, reacting to cytoskeletal forces and mediating downstream biochemical responses. The nucleus responds through a host of mechanisms, including partial unfolding, conformational changes, and phosphorylation of nuclear envelope proteins; modulation of nuclear import/export; and altered chromatin organization, resulting in transcriptional changes. It is unclear which of these events present direct mechanotransduction processes and which are downstream of other mechanotransduction pathways. We critically review and discuss the current evidence for nuclear mechanotransduction, particularly in the context of stem cell fate, a largely unexplored topic, and in disease, where an improved understanding of nuclear mechanotransduction is beginning to open new treatment avenues. Finally, we discuss innovative technological developments that will allow outstanding questions in the rapidly growing field of nuclear mechanotransduction to be answered.

Contents

1. INTRODUCTION

Mechanotransduction refers to the process by which cells convert mechanical stimuli from their extracellular environment or cell-generated forces into biochemical signals to induce downstream cellular responses. Mechanical forces can propagate along the cytoskeleton and travel at speeds of up to 30 μm/s, an impressive rate that is 25 times faster than molecular motor transport and 12.5 times faster than passive diffusion of signaling molecules (1). This rapid conversion of physical to biochemical response enables the rapid adaptation of cells to their changing physical environment (2, 3). Mechanotransduction can play a critical role in cell and tissue differentiation, maintenance, and disease, for example, in the adaptation of bones and muscle to exercise or the alignment of endothelial cells to fluid shear (4).

Since the term mechanotransduction is often used more broadly to refer to any cellular responses to mechanical stimuli, including events downstream of the original transduction event, in this review we use the following definitions: Mechanotransmission refers to the transmission of mechanical forces through cellular components, such as along actin stress fibers or microtubules, but does not include the actual mechanotransduction process. Mechanosensing refers to the actual transduction process, which is typically limited to some specialized proteins and locations within the cell; many of these proteins, including specific focal adhesion proteins and stretch-sensitive ion

channels in the plasma membrane (5, 6), have been recognized in the last three decades, but others may remain to be identified. Mechanotransduction signaling describes the signaling pathways that are downstream of the initial mechanosensing event. Importantly, many of these pathways, such as mitogen-activated protein kinase (MAPK) signaling or YAP/TAZ translocation, can be activated by a variety of upstream signals, not only mechanical stimuli but also biochemical signals, such as growth factor binding to cell surface receptors (7–9).

Recently, a growing number of studies, including some on isolated nuclei, have implicated the nucleus itself as a mechanosensing element (10–12). Several models have been proposed to explain how mechanical forces acting on the nucleus could induce changes in nuclear envelope composition, chromatin organization, and gene expression, which then drive downstream cellular responses (13, 14), including in stem cell differentiation. At the same time, many of the reported findings linking mechanical factors and nuclear changes have been rather correlative (3, 14), and it often remains unclear whether the observed nuclear changes were upstream or downstream of other events, including established cytoplasmic mechanotransduction pathways.

In this review, we provide a summary of nuclear structure and describe how nuclear components contribute to nuclear mechanics, mechanotransmission, and mechanosensing. As many current efforts seek to understand how stem cells respond to their mechanical microenvironment to control differentiation and cell fate commitment, we discuss how nuclear mechanotransduction may be involved. Since defects in nuclear mechanics and mechanotransmission are linked to impaired mechanotransduction signaling and several human diseases, particularly those affecting skeletal and cardiac muscle (4), we discuss the current understanding of nuclear mechanotransduction in disease pathogenesis. Finally, we outline some of the recent technological advances in unraveling the mechanisms by which the nucleus acts in mechanotransduction and in deepening our understanding of the diseases caused by such mechanisms.

2. THE NUCLEUS AND NUCLEAR MECHANICS

2.1. Nuclear Structure and Organization

As the compartment containing the vast majority of the genome and the site of gene transcription, the nucleus arguably plays the most important role in guiding cellular fate, behavior, and adaptation. The nucleus contains DNA that is wrapped around histones, which are organized into higher-order structures, broadly categorized as either open, transcriptionally active euchromatin or condensed, inactive heterochromatin. The nuclear envelope consists of outer and inner nuclear membranes (ONM and INM, respectively) separated by the 30–50-nm-wide perinuclear space (PNS) (**Figure 1**). This double membrane serves as a physical barrier to protect the nuclear contents and to control exchange of large (>30-kDa) molecules between the cytoplasm and the nuclear interior through nuclear pore complexes (NPCs). NPCs regulate exchange across the nuclear envelope, directly connect to both the nucleoskeleton and the cytoskeleton, and interact with chromatin (15).

Below the INM exists the 10–30-nm-thick, fibrous meshwork of the nuclear lamina (16). The nuclear lamina is composed mostly of lamins, which are type V nuclear intermediate filament proteins nearly ubiquitously expressed in differentiated cell types. Mammalian cells express two types of lamins—A-type and B-type—as products of three genes. In somatic cells, the *LMNA* gene gives rise to two major A-type lamin isoforms, Lamin A and Lamin C, plus some less common isoforms, as the result of alternative splicing; the *LMNB1* and *LMNB2* genes encode Lamins B1 and B2, respectively. Lamins A and C are developmentally regulated and appear during cellular differentiation. In contrast, all cells express at least one B-type lamin, even though recent studies show that cells lacking both Lamin B1 and B2 are viable (17, 18). The various lamin isoforms

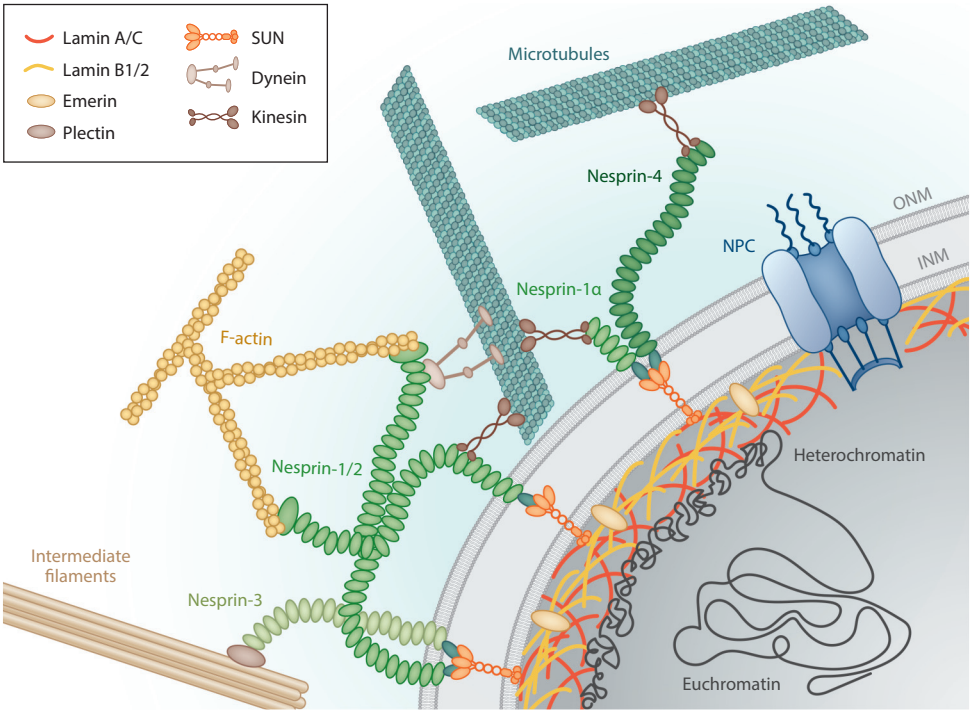

Figure 1

Constituents of the nucleus and nuclear envelope involved in mechanotransduction. The LINC (linker of the nucleoskeleton and cytoskeleton) complex—nesprins at the outer nuclear membrane (ONM) and SUN (Sad1p and UNC-84 homology)-domain proteins at the inner nuclear membrane (INM)—spans the nuclear envelope, interacting with cytoskeletal filaments and associated proteins and the nuclear lamina to enable force transmission between the cytoskeleton and nuclear interior. Nuclear lamins (A/C and B1/2) form independent yet interacting meshworks underneath the INM and are responsible for maintaining nuclear shape and stiffness. Both A- and B-type lamins interact with nuclear pore complexes (NPCs), chromatin, and various other binding partners at the nuclear envelope and the nuclear interior. NPCs enable molecular transport between the cytoplasm and nucleoplasm.

form independent yet interacting meshworks with a highly branched architecture at the nuclear periphery (19, 20). Surprisingly, recent cryo–electron tomography (cryo-ET) studies indicated that A- and B-type lamins form 3.5-nm-diameter tetrameric filaments, which are substantially thinner than the 10-nm-diameter cytoplasmic intermediate filaments (16). Notably, a fraction of lamins, particularly A-type, also exist in the nucleoplasm. Lamins have many binding partners, including chromatin, transcription factors, and LEM (LAP2, Emerin, and MAN1) family proteins, that play critical roles in gene regulation (21).

Since their discovery four decades ago (22), nuclear lamins have attracted increased interest as more evidence of their vital roles in cellular functions and disease has emerged. Within the nucleus, lamins regulate transcription, DNA replication and repair, and chromatin organization (23, 24). Heterochromatin exists at the nuclear periphery and interacts with the nuclear lamina in Lamin-associated domains (LADs) (25, 26) and via Lamin-associated protein 2 (LAP2) and its binding partner, barrier to autointegration factor (BAF) (27, 28). These interactions may directly affect chromatin organization, nuclear mechanotransduction, and gene expression and may contribute to stem cell differentiation (see Sections 3 and 4). Furthermore, Lamin A is required to

retain Emerin at the INM (29, 30), which in turn modulates expression of mechanosensitive genes (31) and is required for the Nesprin-1-mediated nuclear envelope remodeling in response to mechanical force (10). Depletion of Lamin B1 results in an enlarged or loose Lamin A/C meshwork with blebs of the nuclear envelope that contain Lamin A/C and euchromatin (19, 29, 32). Similarly, depletion of Lamin A/C causes loosening of the Lamin B1 meshwork and mislocalization of Emerin and other nuclear envelope proteins away from the nuclear envelope, highlighting the interconnections between various nuclear envelope components (19, 32).

At the nuclear envelope, lamins are responsible for positioning and distribution of NPCs, with both A- and B-type lamins binding nucleoporin (Nup153). Lamins also modulate nuclear assembly and disassembly during cellular replication (24), as well as nuclear shape, stiffness, and structure by regulating cytoskeletal organization (32–34). Loss of Lamin A/C results in disturbed perinuclear actin, microtubule, and intermediate filament organization and changes in focal adhesions (35–39). On a larger scale, lamins play a critical role in migration through three-dimensional (3D) environments by governing the deformability of the large nucleus, which constitutes a rate-limiting factor in confined migration (reviewed in Reference 40).

2.2. Nucleo-Cytoskeletal Connections

The LINC (linker of the nucleoskeleton and cytoskeleton) complex connects the nuclear lamina to the cytoskeleton (41) and is critical in force transmission from the cytoskeleton to the nuclear interior, termed nucleo-cytoskeletal coupling (35). The LINC complex consists of SUN (Sad1p and UNC-84 homology)- and KASH (Klarsicht, ANC-1, and Syne homology)-domain proteins, named after their conserved C-terminal domains that interact across the luminal space. LINC complex proteins span the nuclear envelope (**Figure 1**) and are anchored at the nuclear envelope via lamins, NPCs, and interaction with chromatin (41). In mammalian somatic cells, Sun1 and Sun2 constitute the SUN-domain proteins; Nesprin-1, -2, -3, and -4, each with multiple isoforms, the KASH-domain proteins. Germ cells express additional LINC complex proteins. SUN-domain protein trimers in the INM interact with the lamina at the INM and KASH-domain proteins in the PNS (42). KASH-domain proteins in the ONM protrude into both the PNS and cytoplasm, where they bind the cytoskeleton. Nesprin family proteins include isoforms that can directly bind F-actin, interact with the microtubule motors kinesin and dynein and with each other, and bind the adaptor protein plectin to interact with intermediate filaments (43). The LINC complex plays crucial roles in mechanical processes such as nuclear movement, positioning, and shape, as well as chromatin positioning and gene expression (44, 45). Disruption of the interaction between nuclear lamins and LINC complex proteins, for example, through mutations in the *LMNA* gene responsible for various diseases (see Section 5), results in loss of nucleo-cytoskeletal coupling, perturbed cytoskeletal organization, loss of nuclear stiffness, and inability of the nucleus to properly respond to force (46).

In cells adhering on rigid two-dimensional (2D) surfaces, a perinuclear organization of dynamic apical actomyosin filaments (referred to as a perinuclear actin cap by some authors) spans the top of the nucleus and connects to the nuclear interior via the LINC complex (36). Anchored at focal adhesions at the cellular basal surface, these perinuclear actin filaments apply compressive forces to the apical surface of the nucleus (47). Together with lateral forces transmitted to the nucleus from other cytoskeletal structures, such as microtubules, these forces strongly influence nuclear shape (48, 49). This concept is discussed further in the context of mechanotransduction in Section 3.

2.3. Nuclear Mechanics

Together, the highly interconnected nuclear constituents described above mediate the transmission of mechanical forces from the cytoskeleton to the nucleus, while providing structural support

to the nucleus and defining its mechanical properties (46). The nucleus exhibits elasticity and compressibility that enable the nucleus to act as a mechanical shock absorber (50). Both the nuclear lamina and chromatin contribute to nuclear mechanical response to strain (51, 52). Nuclear lamina stretch dominates at nuclear strains above 30%, while the mechanical properties of chromatin, which exhibits viscoelastic properties, govern nuclear deformation at lower strains (51). Physical cross-links between chromatin and INM proteins such as SUN-domain proteins can provide further mechanical stability to the nucleus (53). Prolonged mechanical stress can cause irreversible deformation and reorganization of chromatin, which may correspond to altered transcriptional or differentiation states (54). Lamin A/C levels correlate with nuclear stiffness and ability to withstand force: Increased levels result in stiffer and more viscous nuclei (11, 55), whereas decreased levels correspond to softer, more deformable nuclei with increased fragility (33, 55–57). Lamin phosphorylation results in increased solubility of lamins, decreased polymerization of the lamina, increased lamin turnover, and reduction of cellular tension and nuclear stiffness (11, 58).

3. THE ROLE OF THE NUCLEUS IN MECHANOTRANSDUCTION

Many non-mutually-exclusive mechanisms of nuclear mechanotransduction have been proposed to date. In this section, we briefly discuss the major proposed mechanisms and the evidence supporting them (**Figure 2**); we refer readers to excellent recent reviews (13, 14) for more details and additional proposed mechanisms. Our discussion focuses on general mechanisms of nuclear mechanotransduction; it is important to recognize that different cell types may respond differently to mechanical stimuli owing to differences in both structural organization (e.g., when comparing epithelial cells, mesenchymal fibroblasts, leukocytes, and muscle cells) and cell-type-specific signaling pathways downstream of the mechanosensing event.

3.1. Nuclear Membrane and Pore Stretching

During nuclear membrane stretch, NPCs take on a dilated, more open conformation (59, 60). Although NPCs make up less than 10% of the nuclear surface area at rest (61), the mechanically induced increase in NPC diameter accounts for one-sixth of the total increase in nuclear membrane surface area in HeLa cells during nuclear swelling (59). Force application to the nucleus, such as during cell spreading on a 2D substrate or by indentation with an atomic force microscopy tip, triggers partial opening of nuclear pores, promoting active nuclear import of YAP (60). Osmotic swelling, however, does not trigger YAP import (60), suggesting that some elements, such as Nesprin-1 (8) or other LINC complex constituents, are required for the opening of nuclear pores and the mechanosensing process.

Flux of calcium in response to force application or nuclear stretching may constitute another nuclear mechanosensing mechanism. NPCs and calcium channels on the nuclear envelope, including L-type, $InsP_3$, cyclic ADP ribose-modulate, and possibly others, regulate the influx and efflux of calcium from the nucleus (62–64). Cell spreading and nuclear stretching increase nuclear calcium through stretch-activated calcium channels on the nuclear membrane, which enhances transcription factor (CREB) expression and regulates gene transcription, protein import, apoptosis (63, 64), and downstream mechanosignaling (65).

In addition to the opening of NPCs and channels, nuclear envelope stretch loosens packing of the nuclear membrane phospholipid bilayers, allowing for the insertion of hydrophobic protein residues into the bilayer (65). Osmotic swelling in response to tissue damage triggers nuclear translocation of cytosolic phospholipase A_2 ($cPLA_2$) and 5-lipoxygenase (5-LOX) and incorporation of these proteins into the INM, where their activity triggers downstream inflammatory

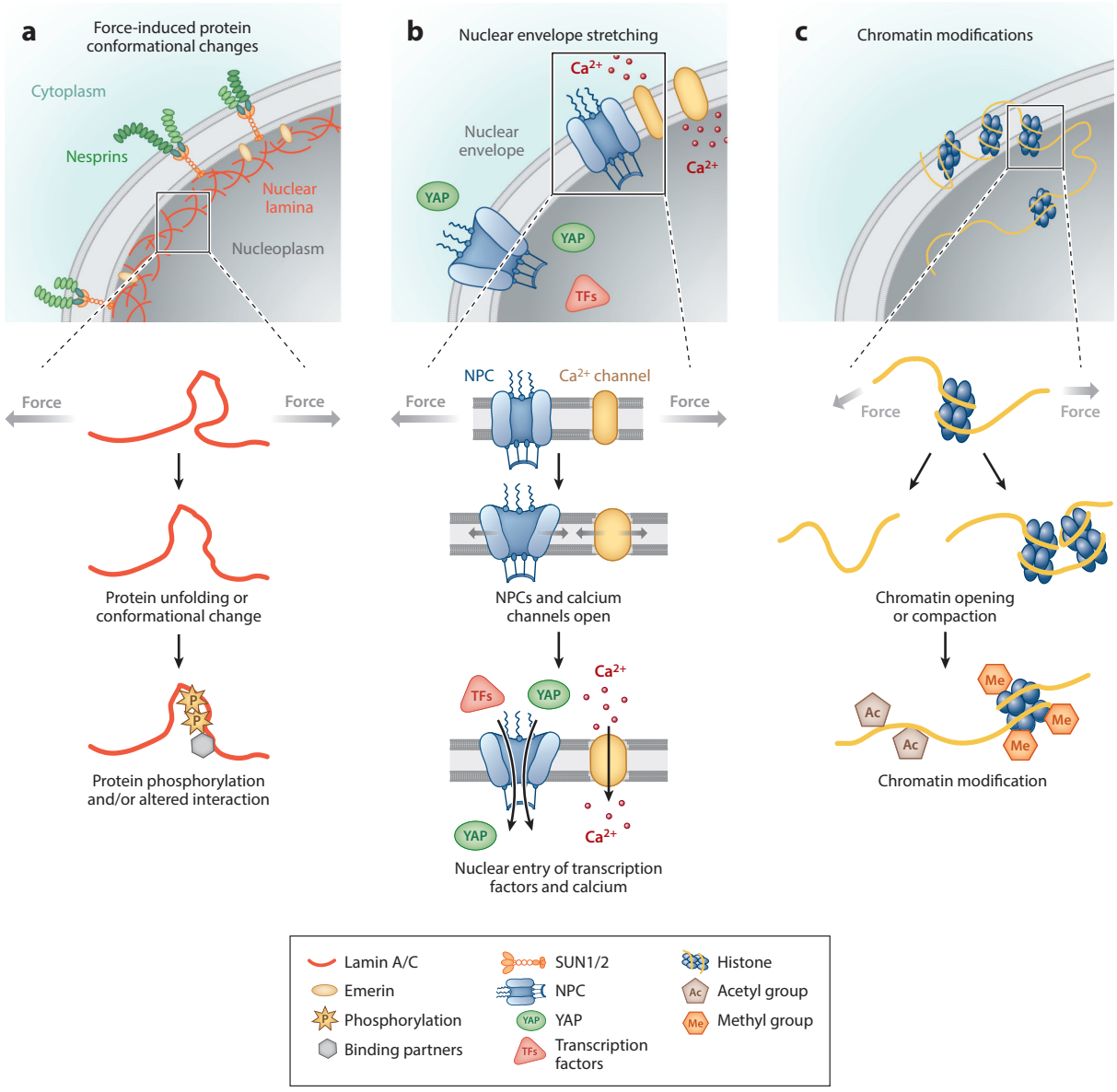

Figure 2

Proposed mechanisms of nuclear mechanotransduction. (*a*) Force application to the nucleus can results in conformational changes of nuclear envelope proteins, such as partial unfolding of lamins (11, 71), and phosphorylation of nuclear proteins, including lamins, SUN-domain proteins, and Emerin (10, 11, 58). (*b*) Nuclear membrane stretch in response to force opens nuclear pore complexes (NPCs) (59, 60) and calcium channels (65, 66) on the cytoplasmic side, thus increasing molecular influx into the nucleoplasm. The increased import of transcription factors (TFs) into the nucleoplasm can alter gene expression (60). (*c*) Mechanical forces acting on the nucleus can induce chromatin stretching, opening, and compaction, including DNA and histone modifications, that alter accessibility to transcription factors and lead to changes in gene expression (72–77, 82).

signaling cascades (65). Mechanosensitive incorporation of $cPLA_2$ and 5-LOX is regulated by increased calcium levels in the cell, which aids residue insertion into the membrane (65, 66), and by nuclear lamina rigidity, as a stiff nuclear lamina may not as readily allow stretching of the INM and therefore reduces protein incorporation into the INM (52, 65).

3.2. Protein Phosphorylation and Conformation Change in Response to Mechanical Force

Phosphorylation states serve as common mechano-switches in mechanical response, such as cytoskeletal stretch-dependent phosphorylation of Cas (67, 68) for contraction or phosphorylation of Paxillin and Vinculin during tension-mediated focal adhesion maturation (69). In the nucleus, Lamin A/C and Emerin phosphorylation modulate nuclear stiffness and nucleo-cytoskeletal coupling in response to mechanical stimulation (10, 11, 58). Lamin A/C phosphorylation increases in cells with low cytoskeletal tension, that is, when cells are grown on soft substrates (11, 58), increasing Lamin A/C mobility and turnover (58, 70). Conversely, when forces are applied to the nucleus via nesprins, Src-mediated Emerin phosphorylation recruits Lamin A/C to the nuclear periphery and promotes Sun2–Lamin A/C interactions (10). The precise mechanism by which mechanical forces can modulate phosphorylation of nuclear envelope proteins remains unclear, including whether this process is regulated by altering kinase activities or accessibility of the kinase substrate amino acids. Regardless, the observed mechanically induced phosphorylation implicates a structural role for phosphorylation in mechanotransduction through control of nuclear stiffening and nucleo-cytoskeletal coupling (10, 11, 58), which can also affect downstream transcription by downregulating some mechanoresponsive genes (*VCL* and *SRF*) and reducing YAP/TAZ translocation into the nucleus (10).

Alongside phosphorylation, protein conformation plays a role in mechanical response at the nuclear envelope. Partial unfolding of the Lamin A C-terminal immunoglobulin (Ig)-like fold in response to mechanical forces may expose normally hidden residues, such as Cys^{522} (11, 71). This conformational change could alter interaction with binding partners, expose cryptic signaling sites, or destabilize the protein. Unfolding may expose some amino acid residues to kinases, thus allowing for altered phosphorylation and modulating downstream signaling.

3.3. Chromatin Stretching, Organization, and Modification

Mechanical microenvironmental cues, such as architecture and mechanical loading (e.g., tension and compression), alter chromatin modifications and condensation to control gene expression (72–77). Dynamic mechanical loading can cause rapid short-lived, prolonged, and even irreversible changes in chromatin condensation, depending on the intensity and duration of the mechanical load (75–77). Highly transcriptionally active chromosomes preferentially orient along the mechanical axis of the nucleus on anisotropic micropatterned materials (73, 78, 79), demonstrating that chromatin organization is responsive to extracellular and cytoskeletal mechanical cues. Such changes in chromatin organization likely affect the transcriptional profile of the cells. Although these phenomena are widely observed, the specific mechanisms guiding mechanoresponsive gene expression are not well characterized. In particular, it remains unclear whether these changes are direct responses to forces acting on the nucleus or are downstream of other mechanotransduction events.

Importantly, the observed changes in chromatin organization, condensation, and modification are dependent on the actin cytoskeleton and LINC complex (75–77, 80). Perinuclear actin filaments bind to the LINC complex on the apical surface of the nucleus and cause

accumulation of Lamin A/C and hyperacetylated, transcriptionally active euchromatin at the INM, demonstrating that the perinuclear actin filaments interact with euchromatin via nucleocytoskeletal coupling (81). Furthermore, cytoskeletal contraction triggers mechanosensitive ATP release and calcium signaling to mediate nuclear import and activation of the histone–lysine *N*-methyltransferase EZH2 and histone deacetylase (HDAC) (73, 75–77), which stimulates gene silencing by altering methylation (74) and gene transcription by increasing histone acetylation (72, 73). Prolonged force application drives changes in methylation states for gene regulatory control by decoupling heterochromatin from the nuclear lamina, and driving chromatin compaction, and a switch from H3K9me3 to H3K27me3to attenuate transcription and silence promotors (74).

Previous research suggested that force-dependent transcriptional regulation depends upon lamin–chromatin interactions (32), but until recently, studies have struggled to show a direct effect of mechanical force on chromatin to control transcription. Wang and colleagues (82) used 3D magnetic twisting cytometry to apply extracellular stretching with RGD-coated magnetic beads, which demonstrated the direct stretching of a reporter transgene flanked by two green fluorescent protein–labeled loci and rapid, stretch-dependent transcription of the reporter gene. This study suggests that force is transmitted through integrins, the actin cytoskeleton, the LINC complex, and then lamin–chromatin interactions, which stretch chromatin and result in upregulation of transcription (82). Disruption of any one of these components weakens the mechanically induced response (82). Nonetheless, studies using endogenous genes will be required to confirm these findings in a general context, and it remains unclear how chromatin stretching results in activation of specific mechanosensitive genes. Euchromatin endures greater deformation under strain than heterochromatin, which would induce larger conformational changes (77), and may promote stretch-dependent transcription.

3.4. Nuclear and Perinuclear Actin

Recently, nuclear and perinuclear actin assemblies have emerged as key players in nuclear mechanotransmission and mechanosignaling. Nuclear actin polymerization regulates nuclear structure and gene expression (28, 83–86). The LINC complex mediates nuclear actin polymerization in response to cell spreading to form a nuclear scaffold (1, 87), which is accelerated by Emerin binding to the actin pointed end (28, 83). Both Lamin A/C and Emerin bind nuclear actin, thereby increasing nuclear strength (28, 83). Furthermore, nuclear actin acts as a transcriptional cofactor for polymerases I, II, and III (84). Nuclear actin polymerization can regulate transcription factor activity via increased import and export, primarily through myocardin-related transcription factor A (MRTF-A) and serum response factor (SRF), which demonstrates the downstream effects of force-driven nuclear actin dynamics (85, 86). Highlighting the interplay between nuclear envelope proteins, actin, and MRTF-A/SRF, loss of Lamin A/C and Emerin disturbs nuclear and cytoskeletal actin dynamics and impairs MRTF-A/SRF signaling (88).

Applied force can induce perinuclear actin filament assembly within minutes (77, 89), in a process that requires Lamin A/C, Emerin, and the LINC complex (35–37, 47). The presence of perinuclear actin is key in mechanotransmission of forces to the nucleus via the LINC complex, but the initial polymerization reaction likely occurs downstream of Rho GTPase (77) and calcium mechanosignaling (89). Thus, perinuclear actin plays a crucial role in mechanotransmission to the nucleus, a requirement for nuclear mechanotransduction. At the same time, perinuclear—and nuclear—actin polymerization is downstream of other mechanoresponsive signaling pathways and can further modulate mechanotransduction signaling by interaction with MRTF-A and SRF. As a whole, this mechanosensitive mechanistic web is thought to work to guide cellular functions, such

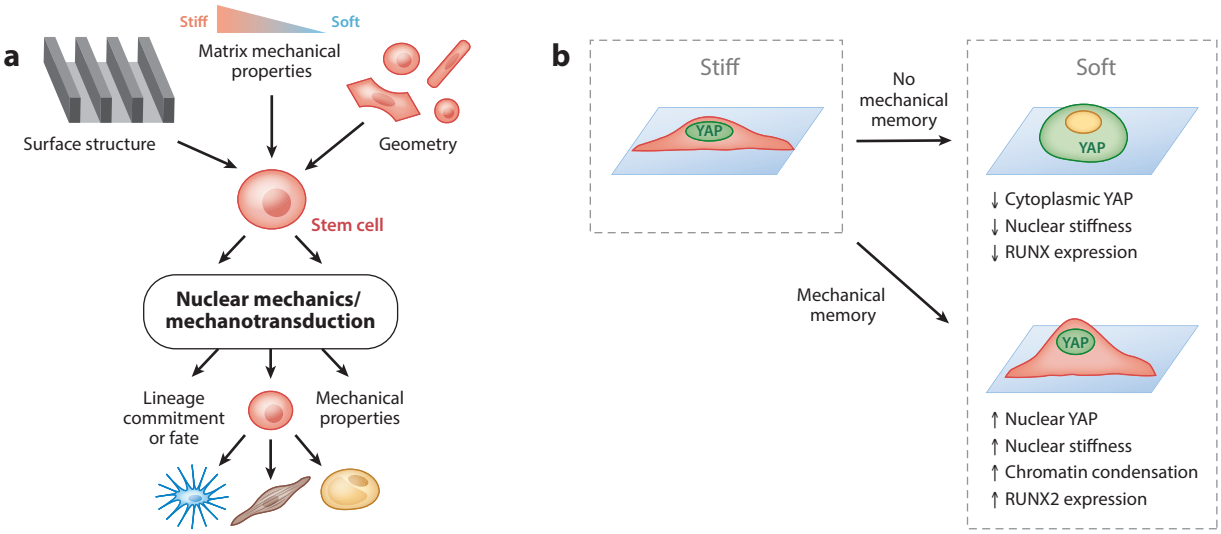

Figure 3

Nuclear mechanics guide stem cell fate and mechanical memory. (*a*) Stem cells may undergo mechanically induced differentiation in response to matrix mechanical properties, surface structure, and geometry. Nuclear mechanotransduction in response to matrix sensing alters the transcriptional program to ultimately guide downstream lineage commitment and cellular mechanical properties. (*b*) Substrate stiffness may enable stem cells to exhibit mechanical memory, in which a stiff phenotype is remembered upon transfer to culture on a soft substrate, via nuclear YAP retention and chromatin condensation. Mechanical memory can include increases in nuclear levels of YAP, nuclear stiffness, chromatin condensation, and expression of Runt-related transcription factor 2 (RUNX2).

as stem cell fate (discussed in Section 4), and disruption of this intricate network can cause a host of human diseases (see Section 5).

4. NUCLEAR MECHANICS GUIDE STEM CELL FATE

In addition to soluble factors, the stem cell microenvironment provides mechanical stimulation to guide lineage commitment and differentiation. Seminal research by Engler et al. (90) demonstrated that mesenchymal stem cell (MSC) fate is guided by extracellular matrix (ECM) elasticity. Motivated by these findings, researchers have focused on harnessing the mechanical environment for directing stem cell differentiation (i.e., mechanically induced differentiation), both with (90–92) and without (75, 93) the use of soluble factors. It is now recognized that matrix geometry, stiffness, adhesion, stress relaxation, micro- and nanopatterned surfaces, and applied cellular stretch can guide stem cell fate (8, 75, 91–93). Nonetheless, the specific mechanisms by which stem cell nuclei adapt to and differentiate within their mechanical environments remain incompletely understood. Thus, this section highlights nuclear mechanotransduction mechanisms guiding stem cell fate and describes how mechanotransduction can instill mechanical memory of differentiation states (**Figure 3**).

4.1. Mechanisms of Stem Cell Nuclear Mechanotransduction for Guiding Cell Fate

Compared with somatic cells, stem cells exhibit altered DNA and histone modifications (94), including highly condensed chromatin conformations, primarily at the nuclear periphery (95, 96), and altered expression of nuclear envelope proteins (54, 97, 98). Stem cells either completely lack

or have reduced levels of Lamin A/C, resulting in more deformable nuclei (54). Lamin A/C interacts with chromatin to control gene expression (99) and restricts heterochromatin protein dynamics (97, 98). However, lamins are not required for differentiation. Embryonic stem cells (ESCs) lacking Lamin A/C, B1, and B2 [i.e., triple knockout (TKO)] differentiate into all three germ layers in vitro (18); keratinocyte-specific lamin TKO does not interfere with gestation in vivo but causes fatal skin defects upon birth (100). Together, these results suggest that lamins may be required for proper tissue architecture, rather than differentiation or organogenesis (18, 100). Nonetheless, experiments with MSCs and pluripotent stem cells (PSCs) indicate an intriguing connection between Lamin A/C and mechanically induced differentiation. MSCs, which express Lamin A/C, can undergo mechanically induced differentiation (75, 90–93), whereas minimal progress has been made toward mechanically induced differentiation in PSCs, which express little to no Lamin A/C (101). One potential pathway is the mechanosensitive phosphorylation of Lamin A/C, which enables nucleoplasmic Lamin A/C–LAP2α complex formation and subsequent regulation of adult stem cell proliferation and differentiation pathways, such as through retinoblastoma protein, to control stemness (102, 103). Given the intimate role of Lamin A/C in mechanotransduction, its specific contributions in regulation of mechanically induced stem cell differentiation should be further explored.

In addition to lamins, LINC complex proteins play a role in mechanically induced differentiation of MSCs. Nesprin-1 promotes mechanoresponsive YAP nuclear import (8) and is required for force transmission to the nuclear lamina and chromatin. Conversely, cyclic tensile strain downregulates Sun2 in MSCs, causing a global drop in transcription (104), downregulation of tubulin expression (105), and disturbed perinuclear microtubule organization (105), causing impaired nucleo-cytoskeletal decoupling. Taken together, these results suggest both positive and negative roles of the LINC complex and nuclear envelope in mechanically induced differentiation by mediating cytoskeletal organization, nucleo-cytoskeletal coupling, and regulation of gene expression through transcription factor import and signaling regulation. However, future studies should aim to further elucidate the roles of LINC complex proteins in nuclear mechanotransduction and mechanically induced differentiation of stem cells.

Additionally, stem cell pluripotency genes may be subject to mechanosensitive activation and silencing via downstream transcriptional control and chromatin modifications (74, 106). Mechanical strain independently localizes Emerin to the ONM (74, 107), which reduces H3K9me3-silenced heterochromatin, promotes the polymerization of perinuclear actin, and reduces nuclear actin levels (74). The decrease in nuclear actin diminishes RNA polymerase II activity, resulting in attenuated transcription, accumulation of phosphorylation, and H3K27me3 modification of chromatin, which corresponds to a more silenced state (74). Inhibiting this mechanism reduces methylation-mediated silencing, lineage commitment, and morphogenesis (74). Thus, this mechanism could explain how mechanically induced differentiation without soluble factors may be achieved: through regulation of stemness or promotion of differentiation.

4.2. Mechanically Induced Differentiation and Mechanical Memory

Mechanically induced differentiation has introduced the intriguing concept that stem cells can exhibit so-called mechanical memory. Whereas mechanotransduction typically involves rapid responses to changes in the physical environment of cells, this mechanical memory may allow stem cells to retain information and results of past mechanical conditions, which influences their future behavior and phenotype (**Figure 3*b***). For example, culture of stem cells on stiff materials results in sustained nuclear YAP localization and osteogenic *RUNX2* expression, even when cells are transferred to a soft substrate, on which YAP is typically cytoplasmic and *RUNX2* is not expressed (108).

Initial nuclear YAP translocation is likely mediated by cytoskeletal mechanotransduction and nuclear membrane stretch to open NPCs (60) via nucleo-cytoskeletal coupling through Nesprin-1 (8, 107). Subsequent nuclear stiffening, triggered by phosphorylation of Emerin to facilitate recruitment of Lamin A/C to the nuclear envelope (8), may contribute to the memory effect. Additionally, condensed chromatin stabilized via actin polymerization can persist after mechanical loading to create mechanical memory (75). Both of these mechanisms trigger chromatin condensation and nuclear stiffening, which correspond to a more differentiated state (93).

As mechanotransduction and signaling typically result in rapid adaptation to the mechanical environment, the concept of sustained mechanical memory is somewhat paradoxical: How do the classical mechanosensing mechanisms achieve permanent changes that resist further adaptation when the mechanical conditions have changed? The answer may lie in the persistent changes associated with stem cell differentiation. Mechanically induced stem cell differentiation causes altered chromatin organization, chromatin modifications, and gene expression, including that of nuclear and cytoskeletal proteins, thereby affecting nuclear mechanics, mechanotransmission, and mechanotransduction. These mechanoresponsive changes may be permanent and cannot easily be overcome by subsequent changes in the physical microenvironment, such as stiff to soft substrates or cessation of loading. However, further research is needed to fully elucidate the molecular events underlying the mechanical memory of stem cells and to determine how to harness this knowledge for applications using stem cells.

5. NUCLEAR MECHANOTRANSDUCTION GONE WRONG: SPOTLIGHT ON LAMINOPATHIES

Collectively, the laminopathies refer to diseases arising from mutations in the *LMNA* and *LMNB* genes. More than 450 different *LMNA* mutations give rise to ∼14 different human diseases (see **http://www.umd.be/LMNA/**). Examples of human *LMNA* laminopathies include autosomal dominant Emery–Dreifuss muscular dystrophy (EDMD), dilated cardiomyopathy (DCM) with conduction defects, and Hutchinson–Gilford progeria syndrome. Many laminopathies primarily affect mechanically stressed tissues such as skeletal muscle, heart, and tendons. In contrast, only two human diseases have been associated with the *LMNB1* and *LMNB2* genes to date: adult-onset autosomal dominant leukodystrophy, resulting from duplication of the *LMNB1* gene (109), and acquired partial lipodostrophy, associated with mutations in the *LMNB1* gene (110). Most laminopathies are currently incurable, and several result in premature death. Intriguingly, mutations in genes encoding the LINC complex proteins (Emerin, Nesprin-1/2, Sun1/2) can cause several of the same or similar human diseases as *LMNA* mutations, including EDMD, DCM, and Charcot–Marie–Tooth syndrome (reviewed in Reference 41). Thus, these diseases are also referred to as nuclear envelopathies. With similar disease phenotypes observed in these nuclear envelopathies, altered nucleo-cytoskeletal coupling, nuclear mechanics, and disturbed mechanotransduction could be clear culprits in the disease pathology.

Classically, two cellular mechanisms by which laminopathies act in disease have been suggested: structural disruption and gene misregulation. The structural hypothesis proposes that mutant lamins cause nuclear fragility, leading to increased nuclear damage and cell death, particularly in mechanically stressed tissues. The gene regulation hypothesis suggests that lamin mutations play a tissue-specific role in gene expression by altering gene activation and silencing (99) or by inhibiting tissue-specific factor binding (111). Impaired stem cell differentiation caused by mutant lamins has been proposed as part of the gene regulation hypothesis. A third hypothesis, disrupted nuclear mechanotransduction, can bridge the mechanistic gap between the structural and gene regulation hypotheses, as disturbed gene regulation may, at least in part, be the product

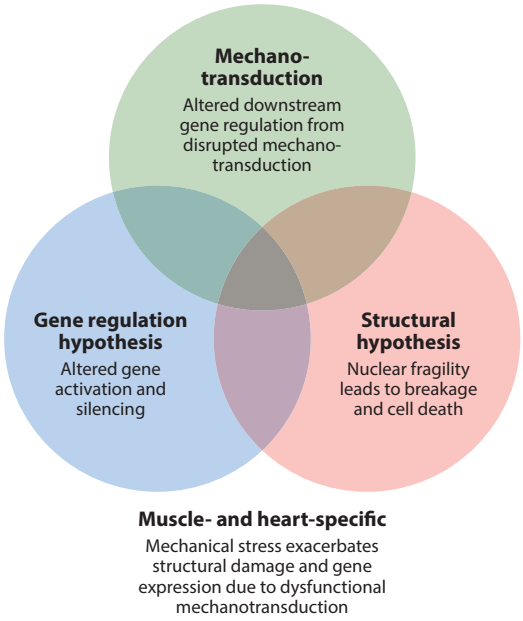

Figure 4

Defective mechanotransduction as a bridge between laminopathy hypotheses. Structural defects (increased nuclear fragility that leads to breakage and cell death) and gene misregulation (altered gene activation and silencing) are the two primary hypothesized mechanisms responsible for the muscle-specific defects in many laminopathies. A third hypothesis—defective nuclear mechanotransduction—synthesizes both the structural disruption and gene misregulation hypotheses, as it can explain how downstream gene misregulation might be a product of nuclear weakness due to disruption of mechanotransduction mechanisms in and on the nucleus.

of physical disruption of nuclear mechanotransmission and mechanosensing (**Figure 4**). In the following subsections, we discuss laminopathies in the context of disrupted nuclear mechanics and mechanotransduction, particularly in light of the mechanisms discussed in Section 3.

5.1. Disrupted Mechanotransduction as a Driver of Laminopathy Pathology

The physical consequences of laminopathies on the structure and function of the nuclear lamina have been known for nearly two decades (112–114). Mutant or mislocalized proteins can lead to disrupted interactions between lamins and their binding partners, thus disturbing the mechanical integrity of the lamina, connections to chromatin and LINC complex proteins, and transcriptional regulators. *LMNA* mutations associated with muscular defects frequently result in reduced nuclear stability (33, 115, 116). Furthermore, *LMNA* mutations increase susceptibility of Lamin A to phosphorylation (117), thereby increasing their solubility and promoting disassembly of the nuclear lamina. *LMNA* mutant nuclei are often subject to nuclear envelope blebbing and both spontaneous rupture and rupture due to mechanical stress (55, 56, 115). Nuclear instability and rupture yield reduced cellular viability (55), loss of cellular compartmentalization that can mislocalize both proteins and whole organelles (56, 118, 119), and DNA damage (116).

Changes in LINC expression or anchoring at the nuclear envelope due to *LMNA* mutations, overexpression of Sun1 (120), loss of Emerin (121), or loss or mislocalization of Nesprin-2G

(33, 122) disrupts mechanotransmission across the nuclear envelope. This impaired nucleo-cytoskeletal coupling (120–122) could explain disturbed nuclear positioning in skeletal muscle (123–125) and the loss of perinuclear actin filaments in *LMNA* mutant cells (36, 37, 47), which is associated with increased nuclear height, abnormal nuclear shape, and impaired YAP translocation into the nucleus (36, 47). Disruption of YAP translocation in response to cyclic stretch results in poor matrix adhesion and decreased cytoskeletal tension (126) that may be due to both loss of mechanically induced NPC opening (60) and Nesprin-1 disruption (8).

Loss of Lamin A/C results in NPC clustering (20, 127, 128), and mutations in the Ig fold of Lamin A/C result in defective binding to nucleoporin (129), which may inhibit the roles of NPCs in mechanosensitive gene regulation. Altered nuclear mechanics and nucleo-cytoskeletal coupling could further disrupt mechanosensitive NPC opening and nuclear import of transcription factors and downstream gene expression (60). Moreover, since nucleoporins interact with transcriptionally active euchromatin (130, 131), improper distribution of NPCs and nucleoporins resulting from *LMNA* mutations may perturb transcriptional regulation. Similarly, as lamin sequesters heterochromatin to the nuclear periphery, altered chromosome location due to *LMNA* mutations could dysregulate chromatin organization and gene expression. Several studies have demonstrated that relevant striated muscle genes are mislocalized to either the nuclear periphery or the center, depending on the mutation (132, 133). Such mislocalization could explain the altered tissue-specific gene expression observed in laminopathies (132–134), a concept that should be further explored using genome mapping technologies (see Section 6).

Furthermore, possibly as a downstream effect of disturbed nuclear or cytoplasmic mechanosensing, several critical signaling pathways regulating differentiation and proliferation are disrupted in *LMNA* mutant muscle. These include transforming growth factors β1 and 2 (135, 136), MyoD (137), MAPK (specifically extracellular signal–regulated kinases 1 and 2, JNK, and p38α) (138, 139), and WNT/β-catenin (138–140), which may compromise tissue homeostasis. Consequently, *LMNA* mutations can disrupt myogenic differentiation in skeletal muscle (123, 137, 141), although other studies found that Lamin A/C–deficient myoblasts differentiation into myotubes is normal (116, 142). Lamin A/C is expressed in both muscle stem cells (MuSCs) and differentiated myofibers. Mutant forms cause improper cell cycle exit, decreased MuSC fusion with myofibers, and increased apoptosis during differentiation (141), as well as slower and less efficient differentiation (137). As a possible explanation for increased muscle wasting, DNA-dependent protein kinase (DNA-PK), which was recently linked to aging-related muscle wasting (143, 144), is activated in response to DNA damage (116). This activation may drive muscle health decline in EDMD, possibly through apoptosis mediated by the activation of Caspase-3 (116).

5.2. Strategies to Remedy Cellular Pathology

Targeting disrupted signaling in *LMNA* laminopathies may open a window for the pharmaceutical treatment of laminopathies (145). WNT/β-catenin stimulation (140) and p38α MAPK inhibition (139, 146, 147) improve cellular pathology and disease outcomes, including improved cellular mechanical properties, cytoskeletal structure, cardiac contractility, and survival. Targeting impaired nuclear stability may present another therapeutic avenue. Pharmaceutical stabilization of microtubules, which reduces nuclear deformation, and depletion of the microtubule motor kinesin 1, involved in nuclear shuttling in skeletal muscle, prevented accrual of nuclear damage by nuclear envelope rupture and chromatin protrusions in Lamin A/C–deficient skeletal muscle cells in vitro (116). Although preliminary, these results demonstrate that reducing mechanical stress on the nucleus can positively influence laminopathic prognosis and represent a new treatment option that should be explored for laminopathies affecting skeletal muscle.

6. CURRENT TECHNOLOGIES FOR THE STUDY OF MECHANOTRANSDUCTION, NUCLEAR MECHANICS, AND RELATED DISEASES

Our knowledge of mechanotransduction and nuclear mechanics in stem cell biology and disease (laminopathies) is often the product of innovative technologies. From nuclear- to cellular- to tissue-level technologies, creative force application methods, imaging techniques, and model systems have defined the study of nuclear mechanotransduction (**Table 1**). In this section, we

Table 1 Prominent technologies for elucidating mechanotransduction mechanisms

Technique	Description	Reference(s)
Detection techniques		
Superresolution microscopy	Imaging techniques (i.e., SIM, dSTORM, cryo-ET) with protein-level resolution. Useful for examining nuclear organization, binding partners, and supramolecular structure.	16, 19, 20
BioID	Proteins are biotinylated when in proximity to an engineered fusion protein (such as Lamin A) to label and identify novel binding partners with mass spectrometry. Can be used to examine protein interactions in mechanically stressed or lamin-mutant nuclei.	20, 171
4D nucleome	Genome mapping techniques (i.e., 4C, 5C, Hi-C, and ChIA-PET), for observing spatial organization and condensation states of chromatin.	148
Genomic labeling	Fluorescence tagging of chromatin using gene editing for tracking mechanosensitive reorganization of (multiple) gene loci.	82, 152, 153
FRAP	A target protein is fluorescently tagged, a small area is photobleached, and time of recovery of fluorescence to the area is measured to understand the recovery dynamics, such as for chromatin histone organization or modifications.	154–157
FRET	Visual monitoring of the interaction between fluorescently tagged proteins, which creates a FRET signal. Diverse applications to mechanotransduction, such as monitoring force-dependent protein interactions, chromatin modification/condensation, and actin assembly or measuring tension forces.	77, 122, 158–160, 172
FLIM	Through fluorescence tagging of chromatin and examining fluorescence lifetime, which corresponds to viscosity due to degree of chromatin packing, can be used for high-throughput spatial tracking of chromatin condensation in the nucleoplasm.	160, 161
Mechanical manipulation techniques		
Isolated nuclei	Removal of the nucleus from a cell for the direct study of the nucleus and its constituents, eliminating any confounding effects from the cytoplasm and/or cytoskeleton. Force can be directly applied to the nucleus, such as for LINC complex force measurement or examination of nuclear changes.	122, 171
LINC complex disruption	Depletion or deletion of LINC complex proteins via gene editing. By examining any subsequent defects resulting from force application, the role of LINC complex proteins in mechanotransduction may be better understood.	35, 41, 82
Tissue-engineering techniques		
Engineered (muscle) tissues	Cells are suspended in an ECM solution, compact to form a tissue between two flexible pillars, and tissues contract to deflect the pillars. Useful for examining cell and tissue structures, tissue generated forces, and improving maturity of tissues.	163–170
Micropatterning, structured, and engineered substrates	Cells are cultured on micrometer- or nanometer-scale geometries/architectures. Examining the subsequent nuclear changes and cellular signaling, behavior, or phentoype can give an understanding of the role of the nucleus in matrix sensation, such as in stem cell differentiation.	72, 73

Abbreviations: ChIA-PET, chromatin-interaction analysis by paired-end tag sequencing; cryo-ET, cryo electron tomography; dSTORM, direct stochastic optical reconstruction microscopy; ECM, extracellular matrix; FLIM, fluorescence lifetime imaging microscopy; FRAP, fluorescence recovery after photobleaching; FRET, Förster resonance energy transfer; LINC, linker of the nucleoskeleton and cytoskeleton; SIM, structured illumination microscopy.

discuss current technological innovations, including superresolution imaging, fluorescence molecular reporters, and engineered tissue constructs for analyzing the role of the nucleus and the corresponding mechanisms in mechanotransduction and disease (laminopathies).

6.1. Molecular Probes for Nuclear Structure

Unraveling nuclear mechanotransduction has remained a challenge due to (*a*) the complex and interconnected nature of the nuclear constituents and (*b*) the microscopic scale required to mechanically probe the nuclear components. Thus, several techniques, such as superresolution microscopy, fluorescence reporters for nanoscale forces and deformation, and tools to probe nuclear structure and organization across the whole genome, stand at the forefront of technologies to overcome such obstacles. Superresolution imaging techniques, such as structured illumination microscopy (19), dSTORM (direct stochastic optical reconstruction microscopy) (20), and cryo-ET (cryo–electron tomography) (16), among others, have enabled the observation of the organization of the nuclear lamina and their binding partners at the protein level and have revealed nuclear supramolecular structures and unexpected details of lamin filament organization (16). To further probe protein–protein interactions at the nuclear envelope in living cells and animals, investigators have developed BioID, in which a protein of interest, such as Lamin A, is fused to a promiscuous version of BirA, an *Escherichia coli* biotin ligase. Proteins in close proximity (∼10 nm) to the protein of interest are biotinylated and can subsequently be identified by mass spectrometry (20, 148). Newer versions of BioID have been developed to reduce the interaction radius and improved control over the timing of the biotinylation (149). BioID evades the removal of proteins from their native environment or the disruption of native protein interactions, as is the case with common alternative methods of yeast two-hybrid and coimmunoprecipitation assays (148). To date, these techniques have been used primarily to interrogate native nuclear protein conformations and Lamin A binding partners (148), but they could easily be applied to examine other key protein players and interactions in mechanically stressed or lamin-mutant nuclei in order to better understand mechanotransduction.

Characterization of the spatial organization of chromatin over time, termed the 4D nucleome (150), has been a rapidly growing point of focus in cell biology. Genome interaction mapping techniques, evolved from the original 3C (chromosome conformation capture) methods to today's 4C, 5C, Hi-C, and ChIA-PET (chromatin-interaction analysis by paired-end tag sequencing), have created high-resolution interaction maps of chromatin (150) and are beginning to be suitable for single-cell analysis. These techniques are now being applied to laminopathies (151), where they can yield novel insights into how transcription may be regulated in response to mechanical force or how chromatin may be disorganized in laminopathies.

6.2. Fluorescence Imaging for Nuclear Mechanics and Mechanotransduction

Chromatin reorganization, dynamics, interactions, condensation, and modifications may be better understood through fluorescence imaging techniques. Fluorescence tagging of chromatin using gene editing has been a common method of tracking reorganization of specific gene loci (82, 152, 153). Such methods and the use of multiple colors may, for example, allow tracking of several mechanosensitive genes simultaneously in response to mechanical force to better understand mechanosensitive chromosome reorganization. FRAP (fluorescence recovery after photobleaching) experiments, using tagging of histones or chromatin modifications via fluorescently labeled specific antigen binding fragments (Fabs), can examine chromatin dynamics in live cells (154–157). These techniques may be particularly useful to understand how mechanical stimulation affects

chromatin dynamics, reorganization, and modification (156). As an additional approach, Förster resonance energy transfer (FRET)-based reporters can be used to monitor chromatin modification and condensation (158–160) in living cells. Recent fluorescence lifetime imaging microscopy experiments have enabled high-throughput spatial tracking of condensation of fluorescently labeled chromatin in the nuclear interior simply by using the viscosity of chromatin and bypassing any gene modification, such as overexpression, required by other techniques (160). Chromatin may be labeled either through fluorescently tagged histones (160) or the use of DNA-binding dyes (161). High chromatin condensation is associated with low viscosity and low fluorescence lifetime, while decondensation causes an increase in viscosity due to reduction in chromatin packing and therefore has a high fluorescence lifetime (161). Thus, epigenetic modifications and changes in nuclear chromatin localization can be spatially and temporally tracked, which is useful for observing changes in response to mechanical stresses, for understanding chromatin changes during stem cell differentiation, and for studying diseases involved with disrupted interactions with chromatin.

In addition to understanding chromatin dynamics, related imaging techniques can be useful for the study of other mechanotransduction mechanisms. FRET between fluorophores of a single type, known as homoFRET (162), has been used to visualize and quantitatively measure changes in F-actin/G-actin ratios upon force application, based on the homoFRET signal produced when actin molecules labeled with enhanced green fluorescent protein assemble into filaments (77). Furthermore, tension-based FRET molecular biosensors, in which the FRET signal inversely correlates with the force transmitted across the tension-sensor-containing molecule (122), enable one to probe mechanotransmission through various LINC complex proteins. This approach has already been successfully applied to measure forces across Nesprin-2G under different mechanical conditions (122). FRET biosensors could be further applied to examine the interactions of and force transmission across the cytoskeleton to other nuclear envelope proteins, reorganization or binding of the nuclear lamina to its many binding partners, or mechanically induced changes within the nucleus.

6.3. Engineered Muscle for Examining Tissue Mechanics in Laminopathies

Current methods for the in vitro study of cardiac and skeletal muscle, particularly in 2D culture, insufficiently recapitulate the native structure and organization of mature muscle cells in tissues. Recently developed engineered skeletal muscle and cardiac tissues more closely mimicking native tissue structure and maturity present an intriguing opportunity for the study of laminopathies and their underlying nuclear and tissue mechanics, and offer better platforms for testing pharmacological treatments compared with 2D culture systems. Consequently, engineered muscle constructs, ranging from the micrometer to the centimeter scale, enable (*a*) examining cell and tissue structures, (*b*) examining tissue-generated forces, and (*c*) improving the maturity of tissues. To form tissues, muscle or heart cells or progenitors, either alone or in direct coculture with fibroblasts or other cell types (163), are suspended in an ECM solution (**Figure 5*a***). Cells remodel and compact the ECM to form a tissue-like structure between two flexible pillars, which apply passive tension across the tissue that results in cytoskeletal and sarcomere alignment (**Figure 5*b***) (164, 165). The engineered muscle tissues further compact over time and begin to contract as the muscle cells mature. The deflection of the flexible pillars (**Figure 5*c***) can used to measure the tissue-generated forces (166). Optionally, mechanical and/or electrical stimulation can be applied to engineered tissues to further improve maturation (165, 167).

To date, engineered muscle has also been employed to study cardiac muscle maturation (165, 167, 168), examine cellular forces and anisotropy (164, 166), analyze generated contraction forces (166, 169, 170), and create disease models for examining cellular phenotype, such as Duchenne's

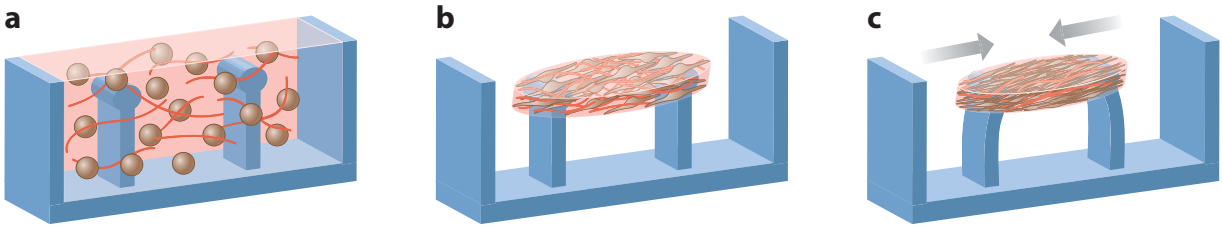

Figure 5

Creation of engineered muscle tissue constructs for the study of tissue morphology and generated forces. (*a*) Devices are loaded with a suspension of cells (*brown spheres*) and extracellular matrix (*red fibers*), and (*b*) cells reorganize and restructure the matrix to form a tissue around elastic pillars. (*c*) Tissues gradually compact and/or contract as cells elongate, thereby deflecting pillars. The force generated by the engineered tissue constructs can be calculated from the measured pillar deflection and the known material properties of the elastic pillars.

muscular dystrophy or EDMD (163). Engineered muscle tissues can be useful for assessing tissue structure or nuclear morphologies for various disease-causing mutations (163), assessing disruption of tissue-generated forces (170), and modeling correction of disease-causing mutations (170). However, tissue and sarcomere maturity still do not fully recapitulate native tissue, particularly for stem cell–derived muscle, motivating further research.

7. CONCLUSIONS AND PERSPECTIVES

Over the past few decades, efforts to obtain a clearer picture of nuclear mechanotransduction have shed light on how the cellular microenvironment and mechanical force guide cellular behavior and phenotype, stem cell differentiation, and human diseases such as laminopathies. Mechanotransmission through perinuclear cytoskeletal assemblies and the LINC complex to the lamina and chromatin governs nuclear mechanical response to force and alters organization of chromatin and gene expression as well as downstream expression of LINC proteins. Mechanosensitive phosphorylation and protein conformation modulate nuclear strength by altering the organization of the nuclear envelope. Nuclear membrane stretch guides downstream mechanosignaling by stretching of NPCs for increased nuclear import of transcription factors and by allowing for mechanosensitive incorporation of proteins into the INM. Finally, chromatin organization, compaction, stretching, and modification control downstream mechanosensitive gene expression, although the specific guiding mechanisms should be further explored. Together, these nuclear mechanotransduction mechanisms guide mechanically induced stem cell differentiation and can instill mechanical memory of differentiation states. Disruption of any component or mechanism, such as in *LMNA* laminopathies, may induce a chain reaction of disrupted nuclear nucleo-cytoskeletal coupling, altered nuclear mechanics, and defective mechanotransduction elements and downstream mechanosignaling to cause human disease. An improved understanding of defective mechanotransmission and mechanotransduction signaling that enables targeting affected pathways and components may ultimately allow these pathologies to be remedied. Future research should aim to gain a more systematic understanding of the cascade of nuclear mechanotransduction events. In particular, which nuclear mechanisms are a direct response to mechanical force (i.e., true mechanosensors), and which are a product of downstream signaling? Elucidation of the positive and negative feedback loops driving nuclear mechanotransduction would clarify how the many individual mechanisms relate and work together to guide downstream cellular phenotype and function and would shed new light on the nucleus as a mechanosensor.

DISCLOSURE STATEMENT

The authors are not aware of any affiliations, memberships, funding, or financial holdings that might be perceived as affecting the objectivity of this review.

ACKNOWLEDGMENTS

The authors apologize to all investigators whose work could not be cited due to space constraints. The writing of this review was supported by awards from the National Institutes of Health (R01 HL082792 and U54 CA210184), the US Department of Defense Breast Cancer Research Program (Breakthrough Award BC150580), and the National Science Foundation (CAREER Award CBET-1254846 and MCB-1715606) and by a National Science Foundation Graduate Research Fellowship to M.M. (2016229710). The content is solely the responsibility of the authors and does not necessarily represent the official views of the National Institutes of Health or the National Science Foundation.

LITERATURE CITED

1. Wang N, Tytell JD, Ingber DE. 2009. Mechanotransduction at a distance: mechanically coupling the extracellular matrix with the nucleus. *Nat. Rev. Mol. Cell Biol.* 10:75–82
2. Doyle AD, Yamada KM. 2016. Mechanosensing via cell–matrix adhesions in 3D microenvironments. *Exp. Cell Res.* 343:60–66
3. Cho S, Irianto J, Discher DE. 2017. Mechanosensing by the nucleus: from pathways to scaling relationships. *J. Cell Biol.* 216:305–15
4. Jaalouk DE, Lammerding J. 2009. Mechanotransduction gone awry. *Nat. Rev. Mol. Cell Biol.* 10:63–73
5. Wang N, Butler JP, Ingber DE. 1993. Mechanotransduction across the cell surface and through the cytoskleton. *Science* 260:1124–27
6. Martinac B. 2004. Mechanosensitive ion channels: molecules of mechanotransduction. *J. Cell Sci.* 117:2449–60
7. Dupont S, Morsut L, Aragona M, Enzo E, Giulitti S, et al. 2011. Role of YAP/TAZ in mechanotransduction. *Nature* 474:179–83
8. Driscoll TP, Cosgrove BD, Heo S-J, Shurden ZE, Mauck RL. 2015. Cytoskeletal to nuclear strain transfer regulates YAP signaling in mesenchymal stem cells. *Biophys. J.* 108:2783–93
9. González JM, Navarro-Puche A, Casar B, Crespo P, Andrés V. 2008. Fast regulation of AP-1 activity through interaction of lamin A/C, ERK1/2, and c-Fos at the nuclear envelope. *J. Cell Biol.* 183:653–66
10. Guilluy C, Osborne LD, Van Landeghem L, Sharek L, Superfine R, et al. 2014. Isolated nuclei adapt to force and reveal a mechanotransduction pathway in the nucleus. *Nat. Cell Biol.* 16:376–81
11. Swift J, Ivanovska IL, Buxboim A, Harada T, Dingal PCDP, et al. 2013. Nuclear Lamin-A scales with tissue stiffness and enhances matrix-directed differentiation. *Science* 341:1240104
12. Guilluy C, Burridge K. 2015. Nuclear mechanotransduction: forcing the nucleus to respond. *Nucleus* 6:19–22
13. Szczesny SE, Mauck RL. 2017. The nuclear option: evidence implicating the cell nucleus in mechanotransduction. *J. Biomech. Eng.* 139:021006
14. Kirby TJ, Lammerding J. 2018. Emerging views of the nucleus as a cellular mechanosensor. *Nat. Cell Biol.* 20:373–81
15. Soheilypour M, Peyro M, Jahed Z, Mofrad MRK. 2016. On the nuclear pore complex and its roles in nucleo-cytoskeletal coupling and mechanobiology. *Cell. Mol. Bioeng.* 9:217–26
16. Turgay Y, Eibauer M, Goldman AE, Shimi T, Khayat M, et al. 2017. The molecular architecture of lamins in somatic cells. *Nature* 543:261–64
17. Yang SH, Chang SY, Yin L, Tu Y, Hu Y, et al. 2011. An absence of both lamin B1 and lamin B2 in keratinocytes has no effect on cell proliferation or the development of skin and hair. *Hum. Mol. Genet.* 20:3537–44

18. Kim Y, Zheng X, Zheng Y. 2013. Proliferation and differentiation of mouse embryonic stem cells lacking all lamins. *Cell Res.* 23:1420–23
19. Shimi T, Kittisopikul M, Tran J, Goldman AE, Adam SA, et al. 2015. Structural organization of nuclear lamins A, C, B1, and B2 revealed by superresolution microscopy. *Mol. Biol. Cell* 26:4075–86
20. Xie W, Chojnowski A, Boudier T, Lim JSY, Ahmed S, et al. 2016. A-type lamins form distinct filamentous networks with differential nuclear pore complex associations. *Curr. Biol.* 26:2651–58
21. Dorner D, Gotzmann J, Foisner R. 2007. Nucleoplasmic lamins and their interaction partners, LAP2α, Rb, and BAF, in transcriptional regulation. *FEBS J.* 274:1362–73
22. Gerace L, Blum A, Blobel G. 1978. Immunocytochemical localization of the major polypeptides of the nuclear pore complex–lamina fraction: interphase and mitotic distribution. *J. Cell Biol.* 79:546–66
23. Gruenbaum Y, Foisner R. 2015. Lamins: nuclear intermediate filament proteins with fundamental functions in nuclear mechanics and genome regulation. *Annu. Rev. Biochem.* 84:131–64
24. de Leeuw R, Gruenbaum Y, Medalia O. 2018. Nuclear lamins: thin filaments with major functions. *Trends Cell Biol.* 28:34–45
25. Kourmouli N, Dialynas G, Petraki C, Pyrpasopoulou A, Singh PB, et al. 2001. Binding of heterochromatin protein 1 to the nuclear envelope is regulated by a soluble form of tubulin. *J. Biol. Chem.* 276:13007–14
26. Gurudatta BV, Shashidhara LS, Parnaik VK. 2010. Lamin C and chromatin organization in *Drosophila*. *J. Genet.* 89:37–49
27. Goldman RD, Gruenbaum Y, Moir RD, Shumaker DK, Spann TP. 2002. Nuclear lamins: building blocks of nuclear architecture. *Genes Dev.* 16:533–47
28. Holaska JM, Lee KK, Kowalski AK, Wilson KL. 2003. Transcriptional repressor germ cell-less (GCL) and barrier to autointegration factor (BAF) compete for binding to Emerin in vitro. *J. Biol. Chem.* 278:6969–75
29. Guo Y, Kim Y, Shimi T, Goldman RD, Zheng Y. 2014. Concentration-dependent lamin assembly and its roles in the localization of other nuclear proteins. *Mol. Biol. Cell* 25:1287–97
30. Vaughan A, Alvarez-Reyes M, Bridger JM, Broers JL, Ramaekers FC, et al. 2001. Both Emerin and Lamin C depend on Lamin A for localization at the nuclear envelope. *J. Cell Sci.* 114:2577–90
31. Lammerding J, Hsiao J, Schulze PC, Kozlov S, Stewart CL, Lee RT. 2005. Abnormal nuclear shape and impaired mechanotransduction in Emerin-deficient cells. *J. Cell Biol.* 170:781–91
32. Shimi T, Pfleghaar K, Kojima S, Pack C-G, Solovei I, et al. 2008. The A- and B-type nuclear lamin networks: microdomains involved in chromatin organization and transcription. *Genes Dev.* 22:3409–21
33. Lammerding J, Schulze PC, Takahashi T, Kozlov S, Sullivan T, et al. 2004. Lamin A/C deficiency causes defective nuclear mechanics and mechanotransduction. *J. Clin. Investig.* 113:370–78
34. Dechat T, Adam SA, Taimen P, Shimi T, Goldman RD. 2010. Nuclear lamins. *Cold Spring Harb. Perspect. Biol.* 2:1–23
35. Lombardi ML, Jaalouk DE, Shanahan CM, Burke B, Roux KJ, Lammerding J. 2011. The interaction between nesprins and SUN proteins at the nuclear envelope is critical for force transmission between the nucleus and cytoskeleton. *J. Biol. Chem.* 286:26743–53
36. Khatau SB, Hale CM, Stewart-Hutchinson PJ, Patel MS, Stewart CL, et al. 2009. A perinuclear actin cap regulates nuclear shape. *PNAS* 106:19017–22
37. Kim JK, Louhghalam A, Lee G, Schafer BW, Wirtz D, Kim DH. 2017. Nuclear Lamin A/C harnesses the perinuclear apical actin cables to protect nuclear morphology. *Nat. Commun.* 8:2123
38. Nikolova V, Leimena C, Mcmahon AC, Tan JC, Chandar S, et al. 2004. Defects in nuclear structure and function promote dilated cardiomyopathy in Lamin A/C–deficient mice. *J. Clin. Investig.* 113:357–69
39. Chandar S, Yeo LS, Leimena C, Tan JC, Xiao XH, et al. 2010. Effects of mechanical stress and carvedilol in Lamin A/C–deficient dilated cardiomyopathy. *Circ. Res.* 106:573–82
40. McGregor AL, Hsia CR, Lammerding J. 2016. Squish and squeeze—the nucleus as a physical barrier during migration in confined environments. *Curr. Opin. Cell Biol.* 40:32–40
41. Crisp M, Liu Q, Roux K, Rattner JB, Shanahan C, et al. 2006. Coupling of the nucleus and cytoplasm: role of the LINC complex. *J. Cell Biol.* 172:41–53

42. Tapley EC, Starr DA. 2013. Connecting the nucleus to the cytoskeleton by SUN-KASH bridges across the nuclear envelope. *Curr. Opin. Cell Biol.* 25:57–62
43. Horn HF. 2014. LINC complex proteins in development and disease. *Curr. Top. Dev. Biol.* 109:287–321
44. Rothballer A, Kutay U. 2013. The diverse functional LINCs of the nuclear envelope to the cytoskeleton and chromatin. *Chromosoma* 122:415–29
45. Banerjee I, Zhang J, Moore-Morris T, Pfeiffer E, Buchholz KS, et al. 2014. Targeted ablation of Nesprin 1 and Nesprin 2 from murine myocardium results in cardiomyopathy, altered nuclear morphology and inhibition of the biomechanical gene response. *PLOS Genet.* 10:e1004114
46. Isermann P, Lammerding J. 2013. Nuclear mechanics and mechanotransduction in health and disease. *Curr. Biol.* 23:R1113–21
47. Shiu J-Y, Aires L, Lin Z, Vogel V. 2018. Nanopillar force measurements reveal actin-cap-mediated YAP mechanotransduction. *Nat. Cell Biol.* 20:262–71
48. Lele TP, Dickinson RB, Gundersen GG. 2018. Mechanical principles of nuclear shaping and positioning. *J. Cell Biol.* 217:3330
49. Tariq Z, Zhang H, Chia-Liu A, Shen Y, Gete Y, et al. 2017. Lamin A and microtubules collaborate to maintain nuclear morphology. *Nucleus* 8:433–46
50. Dahl KN, Kahn SM, Wilson KL, Discher DE. 2004. The nuclear envelope lamina network has elasticity and a compressibility limit suggestive of a molecular shock absorber. *J. Cell Sci.* 117:4779–86
51. Stephens AD, Banigan EJ, Adam SA, Goldman RD, Marko JF. 2017. Chromatin and Lamin A determine two different mechanical response regimes of the cell nucleus. *Mol. Biol. Cell* 28:1984–96
52. Stephens AD, Banigan EJ, Marko JF. 2018. Separate roles for chromatin and lamins in nuclear mechanics. *Nucleus* 9:119–24
53. Schreiner SM, Koo PK, Zhao Y, Mochrie SGJ, King MC. 2015. The tethering of chromatin to the nuclear envelope supports nuclear mechanics. *Nat. Commun.* 6:7159
54. Pajerowski JD, Dahl KN, Zhong FL, Sammak PJ, Discher DE. 2007. Physical plasticity of the nucleus in stem cell differentiation. *PNAS* 104:15619–24
55. Lammerding J, Fong LG, Ji JY, Reue K, Stewart CL, et al. 2006. Lamins A and C but not lamin B1 regulate nuclear mechanics. *J. Biol. Chem.* 281:25768–80
56. De Vos WH, Houben F, Kamps M, Malhas A, Verheyen F, et al. 2011. Repetitive disruptions of the nuclear envelope invoke temporary loss of cellular compartmentalization in laminopathies. *Hum. Mol. Genet.* 20:4175–86
57. Broers JLV, Peeters EAG, Kuijpers HJH, Endert J, Bouten CVC, et al. 2004. Decreased mechanical stiffness in *LMNA*$^{-/-}$ cells is caused by defective nucleo-cytoskeletal integrity: implications for the development of laminopathies. *Hum. Mol. Genet.* 13:2567–80
58. Buxboim A, Swift J, Irianto J, Spinler KR, Dingal PCDP, et al. 2014. Matrix elasticity regulates Lamin-A,C phosphorylation and turnover with feedback to actomyosin. *Curr. Biol.* 24:1909–17
59. Enyedi B, Niethammer P. 2017. Nuclear membrane stretch and its role in mechanotransduction. *Nucleus* 8:156–61
60. Elosegui-Artola A, Andreu I, Beedle AEM, Lezamiz A, Uroz M, et al. 2017. Force triggers YAP nuclear entry by regulating transport across nuclear pores. *Cell* 171:1397–410
61. Mazzanti M, Bustamante JO, Oberleithner H. 2001. Electrical dimension of the nuclear envelope. *Physiol. Rev.* 81:1–19
62. Santella L, Carafoli E. 1997. Calcium signaling in the cell nucleus. *FASEB J.* 11:1091–109
63. Malviya AN, Rogue PJ. 1998. "Tell me where is calcium bred": clarifying the roles of nuclear calcium. *Cell* 92:17–23
64. Itano N, Okamoto S-I, Zhang D, Lipton SA, Ruoslahti E. 2003. Cell spreading controls endoplasmic and nuclear calcium: a physical gene regulation pathway from the cell surface to the nucleus. *PNAS* 100:5181–86
65. Enyedi B, Jelcic M, Niethammer P. 2016. The cell nucleus serves as a mechanotransducer of tissue damage–induced inflammation. *Cell* 165:1160–70
66. Cho W, Stahelin R. 2005. Membrane–protein interactions in cell signaling and membrane trafficking. *Annu. Rev. Biophys. Biomol. Struct.* 34:119–51

67. Tamada M, Sheetz MP, Sawada Y. 2004. Activation of a signaling cascade by cytoskeleton stretch. *Dev. Cell* 7:709–18
68. Sawada Y, Tamada M, Dubin-Thaler BJ, Cherniavskaya O, Sakai R, et al. 2006. Force sensing by mechanical extension of the Src family kinase substrate p130Cas. *Cell* 127:1015–26
69. Pasapera AM, Schneider IC, Rericha E, Schlaepfer DD, Waterman CM. 2010. Myosin II activity regulates vinculin recruitment to focal adhesions through FAK-mediated paxillin phosphorylation. *J. Cell Biol.* 188:877–90
70. Kochin V, Shimi T, Torvaldson E, Adam SA, Goldman A, et al. 2014. Interphase phosphorylation of Lamin A. *J. Cell Sci.* 127:2683–96
71. Ihalainen TO, Aires L, Herzog FA, Schwartlander R, Moeller J, Vogel V. 2015. Differential basal-to-apical accessibility of Lamin A/C epitopes in the nuclear lamina regulated by changes in cytoskeletal tension. *Nat. Mater.* 14:1252–61
72. Li Y, Chu JS, Kurpinski K, Li X, Bautista DM, et al. 2011. Biophysical regulation of histone acetylation in mesenchymal stem cells. *Biophys. J.* 100:1902–9
73. Jain N, Iyer KV, Kumar A, Shivashankar GV. 2013. Cell geometric constraints induce modular gene-expression patterns via redistribution of HDAC3 regulated by actomyosin contractility. *PNAS* 110:11349–54
74. Le HQ, Ghatak S, Yeung CYC, Tellkamp F, Günschmann C, et al. 2016. Mechanical regulation of transcription controls Polycomb-mediated gene silencing during lineage commitment. *Nat. Cell Biol.* 18:864–75
75. Heo S-J, Thorpe SD, Driscoll TP, Duncan RL, Lee DA, Mauck RL. 2015. Biophysical regulation of chromatin architecture instills a mechanical memory in mesenchymal stem cells. *Sci. Rep.* 5:16895
76. Heo SJ, Han WM, Szczesny SE, Cosgrove BD, Elliott DM, et al. 2016. Mechanically induced chromatin condensation requires cellular contractility in mesenchymal stem cells. *Biophys. J.* 111:864–74
77. Iyer KV, Pulford S, Mogilner A, Shivashankar GV. 2012. Mechanical activation of cells induces chromatin remodeling preceding MKL nuclear transport. *Biophys. J.* 103:1416–28
78. Maharana S, Iyer KV, Jain N, Nagarajan M, Wang Y, Shivashankar GV. 2016. Chromosome intermingling—the physical basis of chromosome organization in differentiated cells. *Nucleic Acids Res.* 44:5148–60
79. Wang Y, Nagarajan M, Uhler C, Shivashankar GV. 2017. Orientation and repositioning of chromosomes correlate with cell geometry–dependent gene expression. *Mol. Biol. Cell* 28:1997–2009
80. Kim DI, Birendra KC, Roux KJ. 2015. Making the LINC: SUN and KASH protein interactions. *Biol. Chem.* 396:295–310
81. Kim DH, Wirtz D. 2015. Cytoskeletal tension induces the polarized architecture of the nucleus. *Biomaterials* 48:161–72
82. Tajik A, Zhang Y, Wei F, Sun J, Jia Q, et al. 2016. Transcription upregulation via force-induced direct stretching of chromatin. *Nat. Mater.* 15:1287–96
83. Lattanzi G, Cenni V, Marmiroli S, Capanni C, Mattioli E, et al. 2003. Association of emerin with nuclear and cytoplasmic actin is regulated in differentiating myoblasts. *Biochem. Biophys. Res. Commun.* 303:764–70
84. de Lanerolle P, Serebryannyy L. 2011. Nuclear actin and myosins: life without filaments. *Nat. Cell Biol.* 13:1282–88
85. Olson EN, Nordheim A. 2010. Linking actin dynamics and gene transcription to drive cellular motile functions. *Nat. Rev. Mol. Cell Biol.* 11:353–65
86. Baarlink C, Wang H, Grosse R. 2013. Nuclear actin network assembly by formins regulates the SRF coactivator MAL. *Science* 340:864–67
87. Plessner M, Melak M, Chinchilla P, Baarlink C, Grosse R. 2015. Nuclear F-actin formation and reorganization upon cell spreading. *J. Biol. Chem.* 290:11209–16
88. Ho CY, Jaalouk DE, Vartiainen MK, Lammerding J. 2013. Lamin A/C and Emerin regulate MLK1/SRF activity by modulating actin dynamics. *Nature* 497:507–11
89. Shao X, Li Q, Mogilner A, Bershadsky AD, Shivashankar GV. 2015. Mechanical stimulation induces formin-dependent assembly of a perinuclear actin rim. *PNAS* 112:E2595–601

90. Engler AJ, Sen S, Sweeney HL, Discher DE. 2006. Matrix elasticity directs stem cell lineage specification. *Cell* 126:677–89
91. Lee J, Abdeen AA, Zhang D, Kilian KA. 2013. Directing stem cell fate on hydrogel substrates by controlling cell geometry, matrix mechanics and adhesion ligand composition. *Biomaterials* 34:8140–48
92. Chaudhuri O, Gu L, Klumpers D, Darnell M, Bencherif SA, et al. 2016. Hydrogels with tunable stress relaxation regulate stem cell fate and activity. *Nat. Mater.* 15:326–34
93. Heo SJ, Driscoll TP, Thorpe SD, Nerurkar NL, Baker BM, et al. 2016. Differentiation alters stem cell nuclear architecture, mechanics, and mechano-sensitivity. *eLife* 5:e18207
94. Li E. 2002. Chromatin modification and epigenetic reprogramming in mammalian development. *Nat. Rev. Genet.* 3:662–73
95. Labrador M, Corces VG. 2002. Setting the boundaries of chromatin domains and nuclear organization. *Cell* 111:151–54
96. West AG, Fraser P. 2005. Remote control of gene transcription. *Hum. Mol. Genet.* 14:R101–11
97. Constantinescu D, Gray HL, Sammak PJ, Schatten GP, Csoka AB. 2006. Lamin A/C expression is a marker of mouse and human embryonic stem cell differentiation. *Stem Cells* 24:177–85
98. Melcer S, Hezroni H, Rand E, Nissim-Rafinia M, Skoultchi A, et al. 2012. Histone modifications and lamin A regulate chromatin protein dynamics in early embryonic stem cell differentiation. *Nat. Commun.* 3:910
99. Peric-Hupkes D, Meuleman W, Pagie L, Bruggeman SWM, Solovei I, et al. 2010. Molecular maps of the reorganization of genome–nuclear lamina interactions during differentiation. *Mol. Cell* 38:603–13
100. Jung H-J, Tatar A, Tu Y, Nobumori C, Yang SH, et al. 2014. An absence of nuclear lamins in keratinocytes leads to ichthyosis, defective epidermal barrier function, and intrusion of nuclear membranes and endoplasmic reticulum into the nuclear chromatin. *Mol. Cell. Biol.* 34:4534–44
101. Murphy WL, McDevitt TC, Engler AJ. 2014. Materials as stem cell regulators. *Nat. Mater.* 13:547–57
102. Gotic I, Schmidt WM, Biadasiewicz K, Leschnik M, Spilka R, et al. 2010. Loss of LAP2α delays satellite cell differentiation and affects postnatal fiber–type determination. *Stem Cells* 28:480–88
103. Gesson K, Vidak S, Foisner R. 2014. Lamina-associated polypeptide (LAP)2α and nucleoplasmic lamins in adult stem cell regulation and disease. *Semin. Cell Dev. Biol.* 29:116–24
104. Gilbert HTJ, Mallikarjun V, Dobre O, Jackson MR, Pedley R, et al. 2018. Nuclear decoupling, through regulation of the LINC complex, is part of a rapid, protein-level cellular response to high-intensity mechanical loading. bioRxiv 317404. **https://doi.org/10.1101/317404**
105. Yang Y, Qu R, Fan T, Zhu X, Feng Y, et al. 2018. Cross-talk between microtubules and the linker of nucleoskeleton complex plays a critical role in the adipogenesis of human adipose-derived stem cells. *Stem Cell Res. Ther.* 9:125
106. Chowdhury F, Na S, Li D, Poh Y-C, Tanaka TS, et al. 2010. Material properties of the cell dictate stress-induced spreading and differentiation in embryonic stem cells. *Nat. Mater.* 9:82–88
107. Guilluy C, Osborne LD, Van Landeghem L, Sharek L, Superfine R, et al. 2014. Isolated nuclei adapt to force and reveal a mechanotransduction pathway in the nucleus. *Nat. Cell Biol.* 16:376–81
108. Yang C, Tibbitt MW, Basta L, Anseth KS. 2014. Mechanical memory and dosing influence stem cell fate. *Nat. Mater.* 13:645–52
109. Padiath QS, Saigoh K, Schiffmann R, Asahara H, Yamada T, et al. 2006. Lamin B1 duplications cause autosomal dominant leukodystrophy. *Nat. Genet.* 38:1114–23
110. Hegele RA, Cao H, Liu DM, Costain GA, Charlton-Menys V, et al. 2006. Sequencing of the reannotated *LMNB2* gene reveals novel mutations in patients with acquired partial lipodystrophy. *Am. J. Hum. Genet.* 79:383–89
111. Simon DN, Wilson KL. 2013. Partners and post-translational modifications of nuclear lamins. *Chromosoma* 122:13–31
112. Vigouroux C, Auclair M, Dubosclard E, Pouchelet M, Capeau J, et al. 2001. Nuclear envelope disorganization in fibroblasts from lipodystrophic patients with heterozygous R482Q/W mutations in the lamin A/C gene. *J. Cell Sci.* 114:4459–68
113. Novelli G, Muchir A, Sangiuolo F, Helbling-Leclerc A, D'Apice MR, et al. 2002. Mandibuloacral dysplasia is caused by a mutation in *LMNA*-encoding lamin A/C. *Am. J. Hum. Genet.* 71:426–31

114. Muchir A, Medioni J, Laluc M, Massart C, Arimura T, et al. 2004. Nuclear envelope alterations in fibroblasts from patients with muscular dystrophy, cardiomyopathy, and partial lipodystrophy carrying lamin A/C gene mutations. *Muscle Nerve* 30:444–50
115. Zwerger M, Jaalouk DE, Lombardi ML, Isermann P, Mauermann M, et al. 2013. Myopathic lamin mutations impair nuclear stability in cells and tissue and disrupt nucleo-cytoskeletal coupling. *Hum. Mol. Genet.* 22:2335–49
116. Earle AJ, Kirby TJ, Fedorchak G, Isermann P, Patel J, et al. 2018. Mutant lamins cause mechanically-induced nuclear envelope rupture, DNA damage, and DNA-PK activation in muscle. bioRxiv 364778. **https://doi.org/10.1101/364778**
117. Cenni V, Sabatelli P, Mattioli E, Marmiroli S, Capanni C, et al. 2005. Lamin A N-terminal phosphorylation is associated with myoblast activation: impairment in Emery–Dreifuss muscular dystrophy. *J. Med. Genet.* 42:214–20
118. Fidziańska A, Bilińska ZT, Tesson F, Wagner T, Walski M, et al. 2008. Obliteration of cardiomyocyte nuclear architecture in a patient with *LMNA* gene mutation. *J. Neurol. Sci.* 271:91–96
119. Gupta P, Bilinska ZT, Sylvius N, Boudreau E, Veinot JP, et al. 2010. Genetic and ultrastructural studies in dilated cardiomyopathy patients: a large deletion in the Lamin A/C gene is associated with cardiomyocyte nuclear envelope disruption. *Basic Res. Cardiol.* 105:365–77
120. Chen C-Y, Chi Y-H, Mutalif RA, Starost MF, Myers TG, et al. 2012. Accumulation of the inner nuclear envelope protein Sun1 is pathogenic in progeric and dystrophic laminopathies. *Cell* 149:565–77
121. Hale CM, Shrestha AL, Khatau SB, Stewart-Hutchinson PJ, Hernandez L, et al. 2008. Dysfunctional connections between the nucleus and the actin and microtubule networks in laminopathic models. *Biophys. J.* 95:5462–75
122. Arsenovic PT, Ramachandran I, Bathula K, Zhu R, Narang JD, et al. 2016. Nesprin-2G, a component of the nuclear LINC complex, is subject to myosin-dependent tension. *Biophys. J.* 110:34–43
123. Houben F, Willems CHMP, Declercq ILJ, Hochstenbach K, Kamps MA, et al. 2009. Disturbed nuclear orientation and cellular migration in A-type lamin deficient cells. *Biochim. Biophys. Acta* 1793:312–24
124. Folker ES, Ostlund C, Luxton GWG, Worman HJ, Gundersen GG. 2011. Lamin A variants that cause striated muscle disease are defective in anchoring transmembrane actin-associated nuclear lines for nuclear movement. *PNAS* 108:131–36
125. Mattioli E, Columbaro M, Capanni C, Maraldi NM, Cenni V, et al. 2011. Prelamin A–mediated recruitment of SUN1 to the nuclear envelope directs nuclear positioning in human muscle. *Cell Death Differ*. 18:1305–15
126. Bertrand AT, Ziaei S, Ehret C, Duchemin H, Mamchaoui K, et al. 2014. Cellular microenvironments reveal defective mechanosensing responses and elevated YAP signaling in LMNA-mutated muscle precursors. *J. Cell Sci.* 127:2873–84
127. Sullivan T, Escalante-Alcalde D, Bhatt H, Anver M, Bhat N, et al. 1999. Loss of A-type lamin expression compromises nuclear envelope integrity leading to muscular dystrophy. *J. Cell Biol.* 147:913–20
128. Verga L, Concardi M, Pilotto A, Bellini O, Pasotti M, et al. 2003. Loss of lamin A/C expression revealed by immuno-electron microscopy in dilated cardiomyopathy with atrioventricular block caused by *LMNA* gene defects. *Virchows Arch*. 443:664–71
129. Al-Haboubi T, Shumaker DK, Köser J, Wehnert M, Fahrenkrog B. 2011. Distinct association of the nuclear pore protein Nup153 with A- and B-type lamins. *Nucleus* 2:500–9
130. Kalverda B, Pickersgill H, Shloma VV, Fornerod M. 2010. Nucleoporins directly stimulate expression of developmental and cell-cycle genes inside the nucleoplasm. *Cell* 140:360–71
131. Buchwalter AL, Liang Y, Hetzer MW. 2014. Nup50 is required for cell differentiation and exhibits transcription-dependent dynamics. *Mol. Biol. Cell* 25:2472–84
132. Mewborn SK, Puckelwartz MJ, Abuisneineh F, Fahrenbach JP, Zhang Y, et al. 2010. Altered chromosomal positioning, compaction, and gene expression with a:amin A/C gene mutation. *PLOS ONE* 5:e14342
133. Mattout A, Pike BL, Towbin BD, Bank EM, Gonzalez-Sandoval A, et al. 2011. An EDMD mutation in *C. elegans* lamin blocks muscle-specific gene relocation and compromises muscle integrity. *Curr. Biol.* 21:1603–14

134. Zuela N, Dorfman J, Gruenbaum Y. 2017. Global transcriptional changes caused by an EDMD mutation correlate to tissue specific disease phenotypes in *C. elegans*. *Nucleus* 8:60–69
135. Van Berlo JH, Voncken JW, Kubben N, Broers JLV, Duisters R, et al. 2005. A-type lamins are essential for TGF-β1 induced PP2A to dephosphorylate transcription factors. *Hum. Mol. Genet.* 14:2839–49
136. Bernasconi P, Carboni N, Ricci G, Siciliano G, Politano L, et al. 2018. Elevated TGF β2 serum levels in Emery–Dreifuss muscular dystrophy: implications for myocyte and tenocyte differentiation and fibrogenic processes. *Nucleus* 9:292–304
137. Frock RL, Kudlow BA, Evans AM, Jameson SA, Hauschka SD, Kennedy BK. 2006. Lamin A/C and emerin are critical for skeletal muscle satellite cell differentiation. *Genes Dev*. 20:486–500
138. Muchir A, Pavlidis P, Decostre V, Herron AJ, Arimura T, et al. 2007. Activation of MAPK pathways links LMNA mutations to cardiomyopathy in Emery–Dreifuss muscular dystrophy. *J. Clin. Investig.* 117:1282–93
139. Muchir A, Wu W, Choi JC, Iwata S, Morrow J, et al. 2012. Abnormal p38 mitogen-activated protein kinase signaling in dilated cardiomyopathy caused by Lamin A/C gene mutation. *Hum. Mol. Genet.* 21:4325–33
140. Le Dour C, Macquart C, Sera F, Homma S, Bonne G, et al. 2017. Decreased WNT/β-catenin signalling contributes to the pathogenesis of dilated cardiomyopathy caused by mutations in the Lamin A/C gene. *Hum. Mol. Genet.* 26:333–43
141. Favreau C, Higuet D, Courvalin J-C, Buendia B. 2004. Expression of a mutant lamin A that causes Emery–Dreifuss muscular dystrophy inhibits in vitro differentiation of C2C12 myoblasts. *Mol. Cell. Biol.* 24:1481–92
142. Melcon G, Kozlov S, Cutler DA, Sullivan T, Hernandez L, et al. 2006. Loss of emerin at the nuclear envelope disrupts the Rb1/E2F and MyoD pathways during muscle regeneration. *Hum. Mol. Genet.* 15:637–51
143. Park S-J, Gavrilova O, Brown AL, Soto JE, Bremner S, et al. 2017. DNA-PK promotes the mitochondrial, metabolic, and physical decline that occurs during aging. *Cell Metab*. 25:1135–46
144. Chung JH. 2018. The role of DNA-PK in aging and energy metabolism. *FEBS J*. 285:1959–72
145. Azibani F, Muchir A, Vignier N, Bonne G, Bertrand AT. 2014. Striated muscle laminopathies. *Semin. Cell Dev. Biol.* 29:107–15
146. Laurini E, Martinelli V, Lanzicher T, Puzzi L, Borin D, et al. 2018. Biomechanical defects and rescue of cardiomyocytes expressing pathologic nuclear lamins. *Cardiovasc. Res.* 114:846–57
147. Natl. Inst. Health. 2017. A study of ARRY-371797 in patients with LMNA-related dilated cardiomyopathy. **https://clinicaltrials.gov/ct2/show/NCT02057341**
148. Roux KJ, Kim DI, Raida M, Burke B. 2012. A promiscuous biotin ligase fusion protein identifies proximal and interacting proteins in mammalian cells. *J. Cell Biol.* 196:801–10
149. Schopp IM, Amaya Ramirez CC, Debeljak J, Kreibich E, Skribbe M, et al. 2017. Split-BioID: a conditional proteomics approach to monitor the composition of spatiotemporally defined protein complexes. *Nat. Commun.* 8:15690
150. Dekker J, Belmont AS, Guttman M, Leshyk VO, Lis JT, et al. 2017. The 4D nucleome project. *Nature* 549:219–26
151. McCord RP, Nazario-Toole A, Zhang H, Chines PS, Zhan Y, et al. 2013. Correlated alterations in genome organization, histone methylation, and DNA–Lamin A/C interactions in Hutchinson–Gilford progeria syndrome. *Genome Res*. 23:260–69
152. Ma H, Naseri A, Reyes-Gutierrez P, Wolfe SA, Zhang S, Pederson T. 2015. Multicolor CRISPR labeling of chromosomal loci in human cells. *PNAS* 112:3002–7
153. Shao S, Zhang W, Hu H, Xue B, Qin J, et al. 2016. Long-term dual-color tracking of genomic loci by modified sgRNAs of the CRISPR/Cas9 system. *Nucleic Acids Res*. 44:e86
154. Bhattacharya D, Talwar S, Mazumder A, Shivashankar GV. 2009. Spatio-temporal plasticity in chromatin organization in mouse cell differentiation and during *Drosophila* embryogenesis. *Biophys. J.* 96:3832–39
155. Ramdas NM, Shivashankar GV. 2015. Cytoskeletal control of nuclear morphology and chromatin organization. *J. Mol. Biol.* 427:695–706

156. Harkness T, McNulty JD, Prestil R, Seymour SK, Klann T, et al. 2015. High-content imaging with micropatterned multiwell plates reveals influence of cell geometry and cytoskeleton on chromatin dynamics. *Biotechnol. J.* 10:1555–67
157. Hayashi-Takanaka Y, Yamagata K, Wakayama T, Stasevich TJ, Kainuma T, et al. 2011. Tracking epigenetic histone modifications in single cells using Fab-based live endogenous modification labeling. *Nucleic Acids Res.* 39:6475–88
158. Sasaki K, Ito T, Nishino N, Khochbin S, Yoshida M. 2009. Real-time imaging of histone H4 hyperacetylation in living cells. *PNAS* 106:16257–62
159. Ito T, Umehara T, Sasaki K, Nakamura Y, Nishino N, et al. 2011. Real-time imaging of histone H4K12–specific acetylation determines the modes of action of histone deacetylase and bromodomain inhibitors. *Chem. Biol.* 18:495–507
160. Llères D, James J, Swift S, Norman DG, Lamond AI. 2009. Quantitative analysis of chromatin compaction in living cells using FLIM-FRET. *J. Cell Biol.* 187:481–96
161. Spagnol ST, Dahl KN. 2016. Spatially resolved quantification of chromatin condensation through differential local rheology in cell nuclei fluorescence lifetime imaging. *PLOS ONE* 11:e0154639
162. Vishwasrao HD, Trifilieff P, Kandel ER. 2012. In vivo imaging of the actin polymerization state with two-photon fluorescence anisotropy. *Biophys. J.* 102:1204–14
163. Maffioletti SM, Sarcar S, Henderson ABH, Mannhardt I, Pinton L, et al. 2018. Three-dimensional human iPSC-derived artificial skeletal muscles model muscular dystrophies and enable multilineage tissue engineering. *Cell Rep.* 23:899–908
164. van Spreeuwel ACC, Bax NAM, Bastiaens AJ, Foolen J, Loerakker S, et al. 2014. The influence of matrix (an)isotropy on cardiomyocyte contraction in engineered cardiac microtissues. *Integr. Biol.* 6:422–29
165. Ronaldson-Bouchard K, Ma SP, Yeager K, Chen T, Song L, et al. 2018. Advanced maturation of human cardiac tissue grown from pluripotent stem cells. *Nature* 556:239–43
166. Legant WR, Pathak A, Yang MT, Deshpande VS, McMeeking RM, Chen CS. 2009. Microfabricated tissue gauges to measure and manipulate forces from 3D microtissues. *PNAS* 106:10097–102
167. Abilez OJ, Tzatzalos E, Yang H, Zhao MT, Jung G, et al. 2018. Passive stretch induces structural and functional maturation of engineered heart muscle as predicted by computational modeling. *Stem Cells* 36:265–77
168. Tiburcy M, Hudson JE, Balfanz P, Schlick S, Meyer T, et al. 2017. Defined engineered human myocardium with advanced maturation for applications in heart failure modelling and repair. *Circulation* 135:1832–47
169. Sakar MS, Neal D, Boudou T, Borochin MA, Li Y, et al. 2012. Formation and optogenetic control of engineered 3D skeletal muscle bioactuators. *Lab Chip* 12:4976
170. Long C, Li H, Tiburcy M, Rodriguez-Caycedo C, Kyrychenko V, et al. 2018. Correction of diverse muscular dystrophy mutations in human engineered heart muscle by single-site genome editing. *Sci. Adv.* 4:eaap9004
171. Balikov DA, Brady SK, Ko UH, Shin JH, de Pereda JM, et al. 2017. The nesprin–cytoskeleton interface probed directly on single nuclei is a mechanically rich system. *Nucleus* 8:534–47
172. Grashoff C, Hoffman BD, Brenner MD, Zhou R, Parsons M, et al. 2010. Measuring mechanical tension across vinculin reveals regulation of focal adhesion dynamics. *Nature* 466:263–66

Engineering approaches to study cancer cell migration in 3D environments

Noam Zuela-Sopilniak[1] and Jan Lammerding[1,*]

[1] Nancy E. and Peter C. Meinig School of Biomedical Engineering & Weill Institute for Cell and Molecular Biology; Cornell University; Ithaca, NY; USA
* Correspondence should be addressed to jan.lammerding@cornell.edu

Key words
Decellularized tissue, nuclear mechanics, microfluidics, force generation, intravital imaging, 3D bioprinting

Abstract

Cancer is one of the most devastating diseases of our time, with 18 million new cancer cases and 10 million cancer deaths predicted in 2018 worldwide. The mortality associated with cancer results primarily from metastasis, i.e., the spreading of cancer cells from the primary tumor to other organs. The ability of cells to invade and migrate through basement membranes, tight interstitial spaces, and endothelial cell layers is a key step in the metastatic cascade. Recent studies demonstrated that cell migration through three-dimensional (3D) environments, which mimic the *in vivo* conditions, significantly differs from their migration on 2-D surfaces. Here, we review recent technological advances made in the field of cancer research, which provide more “true to the source” experimental platforms and measurements for the study of cancer cell invasion and migration in 3D environments. These include microfabrication, 3D bioprinting, and intravital imaging tools, along with force and stiffness measurements of cells and their environment. These techniques will enable new studies that better reflect the physiological environment found *in vivo*, thereby producing more robust results. The knowledge achieved through these studies will aid in the development of new treatment options with the potential to ultimately lighten the devastating cost cancer inflicts on patients and their families.

Introduction

Cancer is a major clinical burden and the second leading cause of death worldwide[1]. Most cancer related deaths are due to metastasis, a complex process involving several successive steps: detachment of cells from the primary tumor, invasion of basement membranes, migration through interstitial spaces, intravasation into lymphatic and/or blood vessels, extravasation to distant tissues, and eventually metastatic colonization at distant sites (Fig. 1). Only a small percentage of tumor cells successfully completes this challenge[2]. In recent years, it has become apparent that the ability of cell to migrate through small openings in the ECM network or between other cells, henceforth referred to as 'confined migration', is a key step in metastatic progression. The confinements include micron size pores (1-20 μm in diameter) and fiber-like and channel-like tracks in the interstitial space ranging from 3-30 μm in width and 100-600 μm in length[3], as well as openings with only 1-2 μm in diameter during transendothelial migration[4]. Experimental measurements and computational modeling show that the cell's ability to navigate such tight spaces is primarily determined by four mechanical factors: (1) the pore size[5,6]; (2) the physical properties of the microenvironment[7]; (3) the mechanical deformability of the cell, particularly of the nucleus, which is the largest and stiffest organelle in the cell[8]; and (4) the cell's ability to generate and transmit forces to the nucleus and the extracellular environment and/or to remodel the ECM[5,6]. Nuclear migration arrest occurs at constrictions smaller than ~10% of the undeformed nuclear cross-sectional area, corresponding to ~7-10 μm^2 pore sizes in collagen matrices[6]. Passage through constrictions smaller in size necessitates matrix remodeling or alteration to nuclear stiffness. Modulation of protein levels of the nuclear envelope protein lamin A, which is one of the key components of the nuclear lamina and a major determinant of nuclear stiffness, affects the migratory potential of cancer cells through small (less than 7 μm^2) constrictions[9,10]. While differences in lamin levels correlate with clinical outcome in a variety of cancers[11], it remains unclear whether individual tumor cells can dynamically adjust their lamin levels or organization. Highly invasive cells can generate larger traction forces than less invasive cancer cells and non-tumorigenic cells[12,13], which may further promote their ability to penetrate tight spaces, but most of the current traction force measurements were obtained in 2-D conditions, motivating further research in 3D environments.

Besides imposing a physical barrier to invasion, the 3D tumor microenvironment can also affect tumor progression in additional ways[14]. Collagen crosslinking, which is largely regulated by lysyl oxidase (LOX)[15], and ECM stiffness play a major role in cancer invasion and progression[16]. The changes in ECM structure, organization, and mechanics affect integrins, focal adhesion and ERK and PI3K signaling to promote cancer cell survival, proliferation and progression[17]. In addition, many ECM remodeling enzymes, prominently matrix metalloproteinases (MMPs), are miss-regulated in tumor cells[18]. Furthermore, the physical stress on the cell nucleus during confined migration results in repetitive, transient nuclear envelope rupture, chromatin fragmentation, and DNA damage, which may further drive genomic instability in metastatic cancer cells and promote cancer progression and resistance to therapy[19–21]. Lastly, migration through confined environments may also serve as a physical cue that alters intracellular signaling, gene expression, and cell migration modes[22,23]. Obtaining a better understanding of tumor cell metastasis thus

requires precise measurements of these physical factors governing cell migration in 3D environments, i.e., the degree of confinement (pore size), the mechanical properties of the microenvironment, the (passive) mechanical properties of the migrating cell, and the forces applied by the cell to its environments. However, while the importance of these physical factors of tumor cells and their microenvironment are now well recognized, experimental methods to measure these properties and to generate realistic *in vitro* models that mimic physiological conditions are only beginning to find broader application.

Here, we review some of these emerging technologies to (1) study the physical aspects of cancer cell invasion and the consequences of confined migration, with a particular focus on methods to measure cell generated forces in 3D environments, (2) quantify the physical properties of the extracellular environment, and (3) implement more "true to the source" *in vitro* models of 3D environments. Ultimately, a more comprehensive understanding of the contributors and regulators of metastasis will pave the way towards developing new and more targeted treatment options.

1. Methods to measure cellular mechanics and cell generated forces in 3D environments.

Numerous experimental methods are available to study the (passive) mechanical properties of tumor cells, including atomic force microscopy (AFM), micropipette aspiration, magnetic bead microrheology, particle-tracking, and cellular deformation by optical forces or fluidic shear stress[24]. While many of these techniques are limited to one-cell-at-a-time measurements, microfluidic approaches have recently become available that enable substantially higher throughout measurements and are better suited to address the heterogeneous nature of tumor cells, including the identification of specific sub-populations[24–26]. In contrast, methods to measure cell-generated forces in 3D environments and the physical properties of the tumor microenvironment inside tissues are only now emerging and are discussed in detailed below.

1.1. Traction Force measurements

Migration through confining spaces requires cells to generate traction forces through the contraction of actomyosin, which are then transmitted to the microenvironment through adhesions[27]. Alternatively, some cells utilize an amoeboid migration mode that relies on pressure-driven membrane blebbing, friction with the environment, and 'chimneying' within the confinement[23]. In case the forces applied by the cell are insufficient for cell passage, cells may enzymatically degrade the surrounding matrix to decrease the steric hindrance imposed by the matrix[28]. The forces exerted by cells on different matrices can be measured using traction force microscopy (TFM). TFM experiments are most commonly performed on cells cultured on 2D gels. In this case, the traction forces are calculated from the measured displacements of beads embedded in a flexible hydrogel with known elastic properties[29,30]. Since cellular organization, adhesion, and migration in 3D environments is vastly different than in 2D conditions, researchers have strived to develop TFM for cells in 3D environments. One way to overcome the challenges of measuring 3D traction forces has been the use of engineered 3D matrices with elastic material properties, such as spontaneously formed collagen gels[31] and mechanically well-

defined polyethylene glycol (PEG) hydrogels incorporating proteolytically degradable domains and pendant adhesive ligands[32]. These 3D assays use the same principles as 2D TFM, i.e., measuring the displacement of fluorescent beads embedded within the matrix and then inferring the applied forces based on the displacement and the known elastic matrix mechanical properties (Fig. 2A). However, for studies in 3D reconstructed environment using biological materials, one must consider the nonlinear nature of these materials, such as stiffening under shear stress and collapse when stretched[33]. Other approaches for measuring 3D traction forces have been developed to address these issues, for example, modeling the viscoelastic properties of collagen, fibrin and Matrigel matrixes or measuring the deformation of individual collagen fibers[34,35].

Another challenge of experiments in biological matrices is that cells can alter the local and global mechanical properties of the matrix by degrading, remodeling, or synthesizing it, necessitating taking into account local matrix properties. Increasing the density of fluorescent beads embedded within the matrix to increase the spatial resolution must be balanced with the fact that low densities typically increase accuracy of displacement measurements. In either case, tracking fluorescent bead displacement may not provide sufficient indication of local ECM remodeling. This issue can be partially overcome by confocal reflection imaging, which analyzes the fibrous structure of collagen matrices[36], bypassing the need for fluorescent probes. This method uses partial volume correlation (PVC) to quantify cellular contractility in a label free, 3D tissue mimicking configuration, and reveals details about the ECM microstructure remodeling[31,36]. Another limitation of most TFM approaches is that they rely on widefield or confocal microscopy, which limits the analysis depth to at most a few hundred micrometers and can cause photobleaching and phototoxicity on longer time scales. An alternative, which circumvents these limitations, is optical coherence microscopy (OCM), a variation of OCT that has a transverse resolution approaching 1 μm, enabling the capture of cellular level features. This technique also has the ability to enhance tomographic images[37] and displacement sensitivity[38]. Traction forces can be inferred using OCM (TF-OCM) by reconstructing volumetric time-laps data sets of ECM deformation resulting from cell generated forces in a 3D culture[39]. Quantifying cellular generated traction force within 3D native tissues in real time requires an understanding of the exact tissue material composition and a method for tracking deformations. The changes in the shape of micrometer-scale oil droplets coated with surface integrin/cadherin receptor ligands[40] and elastic round microgels with integrin-binding sites for cell adhesion[41], combined with their pre-determined material properties enables the quantification of mechanical forces exerted on the droplets by the surrounding tissue. However, the spatial resolution of this approach is quite limited, given the size and number of the microgels.

1.2. Single molecule force measurements

Most methods aimed at measuring force magnitudes and directionality produced by cells provide μm spatial resolution and nN force sensitivity. However, a wide range of biological processes are modulated by mechanical forces in the pN scale[42,43]. To resolve the adhesion forces transmitted across individual integrin molecules, fluorescent force probes have been developed that rely on Förster resonance energy transfer (FRET) or fluorophore-quencher pairings to detect conformational changes within the reporter once

it reaches a critical force [44,45]. Similar tension sensors, using genetically encoded FRET fluorophore pairs connected by an elastic linker, so that the change in FRET efficiency can be related to the mechanical forces required to stretch/compress the linker, have been developed to measure intracellular forces across focal adhesion proteins[46]. Recent advances using a variety of elastic linkers have now increased the sensitivity and extended the detectable force range of these genetically encoded tension sensors from 3-11 pN[47,48]. To analyze two biosensors simultaneously in the same cell, orthogonal tension sensor modules that can be imaged together with a single excitation wavelength using dual color fluorescence lifetime imaging microscopy (FLIM) were recently developed[47], further expanding the available toolbox.

2. Quantitative measurements of the mechanical properties of 3D environments

The physical pore sizes of interstitial spaces and openings in endothelial layers have been extensively characterized by histological analysis and intravital imaging; these measurements[6] serve as guiding design parameters for engineered *in vitro* models[7,49,50] discussed in Section 3. Besides the geometric constraints, though, information on the physical properties of the microenvironment is critically needed, as the mechanical properties of the environment determine both the cell behavior, e.g., whether cells display invasive and non-invasive phenotypes[51,52], and the ability of cells to penetrate through spaces in the environment[53,54].

Measurements of the mechanical properties of tissues can be performed using the non-invasive and label-free optical coherence elastography (OCE)[55] utilizing the *in vivo* imaging modality optical coherence tomography (OCT). OCT is analogous to ultrasound imaging but uses light instead of sound to perform high-resolution, cross-sectional tomographic imaging of the internal microstructure by measuring backscattered light. OCT provides rapid, 3D images with micrometer resolution at an imaging depth ranging from hundreds of micrometers to a few millimeters[56], making the technique ideal for the study of cell matrix interaction and cellular migration dynamics *in vitro* and *ex-vivo*[57]. Other OCT variations include full-field OCT, used to analyze millisecond-scale cellular dynamics[58]; swept-source OCM, which enables volume acquisition of light sheet microscopy like speeds and sizes[59] and diffusion-sensitive OCT to quantify fiber spacing in the ECM[60]. It is important to note that with the current available technology, OCM/T images contain aberrations, defocus, and a decrease in signal strength away from the focal plane, which can affect the analytical accuracy of measurements [39]. Another contact and label-free method of mapping the 3D intra and extracellular hydromechanical properties of cells is Brillouin optical cell microscopy. This method probes the spontaneous pressure waves within the cell, essentially plotting the uniaxial stress to strain ratio in compression conditions at a high frequency[61]. The noncontact nature of Brillouin microscopy allows mechanical analysis of cells in physiological 3D matrices and has similar, if not better sensitivity than the widely used contact-based measurement tools. Brillouin technology can detect cellular mechanical changes occurring due to alterations in biopolymer polarization, content, branching and liquid-solid volume fraction[62]. However, since biological materials are mainly composed of water, hydration may minimize the elastic contribution of the solid component, and the translation of the

measurements to specific molecular components is not always trivial. An alternative technique of measuring mechanical properties *in vivo* in a quantitative and spatiotemporal manner is introducing biocompatible fluorocarbon-based ferrofluids into tissues and deforming them using a magnetic field; the local tissue mechanical properties can then be inferred by relating the mechanical stresses generated by the droplet to the resulting deformation of the surrounding material[63].

3. Current and emerging models of 3D tumor and tissue microenvironments

Though many important discoveries in tumor cell biology were made using 2D culture conditions, these conditions do not accurately recapitulate cellular morphology, signaling patterns, cellular functions and proper pharmacokinetics in 3D microenvironments[64–66]. Thus, to gain a more comprehensive and accurate understanding of the intricate relationship between cancer cell invasion and the ECM, experimental systems that feature realistic 3D environments are needed. These systems include reconstituted ECM matrices and microfabricated constructs mimicking the geometry of the tumor microenvironment. However, while such systems are convenient and useful, their clinical relevance may be limited because they lack the complexity of the endogenous tumor microenvironment. On the other hand, *in vivo* models provide a more realistic environment to study tumor growth and metastasis, but they come at a much higher cost, and imaging localized invasion, intravasation, and extravasation events remains challenging. Furthermore, the need for immune-compromised mice in xenograft studies presents another limitation. These factors raise the need to bridge the gap between *in vitro* and *in vivo* techniques, creating *in situ* and *ex vivo* experimental platforms containing structures and other cells present at the endogenous tumor microenvironment, while providing more control over experimental and technical parameters.

3.1. Decellularized matrices, in situ and ex vivo

Decellularized platforms, such as decellularized chicken egg chorioallantopic membrane (dCAM)[67], can be used as a complex ECM scaffold that enable the study of tumor cell invasion in realistic 3D environments while offering controlled *in vitro* conditions. Cancer cells and other cell types can be co-cultured on the decellularized matrices for weeks at a time and monitored by live-cell microscopy. Organotypic brain slices, such as cerebral[68] and cerebellar[69] slices, present another *ex vivo* platform, ideally suited for studying brain tumors, which are challenging to propagate under culture conditions and often grow in highly distinct brain locations, impossible to recreate in culture (Fig. 2C). To establish a human derived tumor microenvironment, human uterine leiomyoma tissue is used to study cancer cell invasion. This tissue contains, in addition to the essential tumor microenvironment structural components such as collage and laminin, also stromal cells such as fibroblasts, endothelial, smooth muscle, and inflammatory cells[70]. This model also allows for using hypoxic research conditions[71], thus providing a more comprehensive experimental platform. Lastly, myoma tissues have been used to compare invasiveness of different cell lines[72,73] and to test the effect of different compounds on cellular invasion [70]. Comparison of tumor cell invasion between myoma and non-neoplastic tissue showed that the non-neoplastic tissue was non-conducive to induce invasion of highly metastatic

cancer cell types, as opposed to myoma tissue[74], highlighting the importance of selecting an appropriate ECM model for function studies.

3.2. Engineered 3D microenvironments

While decellularized matrices and *ex vivo* platforms provide the most physiological 3D environment, they offer limited control over the physical confinement, can be highly variable and heterogeneous, and are not always well suited for high resolution imaging conditions. To overcome these challenges, hydrogels, microfabrication, and 3D printing technologies can be used that enable the precise control of variables such as surface geometry, force, and material properties for a more accurate study of cell migration.

3.2.1. Three-dimensional (3D) hydrogels

Hydrogels are hydrophilic 3D cross-linked insoluble polymer networks capable of retaining large amounts of fluid, and can be modulated to resemble the biomechanical properties of native ECM by adjusting the types of polymers used, their concentration, crosslinking density, and by tailoring with various bioactive molecules[75]. Among the polymers used to create hydrogels, collagen[76], fibrin[77], fibronectin and hyaluronic acid[78] are among the most common. 3D self-assembling collagen I hydrogels can be used to distinguish the independent contribution of different ECM parameters such as pore size, fiber alignment, matrix density and stiffness on cell migration[79]. Hydrogels consisting of interpenetrating networks (IPNs) of reconstituted basement membrane molecules (laminin and type IV collagen) and alginate, with the latter allowing for precise control over matrix mechanical properties[54], enable to study the effect of ECM plasticity on cell migration. Hydrogels can be used in combination with microfabricated scaffolds to create chemotactic gradients[80] or for further enhancements, for instance, mineralization to create bone-mimetic fibrillar hydrogels to study the effect of mineralization on breast cancer cell adhesion and migration[81]. However, hydrogels can be challenging to mold with high precision due to swelling, which may alter the dimensions, nano-architecture and the mechanical properties of the gel. These obstacles can be diminished by increasing the hydrophobicity of the polymer backbone[82], reducing swelling and increasing stability.

3.2.2. Microfabrication

Typically, microfabricated structures are most frequently constructed using polydimethylsiloxane (PDMS)[83](Fig. 2B). The resulting structures and multi-compartment devices can have submicron and even nanoscale resolutions[84], although most devices have features on the micrometer scale and larger. Combined with fluorescent subcellular labels and time-lapse microscopy, these devices enable the precise quantification of cancer cell migration speed, direction, and intracellular dynamics at a single cell resolution as the cells squeeze through precisely defined micron-scale constrictions that mimic the *in vivo* environment[7,19,21]. Microfabricated systems can also use ECM proteins instead of PDMS to recreate confined environments[85] and to assess the effect of ECM composition on cancer cell migration[86]. A variety of microfluidic devices have been used to study the effects of microtracks in ECM matrices[87], the presence of vasculature[88], cytokines[89], tumor associated macrophages[90], fibroblasts[91], and endothelial cells[92] on cancer cell invasion. Platforms with local areas of reduced stiffness can be designed to

mimic the heterogeneous composition of the tumor ECM[93]. The increased accessibility of microfabrication techniques has enabled researchers to create sophisticated microenvironments for studying cell migration. Nonetheless, there is still room for further improvements. In some current setups, cell migration can be influenced by unwanted shear stress, the high rigidity of PDMS relative to physiological matrices, the inability of cells to remodel PDMS, fluctuating chemotactic gradients, and altered cell-cell signaling due to flow or adhesion of certain proteins to the device surface. Recently developed microfluidic devices that model multiple organs or tissues, with their interconnectivity[94], may allow a more accurate study of metastasis, although further work is needed to capture the full complexity of *in vivo* system.

3.2.3 Three-dimensional (3D) bioprinting

Bioprinting is an alternative approach to generate precisely defined 3D microenvironments, albeit with lower resolution compared to microfabrication techniques. Bioprinting allows the fabrication of complex 3D *in vitro* culture environments with selected biological components such as cellular composition and controllable mechanical properties[95] to create biomimetic tissue models containing native architecture and vasculature. Applications of these models include the study of cancer invasion and drug screening[96,97]. The incorporation of cells to create a functional biomimetic tissue can be achieved by cell seeding into already fabricated scaffolds or cell encapsulation during the bioprinting process[95].

Multiple printing modes are available for 3D bioprinting, each with its own advantages and limitations. Extrusion-based bioprinting is based on automated motors controlling a printer nozzle and a dispensing system depositing either acellular or cell-laden bio-inks in a layer-by-layer fashion[95] (Fig. 2D). The variety of biocompatible inks, e.g., cell spheroid suspension, decellularized ECM solutions, and hydrogels with a wide range of viscosities, makes this technique ideal for constructing different tissue models[98]. This method has a resolution of around 100 μm, printing speeds of 10-50 μm/s; finer nozzles and higher printing speeds can result in shear induced cell death[98]. Using extrusion printing, a grid cervical tumor model containing HeLa cells embedded in a hydrogel mixture of gelatin, alginate and fibrinogen was fabricated. This model showed higher proliferation rates and MMP expression, as well as increased resistance to anticancer agents as compared to the 2D model[99].

Inkjet-based bioprinting is based on conventional inkjet desktop printers and dispenses precise pico-liter droplets of bio-ink on a printing stage. There are several inkjet approaches, including thermal[100], piezoelectric[101], and electromagnetic[102]. The more common approach is thermal printing due to its user-friendly design, low cost, and relatively high cell viability after printing. The inkjet method is faster than extrusion-based bioprinting (mm/s) and has better resolution (< 50 μm)[103], depending on the nozzle diameter. Smaller nozzle diameters result in higher resolution, but are more prone to clogging, limiting the printable materials to low viscosity or water-based materials, and thus affecting the size and structural integrity of the reproduced structures. To study tumor stroma interaction, a droplet printing technique was used to pattern fibroblasts and human

ovarian cancer cells into Matrigel. The co-cultured construct proliferated to form 3D acinar structures that resembled the ovarian cancer micronodules[104].

Light-assisted techniques are growing in popularity, specifically digital light processing (DLP) and two photon polymerization (TPP) based bioprinting[103]. The DLP system utilizes a computer controlled digital micro mirror device consisting of ~two million micro-mirrors and a motorized stage and printing head. This technique has a microscale resolution and very rapid printing speed (mm^3/s), as well as no interface between droplets or lines as in the case of inkjet and extrusion bioprinting, respectively, resulting in the ability to print more complex structures[105], better mechanical stability, and tunable Poisson ratios[106]. For instance, biomimetic DLP printed chips with embedded vasculature of different size were used to study the effect of vessel geometry on the migration speed of HeLa cells[107], demonstrating more efficient migration through narrow vessels. However, this technique requires photopolymerizable materials, which limits the available selection. The TPP based system uses a rastering laser[108] which polymerizes photo sensitive monomers to create nano- (~100 nm) and microscale structures[109], at a lower speed then DLP (mm/s)[103]. A larger variety of polymers have been successfully printed using this technique, including type-I collagen[110] and laminin[111]. These two techniques offer high cell viability, increased feature resolution, and fast printing speed, but do not provide the flexibility to selectively deposit bio-inks, as compared to the extrusion and inkjet-based methods.

Ultimately, the choice of bioprinting technique is dependent upon the desired application, printing capabilities, and the limitations of each method[95]. Several challenges remain, including the need for increased resolution to produce single cell structures, increased printing speed to enhance cell viability, biocompatibility for future analysis of functional organ studies, and the incorporation of multiple physiologically relevant features to recapitulate a specific microenvironment. Furthermore, printing large, complex structures with many different components can take substantial time. The ultimate goal is to create an integrated platform to study the cooperative effects of multiple miniaturized organs[112].

Conclusions

Tumor cell invasion and migration present critical first steps in the metastatic cascade. It is now well recognized that the structure, composition, and mechanics of the tumor microenvironment strongly affects these processes, and therefore, should be accurately recapitulated, including the 3D nature and confinement of physiological tissues. Recently developed 3D experimental platforms and fabrication techniques are beginning to bridge the gap between *in vitro* research, which offers superb control over experimental conditions and enables live cell imaging at high spatial and temporal resolution, and the actual *in vivo* tumor microenvironments. Despite tremendous progress, the *in vitro* platforms cannot (yet) fully capture the complex settings tumor cells encounter *in vivo*, motivating the continued development of enhanced intravital imaging techniques (Fig. 2E) to achieve higher resolution, longer term imaging, and deeper imaging depths, with the aim to provide a more detailed look at tumor cell migration in the natural context.

Another significant challenge to be overcome is the current low-throughput format of many techniques that operate at single-cell resolution, since the heterogeneous nature of tumors requires measuring large numbers of cells to identify rare subpopulations and events. Overcoming this challenge will require assays capable of higher throughput measurements, as recently developed for single cell mechanics measurements[24,26], as well as automated image analysis of tumor cell invasion time-lapse studies[113].

Taken together, these approaches, particularly when used in combination, will ultimately enable researchers to accurately recreate the *in vivo* intricate tumor microenvironment using the comforts of a controlled *in vitro* experimental platform to study tumor cell migration with single cell resolution. These techniques have the potential to not only reduce the need for animal experiments, thereby reducing costs, improving experimental time-lines, and enabling higher throughput test of therapeutic interference, but to also produce new insights into the molecular mechanisms of tumor cell invasion and metastasis that can offer new targets for cancer therapies.

Acknowledgements
We apologize to all authors whose work could not be included due to space constraints. This work was supported by awards from the National Institutes of Health [R01 HL082792 and U54 CA210184], the Department of Defense Breast Cancer Research Program [Breakthrough Award BC150580], and the National Science Foundation [CAREER Award CBET-1254846 and MCB-1715606].

Competing interest
We have no competing interests.

Figure legends

Figure 1: The metastatic process. Cancer cells detach from the primary tumor, translocate into a distant organ and colonize it to form metastasis. Some cancer cells within the primary tumor acquire an invasion phenotype (**i**), then detach from the primary tumor (**ii**) to invade the surrounding extracellular matrix, likely aided by cancer associated cells such as fibroblasts and macrophages (**ii'**). Tumor cells intravasate lymphatic and blood vessels (**iii**) and are carried by the circulation to distant organs (**iv**), where they extravasate from the blood vessels (**v**) and invade the microenvironment of the distant tissue (**vi'**). There, tumor cells must survive and proliferate to create micro-metastasis (**vi**), which further grow to generate macro metastasis (**vii**).

Figure 2: Methods of studying cancer cell invasion. (**A**). Traction force measurements in 3D. Fluorescent beads (red) are embedded in collagen matrices or engineered hydrogels (yellow) containing tumor cells (gray). The traction forces cells generate are calculated by analyzing the displacement of the fluorescent beads between the strained and un-strained states of the gels. (**B**) A schematic representation of a cell migrating through a microfluidic device mimicking the confined spaces in tissues[114]. Media reservoirs (**i**) allow maintaining cells for multiple days and can be used to establish chemotactic gradients. Cells are loaded through seeding ports (**ii**). Large bypass channels (**iii**) connect the media reservoirs to allow for rapid equilibration of media levels. The central part of the device contains the 5 μm tall constriction channels (**iv**) with constrictions of 1-20 μm in width. Arrow represents direction of cell migration. (**C**) Schematic depiction of a brain organotypic slice and tumor co-culture. Media is added to the bottom of a culture dish; the brain slice is placed on top of a semi-porous membrane. Fluorescently labeled tumor spheroids (green) are implanted into the slice, so that tumor cell invasion can be imaged and tracked. (**D**) Conceptual representation of 3D bioprinting. The printing nozzle dispenses bio-ink to fabricate complex *in vitro* 3D structures using computer guidance. This technique allows control over the cellular composition of the bio-inks, as well as the mechanical properties of the resulting structures. (**E**) Intravital imaging of tumor cell invasion *in vivo*. Imaging chambers/windows can be inserted into the skin in several locations, such as the cranium (**i**), abdomen (**ii**), skin (**iii**) and nipple area (**iv**). Note that actual experiments typically use only a single imaging window.

References

1. Bray F, Ferlay J, Soerjomataram I, Siegel RL, Torre LA, Jemal A. Global cancer statistics 2018: GLOBOCAN estimates of incidence and mortality worldwide for 36 cancers in 185 countries. *CA Cancer J Clin*. 2018;68(6):394-424. doi:10.3322/caac.21492.
2. Valastyan S, Weinberg RA. Tumor Metastasis: Molecular Insights and Evolving Paradigms. *Cell*. 2011;147(2):275-292. doi:10.1016/j.cell.2011.09.024.
3. Wolf K, Alexander S, Schacht V, et al. Collagen-based cell migration models in vitro and in vivo. *Semin Cell Dev Biol*. 2009;20(8):931-941. doi:10.1016/j.semcdb.2009.08.005.
4. Yadav SK, Feigelson SW, Roncato F, et al. Frontline Science: Elevated nuclear lamin A is permissive for granulocyte transendothelial migration but not for motility through collagen I barriers. *J Leukoc Biol*. 2018;104(2):239-251. doi:10.1002/JLB.3HI1217-488R.
5. Kumar S, Das A, Sen S, Van Haastert P. Multicompartment cell-based modeling of confined migration: regulation by cell intrinsic and extrinsic factors. *Mol Biol Cell*. 2018;29(13):1599-1610. doi:10.1091/mbc.E17-05-0313.
6. Wolf K, te Lindert M, Krause M, et al. Physical limits of cell migration: Control by ECM space and nuclear deformation and tuning by proteolysis and traction force. *J Cell Biol*. 2013;201(7):1069-1084. doi:10.1083/jcb.201210152.
7. Lautscham LA, Kämmerer C, Lange JR, et al. Migration in Confined 3D Environments Is Determined by a Combination of Adhesiveness, Nuclear Volume, Contractility, and Cell Stiffness. *Biophys J*. 2015;109(5):900-913. doi:10.1016/j.bpj.2015.07.025.
8. Lammerding J, Schulze PC, Takahashi T, et al. Lamin A/C deficiency causes defective nuclear mechanics and mechanotransduction. *J Clin Invest*. 2004;113. doi:10.1172/JCI19670.
9. Harada T, Swift J, Irianto J, et al. Nuclear lamin stiffness is a barrier to 3D migration, but softness can limit survival. *J Cell Biol*. 2014;204(5):669-682. doi:10.1083/jcb.201308029.
10. Davidson PM, Denais C, Bakshi MC, Lammerding J. Nuclear deformability constitutes a rate-limiting step during cell migration in 3-D environments. *Cell Mol Bioeng*. 2014;7(3):293-306. doi:10.1007/s12195-014-0342-y.
11. Bell ES, Lammerding J. Causes and consequences of nuclear envelope alterations in tumour progression. *Eur J Cell Biol*. 2016;95(11):449-464. doi:10.1016/j.ejcb.2016.06.007.
12. Mekhdjian AH, Kai F, Rubashkin MG, et al. Integrin-mediated traction force enhances paxillin molecular associations and adhesion dynamics that increase the invasiveness of tumor cells into a three-dimensional extracellular matrix. Yap A, ed. *Mol Biol Cell*. 2017;28(11):1467-1488. doi:10.1091/mbc.E16-09-0654.
13. Network TPS-OC, Agus DB, Alexander JF, et al. A physical sciences network characterization of non-tumorigenic and metastatic cells. *Sci Rep*. 2013;3:1449. doi:10.1038/srep01449.
14. Malandrino A, Mak M, Kamm RD, Moeendarbary E. Complex mechanics of the heterogeneous extracellular matrix in cancer. *Extrem Mech Lett*. 2018;21:25-34. doi:10.1016/j.eml.2018.02.003.

15. Barker HE, Chang J, Cox TR, et al. LOXL2-Mediated Matrix Remodeling in Metastasis and Mammary Gland Involution. *Cancer Res*. 2011;71(5):1561 LP-1572. doi:10.1158/0008-5472.CAN-10-2868.
16. Levental KR, Yu H, Kass L, et al. Matrix Crosslinking Forces Tumor Progression by Enhancing Integrin Signaling. *Cell*. 2009;139(5):891-906. doi:10.1016/j.cell.2009.10.027.
17. Northcott JM, Dean IS, Mouw JK, Weaver VM. Feeling Stress: The Mechanics of Cancer Progression and Aggression. *Front Cell Dev Biol*. 2018;6:17. doi:10.3389/fcell.2018.00017.
18. Kessenbrock K, Plaks V, Werb Z. Matrix Metalloproteinases: Regulators of the Tumor Microenvironment. *Cell*. 2010;141(1):52-67. doi:10.1016/j.cell.2010.03.015.
19. Denais CM, Gilbert RM, Isermann P, et al. Nuclear envelope rupture and repair during cancer cell migration. *Science (80-)*. 2016;352(6283):353 LP-358. doi:10.1126/science.aad7297.
20. Shah P, Wolf K, Lammerding J. Bursting the bubble – nuclear envelope rupture as a path to genomic instability? *Trends Cell Biol*. 2017;27(8):546-555. doi:10.1016/j.tcb.2017.02.008.
21. Raab M, Gentili M, de Belly H, et al. ESCRT III repairs nuclear envelope ruptures during cell migration to limit DNA damage and cell death. *Science (80-)*. 2016;352(6283):359 LP-362. doi:10.1126/science.aad7611.
22. Hung W-C, Yang JR, Yankaskas CL, et al. Confinement Sensing and Signal Optimization via Piezo1/PKA 1. *Cell Rep*. 2016;15(7):1430-1441. doi:10.1016/j.celrep.2016.04.035.
23. Liu Y-J, Le Berre M, Lautenschlaeger F, et al. Confinement and Low Adhesion Induce Fast Amoeboid Migration of Slow Mesenchymal Cells. *Cell*. 2015;160(4):659-672. doi:10.1016/j.cell.2015.01.007.
24. Lei C, Kobayashi H, Wu Y, et al. High-throughput imaging flow cytometry by optofluidic time-stretch microscopy. *Nat Protoc*. 2018;13(7):1603-1631. doi:10.1038/s41596-018-0008-7.
25. Nyberg KD, Bruce SL, Nguyen A V, et al. Predicting cancer cell invasion by single-cell physical phenotyping. *Integr Biol*. 2018;10(4):218-231. doi:10.1039/C7IB00222J.
26. Rosendahl P, Plak K, Jacobi A, et al. Real-time fluorescence and deformability cytometry. *Nat Methods*. 2018;15:355. doi:10.1038/nmeth.4639.
27. Schmidt CE, Horwitz AF, Lauffenburger DA, Sheetz MP. Integrin-cytoskeletal interactions in migrating fibroblasts are dynamic, asymmetric, and regulated. *J Cell Biol*. 1993;123(4):977 LP-991. doi:10.1083/jcb.123.4.977.
28. Zaman MH, Trapani LM, Sieminski AL, et al. Migration of tumor cells in 3D matrices is governed by matrix stiffness along with cell-matrix adhesion and proteolysis. *Proc Natl Acad Sci*. 2006;103(29):10889 LP-10894. doi:10.1073/pnas.0604460103.
29. Sabass B, Gardel ML, Waterman CM, Schwarz US. High Resolution Traction Force Microscopy Based on Experimental and Computational Advances. *Biophys J*. 2008;94(1):207-220. doi:10.1529/biophysj.107.113670.
30. Maskarinec SA, Franck C, Tirrell DA, Ravichandran G. Quantifying cellular

traction forces in three dimensions. *Proc Natl Acad Sci*. 2009;106(52):22108 LP-22113. doi:10.1073/pnas.0904565106.
31. Koch TM, Münster S, Bonakdar N, Butler JP, Fabry B. 3D Traction Forces in Cancer Cell Invasion. Mellor H, ed. *PLoS One*. 2012;7(3):e33476. doi:10.1371/journal.pone.0033476.
32. Legant WR, Miller JS, Blakely BL, Cohen DM, Genin GM, Chen CS. Measurement of mechanical tractions exerted by cells within three-dimensional matrices. *Nat Methods*. 2010;7(12):969-971. doi:10.1038/nmeth.1531.
33. Münster S, Jawerth LM, Leslie BA, Weitz JI, Fabry B, Weitz DA. Strain history dependence of the nonlinear stress response of fibrin and collagen networks. *Proc Natl Acad Sci*. 2013;110(30):12197 LP-12202. doi:10.1073/pnas.1222787110.
34. Hall MS, Alisafaei F, Ban E, et al. Fibrous nonlinear elasticity enables positive mechanical feedback between cells and ECMs. *Proc Natl Acad Sci U S A*. 2016;113(49):14043-14048. doi:10.1073/pnas.1613058113.
35. Steinwachs J, Metzner C, Skodzek K, et al. Three-dimensional force microscopy of cells in biopolymer networks. *Nat Methods*. 2015;13:171. doi:10.1038/nmeth.3685.
36. Kim J, Jones CAR, Groves NS, Sun B. Three-Dimensional Reflectance Traction Microscopy. Sznitman J, ed. *PLoS One*. 2016;11(6):e0156797. doi:10.1371/journal.pone.0156797.
37. Adie SG, Graf BW, Ahmad A, Carney PS, Boppart SA. Computational adaptive optics for broadband optical interferometric tomography of biological tissue. *Proc Natl Acad Sci U S A*. 2012;109(19):7175-7180. doi:10.1073/pnas.1121193109.
38. Mulligan JA, Untracht GR, Chandrasekaran SN, Brown CN, Adie SG. Emerging Approaches for High-Resolution Imaging of Tissue Biomechanics With Optical Coherence Elastography. *IEEE J Sel Top Quantum Electron*. 2016;22(3):246-265. doi:10.1109/JSTQE.2015.2481705.
39. Mulligan JA, Bordeleau F, Reinhart-King CA, Adie SG. Measurement of dynamic cell-induced 3D displacement fields in vitro for traction force optical coherence microscopy. *Biomed Opt Express*. 2017;8(2):1152-1171. doi:10.1364/BOE.8.001152.
40. Campàs O, Mammoto T, Hasso S, et al. Quantifying cell-generated mechanical forces within living embryonic tissues. *Nat Methods*. 2014;11(2):183-189. doi:10.1038/nmeth.2761.
41. Mohagheghian E, Luo J, Chen J, et al. Quantifying compressive forces between living cell layers and within tissues using elastic round microgels. *Nat Commun*. 2018;9:1878. doi:10.1038/s41467-018-04245-1.
42. Vogel V, Sheetz M. Local force and geometry sensing regulate cell functions. *Nat Rev Mol Cell Biol*. 2006;7:265. doi:10.1038/nrm1890.
43. Finer JT, Simmons RM, Spudich JA. Single myosin molecule mechanics: piconewton forces and nanometre steps. *Nature*. 1994;368:113. doi:10.1038/368113a0.
44. Brockman JM, Blanchard AT, Pui-Yan Ma V, et al. Mapping the 3D orientation of piconewton integrin traction forces. *Nat Methods*. 2017;15:115. doi:10.1038/nmeth.4536.

45. Morimatsu M, Mekhdjian AH, Adhikari AS, Dunn AR. Molecular Tension Sensors Report Forces Generated by Single Integrin Molecules in Living Cells. *Nano Lett*. 2013;13(9):10.1021/nl4005145. doi:10.1021/nl4005145.
46. Freikamp A, Cost A-L, Grashoff C. The Piconewton Force Awakens: Quantifying Mechanics in Cells. *Trends Cell Biol*. 2016;26(11):838-847. doi:10.1016/j.tcb.2016.07.005.
47. Ringer P, Weißl A, Cost A-L, et al. Multiplexing molecular tension sensors reveals piconewton force gradient across talin-1. *Nat Methods*. 2017;14:1090. doi:10.1038/nmeth.4431.
48. LaCroix AS, Lynch AD, Berginski ME, Hoffman BD. Tunable molecular tension sensors reveal extension-based control of vinculin loading. van Oijen AM, ed. *Elife*. 2018;7:e33927. doi:10.7554/eLife.33927.
49. Keys J, Windsor A, Lammerding J. Assembly and Use of a Microfluidic Device to Study Cell Migration in Confined Environments. In: *Methods in Molecular Biology*. ; 2018:101-118. doi:10.1007/978-1-4939-8691-0_10.
50. Paul CD, Mistriotis P, Konstantopoulos K. Cancer cell motility: lessons from migration in confined spaces. *Nat Rev Cancer*. 2017;17(2):131-140. doi:10.1038/nrc.2016.123.
51. Paszek MJ, Nastaran Z, Johnson KR, Boettiger D, Hammer DA, Weaver VM. Tensional homeostasis and the malignant phenotype. *Cancer Cell*. 2005;8(3):241-254. doi:10.1016/j.ccr.2005.08.010.
52. Wullkopf L, West A-K V, Leijnse N, et al. Cancer cells' ability to mechanically adjust to extracellular matrix stiffness correlates with their invasive potential. *Mol Biol Cell*. 2018;29(20):2378-2385. doi:10.1091/mbc.E18-05-0319.
53. Cao X, Moeendarbary E, Isermann P, et al. A Chemomechanical Model for Nuclear Morphology and Stresses during Cell Transendothelial Migration. *Biophys J*. 2016;111(7):1541-1552. doi:10.1016/j.bpj.2016.08.011.
54. Wisdom KM, Adebowale K, Chang J, et al. Matrix mechanical plasticity regulates cancer cell migration through confining microenvironments. *Nat Commun*. 2018;9(1):4144. doi:10.1038/s41467-018-06641-z.
55. Castillero E, Akashi H, Pendrak K, et al. Attenuation of the unfolded protein response and endoplasmic reticulum stress after mechanical unloading in dilated cardiomyopathy. *Am J Physiol - Hear Circ Physiol*. 2015;309(3):H459 LP-H470. http://ajpheart.physiology.org/content/309/3/H459.abstract.
56. Fujimoto J, Swanson E. The Development, Commercialization, and Impact of Optical Coherence Tomography. *Invest Ophthalmol Vis Sci*. 2016;57(9):OCT1-OCT13. doi:10.1167/iovs.16-19963.
57. Goicoechea SM, Bednarski B, García-Mata R, Prentice-Dunn H, Kim HJ, Otey CA. Palladin Contributes to Invasive Motility in Human Breast Cancer Cells. *Oncogene*. 2009;28(4):587-598. doi:10.1038/onc.2008.408.
58. Apelian C, Harms F, Thouvenin O, Boccara AC. Dynamic full field optical coherence tomography: subcellular metabolic contrast revealed in tissues by interferometric signals temporal analysis. *Biomed Opt Express*. 2016;7(4):1511-1524. doi:10.1364/BOE.7.001511.
59. Bouchard MB, Voleti V, Mendes CS, et al. Swept confocally-aligned planar excitation (SCAPE) microscopy for high speed volumetric imaging of behaving

organisms. *Nat Photonics*. 2015;9(2):113-119. doi:10.1038/nphoton.2014.323.
60. Blackmon RL, Sandhu R, Chapman BS, et al. Imaging Extracellular Matrix Remodeling In Vitro by Diffusion-Sensitive Optical Coherence Tomography. *Biophys J*. 2016;110(8):1858-1868. doi:10.1016/j.bpj.2016.03.014.
61. Scarcelli G, Yun SH. Confocal Brillouin microscopy for three-dimensional mechanical imaging. *Nat Photonics*. 2007;2:39-43. doi:10.1038/nphoton.2007.250.
62. Scarcelli G, Polacheck WJ, Nia HT, et al. Noncontact three-dimensional mapping of intracellular hydromechanical properties by Brillouin microscopy. *Nat Methods*. 2015;12:1132. doi:10.1038/nmeth.3616.
63. Serwane F, Mongera A, Rowghanian P, et al. In vivo quantification of spatially-varying mechanical properties in developing tissues. *Nat Methods*. 2017;14(2):181-186. doi:10.1038/nmeth.4101.
64. Bao M, Xie J, Piruska A, Huck WTS. 3D microniches reveal the importance of cell size and shape. *Nat Commun*. 2017;8:1962. doi:10.1038/s41467-017-02163-2.
65. Tanner K, Gottesman MM. Beyond 3D culture models of cancer. *Sci Transl Med*. 2015;7(283):283ps9-283ps9. doi:10.1126/scitranslmed.3009367.
66. Fan Q, Liu R, Jiao Y, et al. A novel 3-D bio-microfluidic system mimicking in vivo heterogeneous tumour microstructures reveals complex tumour–stroma interactions. *Lab Chip*. 2017;17(16):2852-2860. doi:10.1039/C7LC00191F.
67. Keeton SJ, Delalande JM, Cranfield M, Burns A, Dash PR. Compressed collagen and decellularized tissue -- novel components in a pipeline approach for the study of cancer metastasis. *BMC Cancer*. 2018;18(1):622. doi:10.1186/s12885-018-4533-0.
68. Ren B, Yu S, Chen C, et al. Invasion and Anti-Invasion Research of Glioma Cells in An Improved Model of Organotypic Brain Slice Culture. *Tumori J*. 2015;101(4):390-397. doi:10.5301/tj.5000321.
69. Neve A, Santhana Kumar K, Tripolitsioti D, Grotzer MA, Baumgartner M. Investigation of brain tissue infiltration by medulloblastoma cells in an ex vivo model. *Sci Rep*. 2017;7(1):5297. doi:10.1038/s41598-017-05573-w.
70. Nurmenniemi S, Sinikumpu T, Alahuhta I, et al. A Novel Organotypic Model Mimics the Tumor Microenvironment. *Am J Pathol*. 2009;175(3):1281-1291. doi:10.2353/ajpath.2009.081110.
71. Teppo S, Sundquist E, Vered M, et al. The hypoxic tumor microenvironment regulates invasion of aggressive oral carcinoma cells. *Exp Cell Res*. 2013;319(4):376-389. doi:10.1016/j.yexcr.2012.12.010.
72. Alahuhta I, Aikio M, Väyrynen O, et al. Endostatin induces proliferation of oral carcinoma cells but its effect on invasion is modified by the tumor microenvironment. *Exp Cell Res*. 2015;336(1):130-140. doi:10.1016/j.yexcr.2015.06.012.
73. Korvala J, Jee K, Porkola E, et al. MicroRNA and protein profiles in invasive versus non-invasive oral tongue squamous cell carcinoma cells in vitro. *Exp Cell Res*. 2017;350(1):9-18. doi:10.1016/j.yexcr.2016.10.015.
74. Sundquist E, Renko O, Salo S, et al. Neoplastic extracellular matrix environment promotes cancer invasion in vitro. *Exp Cell Res*. 2016;344(2):229-240. doi:https://doi.org/10.1016/j.yexcr.2016.04.003.

75. Wenger MPE, Bozec L, Horton MA, Mesquida P. Mechanical properties of collagen fibrils. *Biophys J*. 2007;93(4):1255-1263. doi:10.1529/biophysj.106.103192.
76. Gillette BM, Jensen JA, Tang B, et al. In situ collagen assembly for integrating microfabricated three-dimensional cell-seeded matrices. *Nat Mater*. 2008;7:636. https://doi.org/10.1038/nmat2203.
77. Eyrich D, Brandl F, Appel B, et al. Long-term stable fibrin gels for cartilage engineering. *Biomaterials*. 2007;28(1):55-65. doi:https://doi.org/10.1016/j.biomaterials.2006.08.027.
78. Fukuda J, Khademhosseini A, Yeh J, et al. Micropatterned cell co-cultures using layer-by-layer deposition of extracellular matrix components. *Biomaterials*. 2006;27(8):1479-1486. doi:https://doi.org/10.1016/j.biomaterials.2005.09.015.
79. Fraley SI, Wu P-H, He L, et al. Three-dimensional matrix fiber alignment modulates cell migration and MT1-MMP utility by spatially and temporally directing protrusions. *Sci Rep*. 2015;5:14580. doi:10.1038/srep14580.
80. Tayalia P, Mazur E, Mooney DJ. Controlled architectural and chemotactic studies of 3D cell migration. *Biomaterials*. 2011;32(10):2634-2641. doi:10.1016/j.biomaterials.2010.12.019.
81. Choi S, Friedrichs J, Song YH, Werner C, Estroff LA, Fischbach C. Intrafibrillar, bone-mimetic collagen mineralization regulates breast cancer cell adhesion and migration. *Biomaterials*. 2019;198:95-106. doi:https://doi.org/10.1016/j.biomaterials.2018.05.002.
82. Trappmann B, Baker BM, Polacheck WJ, Choi CK, Burdick JA, Chen CS. Matrix degradability controls multicellularity of 3D cell migration. *Nat Commun*. 2017;8(1):371. doi:10.1038/s41467-017-00418-6.
83. Hou X, Zhang YS, Santiago GT, et al. Interplay between materials and microfluidics. *Nat Rev Mater*. 2017;2:17016. http://dx.doi.org/10.1038/natrevmats.2017.16.
84. Qin D, Xia Y, Whitesides GM. Soft lithography for micro- and nanoscale patterning. *Nat Protoc*. 2010;5:491. doi:10.1038/nprot.2009.234.
85. Choi Y, Hyun E, Seo J, et al. A microengineered pathophysiological model of early-stage breast cancer. *Lab Chip*. 2015;15(16):3350-3357. doi:10.1039/C5LC00514K.
86. Anguiano M, Castilla C, Maška M, et al. Characterization of three-dimensional cancer cell migration in mixed collagen-Matrigel scaffolds using microfluidics and image analysis. Deli MA, ed. *PLoS One*. 2017;12(2):e0171417. doi:10.1371/journal.pone.0171417.
87. Carey SP, Rahman A, Kraning-Rush CM, et al. Comparative mechanisms of cancer cell migration through 3D matrix and physiological microtracks. *Am J Physiol - Cell Physiol*. 2015;308(6):C436-C447. doi:10.1152/ajpcell.00225.2014.
88. Supriya N, Danh T, Ghassan M, Mehdi N. Microfluidic Tumor–Vascular Model to Study Breast Cancer Cell Invasion and Intravasation. *Adv Healthc Mater*. 2018;7(9):1701257. doi:10.1002/adhm.201701257.
89. Hsu T-H, Kao Y-L, Lin W-L, et al. The migration speed of cancer cells influenced by macrophages and myofibroblasts co-cultured in a microfluidic chip. *Integr Biol*. 2012;4(2):177-182. doi:10.1039/C2IB00112H.

90. Kitamura T, Qian B-Z, Pollard JW. Immune cell promotion of metastasis. *Nat Rev Immunol*. 2015;15(2):73-86. doi:10.1038/nri3789.
91. Sugimoto M, Kitagawa Y, Yamada M, Yajima Y, Utoh R, Seki M. Micropassage-embedding composite hydrogel fibers enable quantitative evaluation of cancer cell invasion under 3D coculture conditions. *Lab Chip*. 2018;18(9):1378-1387. doi:10.1039/C7LC01280B.
92. Zervantonakis IK, Hughes-Alford SK, Charest JL, Condeelis JS, Gertler FB, Kamm RD. Three-dimensional microfluidic model for tumor cell intravasation and endothelial barrier function. *Proc Natl Acad Sci U S A*. 2012;109(34):13515-13520. doi:10.1073/pnas.1210182109.
93. Domenico LE, Barbara S, Francesco R, et al. Microenvironmental Stiffness of 3D Polymeric Structures to Study Invasive Rates of Cancer Cells. *Adv Healthc Mater*. 2017;6(22):1700888. doi:10.1002/adhm.201700888.
94. Ingber DE. Reverse Engineering Human Pathophysiology with Organs-on-Chips. *Cell*. 2016;164(6):1105-1109. doi:10.1016/j.cell.2016.02.049.
95. Murphy S V, Atala A. 3D bioprinting of tissues and organs. *Nat Biotechnol*. 2014;32:773. doi:10.1038/nbt.2958.
96. Almela T, Al-Sahaf S, Brook IM, et al. 3D printed tissue engineered model for bone invasion of oral cancer. *Tissue Cell*. 2018;52:71-77. doi:https://doi.org/10.1016/j.tice.2018.03.009.
97. Yang Y, Du T, Zhang J, et al. A 3D-Engineered Conformal Implant Releases DNA Nanocomplexs for Eradicating the Postsurgery Residual Glioblastoma. *Adv Sci*. 2017;4(8):1600491. doi:10.1002/advs.201600491.
98. Placone JK, Engler AJ. Recent Advances in Extrusion-Based 3D Printing for Biomedical Applications. *Adv Healthc Mater*. 2017;7(8):1701161. doi:10.1002/adhm.201701161.
99. Zhao Y, Yao R, Ouyang L, et al. Three-dimensional printing of Hela cells for cervical tumor model in vitro. *Biofabrication*. 2014;6(3):35001. doi:10.1088/1758-5082/6/3/035001.
100. Cui X, Boland T, Lotz DDD and MK. Thermal Inkjet Printing in Tissue Engineering and Regenerative Medicine. *Recent Pat Drug Deliv Formul*. 2012;6(2):149-155. doi:10.2174/187221112800672949.
101. Saunders RE, Gough JE, Derby B. Delivery of human fibroblast cells by piezoelectric drop-on-demand inkjet printing. *Biomaterials*. 2008;29(2):193-203. doi:10.1016/j.biomaterials.2007.09.032.
102. Kollamaram G, Hopkins SC, Glowacki BA, Croker DM, Walker GM. Inkjet printing of paracetamol and indomethacin using electromagnetic technology: Rheological compatibility and polymorphic selectivity. *Eur J Pharm Sci*. 2018;115:248-257. doi:10.1016/j.ejps.2018.01.036.
103. Zhu W, Ma X, Gou M, Mei D, Zhang K, Chen S. 3D printing of functional biomaterials for tissue engineering. *Curr Opin Biotechnol*. 2016;40:103-112. doi:https://doi.org/10.1016/j.copbio.2016.03.014.
104. Xu F, Celli J, Rizvi I, Moon S, Hasan T, Demirci U. A three-dimensional in vitro ovarian cancer coculture model using a high-throughput cell patterning platform. *Biotechnol J*. 2011;6(2):204-212. doi:10.1002/biot.201000340.
105. Zhu W, Qu X, Zhu J, et al. Direct 3D bioprinting of prevascularized tissue

constructs with complex microarchitecture. *Biomaterials*. 2017;124:106-115. doi:10.1016/j.biomaterials.2017.01.042.
106. Lee JW, Soman P, Park JH, Chen S, Cho D-W. A Tubular Biomaterial Construct Exhibiting a Negative Poisson's Ratio. Waigh T, ed. *PLoS One*. 2016;11(5):e0155681. doi:10.1371/journal.pone.0155681.
107. Huang TQ, Qu X, Liu J, Chen S. 3D printing of biomimetic microstructures for cancer cell migration. *Biomed Microdevices*. 2014;16(1):127-132. doi:10.1007/s10544-013-9812-6.
108. Cumpston BH, Ananthavel SP, Barlow S, et al. Two-photon polymerization initiators for three-dimensional optical data storage and microfabrication. *Nature*. 1999;398:51. doi:10.1038/17989.
109. Truby RL, Lewis JA. Printing soft matter in three dimensions. *Nature*. 2016;540:371. doi:10.1038/nature21003.
110. Bell A, Kofron M, Nistor V. Multiphoton crosslinking for biocompatible 3D printing of type I collagen. *Biofabrication*. 2015;7(3). doi:10.1088/1758-5090/7/3/035007.
111. Su P-J, Tran QA, Fong JJ, Eliceiri KW, Ogle BM, Campagnola PJ. Mesenchymal Stem Cell Interactions with 3D ECM Modules Fabricated via Multiphoton Excited Photochemistry. *Biomacromolecules*. 2012;13(9):2917-2925. doi:10.1021/bm300949k.
112. Eisenstein M. Artificial organs: Honey, I shrunk the lungs. *Nature*. 2015;519:S16. doi:10.1038/519S16a.
113. Elacqua JJ, McGregor AL, Lammerding J. Automated analysis of cell migration and nuclear envelope rupture in confined environments. Ramchandran R, ed. *PLoS One*. 2018;13(4):e0195664. doi:10.1371/journal.pone.0195664.
114. Davidson PM, Sliz J, Isermann P, Denais C, Lammerding J. Design of a microfluidic device to quantify dynamic intra-nuclear deformation during cell migration through confining environments. *Integr Biol (Camb)*. 2015;7(12):1534-1546. doi:10.1039/c5ib00200a.

Myosin IIA Suppresses Glioblastoma Development In a Mechanically-Sensitive Manner

Hannah S. Picariello[1]*, Rajappa S. Kenchappa[2]*, Vandana Rai[1], James F. Crish[1]*, Athanassios Dovas[3], Katarzyna Pagoda[4], Mariah McMahon[5], Emily S. Bell[6] , Unnikrishnan Chandrasekharan[1], Amanda Luu[2], Rita West[2]; Jan Lammerding[6], Peter Canoll[3]; David J. Odde[5], Paul A. Janmey[7], Thomas Egelhoff[1], and Steven S. Rosenfeld[2,a,]

[1]Lerner Research Institute, Cleveland Clinic, Cleveland, OH 44195; [2]Departments of Molecular Pharmacology and Experimental Therapeutics, Mayo Clinic, Jacksonville FL 32224; [3]Department of Pathology and Cell Biology, Columbia University, New York, NY 10032; [4]Institute of Nuclear Physics, Polish Academy of Sciences, PL-31342 Krakow, Poland; [5]Department of Biomedical Engineering, University of Minnesota, Minneapolis, MN 55455; [6]Weill Institute for Cell and Molecular Biology & Meinig School of Biomedical Engineering, Cornell University, Ithaca, NY, 14853; and [7]Department of Physiology, University of Pennsylvania, Philadelphia, PA 19104

[a]To whom all correspondence should be addressed, at: Department of Molecular Pharmacology and Experimental Therapeutics, Mayo Clinic, 4500 San Pablo Road, Jacksonville, FL 32224; rosenfeld.steven@mayo.edu

*These authors contributed equally

ABSTRACT

The ability of glioblastoma to disperse through the brain contributes to its lethality, and blocking this behavior has been an appealing therapeutic approach. Although a number of pro-invasive signaling pathways are active in glioblastoma, many are redundant, so targeting one can be overcome by activating another. However, these pathways converge on non-redundant components of the cytoskeleton, and we have shown that inhibiting one of these—the myosin II family of cytoskeletal motors—blocks glioblastoma invasion even with simultaneous activation of multiple upstream pro-migratory pathways. Myosin IIA and IIB are the most prevalent isoforms of myosin II in glioblastoma, and we now show that co-deleting these myosins markedly impairs tumorigenesis and significantly prolongs survival in a rodent model of this disease. However, while targeting just myosin IIA also impairs tumor invasion, it surprisingly increases tumor proliferation in a manner that depends on environmental mechanics. On soft surfaces, myosin IIA deletion enhances ERK1/2 activity, while on stiff surfaces, it enhances the activity of NFκB, not only in glioblastoma, but in triple negative breast carcinoma and normal keratinocytes as well. We conclude myosin IIA suppresses tumorigenesis in at least two ways that are modulated by the mechanics of the tumor and its stroma. Our results also suggest that inhibiting tumor invasion can enhance tumor proliferation, and that effective therapy requires targeting cellular components that drive both proliferation and invasion simultaneously.

SIGNIFICANCE STATEMENT

Glioblastoma, the most common and lethal of primary brain tumors, can diffusely infiltrate brain. Because the components of the cytoskeleton that drive tumor invasion are non-redundant, they have been attractive targets for blocking glioblastoma dispersion. However, we find that while targeting one of these—the molecular motor myosin IIA—effectively blocks glioblastoma invasion, it enhances tumor proliferation and lethality. In this study, we have found that myosin IIA functions as a tumor suppressor by reducing signaling of two oncogenes—ERK1/2 and NFκB—in a manner regulated by the mechanics of the tumor and surrounding brain. Our results also argue that effective treatment of glioblastoma will require inhibiting targets that drive both invasion and proliferation.

\body

INTRODUCTION

Glioblastoma (GBM), the most common malignant primary brain tumor, has remained lethal in spite of years of investigation into novel therapeutics (1). Although GBM rarely spreads outside the central nervous system (CNS), its ability to diffusely disperse within the CNS contributes to its highly malignant behavior (2,3). Brain invasion requires cell motility, which is stimulated by the many growth factor receptors that are amplified or dysregulated in GBM (4). Although these receptors and their second messengers can be targeted with highly specific drugs, their efficacy in GBM has been limited by signal cascade redundancy, which allows cells to circumvent blockade of one pathway by activating another (5-7). A more promising approach would be to target downstream components where these redundant signaling pathways converge. These targets include members of the non-muscle myosin II (NMII) family of molecular motors (8). We had previously shown that while the anti-invasive effects of EGFR blockade on GBM could be readily overcome with PDGFRα stimulation, and *vice versa*, pharmacologic inhibition of NMII effectively paralyzes GBM invasion even when both receptors are stimulated simultaneously (9). Nevertheless, our *in vitro and ex vivo* assays do not recapitulate the complexities of tumor behavior in a living host, and this motivated us to determine whether targeting NMII function *in vivo* has similar effects. The NMII family consists of three members—IIA, IIB, and IIC—each with distinct functions (10-12). While their importance in cell motility makes NMII family members appealing targets to block tumor invasion, nearly all tissues express at least one member of this family, so a pan-NMII targeting strategy would likely be toxic. An approach that only targets one of the three NMII isoform might still be effective and associated with fewer side effects. However, two reports have shown that targeting NMIIA induces squamous cell carcinoma in mice (13,14). The mechanism underlying this effect remains unclear. While one report (13) found that NMIIA stabilizes the tumor suppressor p53, a second did not observe this (14).

In this study, we have examined the effects of targeting NMIIA and NMIIB together in GBM *in vivo* and *in vitro*. We find that genetic deletion of both NMIIA and NMIIB reduces tumorigenesis and impairs tumor proliferation. While a therapeutic approach that targets NMIIA might be less toxic than a pan NMII approach, and while targeting NMIIA does markedly impair GBM invasion, we also find paradoxically that it enhances GBM growth and lethality in an *in vivo* rodent model of the disease. These effects are not associated with alterations in p53 levels or function. Instead, they occur hand-in-hand with enhancement in the activity of two signaling molecules, ERK1/2 and NFκB, in a manner that is modulated by the stiffness of the tumor microenvironment. Our results indicate that the tumor suppressive effects of NMIIA are a reflection of this molecular motor's roles in shaping cell mechanics. In conjunction with previous work (15), they also suggest that in GBM, efforts to target tumor invasion can enhance tumor proliferation and *vice versa*, and that effective therapy of GBM requires targeting non-redundant cellular components that drive both of these malignant phenotypes simultaneously.

RESULTS

A retrovirally-driven murine model of GBM provides a way to observe the effect of NMII deletion on tumor biology in vivo. In this study we have used an immunocompetent murine model of GBM (16) in which we inject a bicistronic retrovirus encoding for PDGF and the cre recombinase into the white matter of mice containing a floxed allele for either PTEN or TP53 (**Fig. 1A**). The injected retrovirus integrates into the genome of proliferative, PDGFRα-expressing glial progenitors (17). Tonic stimulation of these cells with PDGF, combined with cre-mediated PTEN or TP53 deletion, leads to development of tumors that closely resemble the proneural subtype of human GBM (16). We measured the stoichiometry of the three NMII isoforms in these tumors using liquid chromatography and tandem mass spectrometry (LC/MS/MS). NMIIA is the predominant isoform, accounting for 56% of the total NMII, while NMIIB accounts for approximately 35% (**Fig. S1A**). NMIIC represents a small fraction (5-8%) of the total, and we elected not to examine this isoform further.

Deleting NMIIA and NMIIB together in a murine GBM model impairs tumor proliferation and reduces tumorigenesis. We modified our retroviral model by generating a mouse strain with floxed alleles for PTEN and for both NMIIA and NMIIB. Injecting the PDGF-IRES-cre retrovirus in the white matter of these mice leads to deletion of the genes for PTEN, NMIIA, and NMIIB in the infected glial progenitor cells. We followed these mice for survival and results are depicted in **Fig. 1B**, which demonstrates that out of 16 NMIIA/NMIIB/PTEN floxed mice, only 2 (12.5%) succumbed to tumor. Necropsy of the remaining mice showed no evidence of PDGF+ tumors (**Fig. S2**). By comparison, 100% of mice with only a PTEN floxed allele develop tumors when injected with the same retrovirus. In order to determine what effect co-deletion of NMIIA and NMIIB has on mitotic function, we injected the PDGF-IRES-cre retrovirus intracerebrally in mice with floxed alleles for PTEN and NMIIA. This procedure generates GBMs that are deleted for NMIIA and PTEN with 100% penetrance (*discussed below*). We generated primary cell lines, measured NMII stoichiometry with LC/MS/MS, and found that NMIIA is barely detectable in these tumors (**Fig. S1B**). The tumor cells are mononuclear; express one pair of γ tubulin-positive centrosomes (**Fig. S3**); and undergo normal cytokinesis, as monitored by expression of an H2B-RFP nuclear reporter (**Supplementary Movie #1**). We then suppressed NMIIB in these cells with shRNA (**Fig. 1C**). The resulting cells are multi-nucleated, contain multiple centrosomes (**Fig. S3**), and are defective in cytokinesis (**Supplementary Movie #2**). We measured the rate of nuclear proliferation by transfecting these cells with an H2B-RFP reporter and monitoring proliferation of red nuclei in the tissue culture incubator (IncuCyte Zoom, Essen, Germany). Deletion/suppression of both NMIIA and NMIIB reduces this rate by approximately 30% (**Fig. 1D**). Since cells deleted for both NMIIA and NMIIB are multinucleated, the reduction in cellular proliferation rate is considerably greater than 30%.

Deleting NMIIA in murine GBM impairs tumor dispersion but enhances tumor proliferation and lethality. Since targeting both NMIIA and NMIIB would likely be toxic, we wondered if targeting only NMIIA might still prevent GBM dispersion (18). We accomplished this by injecting the PDGF-IRES-cre retrovirus into the white matter of mice with floxed alleles for NMIIA and PTEN. Since the PDGF encoded by our bicistronic retrovirus is fused to the HA epitope, we were able to identify PDGF-expressing tumor cells within the host brain with αHA immunohistochemistry. Although both NMIIA intact and deleted tumors cells are found in white matter, those deleted for NMIIA were impaired in migrating through cerebral cortex (CX) (**Figs. 2A, B**), which contains the smallest inter-cellular spaces in the brain (19-21). This implies, consistent with our prior study (22), that NMII isoforms are needed for cells to insinuate themselves through tight intercellular spaces. We tested this by examining migration through a 3 μm Transwell (**Figs. 2C** and **D**), and found that tumor cells deleted (*red*) or shRNA depleted (*grey*) for NMIIA were impaired in this *in vitro* invasion assay**.** However, NMIIA deletion enhances tumor lethality compared to tumors deleted for PTEN alone (**Fig. 3A**). To explain this paradox, we injected mice with floxed alleles for PTEN or for PTEN and NMIIA, respectively, with the PDGF-IRES-cre retrovirus and sacrificed the animals 36 days post injection (dpi). As **Figs. 3B** and **C** illustrate, HA-positive tumors are considerably larger ($p = 0.047$) when NMIIA is co-deleted with PTEN. We also monitored the effect of NMIIA deletion on the kinetics of tumor growth by implanting 50,000 luciferase expressing PTEN-deleted and PTEN/NMIIA-co-deleted tumor cells into the white matter of NSG mice. Luminescence was monitored over the subsequent

54 days. Results are depicted in **Fig. 3D**, and demonstrate that after an initial delay, the increase in luminescence over time fits a single exponential process, defining doubling times of 10.9 and 3.9 days for PTEN-deleted and PTEN/NMIIA co-deleted tumors, respectively.

Two studies using murine models of squamous cell carcinoma demonstrated that NMIIA depletion with shRNA leads to tumor formation (13,14). One of these (13) concluded that NMIIA functions as a tumor suppressor by stabilizing p53, and noted that NMIIA suppression prevents the normal increase in p53 protein levels in response to doxorubicin. In order to determine if this explains our results, we injected PDGF-IRES-cre encoding retrovirus into the white matter of mice with a floxed allele for only NMIIA, and compared survival of these mice to those with a TP53 floxed allele (**Fig. 3A**). As we previously reported (16), TP53-deleted murine GBM tumors are highly aggressive and lead to morbidity within 30-40 days post injection. (**Fig. 3A**, *green*). By contrast, NMIIA-floxed mice injected with retrovirus do not develop any signs of morbidity over 3 months of observation (**Fig. 3A**, *blue*). In contrast to a previous report (13), we find that treatment of both PTEN-deleted and PTEN/NMIIA co-deleted GBM cells with doxorubicin produces a time-dependent rise in p53 levels (**Fig. S4A**). Furthermore, p53 mediated apoptosis is functional even with NMIIA deletion, as treatment of both PTEN deleted and PTEN/NMIIA co-deleted cells with doxorubicin leads to expression of cleaved caspase 3 (**Fig. S4C**).

Deleting NMIIA in murine GBM alters tumor cell morphology and mechanics and shifts the stiffness optimum for proliferation. One of the roles that NMIIA plays is in driving the process of retrograde actin flow (23,24), which counters actin polymerization-induced outgrowth of cellular processes. We examined the consequences of NMIIA suppression on cell morphology by using a microfabricated 3D invasion assay that has been previously described (25). This device (**Fig. S5A**) maintains a stable chemotactic gradient as cells crawl though defined micrometer-sized constrictions formed by PDMS posts. We monitored migration of GFP-expressing, PTEN deleted tumor cells that were treated with non-targeting shRNA (**Fig. S5C**, **Supplementary Movie 3**) or shRNA directed against NMIIA (**Supplementary Movie 4**). Suppression of NMIIA markedly elongates cellular processes that entangle cells as they migrate toward the chemo-attractant. In order to quantify this effect, we transfected PTEN-deleted and PTEN/NMIIA co-deleted GBM cells with an H2B-RFP nuclear reporter. We measured the nuclear transit time through the narrowest constriction in this device (2 μm) and found that NMIIA deletion prolongs nuclear transit time >5 fold (**Fig. S5B**)

NMIIA also forms small bipolar filaments that can cross link actin-containing microfilaments, and as such, it might be expected to shape cell mechanics. Indeed, pharmacologic inhibition of NMII results in a decrease in the apparent Young's modulus of fibroblasts (74). In order to evaluate this, we subjected PTEN-deleted and PTEN/NMIIA co-deleted GBM cells grown on collagen coated glass cover slips to atomic force microscopy (AFM). In the first study, we used a 25 μm diameter AFM probe and 50 nN of applied force to compress tumor cells by ~50% in order to generate global stress curves depicted in **Fig. 4A**. The AFM data demonstrate that NMIIA-deleted GBM cells are less capable of resisting the AFM probe induced deformation, suggesting that NMIIA deletion reduces actin cross linking and the internal stress that leads to stiffening of the actin-based cytoskeleton. In the second study, we measured the stiffness of the cell cortex by using a smaller probe (1 μm), lower force (2 nN), and less compression over 25 positions per cell to calculate an apparent Young's modulus as a function of substrate stiffness (**Fig. 4B, Fig. S6**). As this figure shows, the apparent Young's modulus for both NMIIA intact and deleted cells increases—implying an increase in cortical stiffness—with increasing substrate stiffness. This feature has also been reported for non-transformed cells (71). However, on a soft surface (0.3 kPa) the apparent Young's modulus for NMIIA-deleted cells is significantly lower than for NMIIA-intact cells. This difference diminishes on stiffer surfaces (5 kPa), and reverses on glass (~50 GPa).

Myosin II is also involved in shaping cell geometry, and this led us to measure the effect of NMIIA deletion on surface area, volume, and cell height (**Fig. S7A-C**). To accomplish this, we used GFP-expressing PTEN-deleted and PTEN/NMIIA co-deleted cells that we cultured on Matrigel coated polyacrylamide gels (PAGs) of defined stiffness. Over a range of 0.7-50 kPa, NMIIA-deleted tumor cells consistently have a larger surface area and volume than NMIIA intact tumor cells. In addition to being more spread, PTEN/NMIIA co-deleted cells also appear to be decorated with longer and more numerous cellular processes at their periphery and over a range of substrate stiffness (**Fig. S8**). We also measured cell height from the surface of the Matrigel coated PAGs, and results are depicted in **Fig. S7C.** NMIIA

deletion significantly flattens GBM cells on substrates of low (0.7 kPa) and intermediate (4.6 kPa) stiffness relative to NMIIA intact cells, but this difference disappears on a stiff substrate (50 kPa). To ensure that this result is not affected by the complex matrix composition of Matrigel, we repeated this experiment using a 96 well plate that contains hydrogels of defined stiffness (Softwells, Matrigen, Brea, California), which we coated with a single matrix protein, fibronectin. As shown in **Fig. 4C**, we again observe that NMIIA deletion flattens GBM cells on soft, but not hard surfaces.

Mih *et al*. (26) reported that pharmacologic inhibition of NMII or siRNA suppression of NMIIA enhances proliferation of fibroblasts on soft (1 kPa) but not on rigid (glass) substrates. To test this in our system, we measured proliferation of PTEN-deleted and PTEN/NMIIA co-deleted GBM cells on the same fibronectin-coated Softwell plates that we used in **Fig. 4C**. We found that NMIIA intact tumor cells (**Fig. 4D**, *blue*) show a broad optimum in proliferation between 1-20 kPa. By contrast, NMIIA deletion shifts this optimum to softer surfaces (**Fig. 4D**, *red*). At 0.2 and 0.5 kPa, NMIIA deletion enhances proliferation by approximately 50% ($p=0.012$ and 0.017, respectively) while at a higher range of stiffness, corresponding differences become smaller and not statistically significant. Likewise, proliferation of NMIIA deleted cells on 0.5 kPa substrates is significantly faster than that for the same cells on plastic ($p = 0.04$), while corresponding differences for NMIIA-intact cells are not ($p = 0.15$).

Deleting or suppressing NMIIA in murine GBM alters the activity of signaling effectors in a mechanically-sensitive manner. We wondered if the effect of NMIIA deletion on proliferation (**Fig. 4D**) reflects a differential regulation of intracellular signaling. To test this, we generated lysates of PTEN deleted and PTEN/NMIIA co-deleted cells grown on a hard surface (plastic) and on a 0.5 kPa, fibronectin-coated Softwell hydrogel substrate and subjected them to a phospho-antibody array (Cancer System Signaling, Full Moon Biosystems, Sunnyvale, CA). We corrected for differences in protein loading by dividing each signal by the median overall signal. We then divided these signals by the corresponding total signal for the phosphorylated + non-phosphorylated species. Finally, we divided this normalized phosphorylation for NMIIA-deleted cells by that for NMIIA intact cells on both soft (0.5 kPa) and hard (plastic) surfaces to generate ratios that reflect how NMIIA deletion alters phosphorylation as a function of stiffness. The top panel in **Fig. 5A** lists the ratios for signaling components whose phosphorylation in NMIIA deleted cells is elevated (≥ 2.0) only on a soft surface relative to NMIIA intact cells and the bottom panel lists the corresponding ratios that are elevated only on a hard surface. Each of the proteins whose phosphorylation is upregulated in NMIIA-deleted GBM cells on a soft surface (**Fig. 5A**, *top panel*) are connected to the Ras-Raf-MEK-ERK pathway (27-32). Western blots of these lysates demonstrate that when grown on a soft (0.5 kPa) substrate, NMIIA-deleted cells enhance ERK1/2 phosphorylation approximately 4-fold compared to NMIIA-intact cells. This relative enhancement, however, disappears on a stiff substrate. (**Fig. 5B**). By contrast, AKT (**Fig. S9**) does not show any modulation with either NMIIA deletion or with alteration of substrate stiffness.

If the enhanced growth we see with NMIIA deletion is driven by ERK1/2 activation, then an ERK1/2 inhibitor should be selectively toxic to NMIIA deleted cells, and particularly so on soft surfaces, where ERK1/2 phosphorylation is increased. We tested this hypothesis by treating NMIIA deleted and intact cells grown on Softwell plates with the ERK1/2 inhibitor SCH772984. Results are depicted in **Fig. 5C**. NMIIA intact cells show no sensitivity to SCH772984 over the entire range of stiffness (**Fig. 5C**, *left panel*), implying relatively little dependence on ERK for viability. By contrast, this drug is toxic to NMIIA-deleted cells (**Fig. 5C**, *middle panel*), and more so on soft surfaces. To quantify this effect, we fit the dose response relationship to SCH772984 for NMIIA deleted cells to a set of hyperbolic functions, one for each stiffness, and plotted the maximum degree of cell kill derived from the fitting against substrate stiffness (**Fig. 5C**, *right panel*). As the figure shows, SCH772984 sensitivity drops sharply above 10 kPa. This suggests that NMIIA deleted cells depend on ERK1/2 for viability over the stiffness range that has been measured in brain (47-50).

NMIIA deleted GBM cells on a hard surface show a ≥ 2-fold increase in phosphorylation of a number of signaling kinases and regulators (**Fig. 5A***, lower panel*). Among these are MEK1, whose phosphorylation at T291 reduces ERK signaling (33), and two IκB isoforms, IκBα and IκBε. Phosphorylation of IκB causes it to dissociate from NFκB, releasing the latter to induce transcription of a wide array of genes (34-36). To confirm that NMIIA deletion enhances NFκB activity in cells cultured on a hard surface, we transfected GBM cells with a luciferase gene under control of the NFκB response

element, along with a mammalian expression vector for β-galactosidase (pCMV-βgal) to normalize for transfection efficiency. Since we were unable to efficiently transfect our NMIIA deleted GBM cells with this NFκB reporter system, we utilized PTEN-deleted GBM cells infected with non-targeting or NMIIA targeting shRNA-expressing lentiviruses to knock down NMIIA >95% (**Fig. S5B**). We also utilized this approach to determine if NMIIA suppression (**Fig. S5C**) similarly alters NFκB activity in a human triple negative breast carcinoma (MDA-MB-231) and in a non-transformed primary human keratinocyte line cultured on a plastic substrate. As **Figs. 6A-C** demonstrate, NMIIA suppression enhances NFκB activity 3-8 fold in our PTEN-deleted murine GBM cells, 5-7 fold in MDA-MB-231 cells, and 5-6 fold in human keratinocytes. To further test the specificity of this finding, we examined whether expression of an shRNA-resistant NMIIA heavy chain could restore baseline NFκB activity. MDA-MB-231 cells that expressed a shRNA targeting human NMIIA were stably transfected with a shRNA-resistant human NMIIA-GFP fusion protein. As **Fig. 6D** demonstrates, this restores NFκB activity to near control levels. We were not able to perform a similar experiment our PTEN-deleted GBM cells, as they could not tolerate stable transfection of an NMIIA-GFP construct.

NFκB plays an important role in the biology of tumor initiating cells (37), in part by regulating the expression of stem cell transcription factors, including Sox2 (38-40), which is expressed in our murine GBM cell lines (41), and Nanog, which is expressed in MDA-MB-231 cells (42). We therefore examined the effect of shRNA mediated NMIIA suppression on the activity of these transcription factors, utilizing a luciferase reporter under the control of either the Sox 2 or the Nanog promoter. We found a 6-8 fold increase in Sox2 activity in NMIIA-depleted GBM cells (**Fig. 6E**) and a 1.5-2 fold increase in Nanog activity in NMIIA-depleted MDA-MB-231 cells (**Fig. 6F**). We also examined the effect of targeting NMIIA on tumorsphere formation—a surrogate marker for tumor stem cell content—by applying a limiting dilution assay to both our rodent GBM as well as to human MDA-MB-231 cells (38). As illustrated in **Fig. S10**, deletion or shRNA depletion of NMIIA increases tumorsphere size and tumorsphere frequency, implying that targeting NMIIA enhances proliferative and tumor initiating capacity, respectively.

DISCUSSION

Myosin II represents a "point of convergence" for signaling pathways that are dysregulated in cancer. We previously showed in an *ex vivo* murine model of glioblastoma invasion that the pro-migratory effects produced by simultaneously activating EGFR and PDGFR could be overcome with pharmacologic blockade of NMII (9). However, tumors can adapt to long-term inhibition of therapeutic targets, and this motivated us to examine the effect of deleting both NMIIA and NMIIB in our glioblastoma model. We found that this markedly reduces tumorigenesis and enhances survival (**Fig. 1**). The tumor cells deleted/suppressed for both NMIIA and NMIIB are polyploid (**Fig. S3**), consistent with the role NMII plays in driving cytokinesis (43). Polyploidy and high degrees of aneuploidy enhance tumor cell fragility (44-46), and this effect, combined with the inhibition of tumor cell motility, explains the pronounced survival advantage that combined deletion of NMIIA and IIB provides (**Fig. 1B**). While dual inhibition of both NMIIA and IIB would likely be toxic, NMIIA is the predominant NMII isoform in our glioblastoma model (**Fig. S1A**) and is a minor component of the NMII expressed in normal brain (22). This motivated us to examine the consequences of targeting just NMIIA.

Targeting NMIIA impairs glioblastoma invasion but enhances tumor lethality. We found that while it effectively blocks GBM invasion (**Fig. 2**), deleting NMIIA also enhances GBM lethality and proliferation (**Fig. 3**). Two prior studies also showed that NMIIA suppression enhances tumorigenesis (13,14). Several possibilities may explain this effect. First, NMIIA deletion could produce a defect in p53-mediated apoptosis. However, we find that in the presence of doxorubicin, NMIIA deletion does not prevent upregulation of p53 nor block cleavage of caspase 3 (**Fig. S4**). A second possible explanation is that since NMIIA plays a role in cytokinesis, its deletion might lead to aneuploidy. While severe degrees of aneuploidy or polyploidy place a metabolic burden that would slow tumor proliferation, lesser degrees can be associated with enhanced proliferation and malignant behavior (44-46). We therefore examined G-banded metaphase spreads from 20 PTEN-deleted and 20 PTEN/NMIIA co-deleted tumor cells (Creative Bioarray, Shirley, NY). While normal diploid mouse cells have 40 chromosomes, we found that 30% of PTEN-deleted cells have 41-53 chromosomes and another 50% have >67 chromosomes, with 10% containing >100. A similar analysis of PTEN/NMIIA co-deleted cells showed that 20% have 41-44 chromosomes and 70% have 72-76 chromosomes. Thus, both NMIIA intact and deleted tumor cells are characterized by significant but similar degrees of aneuploidy; and we conclude that the presence of aneuploidy does not by itself explain the effect that NMIIA deletion has on tumor proliferation or lethality. Finally, by reducing tumor invasion we would expect that NMIIA deletion would make GBMs more compact and nodular (**Figs. 2A, B**). A recent report has demonstrated that among primary and metastatic brain tumors, nodular tumors generate more local brain compression, resulting in reduced vascular perfusion and enhanced neuronal death and neurologic disability (73). We therefore conclude that the effects of NMIIA deletion reflect enhanced proliferation in a tumor that is also more likely to damage normal neurologic structures because of its impairment in tumor dispersion.

The roles that NMIIA plays in tumor biology are modulated by the mechanics of the tumor microenvironment. Our data imply that NMIIA acts as a tumor suppressor by antagonizing ERK1/2 and NFκB in a manner regulated by environmental mechanics. We conclude that ERK1/2 is the major driver of the increase in proliferation that we see for NMIIA-deleted cells on soft surfaces, since this increase can be blocked with an ERK1/2 inhibitor (**Fig. 5C***, middle and right panels*). That SCH772984 is appreciably toxic for NMIIA deleted cells over a fairly broad mechanical range (**Fig. 5C**, *right panel*) implies that ERK activation in these cells is likely to also present over a similarly broad range of stiffness. This in turn raises the question of how physiologically relevant our findings are to the mechanics of the GBM microenvironments. Both non-invasive and invasive measures of the Young's modulus of brain range from 0.1-10 kPa (47-50,77), and a similar range has been reported for human glioblastoma tissue as well (77). Nevertheless, these macroscopic measures do not necessarily reflect the microscopic mechanical features that individual cells experience within a tumor—features that could be dominated by cell processes, such as axons and dendrites, which are filled with relatively incompressible microtubules. Thus, it seems likely that individual GBM cells could experience a broad range of stiffness *in situ*.

We find that NMIIA deletion has significant effects on cell morphology, including height, volume, and surface area (**Figs. S7,8**), and prior studies have shown that cellular geometry correlates with proliferation (26,53,54). Hence, the change in the stiffness optimum for proliferation that we see with NMIIA deletion (**Fig. 4D**) may be due the effect of altering GBM cell morphology on ERK1/2 signaling. Three possible mechanisms could explain this. First, ERK is well-known to be regulated by integrin activity (75), which in turn depends on engagement with the extracellular matrix (ECM). Consequently, cells that have a larger surface area and volume, such as those deleted for NMIIA, might be expected to have enhanced integrin-ECM attachment with subsequent increased downstream signaling to ERK. However, we note that while surface area and volume of NMIIA deleted cells on hydrogels remain larger than for NMIIA intact cells from soft to stiff surfaces (0.7-50 kPa), proliferation is only enhanced on the soft (0.2-1.0 kPa) end of this range. Second, both proliferation rate and cell height vary with substrate stiffness (**Fig. 4B,C**), and a mechanism that could explain this correlation has been previously proposed (55). It argues that phosphorylated second messengers have to "run a gauntlet" of cytoplasmic phosphatases in order to reach their targets, and cell flattening enhances the probability that these signaling molecules could phosphorylate their targets before colliding with a phosphatase. This model is consistent with our observation that cell flattening is most pronounced in NMIIA-deleted cells on low stiffness substrates, where both proliferation and ERK1/2 phosphorylation are increased (**Figs. 4B,C**; **Fig. 5B**). However, it would also predict that there should be a corresponding increase in phosphorylation of other second messengers, such as AKT, which we do not see (**Fig. 5C**). Finally, the Young's modulus of our GBM cells also varies with substrate stiffness (**Fig. 4A**), and is lowest on the softest surfaces. We could therefore alternatively explain our results if we argue that the activity of ERK1/2 is fine-tuned to cortical stiffness, with greater ERK1/2 phosphorylation in cells that are relatively soft. Metastatic tumor cells typically are softer than non-metastatic tumor or normal cells (51,52), and our results suggest that this softening selects for ERK1/2-driven tumor proliferation and invasion. Our results are also consistent with a recent report, which found that while stretching of the tissue in the *Drosophila* pupal notum enhances ERK activity, compaction of this tissue inhibits it (56).

On a stiff surface, NMIIA deletion does not activate ERK1/2. This may reflect the increased phosphorylation of MEK1 at threonine 291 (**Fig. 5A**), which regulates ERK1/2 activity through a negative feedback loop (33). However, we do observe increased phosphorylation of two members of the IκB family, which explains the enhanced NFκB transcriptional activity that we observe (**Fig. 6A-D**). In endothelial cells, the NMII regulatory light chain tonically suppresses NFκB activity through its antagonism of TRAF2 binding to the TNF receptor superfamily (57). In cells such as GBM, where NMIIA is the major isoform, this would predict enhanced NFκB activity with NMIIA deletion over the entire range of substrate stiffness (**Fig. 6**). However, in endothelial cells, ERK can block the activation of NFκB (58). Were this mechanism active in in our murine GBM cells as well, then the increased ERK activity that we see on soft surfaces might explain why we do not see an increase in NFκB activity under these conditions. NFκB has been shown to play a central role in the maintenance of tumor stem cells (59-63), and this is consistent with our finding that on a hard surface, NMIIA suppression enhances the activity of Sox2 in GBM and Nanog in breast carcinoma (**Fig. 6E,F**). Our findings that NMIIA deletion leads to activation of stem cell transcription factors is consistent with reports that NMII inhibition enhances survival of pluripotent stem cells *in vitro* (64,76).

In both neurons and glioblastoma, cell migration varies with substrate stiffness in a manner that is characterized by a stiffness optimum. We have previously shown that two factors determine the position of this optimum—the internal, retrograde force generated by myosin motors on actin filaments, and the compliance of cell-ECM attachments (78). Our current data suggests that there is a similar optimality in the dependence of growth on substrate stiffness—one that is also modulated by myosin (**Fig. 4D**). The relevance of microenvironmental mechanics to tumor growth is also consistent with evidence that enhanced ECM stiffness can make glioblastoma more aggressive (78). Taken together, our results imply that NMIIA functions as a tumor suppressor in GBM by inhibiting the activity of two drivers of the malignant phenotype, ERK1/2 and NFκB, in a manner modulated by microenvironmental mechanics

As noted above, co-deletion of NMIIA and NMIIB, which together comprise 92-95% of the total NMII in our GBM model, markedly impairs tumorigenesis (**Fig. 1**). A recent report has also observed that inhibition of NMII suppresses tumor growth in melanoma (72). While we propose that the anti-tumor effect of NMIIA and NMIIB co-deletion is due to simultaneous defects in both tumor migration and mitosis (**Fig 1**,

Supplementary Movies 1 and **2**), the authors of this study also observed that pan NMII inhibition suppresses both secretion of inflammatory cytokines and formation of tumor promoting macrophages in melanoma. We have not determined whether this mechanism contributes to the enhanced survival that we see when we delete NMIIA and NMIIB in our immunocompetent rodent model of GBM. Nevertheless this mechanism cannot be relevant to our NMIIA-deleted GBMs, which demonstrate enhanced lethality (**Fig. 3**).

Tumor invasion, like other forms of cell motility, requires tight spatial and temporal control of NMII activity, which is regulated by rho kinase (ROCK)-mediated phosphorylation of the NMII regulatory light chain. While we have shown that suppression of NMII activity can block tumor invasion, so too can over-expression of NMII or of a constitutively active rho kinase (65). Furthermore, mice bearing orthotopic human GBMs that express a constitutively active form of RhoA survive longer than those with control GBMs. While transfection with NMII or rho kinase may not be therapeutically practical, a small molecule activator of NMIIB and IIC, 4 hydroxyacetophenone, also blocks invasion of pancreatic adenocarcinoma (66), suggesting that enhancement of tumor contractility may have therapeutic potential.

Our results imply that in GBM, tumor proliferation and tumor invasion are linked, and that effective therapy requires targeting both phenotypes. Our finding that there is a dichotomy between ERK1/2 and NFκB signaling in GBM that is connected to environmental mechanics is reminiscent of an earlier study (67) which demonstrated that there is a dichotomy in the behavior of GBM tumor cells between two phenotypes—one characterized by high proliferation and the other by high dispersion. This dichotomy, referred to as "Go or Grow" is associated with corresponding differences in the expression of key transcriptional factors (15). The proliferation-dominant GBM cells, found in the core of the tumor, up-regulate several transcription factors that are downstream of ERK1/2, including MYC, CREB, and CRE-ATF, while the invasion-dominant GBM cells, found at the tumor/brain interface, up-regulate NFκB. Furthermore, prior studies with anti-angiogenics have found that this anti-proliferative therapy enhances tumor invasion (68,69). Combined with our results, this suggests that targeting GBM proliferation may enhance GBM invasion and *vice versa*. If this premise is correct, we would predict that for a GBM therapy to be effective, it must inhibit both invasion and proliferation simultaneously. Our finding that co-deletion of NMIIA and IIB prevents tumorigenesis supports this premise. While a pan NMII targeting approach is likely to be too toxic to be clinically practical, we note that a number of other molecular motors, including several mitotic kinesins (70), drive both tumor proliferation and invasion, and may serve as effective targets for blocking the two defining phenotypes of GBM.

REFERENCES

1. Puduvalli, VK and Hoang, N (2018) Chemotherapy of high grade astrocytomas in adults. *Progress in Neurological Surgery*. **31**:116-144.
2. Giese A, Westphal M (1996) Glioma invasion in the central nervous system. *Neurosurgery.* **39**(2):235–250; discussion 250-252.
3. Burger PC, Kleihues P (1989) Cytologic composition of the untreated glioblastoma with implications for evaluation of needle biopsies. *Cancer* **63**(10):2014–2023.
4. Geschwind A, Fischer OM, Ullrich A (2004) The discovery of receptor tyrosine kinases: targets for cancer therapy. *Nat Rev Cancer* **4**(5):361–370.
5. Ahluwalia MS, *et al*. (2011) Phase II trial of ritonavir/lopinavir in patients with progressive or recurrent high-grade gliomas. *J Neurooncol* **102**(2):317–321.
6. Raizer JJ, *et al.* (2016) A phase II study of bevacizumab and erlotinib after radiation and temozolomide in MGMT unmethylated GBM patients. *J Neurooncol* **126**(1):185–192.
7. de Groot JF, Gilbert MR (2007) New molecular targets in malignant gliomas. *Curr Opin Neurol* **20**(6):712–718.
8. Vicente-Manzanares M, Ma X, Adelstein RS, Horwitz AR (2009) Non-muscle myosin II takes centre stage in cell adhesion and migration. *Nat Rev Mol Cell Biol* **10**(11):778–790.
9. Ivkovic S, *et al.* (2012) Direct inhibition of myosin II effectively blocks glioma invasion in the presence of multiple motogens. *Mol Biol Cell* **23**(4):533–542.
10. Kovács M, Wang F, Hu A, Zhang Y, Sellers JR (2003) Functional divergence of human cytoplasmic myosin II: kinetic characterization of the non-muscle IIA isoform. *J Biol Chem* **278**(40):38132–38140.
11. Wang F *et al.* (2003) Kinetic mechanism of non-muscle myosin IIB: functional adaptations for tension generation and maintenance. *J Biol Chem* **278**(30):27439–27448.
12. Billington N, Wang A, Mao J, Adelstein RS, Sellers JR (2013) Characterization of three full-length human nonmuscle myosin II paralogs. *J Biol Chem* **288**(46):33398–33410.
13. Schramek D, et al. (2014) Direct in vivo RNAi screen unveils myosin IIa as a tumor suppressor of squamous cell carcinomas. *Science* **343**(6168):309–313.
14. Conti MA, Adelstein RS (2015) Conditional deletion of nonmuscle myosin II-A Leads to squamous cell carcinoma of the tongue. *Scientific Reports* **5:**14068 | DOI: 10.1038/srep14068.
15. Dhruv, H, McDonough Winslow, WS, *et al.* (2013) Reciprocal activation of transcription factors underlies the dichotomy between proliferation and invasion of glioma cells. *PLOS One*, **8**, e72134.
16. Lei L, *et al.* (2011) Glioblastoma models reveal the connection between adult glial progenitors and the proneural phenotype. *PloS One* **6**(5):e20041.
17. Assanah MC, *et al.* (2009) PDGF stimulates the massive expansion of glial progenitors in the neonatal forebrain. *Glia* **57**(16):1835–1847.
18. Ma X, Adelstein RS (2014) The role of vertebrate nonmuscle myosin II in development and human disease. *Bioarchitecture* **4**(3):88–102.
19. Thorne RG, Nicholson C (2006) In vivo diffusion analysis with quantum dots and dextrans predicts the width of brain extracellular space. *Proc Natl Acad Sci U S A* **103**(14):5567–5572.
20. Cuddapah VA, Robel S, Watkins S, Sontheimer H (2014) A neurocentric perspective on glioma invasion. *Nat Rev Neurosci* **15**(7):455–465.
21. Nicholson C, Hrabětová S (2017) Brain Extracellular Space: The Final Frontier of Neuroscience. *Biophys J* **113**(10):2133–2142.
22. Beadle C, et al. (2008) The role of myosin II in glioma invasion of the brain. *Mol Biol Cell* **19**(8):3357–3368.
23. Bangasser BL, Rosenfeld SS, Odde DJ (2013) Determinants of maximal force transmission in a motor-clutch model of cell traction in a compliant microenvironment. *Biophys J* **105**(3):581–592.
24. Chan CE, Odde DJ (2008) Traction dynamics of filopodia on compliant substrates. *Science* **322**(5908):1687–1691.

25. Davidson, PM *et al*. (2015) Design of a microfluidic device to quantify dynamic intra-nuclear deformation during cell migration through confining environments. *Integr. Biol (Camb),* **7**, 1534-66.
26. Mih, JD, Marinkovic, A, *et al.* (2012) Matrix stiffness reverses the effect of actomyosin tension on cell proliferation. *J. Cell Sci*., **125**, 5974-5983.
27. Pircher, TJ, Petersen, H, *et al.* (1999) Extracellular signal-regulated Kinase (ERK) interacts with signal transducer and activator oftranscription (STAT) 5a. *Mol. Endocrinology,* **13**, 555-565.
28. Malmlo, M, Emilie Roudier, E, *et al. (*2006) MEK-ERK-mediated phosphorylation of Mdm 2 at serine 166 in hepatocytes. *J. Biol. Chem*., **282**, 2288-2296.
29. Deng, Z, Sui, G, *et al.* (2012) Radiation-induced c-Jun activation depends on MEK1-ERK1/2 signaling pathway in microglial cells. *PLOS One*, **7**, e36739.
30. Baruah, PS, Beauchemin, M *et al.* (2016) Dynamic Bcl-xL (S49) and (S62) phosphorylation dephosphorylation during mitosis prevents chromosome instability and aneuploidy in normal human diploid fibroblasts. PLOS One, DOI:10.1371.
31. Cipolletta E, Rusciano MR *et al.* (2015) Targeting the CAMKII/ERK interaction in the heart prevents cardiac hypertrophy. PLOS One, DOI:10.1371.
32. Wei, F, Xie, Y, *et al.* (2010) Both ERK1 and ERK2 kinases promote G2/M arrest in etoposide-treated MCF7 cells by facilitating ATM activation. *Cell Signal*, **22**, 1783-9.
33. Eblen, ST, Slack-Davis, JK, et al. (2004) Mitogen-activated protein kinase feedback phosphorylation regulates MEK1 complex formation and activation during cellular adhesion. *Mol. Cell. Biol.*, **24**, 2308-2317.
34. Solt LA and May MJ. (2008) The IkappaB kinase complex: master regulator of NF-kappaB signaling. *Immunologic Research*, **42**(1-3):3-18.
35. Hayden MS and Ghosh S. (2012) NF-kappaB, the first quarter-century: remarkable progress and outstanding questions. *Genes & Development*, **26**(3):203-34.
36. Karin M and Lin A. (2002) NF-kappaB at the crossroads of life and death. *Nature* Immunology, **3**(3):221-7.
37. Rinkenbaugh AL, Baldwin AS (2016) The NF-κB Pathway and Cancer Stem Cells. *Cells,* **5(**2). doi:10.3390/cells5020016.
38. Lathia JD, Mack SC, Mulkearns-Hubert EE, Valentim CLL, Rich JN (2015) Cancer stem cells in glioblastoma. *Genes Dev* **29**(12):1203–1217.
39. Gangemi RMR, *et al.* (2009) SOX2 silencing in glioblastoma tumor-initiating cells causes stop of proliferation and loss of tumorigenicity. *Stem Cells* **27**(1):40–48.
40. Suvà ML, et al. (2014) Reconstructing and reprogramming the tumor-propagating potential of glioblastoma stem-like cells. *Cell* **157**(3):580–594.
41. Gil, BJ, Pisapia, DJ *et al.* (2014) MRI-localized biopsies reveal subtype-specific differences in molecular and cellular composition at the margins of glioblastoma. *Proc. Nat. Acad. Sci. USA*, **111**, 12550-12555.
42. Han, J, Zhang, F, et al. (2012) RNA interference-mediated silencing of Nanog reduces cell proliferation and induces G0/G1 cell cycle arrest in breast cancer cells. *Cancer Lett*., **321**, 80-88.
43. Robinson, DN and Spudich, JA (2004) Mechanics and regulation of cytokinesis. *Curr. Opin. Cell Biol.*, **16**, 182-88.
44. Tang, YC and Amon, A. (2013) Gene copy number alterations: a cost-benefit analysis. *Cell,* **152**, 394-405.
45. Siegel, JJ and Amon, A (2012) New insights into the troubles of aneuploidy. *Ann. Rev. Cell Dev. Biol.* **28**, 189-214.
46. Gordon, DJ, Resio, B, and Pellman, D (2012) Causes and consequences of aneuploidy in cancer. *Nat. Rev. Genetics*, **13**, 189-203.
47. Pepin, KM, McGee, KP, *et al.* (2018) MR elastography analysis of glioma stiffness and IDH1-mutation status. *Am. J. Neurorad.,* **39**, 31-36.
48. Streitberger, K-J, Reis-Zimmerman, M *et al.* (2014) High-resolution mechanical imaging of glioblastoma by multifrequency magnetic resonance elastography. *PLOS One*, **9**, e110588.

49. Cheng S, Clarke E C and Bilston L E (2008) Rheological properties of the tissues of the central nervous system: a review. *Med. Eng. Phys*. **30,** 1318–37.
50. Chatelin S, Constantinesco A and Willinger R (2010) Fifty years of brain tissue mechanical testing: from *in vitro* to *in vivo* investigations. *Biorheology* **47,** 255–76
51. Swaminathan, V, et al. (2011) Mechanical stiffness grades metastatic potential in patient tumor cells and in cancer cell lines. *Cancer Res*., **71**, 5075–5080.
52. W. Xu, R. Mezencev, B. Kim, L. Wang, J. McDonald and T. Sulchek, (2012) Cell stiffness Is a biomarker of the metastatic potential of ovarian cancer cells. *PLoS One*, **7**, e46609.
53. Folkman, J. and Moscona, A. (1978) Role of cell shape in growth control. *Nature,* **273**,345-349.
54. Chen, C. S., Mrksich, M., Huang, S., Whitesides, G. M. and Ingber, D. E. (1997) Geometric control of cell life and death. *Science,* **276**, 1425-1428.
55. Meyers, J, Craig, J, and Odde, DJ (2006) Potential for control of signaling pathways via cell size and shape. *Current Biology,* **16**, 1685-1693.
56. Moreno, E., Valon, L., *et al*. (2019) Competition for space induces cell elimination through compaction-driven ERK downregulation. *Current Biology*, **29**, 23-34.
57. Chandrasekharan, U, *et al.* (2013) Release of nonmuscle myosin II from the cytosolic domain of tumor necrosis factor receptor 2 Is required for target gene expression. *Science Signalling*, **6**(284), 1-13.
58. Maeng, Y-S *et al.* (2006) ERK is an anti-inflammatory signal that suppresses expression of NF-κB-dependent inflammatory genes by inhibiting IKK activity in endothelial cells. *Cellular Signalling* **18**, 994–1005.
59. Rinkenbaugh AL, Baldwin AS (2016) The NF-κB Pathway and Cancer Stem Cells. *Cell,s* **5**(2). doi:10.3390/cells5020016.
60. Guzman ML, *et al.* (2001) Nuclear factor-kappaB is constitutively activated in primitive human acute myelogenous leukemia cells. *Blood* **98**(8):2301–2307.
61. Rajasekhar VK, Studer L, Gerald W, Socci ND, Scher HI (2011) Tumour-initiating stem-like cells in human prostate cancer exhibit increased NF-κB signalling. *Nat Commun* **2**:162.
62. Myant KB, *et al.* (2013) ROS production and NF-κB activation triggered by RAC1 facilitate WNT-driven intestinal stem cell proliferation and colorectal cancer initiation. *Cell Stem Cell* **12**(6):761–773.
63. Cao L, *et al.* (2015) Osteopontin promotes a cancer stem cell-like phenotype in hepatocellular carcinoma cells via an integrin-NF-κB-HIF-1α pathway. *Oncotarget* **6**(9):6627–6640.
64. Walker, A *et al.* (2010) Non-muscle myosin II regulates survival threshold of pluripotent stem cells. *Nature Com.*, **1**(71), 1-9.
65. Wong, SY, *et al.* (2015) Constitutive activation of myosin-dependent contractility sensitizes glioma tumor-initiating cells to mechanical inputs and reduces tissue invasion. *Cancer Research*, **75**, 1113-1122.
66. Surcel, A et al. (2015) Pharmacological activation of myosin II paralogs to correct cell mechanics defects. *Proc. Nat. Acad. Sci. USA*, **112**(5), 1428-1433.
67. Xie, Q, Mittal, S, and Berens, ME (2014) Targeting adaptive glioblastoma: an overview of proliferation and invasion. *Neuro Oncol*, **16**(2), 1575-84.
68. Lu, KV, Chang, JP, *et al.* (2012) VEGF inhibits tumor cell invasion and mesenchymal transition through a Met/VEGFR2 complex. *Cancer Cell*, **22**(1), 21-35.
69. Norden, AD, Young, GS *et al.* (2008) Bevacizumab for recurrent malignant gliomas: efficacy, toxicity, and patterns of recurrence. *Neurology,* **70**(10), 779-87.
70. Venere, M, *et al.* (2015) The mitotic kinesin Kif11 is a central driver of invasion, proliferation, and self renewal in glioblastoma. *Science Translational Medicine*, **7**(304), 304ra143.
71. Lu, H, Sun, Y, and Simmons, CA (2013) Determination of local and global elastic moduli of valve interstitial cells cultured on soft substrates. *J. Biomechanics*, **46**, 1967-71.
72. Georgouli, M *et al.* (2019) Regional activation of myosin II in cancer cells drives tumor progression via a secretory cross-talk with the immune microenvironment. *Cell*, **176**, 1-18.
73. Seano, G. et al. (2019) Solid stress in brain tumours causes neuronal loss and neurological dysfunction and can be reversed by lithium. *Nature Biomedical Engineering*, https://doi.org/10.1038/s41551-018-0334-7.

74. Schafer, A and Radmacher, M (2005) Influence of myosin II activity on stiffness of fibroblast cells. *Acta Biomater.*, **1**, 273-80.
75. Schwartz, MA, Assoian, RK (2001) Integrins and cell proliferation: regulation of cyclin dependent kinases via cytoplasmic signaling pathways. *J. Cell Sci.* **114**, 2553-2560.
76. Watanabe, K *et al.* (2007) A ROCK inhibitor permits survival of dissociated human embryonic stem cells. *Nature Biotechnology*, **25**, 681-686.
77. Miroshnikova, YA *et al.* (2014) Tissue mechanics promote IDH1-dependent HIF1α–tenascin C feedback to regulate glioblastoma aggression. *Nature Cell Biology*, **18**, 1336-1345.
78. Bangasser, BL *et al.* (2017) Shifting the optimal stiffness for cell migration. *Nature Comm.*, 8:15313.

FIGURE LEGENDS

Fig. 1: Deletion of NMIIA and NMIIB in GBM increases survival, and reduces proliferation. (A) Mouse model of GBM. (B) Kaplan-Meier curves comparing the survival of retrovirally-induced GBMs in mice with floxed alleles for PTEN (n=9) and for NMIIA, NMIIB and PTEN (n=16) (C) Western blot demonstrating depletion of NMIIB heavy chain isoform using sh-RNA lentivirus from glioma cell lines genetically deleted for NMIIA with PDGF-IRES-cre retrovirus. (D) Nuclear doubling rate as measured by nuclear count every 3 hours for 5 days, using Histone 2B-RFP expressing glioma cells (n=3).

Fig. 2: NMIIA is necessary glioma migration and dispersion. (A) Immunohistochemistry (IHC) of end stage tumor sections stained for the HA epitope on infected tumor cells. (B) Higher magnification of (A). *T* indicates tumor, *CX* indicates cerebral cortex. While tumors deleted for both PTEN and NMIIA are able to disperse through white matter, their invasion into the cortex is impaired. (C) Migration through 3μm Transwell pore membrane towards 10% FBS (scale bar 200 μm). (D) Mean number of DAPI-stained nuclei per high power field (n=8-10) migrating through 3μm Transwells for PTEN-deleted and PTEN, NMIIA co-deleted tumors, along with corresponding results for murine PTEN-deleted GBMs where NMIIA expression was suppressed with shRNA, compared to PTEN-deleted tumor cells transfected with non targeting (NT) shRNA.

Fig. 3: Loss of NMIIA decreases survival in GBM and creates larger tumors. (A) Kaplan-Meier curves of mice bearing retrovirally-induced GBMs deleted for PTEN (*black*, n=9), NMIIA and PTEN (*red*, n=13), TP53 (*green*, n=6) and NMIIA (*blue*, n=8). Median survivals are 79 dpi, 62 dpi , 31 dpi, and not determined, respectively. Log-rank p values are PTEN-/- vs. PTEN-/-NMIIA-/- $p=0.0003$, NMIIA-/- vs. PTEN-/-NMIIA-/- $p<0.0001$, p53-/- vs. PTEN-/-NMIIA-/- $p<0.0001$, and p53-/- vs. NMIIA-/- $p<0.0001$. (B) Anti-HA IHC of brains from mice with floxed alleles for PTEN or PTEN and NMIIA that were injected 35 days prior with retrovirus encoding a PDGF-HA fusion protein and the cre recombinase. (C) Area of HA-positive tumor measured by number of HA-positive pixels for PTEN-deleted (*black*) compared to PTEN/MNNIIA co-deleted (*red*) tumors. (D) 50,000 luciferase expressing PTEN-deleted and PTEN/NMIIA-co-deleted tumor cells were injected into the white matter of NSG mice. Luminescence was monitored over the subsequent 54 days, and photon flux is plotted on a logarithmic scale versus days after injection. For PTEN-deleted cells (*blue*), the terminal growth data fits a single exponential process, defining a doubling time of 10.9 days. The corresponding doubling time for PTEN/NMIIA co-deleted cells (*red*) is 3.9 days.

Fig. 4: NMIIA deletion alters GBM cell mechanics in a manner influenced by the stiffness of the tumor environment. (A) Global cell deformation was performed using a JPK Nanowizard 4 Atomic Force Microscope equipped with cantilevers of a nominal stiffness of 2.4 N/m with a 25 μm diameter sphere attached (Novascan). Measurements of cell deformability were made on PTEN-deleted (black) and PTEN/NMIIA co-deleted cells grown on glass coverslips coated with collagen I. Force *versus* distance curves were converted into stress *versus* percentage of unstressed cell height curves with the assumption that normal stress can be calculated as the ratio of the applied force to the area of deformation. The (%) cell height was calculated as the percentage of the total cell height that underwent indentation at a given force. (B) The local Young's modulus was calculated from local cell cortex deformation measurements on PTEN deleted (*blue*) and PTEN/NMIIA co-deleted (*red*) murine GBM cells, cultured on a range of substrate stiffness. Data are plotted as mean ± SEM. This reveals that NMIIA deletion reduces Young's modulus compared to NMIIA intact cells on soft surfaces, and increases it on hard surfaces. (C) Cell height was measured on NMIIA intact (*blue*) and deleted (*red)* tumor cells cultured on fibronectin-coated hydrogels (Softwell, Matrigen, Brea, CA) covering a range of stiffness from 0.2 kPa to plastic. NMIIA-deleted cells are shorter than NMIIA intact ones, and this difference decreases with increasing stiffness. Cell height for NMIIA-deleted cells on plastic is also significantly increased compared to the same cells grown on a 1 kPa surface (D) Plot of proliferation rate constant *versus* substrate stiffness for PTEN-deleted (*blue*) and PTEN/NMIIA co-deleted (*red*) tumor cells grown on fibronectin-coated Softwells (Matrigen, Brea, California). Growth kinetics were fit to a single exponential growth equation to yield rate constants, and each point represents the mean ± SEM of 5 replicates. Differences in rate constants

between PTEN-deleted and PTEN/NMIIA co-deleted were significant on substrates of 0.2 and 0.5 kPa (***p=0.012; **p=0.017). Furthermore, the difference in rate constant for PTEN/NMIIA co-deleted cells grown on 0.5 kPa and on plastic is also significant (*p=0.04).

Fig. 5: NMIIA deletion alters phosphorylation of signaling molecules in a manner that is modulated by substrate stiffness. (A) Ratios of normalized phosphorylation signal for PTEN/NMIIA co-deleted to PTEN deleted tumors. *Upper Panel*: Phospho-proteins with ratios ≥ 2.0 on fibronectin-coated soft (0.5 kPa) but not hard (plastic) surfaces. *Lower Panel*: Phospho-proteins with ratios ≥2.0 on hard but not soft surfaces. (B) *Left*: Lysates from PTEN/NMIIA co-deleted (PTEN/NMIIA-/-) and PTEN deleted (PTEN-/-) cells cultured on 0.5 kPa Softwells (*Soft*) and plastic (*Hard*) were blotted with antibodies to ERK1/2 and to pT202/pY204 ERK1/2. *Right:* Plot of the phosphoERK/Total ERK ratio for PTEN-deleted and PTEN/NMIIA co-deleted cells cultured on 0.5 kPa and plastic substrates (n=4). (C) *Left:* NMIIA-intact murine GBM cells were plated on 96 well Softwell plates, with substrate stiffness ranging from 0.2 kPa to glass, and treated with a range of concentrations of the ERK1/2 inhibitor SCH772984. Fractional cell viability, relative to vehicle (DMSO) treated cells is plotted as a function of drug concentration and over the range of substrate stiffness. This shows that SCH772984 has no effect over this stiffness range. *Middle:* The corresponding experiment using NMIIA-deleted cells. Data are fit to hyperbolic dose response relationships for all but the 50 kPa and glass surfaces, and the fitting defines maximum extrapolated degrees of cell kill. *Right:* Plot of maximum cell kill versus substrate stiffness from the data in the middle panel.

Fig. 6. NMIIA deletion enhances the activity of NFκB, Sox2, and Nanog in cells grown on a stiff substrate. (A) Two PTEN-deleted GBM cell lines were infected with non-targeting (NT) or NMIIA-targeting shRNA-encoding lentiviruses. They were transiently transfected with a luciferase gene under control of an NFκB response element and a mammalian expression vector for β-galactosidase (pCMV-βgal). NFκB-dependent luciferase activity is plotted as mean +/-SEM (n = 12). (B) NFκB luciferase reporter assays were performed MDA-MB-231 cells expressing non-targeting or either of two NMIIA-targeting shRNA as above. Data is plotted as mean +/-SEM (n = 9). (C) NFκB luciferase reporter assays were performed on non-transformed keratinocytes that were treated with either NT shRNA or two different NMIIA-targeting shRNAs. (n=8) (D) The MDA-MB-231 cells depleted for NMIIA were stably transfected with an shRNA resistant GFP-NMIIA heavy chain fusion protein and sorted for GFP expression. While NFκB luciferase activity was significantly increased in cells depleted of NMIIA, expression of the GFP-NMIIA heavy chain returned NFκB activity to baseline. Data is plotted as mean +/- SEM (n = 17). (E) GBM cell lines treated with NT or NMIIA-targeting shRNA were transiently transfected with the Sox2 response element luciferase reporter and normalized luciferase activity was measured (n=6). (F) MDA-MB-231 cells were transiently transfected with luciferase reporter construct under the control of Nanog transcriptional response element along with a control vector (pCMV-Renilla). Promoter activity was measured by luciferase activity. Values were normalized to Renilla activity to correct for transfection efficiency (n=9).

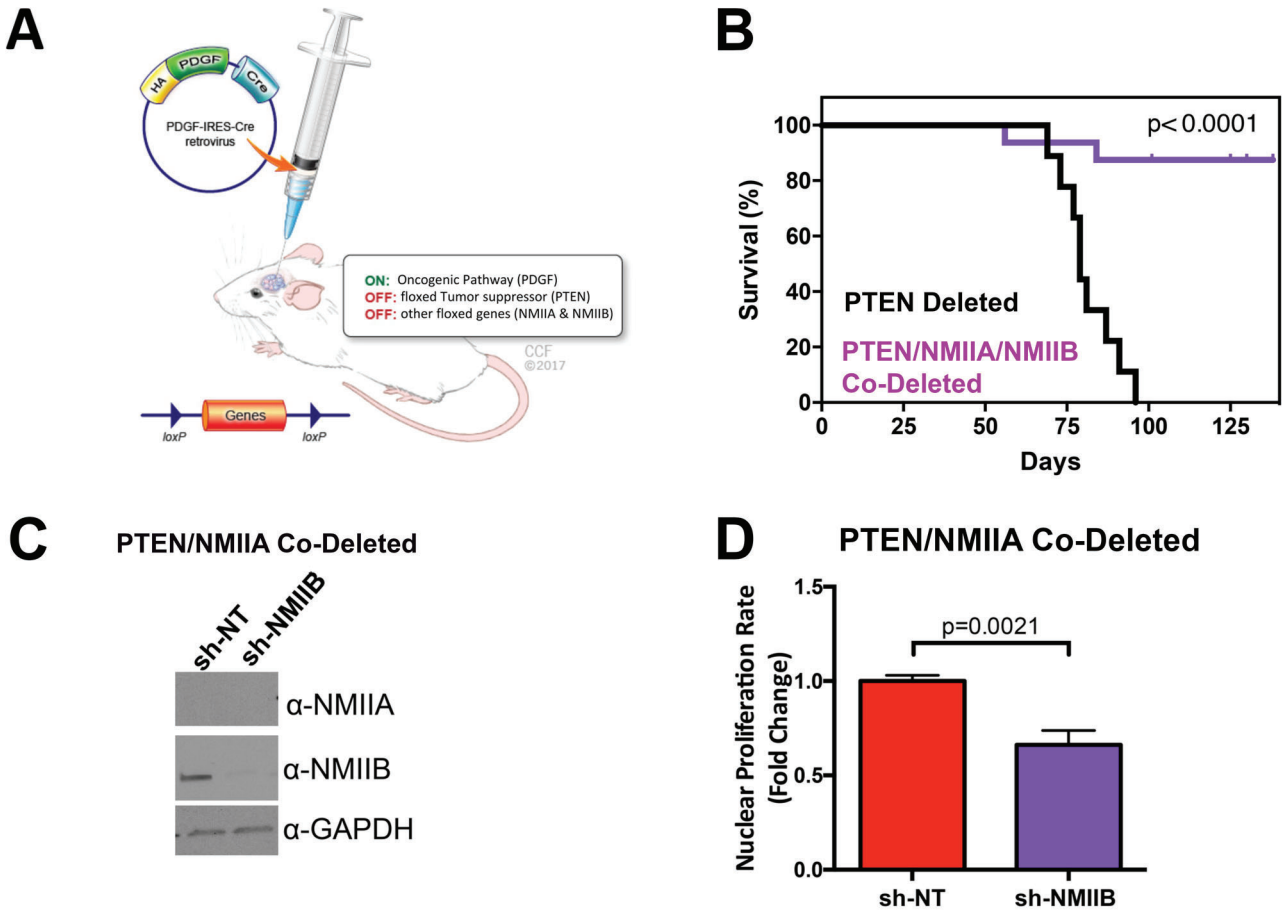
A
HA
PDGF
Cre
PDGF-IRES-Cre retrovirus
ON: Oncogenic Pathway (PDGF)
OFF: floxed Tumor suppressor (PTEN)
OFF: other floxed genes (NMIIA & NMIIB)
CCF ©2017
Genes
loxP
loxP
B
p< 0.0001
Survival (%)
PTEN Deleted
PTEN/NMIIA/NMIIB Co-Deleted
Days
C
PTEN/NMIIA Co-Deleted
sh-NT
sh-NMIIB
α-NMIIA
α-NMIIB
α-GAPDH
D
PTEN/NMIIA Co-Deleted
p=0.0021
Nuclear Proliferation Rate (Fold Change)
sh-NT
sh-NMIIB

Figure 1

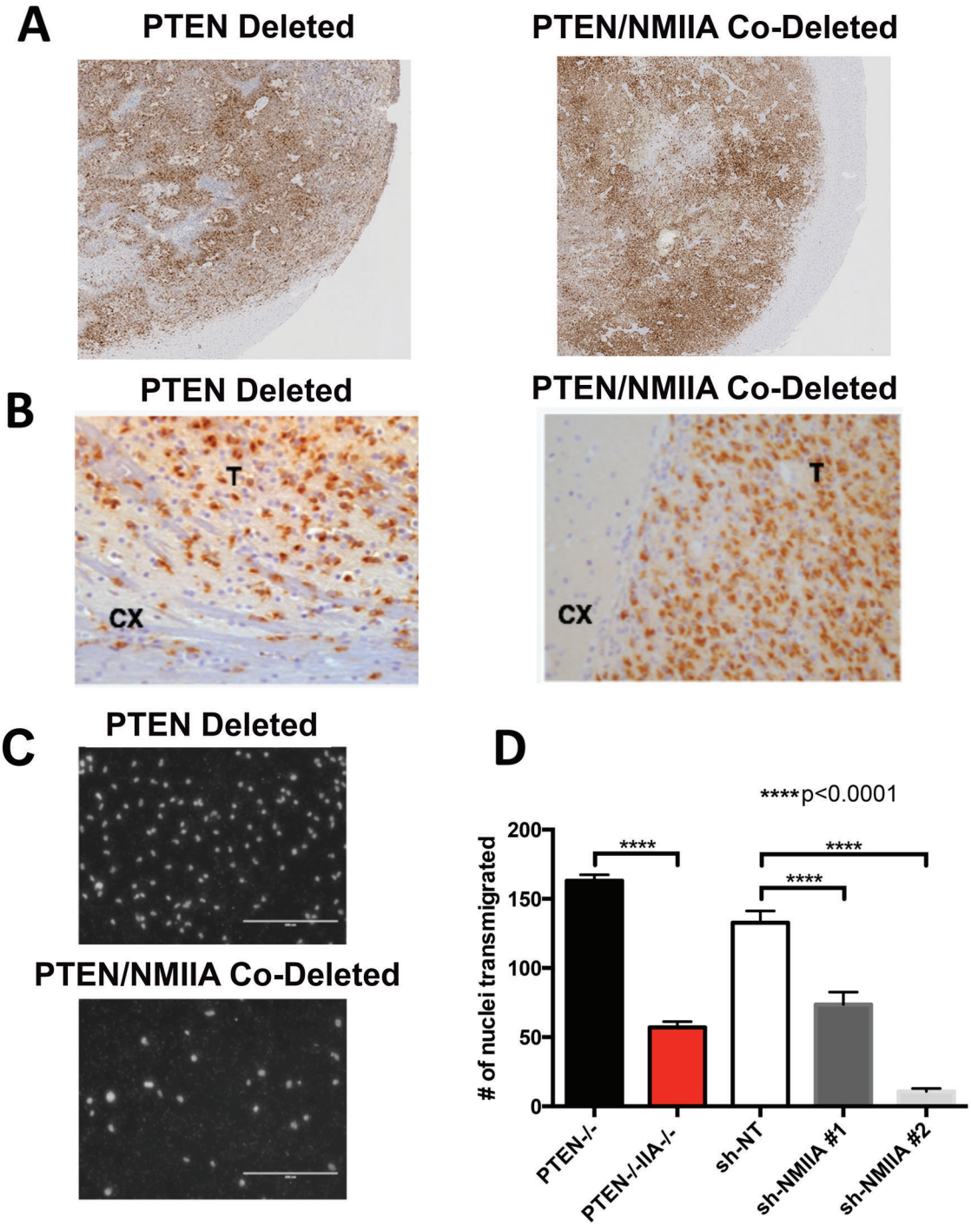
A
PTEN Deleted
PTEN/NMIIA Co-Deleted
B
PTEN Deleted
PTEN/NMIIA Co-Deleted
T
CX
T
CX
C
PTEN Deleted
PTEN/NMIIA Co-Deleted
D
****p<0.0001
# of nuclei transmigrated
200
150
100
50
0
****
****
****
PTEN-/-
PTEN-/-IIA-/-
sh-NT
sh-NMIIA #1
sh-NMIIA #2

Figure 2

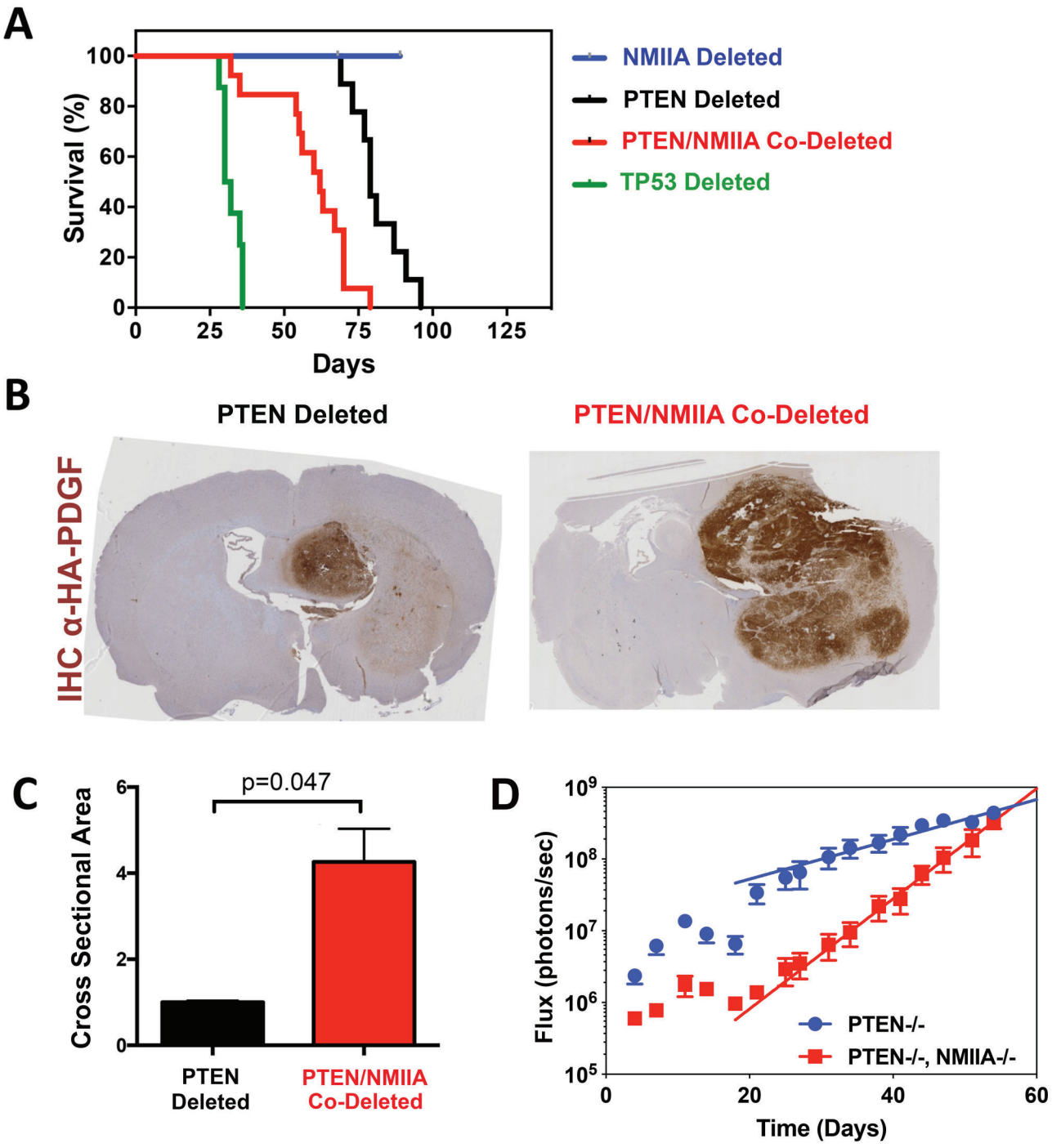
A
Survival (%)
100
80
60
40
20
0
0
25
50
75
100
125
Days
NMIIA Deleted
PTEN Deleted
PTEN/NMIIA Co-Deleted
TP53 Deleted
B
PTEN Deleted
PTEN/NMIIA Co-Deleted
IHC α-HA-PDGF
C
p=0.047
Cross Sectional Area
6
4
2
0
PTEN Deleted
PTEN/NMIIA Co-Deleted
D
Flux (photons/sec)
10^9
10^8
10^7
10^6
10^5
0
20
40
60
Time (Days)
PTEN-/-
PTEN-/-, NMIIA-/-

Figure 3

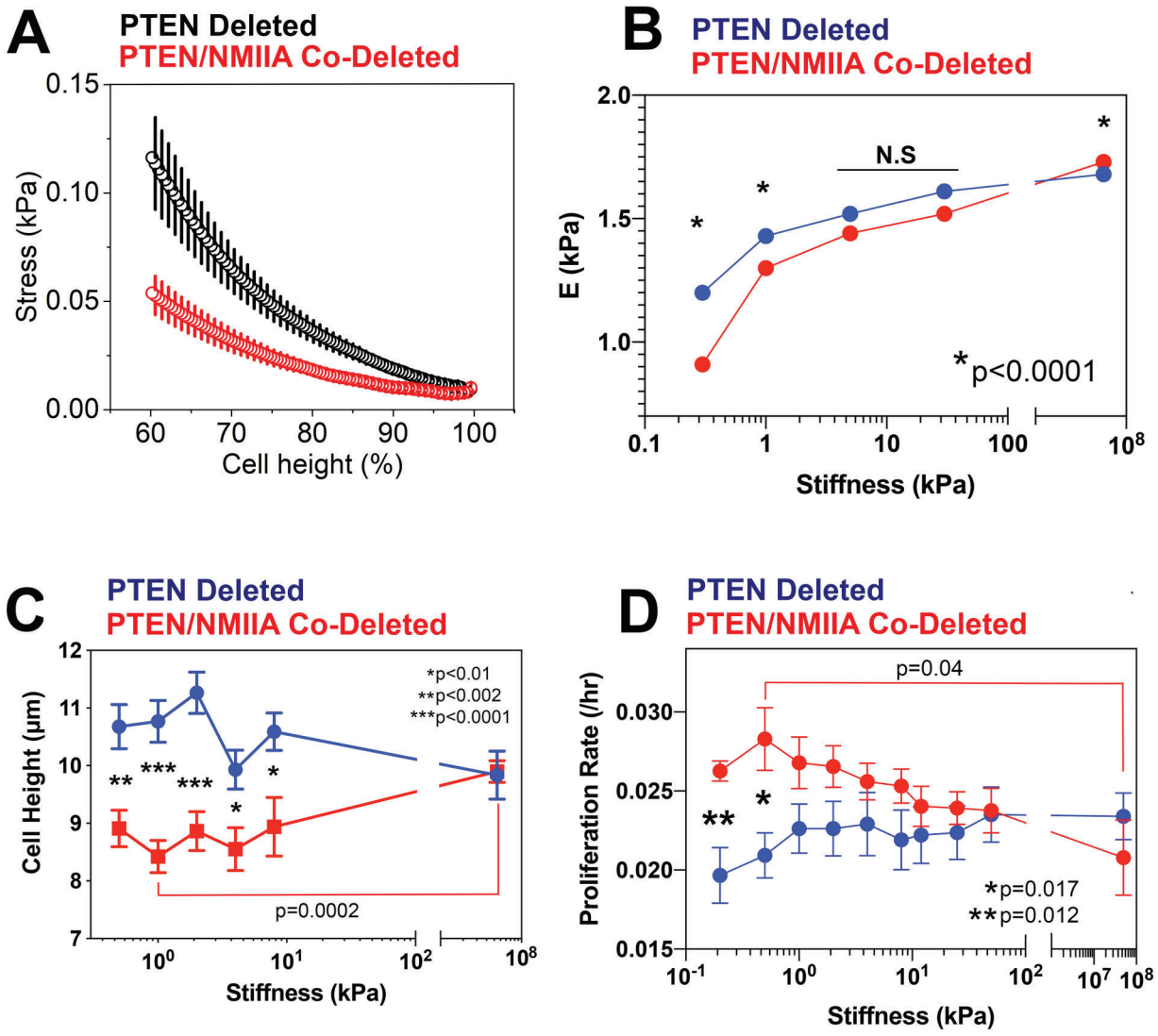
A
PTEN Deleted
PTEN/NMIIA Co-Deleted
Stress (kPa)
Cell height (%)
B
PTEN Deleted
PTEN/NMIIA Co-Deleted
E (kPa)
N.S
*p<0.0001
Stiffness (kPa)
C
PTEN Deleted
PTEN/NMIIA Co-Deleted
Cell Height (μm)
*p<0.01
**p<0.002
***p<0.0001
p=0.0002
Stiffness (kPa)
D
PTEN Deleted
PTEN/NMIIA Co-Deleted
Proliferation Rate (/hr)
p=0.04
*p=0.017
**p=0.012
Stiffness (kPa)

Figure 4

A

Protein	Site	Effect of Phosphorylation	Soft	Hard
STAT5A	S780	regulates transcriptional activity	3	1.6
cJUN	S73	produces anti-apoptotic effect	2.6	1.1
MDM2	S166	ubiquitinates p53	2.4	1.7
BCL-XL	S62	maintains chromosome integrity in mitosis	2.3	1.3
CAMK II	T286	activates MEK/ERK pathway	2.3	1.4
CHK2	T68	maintains mitotic checkpoint	2	1.6
IκBε	S22	releases NFκB from IκB inhibition	1.5	3
14-3-3ζ	S58	activates stress response	1	2.9
P38MAPK	Y182	regulates downstream effector, including Tau	1.6	2.5
MEK1	T291	reduces ERK signaling	1.2	2.3
HSP90B	S254	reduces chaperone activity	1.1	2.3
βcatenin	S37	enhances proteosomal degradation	1	2.1
TAU	S404	regulates microtubule binding	1.7	2.1
P70S6	S424	activates S6 kinase, increasing translation	0.9	2.1
IκBα	Y42	releases NFκB from IκB inhibition	1.1	2

B

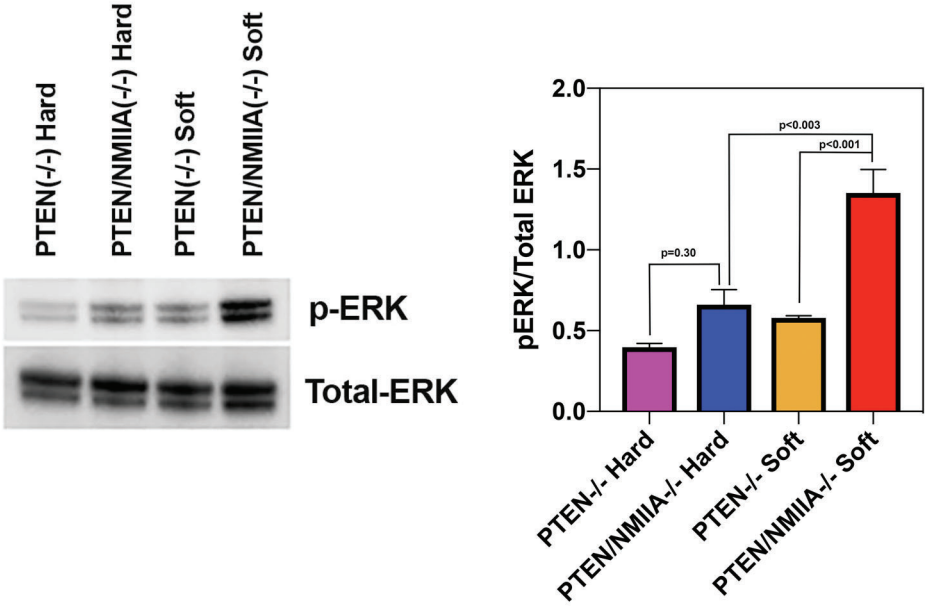

C

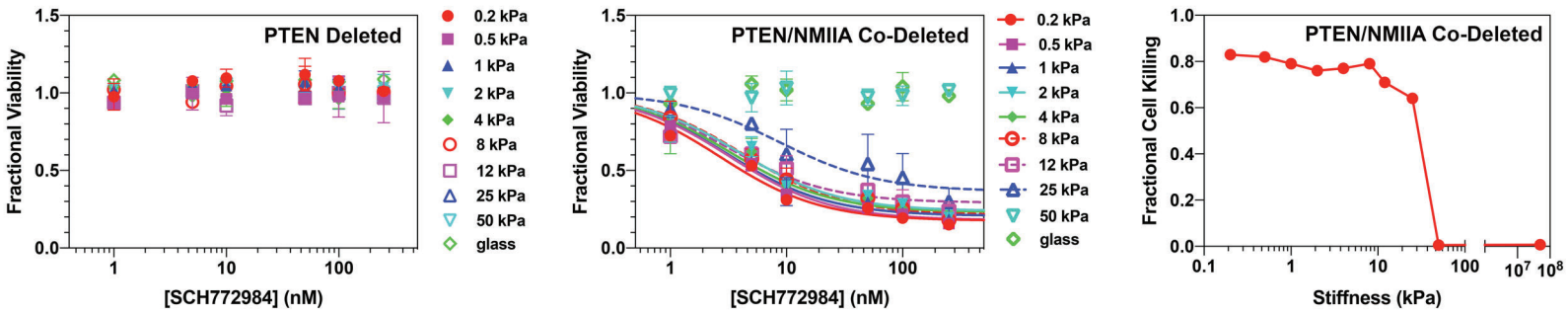

Figure 5

** p≤0.01
*** p≤0.001
**** p≤0.0001

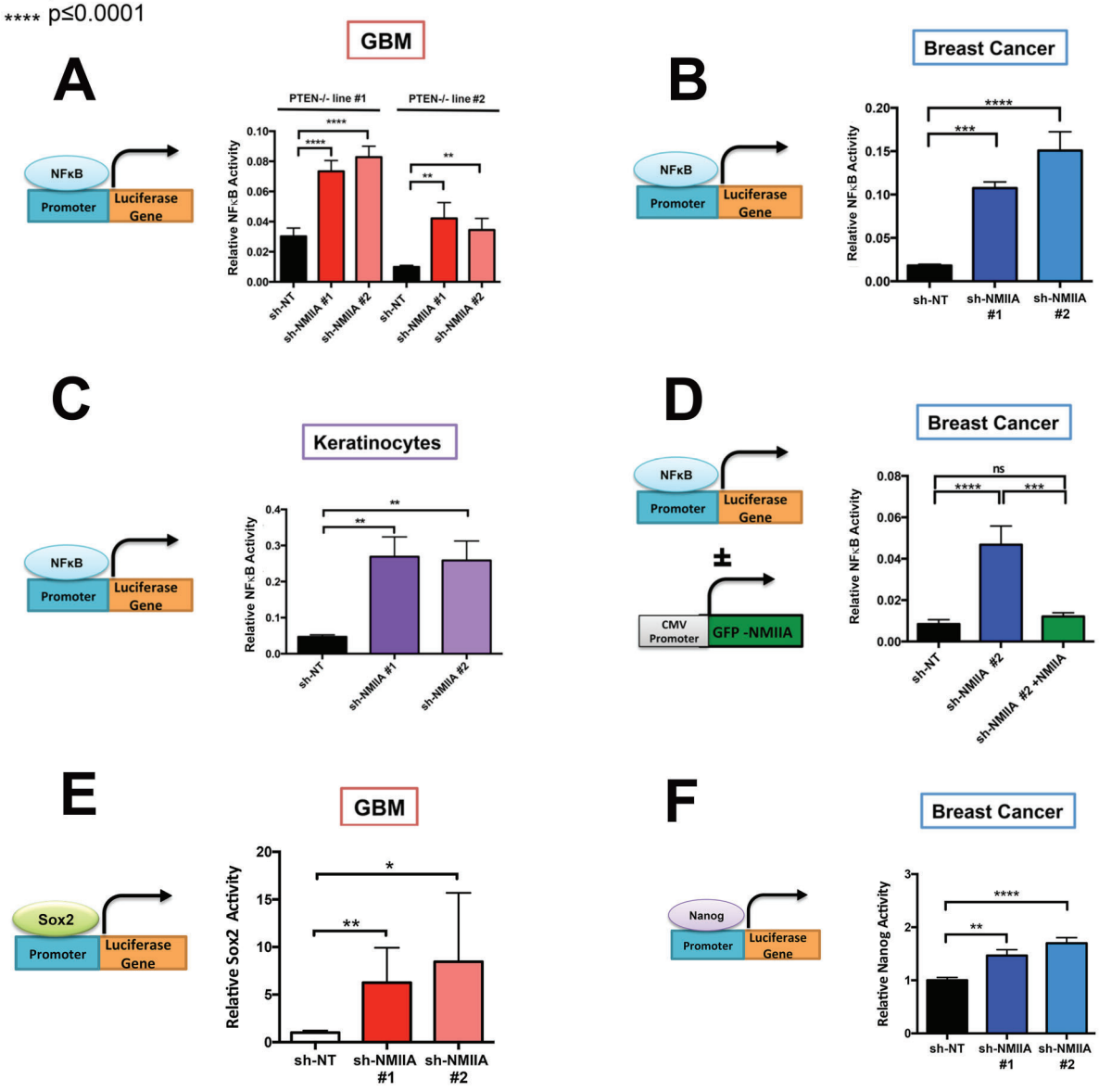

Figure 6

MATERIALS AND METHODS

A complete discussion of all methods, including generation of murine tumors, reporter assays, tumor invasion assays, and histologic analysis is included in the SI Appendix.

ACKNOWLEDGEMENTS

This work was supported by NIH grants CA172986, CA210910, and NS073610 (to SSR), GM050009 (to TE), NS073610 and NS052738 (to PC), CA210184 and HL082792 (to JL), GM111942 and CA193417 (to PAJ), CA210190 and CA172986 (to D.J.O), and by awards from the Department of Defense Breast Cancer Research Program (Breakthrough Award BC150580 to JL), and the National Science Foundation [CAREER Award CBET-1254846 to JL]. This work was performed in part at the Cornell NanoScale Facility, an NNCI member supported by NSF Grant NNCI-1542081.

COMPETING INTERESTS

The authors declare that they have no competing interests.

AUTHOR CONTRIBUTIONS

HSP, RSK, VR, JFC, JL, PC, TE, PJ, DJO, UC, and SSR conceived of the study; and HSP, RSK, VR, JFC, AD, KP, MM, AL, ESB, RW, JL, PC, DJO, PJ, TE, and SSR designed and conducted the experiments. The manuscript was written by HSP, RSK, TE, and SSR. All of the authors discussed the results and edited and approved the final manuscript.

SUPPLEMENTARY METHODS

Mice

All mouse procedures were performed with adherence to protocols approved by the Institute Animal Care and Use Committees at the Lerner Research Institute of the Cleveland Clinic and the Mayo Clinic. The homozygous floxed PTEN mice used as controls were obtained from Jackson Laboratory (Stock # 004597 Strain Name: C;129S4-Pten^{tm1Hwu}IJ). These mice were bred with homozygous floxed NMIIA mice (MMRRC #32096) (1) and homozygous floxed NMIIB mice (MMRRC# 016981-UNC) (2) generously provided by Dr. Robert S. Adelstein.

Retrovirus production and intracerebral injections

The PDGF-IRES-cre and PDGF-IRES-GFP retroviruses were generated according to methods described previously (3). Briefly, the self-inactivating bicistronic expression vectors consist of a 0.8 kb fragment that codes for a PDGF-B hemagglutinin (HA) fusion protein, cloned into the first multiple cloning site of the pQC-X-I-X vector (Clontech). Replication-deficient retroviruses pseudotyped with VSV-G coats were produced by transient transfection of GP2-293 cells. Viral supernatants were collected at 36 h post-transfection. Subsequently, the viral supernatant was concentrated by high-speed centrifugation, and the concentrated virus stock was resuspended in Opti-MEM media. The viral titer was determined by transducing RiboTag cells with serial 1:10 dilutions from the concentrated virus stock in a total volume of 1 ml. At 48 h after infection, HA positive cell clusters or GFP positive cell clusters were determined by immunofluorescence with a secondary antibody to either HA (PDGF-I-cre) or GFP (PDGF-IRES-GFP).

For intracranial retrovirus injection, adult mice (8-10 weeks post natal) were anesthetized with ketamine/xylazine cocktail. The mice were immobilized on a stereotactic fixation instrument (Kopf Model 926, Brain Tree). A lateral incision of the scalp was made and the skull exposed. The site of the burr hole (Micro-Drill, Cellpoint Scientific Inc) through the skull was determined by the stereotactic coordinates relative to the bregma: 2 mm rostral, 2 mm lateral and 1.5 mm deep. One microliter of retrovirus at a titer of 10^5 CFU/ml was injected through the burr hole at a rate of 0.2 µl/min with a Hamilton syringe (Model 801, Hamilton Company). To avoid retrovirus extrusion, the Hamilton needle (Hamilton, Cat No. 7762-01) was left in place for two minutes before withdrawal at a speed of 1 mm per minute. The adult mice were observed daily and sacrificed when they showed symptoms of morbidity.

Glioma cell line isolation and culture:

The protocol for primary tumor isolation is based on a published report (4) and adapted as described (5). Selection of the euthanasia method was based on the IACUC guidelines of the Cleveland Clinic and the Mayo Clinic. Each cell line was isolated from one GBM tumor-bearing mouse that was deeply anesthetized, as demonstrated by loss of nose, tail and hind limb pinch response, with an intraperitoneal injection of a mixture of ketamine (100 mg/kg) and xylazine (10 mg/kg). After decapitation, an *ex-vivo* gross total resection of the tumor was performed and the tumor region was minced with a razor blade. Tumor tissue was resuspended in 2.5% TrypLE (Gibco 12604-013) 1X Anti Anti 100X (Gibco 15240-062) for enzymatic and mechanical dissociation. First, cells were incubated for 5 minute in a 37 °C shaking bath, followed mechanical dissociation using two different sized needles (i.e. 16 ½ G and 18 ½ G). After the dissociation, cells were filtered through a 70µm mesh (BD Falcon) into DMEM media containing 10% heat-inactivated FBS in order to inactivate the trypsin. Cells were centrifuged for 3 minutes at 1000 RPM, and then re-suspended and grown in murine GBM media containing a 2:1 mixture of basal media and B104 conditioned media (6), further supplemented with 10 ng/ml PDGF-AA (Sigma P3076) and 10 ng/ml FGFb (Sigma F0291). Basal media contained N2 supplement (Gibco), 20 ng/ml T3 (Sigma), 0.5% FBS, and penicillin/streptomycin/amphotericin (Invitrogen) in DMEM (Gibco). B104 conditioned media was collected from confluent cultures of the B104 neuroblastoma cell line maintained in basal media for 48 hours. Primary glioma cells were grown on tissue culture plates coated with 10µg/mL Fibronectin (Sigma F1141).

MDA-MB-231 cell culture

Human triple-negative–like breast carcinoma MDA-MB-231 cells were purchased from The American Tissue Culture Collection (ATCC, Manassas, VA) and maintained in complete RPMI 1640 media containing 10% fetal bovine serum at 37°C in a humidified atmosphere (5% CO2).

Lentiviral production and transduction

Knockdown of NMIIA was achieved via lentiviral infection with shRNA-encoding constructs. The lentiviral plasmid vector pLKO.1-puro based shRNA clones and control shRNA vector were purchased from Sigma-Aldrich (St Louis, MO, USA) and, after initial screening for effectiveness, the following constructs were used in MDA-MB-231 cells for these studies: Non targeting control (SHC002); NMIIA sh-RNA [TRCN000029468 (sh-NMIIA #1), TRCN0000285480 (sh-NMIIA #2), TRCN0000276055 (sh-NMIIA #3)]. The following constructs were used in the mouse glioma cells for these studies: Non targeting control (SHC002); NMIIA sh-RNA [TRCN0000071504 (sh-NMIIA #1), TRCN0000304377 (sh-NMIIA #2). RFP-Histone H2B fluorescent tags, were purchased from Addgene and packaged in HEK293t cells, as described for shRNA constructs. Each of the pLK0.1 targeting constructs was co-transfected with pCMV-R8.2 and pCMV-VSVG helper plasmids into HEK-293T cells via Lipofectamine 3000 transfection agent (Life Technologies, catalog # 11668027) in serum-free medium. After an 8 hour incubation, viral particle containing medium was removed and replaced with fresh complete medium. Transfected cells were then grown in DMEM media containing 10% FBS for 24 hours at 37ºC, 5% CO_2. Media containing virus was harvested and centrifuged for 10 mins in a clinical specimen centrifuge and then filtered through a 0.45 µm filter. MDA-MB-231 or mouse glioma cells were infected by incubating with virus containing media overnight. Cells were selected for positive shRNA infection using puromycin (1ug/ml) for five to seven days and maintained in 0.1ug/mL puromycin containing media.

Proteomics

To determine the relative quantification of the three NMII isoforms, protein lysates made from PTEN-deleted and PTEN/NMIIA co-deleted primary GBM cell lines were subjected to electrophoresis using 4–12% polyacrylamide gradient gels in SDS running buffer followed by staining with Coomassie blue. Protein concentrations were normalized using the Pierce BCA assay (Thermo Sci) and then equal amount of total protein lysates loaded in each gel lane. After destaining, the region of the gel containing the myosin II heavy chain was excised. For the protein digestion, the bands were then washed/destained in 50% ethanol, 5% acetic acid and then dehydrated in acetonitrile. The samples were then reduced with DTT and alkylated with iodoacetamide prior to the in-gel digestion. All bands were digested in-gel using trypsin, by adding 10 µL 5 ng/µL trypsin in 50 mM ammonium bicarbonate and incubating overnight at room temperature to achieve complete digestion. The peptides that were formed were extracted from the polyacrylamide in two aliquots of 30 µL 50% acetonitrile with 5% formic acid. These extracts were combined and evaporated to <10 µL in a Speedvac and then resuspended in 1% acetic acid to make up a final volume of ~30 µL for LC-MS analysis. The LC-MS system was a Finnigan LTQ-Obitrap Elite hybrid mass spectrometer system. The HPLC column was a Dionex 15 cm x 75 µm id Acclaim Pepmap C18, 2µm, 100 Å reversed phase capillary chromatography column. Five µL volumes of the extract were injected and the peptides eluted from the column by an acetonitrile/0.1% formic acid gradient at a flow rate of 0.3 µL/min were introduced into the source of the mass spectrometer on-line. The nano electrospray ion source is operated at 1.9 kV. The digest was analyzed using the data dependent multitask capability of the instrument acquiring full scan mass spectra to determine peptide molecular weights and product ion spectra to determine amino acid sequence in successive instrument scans. The data was analyzed by using all CID spectra collected in the experiment to search mouse reference sequence databases with the search program Mascot. Sequest searches were also performed against mouse myosin IIA, IIB, and IIC protein sequences to confirm the identifications and sequence coverage.

Limiting dilution assays

The *in vitro* limiting dilution/ tumorsphere formation assays were performed on cells that were cultured in duplicate rows of serial dilutions per well (1, 5, 10, 20 cells) in a 96-well ultra-low adhesive plates with 200µl serum-free DMEM/F12 medium supplemented with 20ng/ml basic fibroblast growth factor (Invitrogen), 10ng/ml epidermal growth factor (BioSource, Grand Island, NY, USA), 2% B27 (Invitrogen), 10µg/ml insulin. The frequency of sphere formation was calculated in such a way that a well with a tumorsphere was counted as a positive well. Tumorspheres were counted and diameters measured after 2 weeks, using a phase contrast microscope. The stem frequencies were calculated using an extreme limiting dilution algorithm (ELDA) (http://bioinf.wehi.edu.au/software/elda/).

NFκB Luciferase assay

NFκB reporter and β-galactosidase Luciferase reporter assays were performed by co-transfecting MDA-MB-231 cells or mouse glioma cells with the NFκB reporter construct (Agilent #219078) and a β-galactosidase-expressing control plasmid (Clonetech # 631719), using Fugene reagent according to the manufacturer's instruction. The cells were incubated for 24 hours in serum free media, and then lysed 48 hours after transfection with using lysis buffer (Dual-Luciferase Reporter Assay System, Promega, Madison, WI) according to the manufacturer's instructions. Luciferase activity in the cell extract was determined using luciferase assay buffer and luciferase assay substrate according to the manufacturer's protocol.

For NMIIA rescue experiments, we utilized a plasmid (pEGFP-NMHC-IIA-C3) under the control of a CMV promoter that expresses full-length human NMIIA heavy chain fused to GFP at the amino terminus was utilized (gift of Dr. Anne Bresnick, Albert Einstein College of Medicine, Bronx, NY) as described previously (8–10). For the rescue experiments in MDA-MB-231 cells the pEGFP-NMHC-IIA-C3 plasmid was transfected into the sh-NMIIA #1 expressing cell line and stable clones were selected for using G418. GFP positive cells were isolated using flow cytometry. The relative activity of NFκB was measured in these GFP positive cells as described above.

Transcription factor activity assays

To monitor the activity of transcription factors (Nanog, Sox2) an inducible firefly luciferase reporter construct that encodes the reporter gene under the control of each transcription factors' specific transcriptional response elements joined to the basal promoter (TATA) were used according to the CIGNAL Reporter Assay Kit (Qiagen). The negative control for these experiments has a non-inducible firefly luciferase construct. Each Cignal DNA reagent contains one of these firefly luciferase constructs along with a constitutively expressing Renilla construct to control for transfection efficiency. Murine GBM or MDA-MB-231 cells grown in 24 wells plates overnight were transfected with 250 ng Cignal DNA using Fugene reagent according to manufacturer's instruction. Twenty-four hours after transfection, media was replaced on the cells and the cells were incubated for another 24 hours. Transcription factor activity was determined by monitoring luciferase/Renilla levels using the Dual Glo Luciferase assay (Promega, Madison, WI, USA).

Proliferation assays

To determine the effect of loss of both NMIIA and NMIIB on proliferation, cells expressing Histone-2B-RFP were plated 1000 cells/well in 96-well plates. The plate was scanned and fluorescent and phase-contrast images (4 per well) were acquired in real time every 3 hours for 5 days using IncuCyte Zoom Live-Cell Imaging system (Essen Bioscience, Ann Arbor, MI). Normalized RFP object count per well at each time point was quantified and time-lapse curves were generated. The exponential growth rate was calculated from the time-lapse curves based on nuclear doubling time.

We utilized Softwell 96 HTS plates (Matrigen) to determine the effect of loss of NMIIA on proliferation over a range of substrate stiffness. These 96 well plates contain one column each of 0.2, 0.5, 1, 2, 4, 8, 12, 25, and 50 kPa hydrogels that were coated with fibronectin. One thousand cells were plated per well and relative cell count was determined using an ATP-dependent cell viability assay (Cell Titer Glo) at 5 times after plating (24, 48, 72, 96, and 120 hrs). Data was normalized to 24 hour time point, and relative cell count as a function of time after plating was fit to a set of single exponential growth equations to derive rate constants for growth.

Immunofluorescece measurements

Cells were grown on fibronectin (10 μg/ml) coated coverslips and fixed with ice-cold 100% methanol for 5 minutes at room temperature. After washing with PBS three times, cells were permeabilized with 0.25% Triton X-100 PBS, then washed three more times. Cells were incubated with 1% BSA in PBST (PBS+ 0.1% Tween 20) for 30 min to block non-specific binding of the antibodies. The primary antibody (anti γ-tubulin; AbCam ab-11316, diluted 1:500) was incubated with cells overnight at 4°C. Following washing, a secondary antibody (goat anti-mouse IgG-Alexa 594; Thermo Fisher A-11005) diluted 1:750 in 1% BSA was applied to cells and incubated 1 h at room temperature in the dark. The coverslips were

then mounted to glass slides using Vectashield (#H-1200; Vector Laboratories). Cells were visualized using an UltraView VOX Spinning Disk Confocal Imaging System (PerkinElmer) with a DM1-6000 SD inverted microscope (Leica) and an electron multiplying charge coupled device C9100-13 camera (63×/NA 1.47 oil; Hamamatsu Photonics) or a TCS SP5 II laser scanning confocal imaging system with five spectral detectors (63×/NA 1.40 oil; Leica).

Cells grown on polyacrylamide hydrogels for 24 h were fixed with 4% paraformaldehyde (Sigma-Aldrich) for 20 minutes and washed with PBS. Cell membrane permeabilization was performed using cold (4˚C) 0.2 % Triton X-100 in PBS (Sigma-Aldrich). Next, cells were stained for F-actin with Alexa 488-phalloidin (Molecular Probes) for 30 minutes, for the nucleus with DAPI (Molecular Probes) for 5 minutes and for vimentin intermediate filaments with primary anti-vimentin antibody (Novous Biological) for 1 h and Alexa Fluor 647 secondary antibody (Molecular Probes) for 1 h. Each incubation was followed by multiple PBS washing and performed at room temperature unless otherwise stated. Fluorescence images were recorded using a Leica DMIRE2 inverted microscope (Leica, Buffalo Grove, IL) equipped with a mercury lamp and Hamamatsu camera (Hamamatsu, Japan) with 63× oil lens. Scale bar on all fluorescence images equals 20 μm.

Measurements of Cell Volume, Surface Area, and Height

Cells were grown to 70% confluency, trypsinized, and resuspended 2 mL of glioma media basal media supplemented with 10 ng/ml PDGF-AA (Sigma P3076) and 10 ng/ml FGFb (Sigma F0291), N2 supplement (Gibco), 20 ng/ml T3 (Sigma), 0.5% FBS, and penicillin/streptomycin/amphotericin (Invitrogen) in DMEM (Gibco). The suspended cells were incubated in 2μL/mL Vybrant DiO Cell-Labeling solution (ThermoFisher V22886) at 37°C for one hour, counted, and plated on PAGs coated in Matrigel (186μg/mL Corning 354248) at approximately 20,000 cells per dish (Mattek P35G-0-20-C). Cells were allowed to adhere overnight and imaged the following day using Zeiss LSM7 Live Confocal Microscope system with 0.38μm z-steps (40x/NA 0.95; Zeiss). Using Imaris Software provided by the University of Minnesota Imaging Center, z-stack images were reconstructed into 3D object renderings. Images were manually cropped and thresholded then automatically smoothed and segmented. Imaris surface analysis of volume, surface area, and Z-plane height-of-object were then recorded.

Polyacrylamide gel formulation and mechanical testing

Polyacrylamide hydrogels were prepared according to a previously published protocol (15). Briefly, 40% acrylamide (aa) and 2% bis-acrylamide (bis) stock solutions (BIO-RAD Laboratories, Hercules, CA) were mixed together with ddH_2O at the ratios of 3%aa/0.06%bis, 5%aa/0.1%bis, 7%aa/0.2%bis and 12%aa/0.4%bis and polymerized between two pretreated coverslips with the addition of TEMED electrophoresis grade (Fisher BioReagents, Pittsburgh, PA) and ammonium persulfate (Thermo Fisher Scientific, Rockford, IL). The bottom coverslip was pretreated with glutaraldehyde to ensure adhesion of the gel, and the top coverslip was silane-treated to allow for removal once the polymerization was complete. The UV-activated crosslinker sulfo-SANPAH (Thermo Fisher Scientific) was used to covalently bind 0.1 mg/ml collagen I (BD Bioscience, San Diego, CA) to the polyacrylamide gel surface. After the adhesive collagen coating was formed gels were soaked in cell culture medium for 1 h at 37°C prior to cell seeding. The shear modulus of the gels was tested using a Rheometrics fluids spectrometer III (Rheometrics, Piscataway, NJ) with 20 mm parallel plate geometry using a 2% oscillatory shear strain at a frequency of 2 rad/s. The shear moduli of different gel formulations were 0.30 ± 0.03 kPa, 1.09 ± 0.06 kPa, 5.1 ± 0.3 kPa and 30.6 ± 1.2 kPa and for clarity will be described as 0.3 kPa, 1 kPa, 5 kPa and 30 kPa through the manuscript.

Atomic force microscopy

Local cell cortex deformation in living cells was performed using a JPK Nanowizard 4 Atomic Force Microscope equipped with cantilevers of a nominal stiffness of 0.07 N/m to which a 1 μm diameter silica sphere was attached (Novascan). Cells grown on PAA hydrogels and glass coverslips coated with collagen I were kept in the culture medium and indented with the constant force of 2 nN at 25 different locations over the cell body (*Fig. 1A*), to obtain 25 force vs distance curves per cell. All the curves were analyzed as previously described in the frame of Hertz contact mechanics assuming a spherical indenter and a Poisson ratio of the sample equal to 0.5 [1],[2]. The apparent Young`s modulus values of the cell

cortex calculated for every measured location were used to perform distribution plots and finally, mean ± SE were calculated. Data from 50 cells were collected for each condition.

Global cell deformation was performed using a JPK Nanowizard 4 Atomic Force Microscope equipped with cantilevers of a nominal stiffness of 2.4 N/m with a 25 μm diameter sphere attached (Novascan), (*Fig. 1B*). Cells grown on glass coverslips coated with collagen I were kept in the culture medium and indented as follows. First, the highest point detectable over the cell body was recorded and assumed to reflect the total cell height. Second, each cell was indented at a constant speed of 10 μm/s until 50 nN force was reached. Force vs distance curves were then converted into stress vs (%) cell height curves with the assumption that normal stress can be calculated as the ratio of the applied force (*F*) to the area of deformation (*A*), (*Fig. 1C*). The area of deformation was calculated as a spherical cap of the sphere that was used as the indenter from the equation $A = 2\pi rh$, where *r* is the radius of the sphere and *h* is the depth at which cell was indented. The (%) cell height was calculated as the percentage of the total cell height that underwent indentation at a given force.

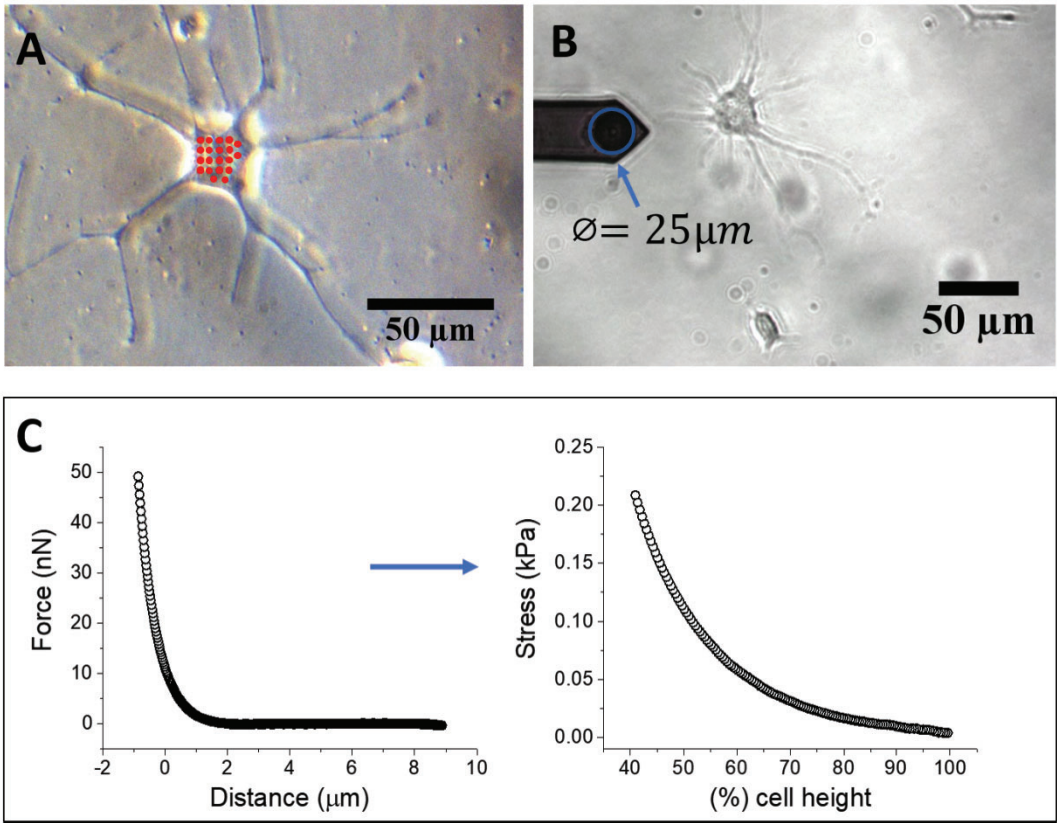

Figure 1. AFM mechanical testing of the cells. (A) Local cell cortex mechanical measurements at multiple locations over the cell body, (B) Global cell deformation obtained with the 25μm spherical indenter and (C) an example of the conversion of force vs distance to stress vs (%) cell height.

Brain histological and immunohistochemical analysis

Each GBM tumor bearing mouse was deeply anesthetized with intraperitoneal injection of a mixture of ketamine (100 mg/kg) and xylazine (10 mg/kg) as demonstrated by loss of nose, tail and hind limb pinch response—a euthanasia method based on the IACUC guidelines of the Cleveland Clinic. As described previously (5), mice were transcardially perfused with 15 ml ice cold PBS, followed by 15 ml cold 4% paraformaldehyde (PFA). Brains were removed and fixed overnight at 4 degrees in 4% PFA. Brains were paraffin embedded and microtome sectioned (5 μm thick) and then processed for histological analysis. Immunohistochemical staining was performed using the Discovery ULTRA automated stainer from Ventana Medical System Inc. (Tuscon, AZ). In brief, antigen retrieval was performed using a Tris/borate/EDTA buffer (Discovery CC1, 06414575001; Ventana), pH 8.0 to 8.5, for 64 minutes at 95°C. Slides were incubated with anti Ki67 at 1:1000 (VP-K451, Vector Laboratories) or HA at 1:1000 (11 867 423 001, Sigma-Aldrich), for 2 Hours at Room Temperature. The antibodies were visualized using biotinylated goat anti-rabbit and rabbit anti-rat secondary at 1:200 (BA-1000/BA-4001; Vector

Laboratories, Burlingame, CA) and the DABMap detection kit (0526636001; Ventana). Finally, the slides were counterstained with hematoxylin and bluing.

To measure GBM tumor size and HA-PDGF levels in the tumor, image processing was done using Fiji software (11). Using the IHC toolbox plugin (second version 2015/Jan/24 https://imagej.nih.gov/ij/plugins/ihc-toolbox/index.html) and H-DAB setting, image was processed to isolate just DAB staining by clicking color. After th4 image was inverted and a region of interest was drawn around tumor, the area of tumor and mean intensity was analyzed by clicking "Analyze and Measure".

Transwell migration assays

Flouroblok Transwell inserts were incubated with 5 µg/ml laminin (Sigma L2020-1MG), then washed prior to adding 150,000 cells. The Transwells were added to wells containing 10% FBS in glioma media as a chemoattractant. Cells were incubated for 18 hours at 37^{o}C, the Transwells were then washed then fixed in 4% PFA for 15 min. and then washed twice more with PBS before staining with DAPI. Images at 20X magnification were captured using an EVOS microscope 20X, and images were analyzed with Fiji software for nuclear count.

3D migration assay

The 3D migration devices were designed and fabricated at the Cornell NanoScale Science and Technology Facility in the laboratory of Dr. Jan Lammerding, as described previously (14). Briefly, the PDMS device was cast from SU-8 molds and then bonded onto glass slides. The device was made of two layers: one 5-µm-tall layer to form the constrictions channels and one 250-µm-tall layer to create two larger chambers. One large chamber is where cells are seeded and the other chamber is where the chemoattractant is added and is where migrate after having passed through the constrictions. The constriction channels consist of a series of round pillars forming consecutively narrower openings measuring 5, 3, and 2 µm in width. The device was coated with 33 µg/mL Laminin (Sigma L2020-1MG) and 50,000 cells were loaded into one side using loading ports. Cells were then incubated overnight in murine GBM medium, which was then removed. Fresh murine GBM medium was loaded into the chamber which contained cells, while the opposite chamber was loaded identical medium supplemented with 10% FBS as a chemoattractant. Cells were then analyzed over 48 hours using an UltraView VOX Spinning Disk Confocal Imaging System with a DM1-6000 SD inverted microscope (10×/NA 0.7 air; 37°C with 5% CO2) on a C9100-13 camera and analyzed using Volocity Software. To quantify nuclear translocation rate, kymographs were generated transecting the area of the opening of a 2-µm constriction point.

Immunoprecipitation

Immunoprecipitation analyses were described previously (9). Supernatants from cell lysates were incubated with anti-NMIIA or EGFR antibodies for 9 hours in binding buffer (50 mm Tris-HCl, pH 8.0, 0.3 m NaCl, 1% Triton X-100, 0.25% Na-deoxycholate, 10 mm MgCl2, 5 mm EDTA, 1 mm EGTA, 1 mm DTT, 10 mm ATP, 3 mm NaN_3, 1 mm PMSF, protease inhibitor mixture, and phosphatase inhibitor mixture) and these immunocomplexes were recovered by incubation with protein A-Sepharose beads for 2 hours. Immunoprecipitates were denatured by incubation at 95 °C for 5 min in Laemmli sample buffer, and then separated by SDS 6% or 4–20% PAGE, and finally transferred to nitrocellulose membranes. Detection of peptides was performed using an enhanced chemiluminescence kit (Pierce).

Western blot analysis

Cells with or without NMIIA were gently lifted and incubated at 37^{o}C for 1 hour in suspension in Eppendorf tubes followed by time course EGF stimulation (10 ng/ml). Whole-cell lysate were prepared by incubating cell pellets in lysis buffer (50 mM Tris HCl at pH 7.40, 150 mM NaCl, 1 mM EDTA, 1.0% Nonidet P-40, and a mixture of protease and phosphatase inhibitors), on ice for 30 min. Cell debris was removed by centrifugation for 10 mins at high speed on table top centrifuge at 4oC. Cell extracts proteins were determined by the Bradford method and, were separated by SDS/PAGE [10% (vol/vol) acrylamide] and transferred to polyvinylidene difluoride membranes. The membranes were incubated with primary antibody for 2 h, followed by incubation with secondary antibody for 1 hour at room temperature, and

developed by using the enhanced chemiluminescence solution. All anti-phospho antibodies incubated for 2 hours in 5% BSA. Total proteins diluted in 5% milk for 2 hours.

Cytokinesis monitoring

Murine GBM cells expressing RFP-Histone H2B fluorescent proteins were grown on glass bottom dishes coated with 10ug/mL Fibronectin (Sigma F1141) in murine GBM media. Cells were imaged using an UltraView VOX Spinning Disk Confocal Imaging System with a DM1-6000 SD inverted microscope (10×/NA 0.7 air; 37°C with 5% CO2) on a C9100-13 C9100-13 camera and analyzed using Volocity Software.

Orthotopic Tumor Implantation and Bioluminescence Monitoring of Tumor Growth

Intracranial tumor implantation was performed on 8 week old female NOD-SCID mice obtained from Jackson laboratory (stock #005557). Under ketamine-induced anesthesia, 50,000 luciferase expressing PTEN deleted and PTEN/NMIIA co-deleted murine GBM cells were injected in 2μL of culture media at coordinates X=1.5mm, Y=1.5mm and Z=2.5mm relative to the bregma. Tumor formation was monitored by intraperitoneal injection of 3 mg/kg body weight of D-luciferin (Xenolight D-Luciferin firefly potassium salt, PerkinElmer, catalog# 122799) in sterile phosphate buffered saline (PBS) followed by IVIS imaging. IVIS imaging was performed for every 3-4 days and photon flux was calculated from the resulting signal.

Antibodies

Antibody	**Company**	**Catalog #**	**Assay**	**Dilution**
γ-tubulin	Ab Cam	Ab-11316	IF	1:500
goat anti-mouse IgG-Alexa 594	Thermo Fisher	A-11005	IF	1:750
Phospho-ERK (Thr202/Tyr204)	Cell Signaling	9101S	WB	1:1000
Phospho-AKT (Ser473)	Cell Signaling	9271S	WB	1:1000
Total ERK (p44/42 MAP Kinase)	Cell Signaling	9102S	WB	1:1000
Total AKT	Cell Signaling	9272S	WB	1:1000
Myosin IIA	BioLegend	PRB-440P	WB&IP	1:1000
Myosin IIB	BioLegend	PRB-445P	WB	1:1000
TP53 (human)	Santa Cruz	Sc-126	WB	1:500
TP53 (murine)	Leica	NCL-L-p53-CM5p	WB	1:2000
Ki67	Vector	VP-K451	IHC	1:1000
HA	Sigma-Aldrich	11 867 423 001	IHC	1:1000

SUPPLEMENTARY REFERENCES

1. Jacobelli J, et al. (2010) Confinement-optimized three-dimensional T cell amoeboid motility is modulated via myosin IIA-regulated adhesions. *Nat Immunol* 11(10):953–961.

2. Ma X, et al. (2009) Conditional ablation of nonmuscle myosin II-B delineates heart defects in adult mice. *Circ Res* 105(11):1102–1109.

3. Assanah MC, et al. (2009) PDGF stimulates the massive expansion of glial progenitors in the neonatal forebrain. *Glia* 57(16):1835–1847.

4. Mayer-Pröschel M (2001) Isolation and generation of oligodendrocytes by immunopanning. *Curr Protoc Neurosci* Chapter 3:Unit 3.13.

5. Lei L, et al. (2011) Glioblastoma models reveal the connection between adult glial progenitors and the proneural phenotype. *PloS One* 6(5):e20041.

6. Canoll PD, et al. (1996) GGF/neuregulin is a neuronal signal that promotes the proliferation and survival and inhibits the differentiation of oligodendrocyte progenitors. *Neuron* 17(2):229–243.

7. Thiagarajan PS, et al. (2015) Development of a Fluorescent Reporter System to Delineate Cancer Stem Cells in Triple-Negative Breast Cancer. *Stem Cells Dayt Ohio* 33(7):2114–2125.

8. Wei Q, Adelstein RS (2000) Conditional expression of a truncated fragment of nonmuscle myosin II-A alters cell shape but not cytokinesis in HeLa cells. *Mol Biol Cell* 11(10):3617–3627.

9. Bao J, Jana SS, Adelstein RS (2005) Vertebrate nonmuscle myosin II isoforms rescue small interfering RNA-induced defects in COS-7 cell cytokinesis. *J Biol Chem* 280(20):19594–19599.

10. Dulyaninova NG, House RP, Betapudi V, Bresnick AR (2007) Myosin-IIA heavy-chain phosphorylation regulates the motility of MDA-MB-231 carcinoma cells. *Mol Biol Cell* 18(8):3144–3155.

11. Schindelin J, et al. (2012) Fiji: an open-source platform for biological-image analysis. *Nat Methods* 9(7):676–682.

12. Shu J, Dolman GE, Duan J, Qiu G, Ilyas M (2016) Statistical colour models: an automated digital image analysis method for quantification of histological biomarkers. *Biomed Eng OnLine* 15. doi:10.1186/s12938-016-0161-6.

13. Lánczky A, et al. (2016) miRpower: a web-tool to validate survival-associated miRNAs utilizing expression data from 2178 breast cancer patients. *Breast Cancer Res Treat* 160(3):439–446.

14. Davidson PM, Denais C, Bakshi MC, Lammerding J (2014) Nuclear deformability constitutes a rate-limiting step during cell migration in 3-D environments. *Cell Mol Bioeng* 7(3):293–306.

15. Pogoda K, et al. (2014) Compression stiffening of brain and its effect on mechanosensing by glioma cells. *New J Phys*. 2014 **16**:075002.

16. K. Pogoda *et al.*, (2012) Depth-sensing analysis of cytoskeleton organization based on AFM data. *Eur. Biophys. J.*, **41**,79–87.

17. K. Pogoda *et al.*, "Soft Substrates Containing Hyaluronan Mimic the Effects of Increased Stiffness on Morphology, Motility, and Proliferation of Glioma Cells," *Biomacromolecules*, vol. 18, no. 10, pp. 3040–3051, Oct. 2017.

SUPPLEMENTARY FIGURE LEGEND

Fig. S1: NMII isoform composition of murine GMB cell lines. (A) NMII isoform composition of a glioma cell line isolated from GBM-bearing floxed/floxed PTEN mouse as determined by LC/MS/MS. (B) NMII isoform composition of a glioma cell line isolated from GBM bearing mice with homozygous floxed alleles for PTEN and NMIIA, as determined by LC/MS/MS.

Fig. S2: Histologic section of brains from mice with homozygous floxed alleles for PTEN, NMIIA, and NMIIB injected with PDGF-IRES-cre retrovirus. Mice were injected intracranially with a PDGF-IRES-cre encoding retrovirus, and animals were sacrificed and necropsied at 125-130 days post injection. Coronal histologic sections through the injection site were immunohistochemically stained with an anti-HA antibody to mark tumor cells expressing the PDGF-HA fusion protein. No tumor cells could be detected.

Fig. S3: Staining of murine GBM tumor cells with DAPI and anti-γ tubulin. Cells deleted for PTEN and NMIIA were treated with either non-targeting (NT) shRNA or shRNA directed against NMIIB. Cells were stained with an anti γ-tubulin (red) to reveal the number of centrosomes and DAPI (blue). Glioma cells lacking both NMIIA and NMIIB become multinucleated with multiple centrosomes. (A) 40X image magnification. (B) Enlarged images of individual cells.

Fig. S4: Response of PTEN-deleted and PTEN/NMIIA co-deleted cells to doxorubicin. (A) 100,000 PTEN deleted (*PTEN(-/-)*) and PTEN/NMIIA co-deleted (*PTEN(-/-)/NMIIA(-/-)*) cells were plated on fibronectin-coated tissue culture plates (Raj—please insert dimensions) and grown to confluence. Lysates were generated prior to adding doxorubicin (1 mM) and at 2, 3, 6, and 12 hours after adding doxorubicin and probed with Western blots using an anti-p53 antibody with a βactin loading control. (B) Quantification of p53 staining, normalized to βactin, as a function of time after addition of 1 mM doxorubicin. Data are depicted as mean ± SEM (n=4). (C) PTEN-deleted and PTEN/NMIIA co-deleted cells were plated as described above and treated with 1 mM doxorubicin for 15 and 24 hr or left untreated. Lysates were probed with Western blots using antibodies against caspase-3 and β actin.

Fig. S5: NMIIA is integral for glioma migration through 3D constrictions. (A) Graphical representation of the migration device. Cells are seeded in the lower chamber (green) and are induced to migrate to the upper chamber, which contains a chemoattractant. Between these two chambers are a series of posts that are separated from each other by 5, 3, and 2 μm spaces. The device sits on top of a cover slip, allowing time-lapse microscopy using an inverted, environmentally-controlled confocal microscope. (B) Transit time for nuclear transit through the 2 μm space for PTEN-deleted (*black*) and PTEN/NMIIA co-deleted (*red*) cells, utilizing Histone 2B-DsRed as a nuclear marker. (C) Western blots demonstrating that both NMIIA deletion with the cre-recombinase and NMIIA suppression with lentiviruses expressing NMIIA-targeting shRNA produce non-detectable levels of NMIIA in murine GBM, compared to non targeting (NT) shRNA. (D), (E) NMIIA expression in human MDA-MB-231 breast carcinoma and in normal human primary keratinocytes can also be efficiently suppressed with shRNA.

Fig. S6: Plot of the Young's modulus for PTEN-deleted (*black*) and PTEN/NMIIA-co-deleted (*red*) cells as a function of substrate stiffness. Cells were plated on collagen I-coated polyacrylamide gels with stiffness of 0.3, 1, and 5 kPa, as well as on a glass surface. The Young's modulus was measured with a 1 μm atomic force microscope spherical probe, with 25 measurements made on 50 cells

Fig. S7: Effect of substrate stiffness on cell surface area, volume, and height for PTEN-deleted (*blue*) and PTEN/NMIIA-co-deleted (*red*) cells. PTEN-deleted and PTEN/NMIIA co-deleted tumor cells that express cytoplasmic GFP were cultured on Matrigel-coated polyacrylamide gels with stiffness of 0.7, 4.6, and 50 kPa, and spread surface area (A), cell volume (B) and maximum cell height in the Z-axis (C) were measured using a confocal microscope.

Fig. S8: Effect of substrate stiffness on morphology of PTEN-deleted and PTEN/NMIIA co-deleted cells. Cells were grown on polyacrylamide hydrogels of defined stiffness, fixed with paraformaldehyde, permeabilized, and stained with Alexa 488-phalloidin and DAPI to visualize polymerized actin and DNA, respectively. Fluorescence images were recorded using a Leica DMIRE2 inverted microscope (Leica, Buffalo Grove, IL) equipped with a mercury lamp and Hamamatsu camera (Hamamatsu, Japan) with 63× oil lens. Scale bar on all fluorescence images equals 20 μm.

Fig. S9: Phosphorylation of AKT is not altered by NMIIA deletion or substrate stiffness. 100,000 PTEN-deleted and PTEN/NMIIA co-deleted were seeded on a 0.5 kPa fibronectin-coated Softwell plate or on plastic, grown to 80% confluence, cell lysates were generated, and probed on a Western blot for total AKT and pS473 AKT (*top*). Quantification of multiple blots (n=3, *bottom*) reveals no significant difference in the pS473 AKT/total AKT ratio between PTEN deleted and PTEN/NMIIA co-deleted cells on either the soft or hard substrates.

Fig. S10: Increased tumorsphere volume and frequency in NMIIA-deleted GBM and NMIIA suppressed MDA-MB-231. (A) GBM cell lines were grown as tumorspheres for 2 weeks. Scale bar represents 200 μm. (B) MDA-MB-231 cells transfected with non-targeting and NMIIA-targeting shRNA were grown from single cells as tumorspheres for 2 weeks. Scale bar represents 200 μm. (C) Graphical representation of GBM tumorsphere diameter (n=24). (D) Graphical representation of MDA-MB-231 tumorsphere diameter (n=24). (E) Limiting dilution analysis of GBM cell lines showing increased tumorsphere forming frequency in cells lacking NMIIA. (F) Corresponding limiting dilution analysis in MDA-MB-231 cells after depletion with non-targeting or NMIIA shRNA.

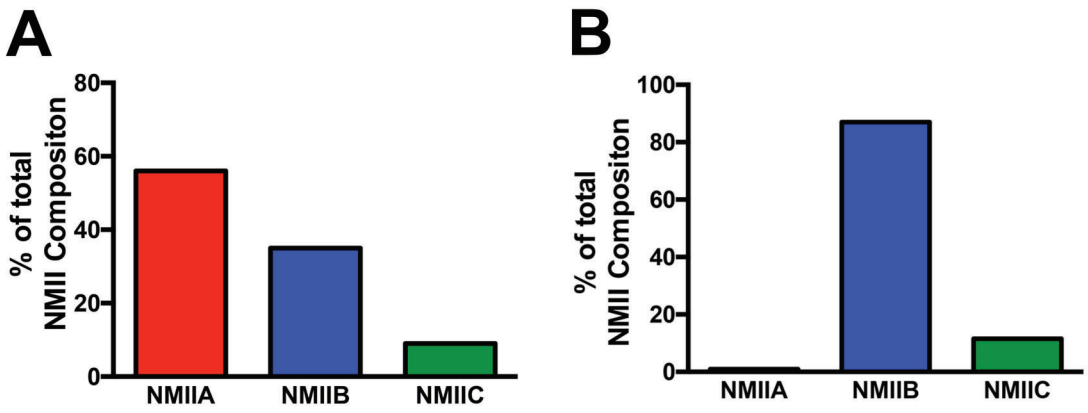
A
% of total NMII Compositon
80
60
40
20
0
NMIIA
NMIIB
NMIIC
B
% of total NMII Compositon
100
80
60
40
20
0
NMIIA
NMIIB
NMIIC

Figure S1

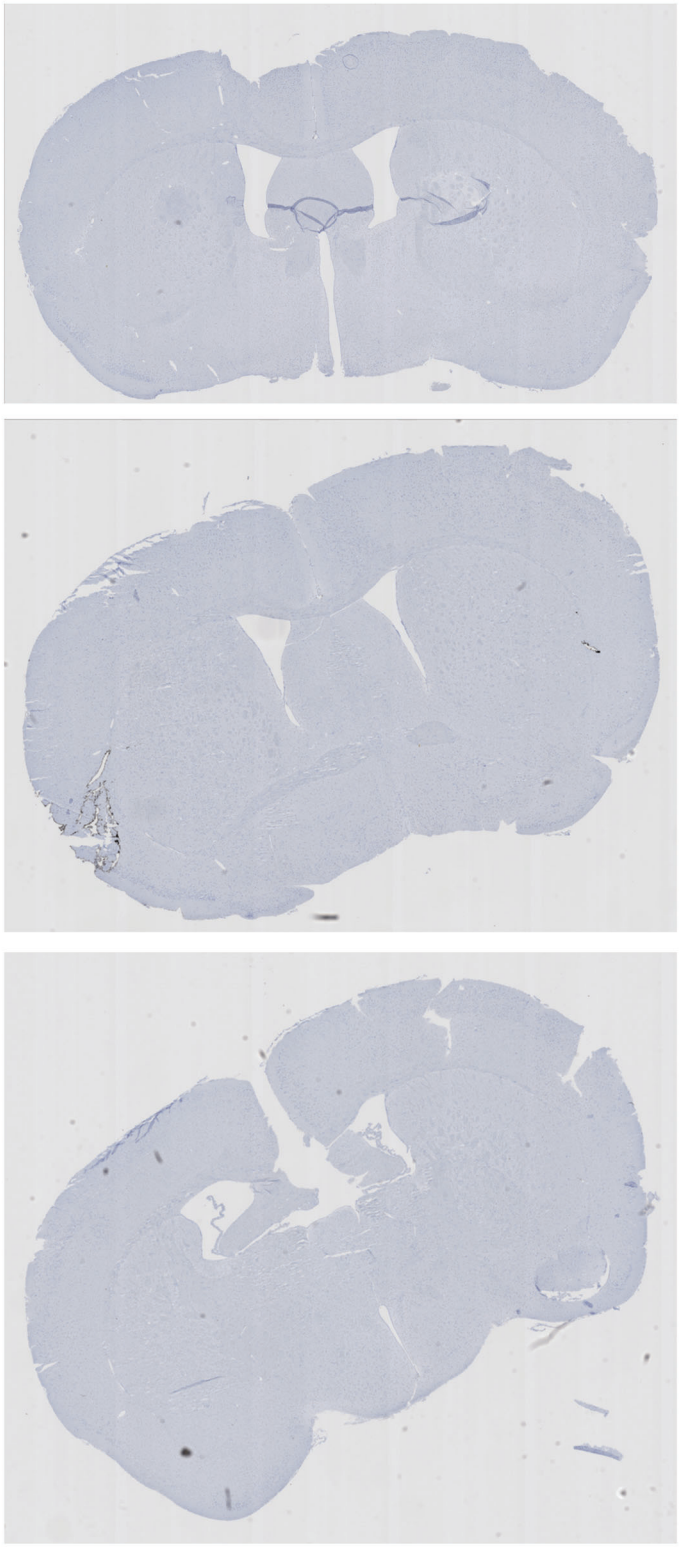

Figure S2

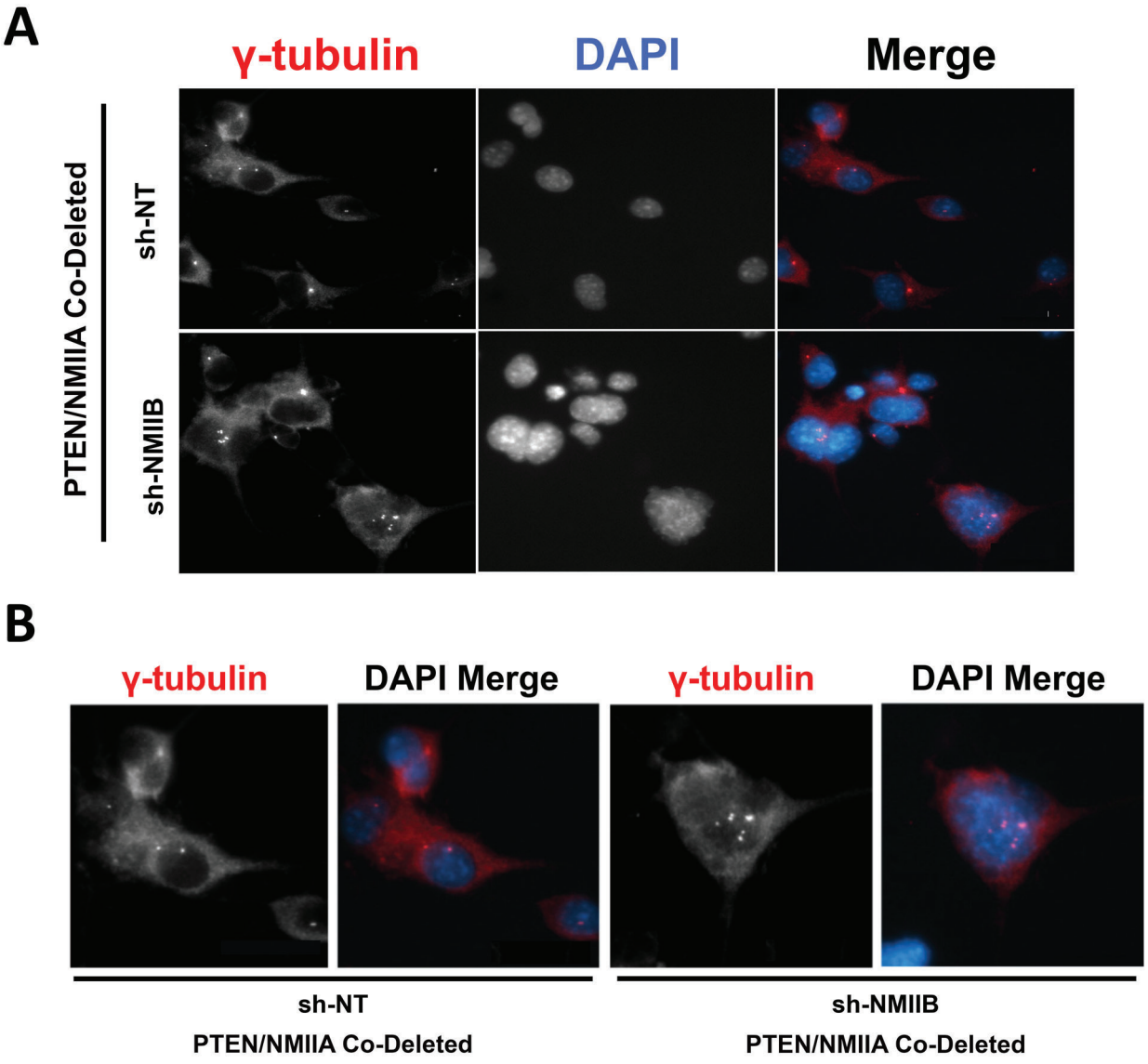
A
γ-tubulin
DAPI
Merge
PTEN/NMIIA Co-Deleted
sh-NT
sh-NMIIB
B
γ-tubulin
DAPI Merge
γ-tubulin
DAPI Merge
sh-NT
PTEN/NMIIA Co-Deleted
sh-NMIIB
PTEN/NMIIA Co-Deleted

Figure S3

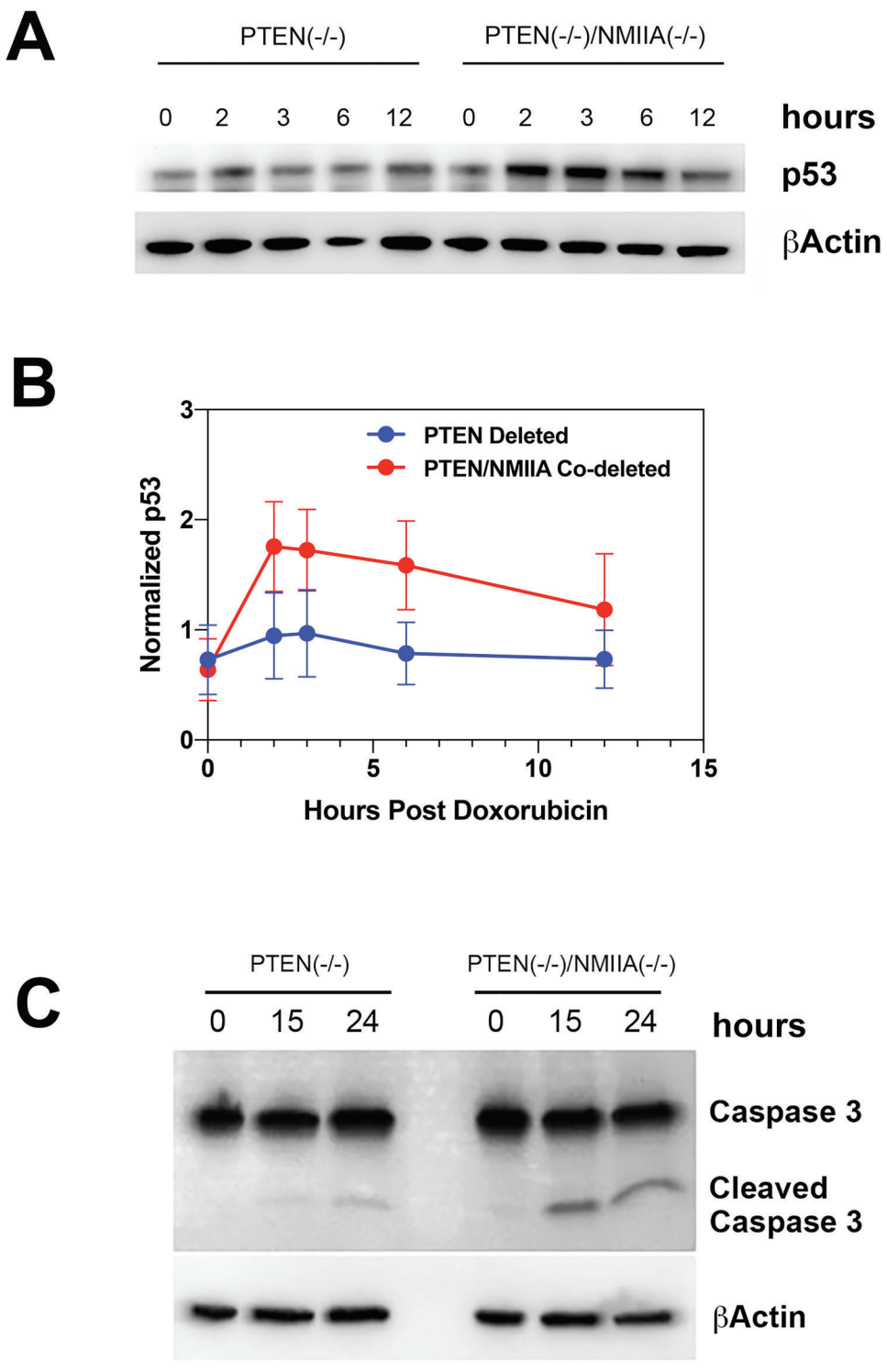
A
PTEN(-/-)
PTEN(-/-)/NMIIA(-/-)
0 2 3 6 12 0 2 3 6 12
hours
p53
βActin
B
PTEN Deleted
PTEN/NMIIA Co-deleted
Normalized p53
0
1
2
3
0
5
10
15
Hours Post Doxorubicin
C
PTEN(-/-)
PTEN(-/-)/NMIIA(-/-)
0 15 24 0 15 24
hours
Caspase 3
Cleaved Caspase 3
βActin

Figure S4

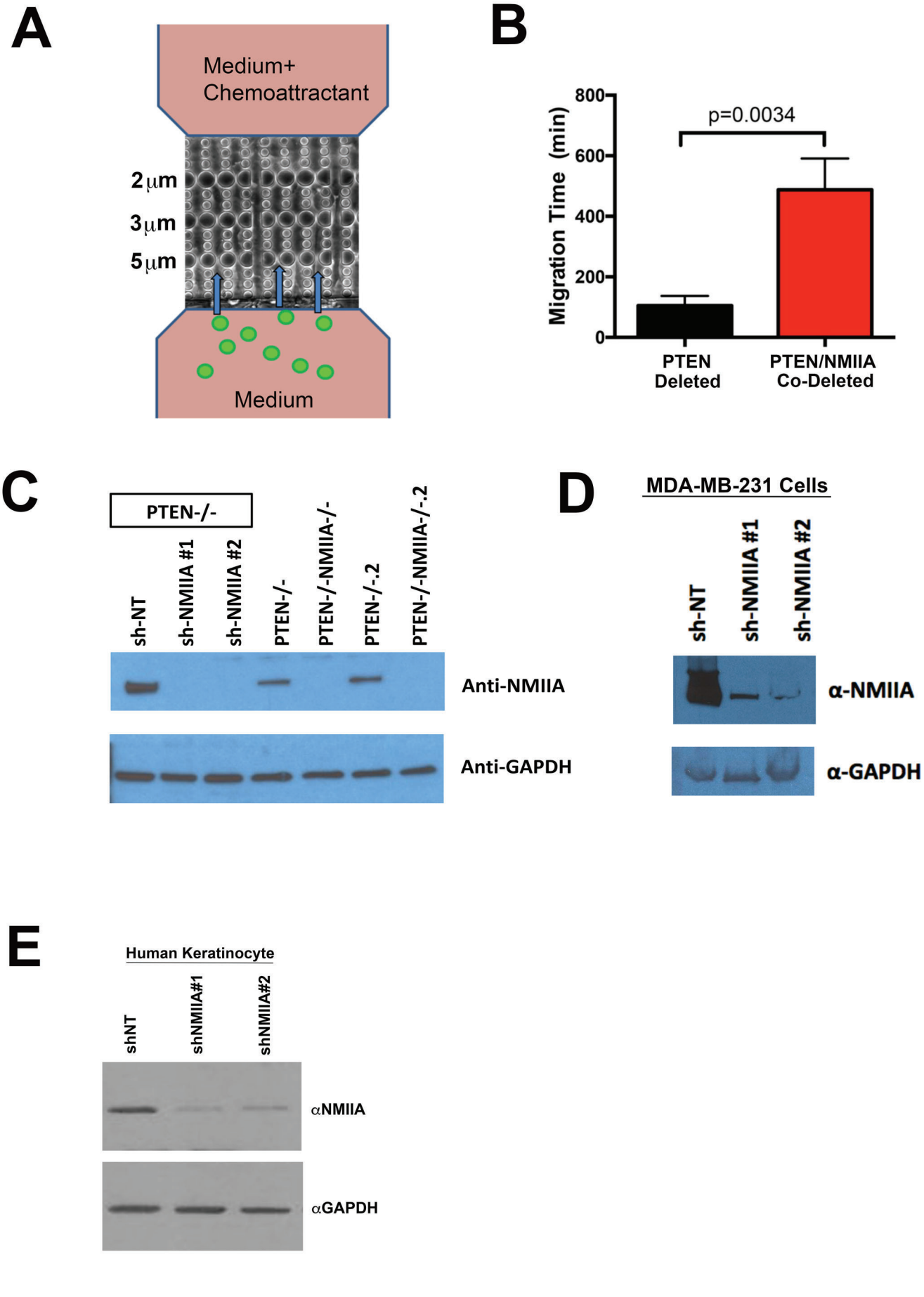
A
Medium+
Chemoattractant
2μm
3μm
5μm
Medium
B
Migration Time (min)
800
600
400
200
0
p=0.0034
PTEN
Deleted
PTEN/NMIIA
Co-Deleted
C
PTEN-/-
sh-NT
sh-NMIIA #1
sh-NMIIA #2
PTEN-/-
PTEN-/-NMIIA-/-
PTEN-/-.2
PTEN-/-NMIIA-/-.2
Anti-NMIIA
Anti-GAPDH
D
MDA-MB-231 Cells
sh-NT
sh-NMIIA #1
sh-NMIIA #2
α-NMIIA
α-GAPDH
E
Human Keratinocyte
shNT
shNMIIA#1
shNMIIA#2
αNMIIA
αGAPDH

Figure S5

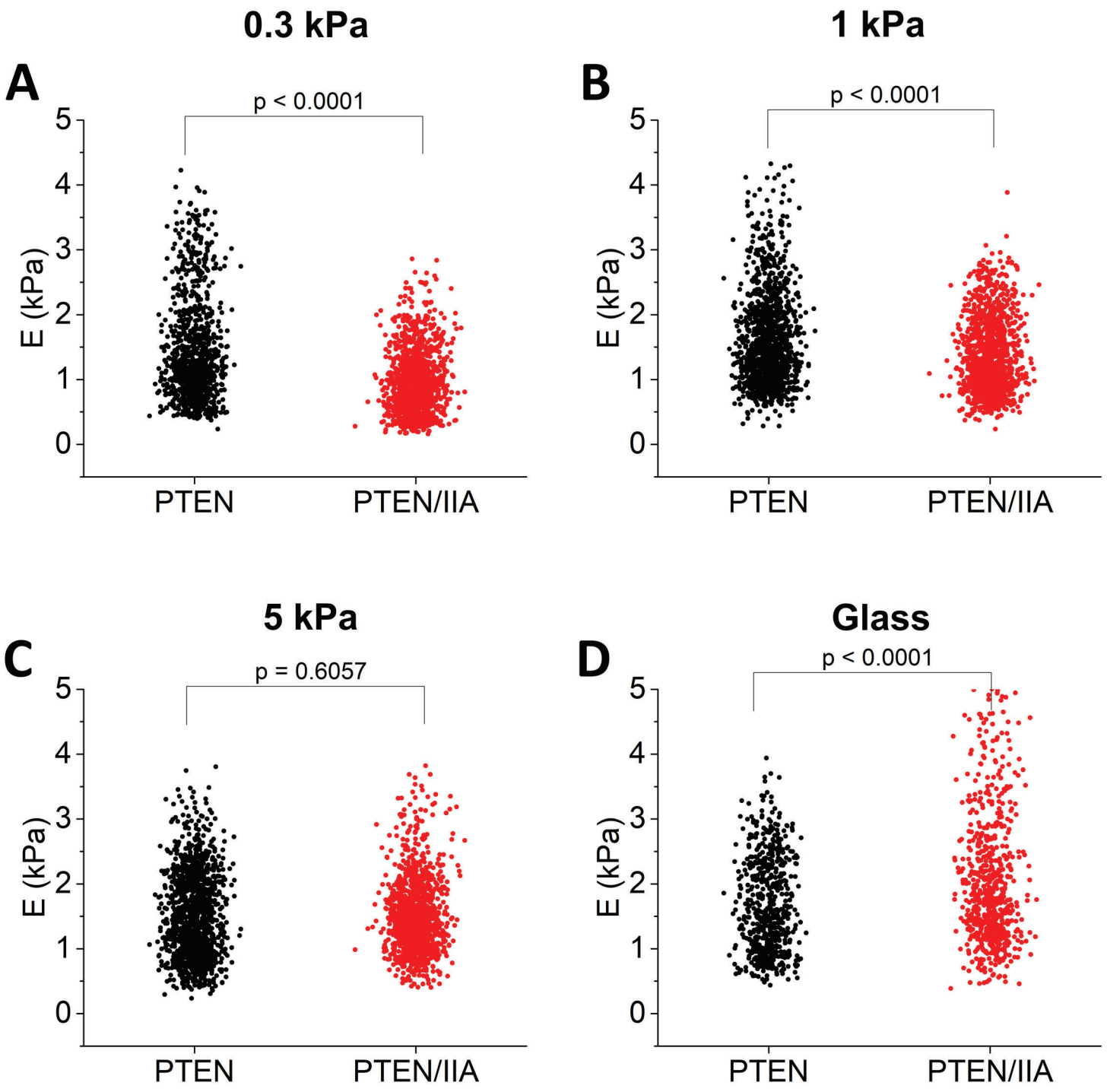
A
0.3 kPa
p < 0.0001
E (kPa)
0
1
2
3
4
5
PTEN
PTEN/IIA
B
1 kPa
p < 0.0001
E (kPa)
0
1
2
3
4
5
PTEN
PTEN/IIA
C
5 kPa
p = 0.6057
E (kPa)
0
1
2
3
4
5
PTEN
PTEN/IIA
D
Glass
p < 0.0001
E (kPa)
0
1
2
3
4
5
PTEN
PTEN/IIA

Figure S6

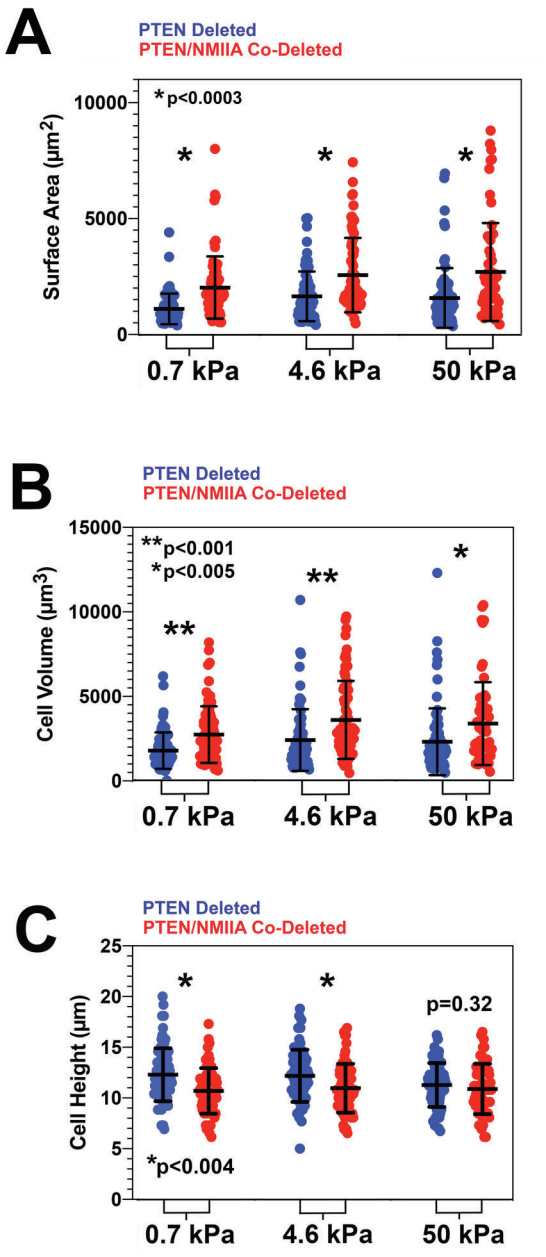
A
PTEN Deleted
PTEN/NMIIA Co-Deleted
*p<0.0003
Surface Area (μm²)
10000
5000
0
0.7 kPa
4.6 kPa
50 kPa
B
PTEN Deleted
PTEN/NMIIA Co-Deleted
**p<0.001
*p<0.005
Cell Volume (μm³)
15000
10000
5000
0
0.7 kPa
4.6 kPa
50 kPa
C
PTEN Deleted
PTEN/NMIIA Co-Deleted
p=0.32
*p<0.004
Cell Height (μm)
25
20
15
10
5
0
0.7 kPa
4.6 kPa
50 kPa

Figure S7

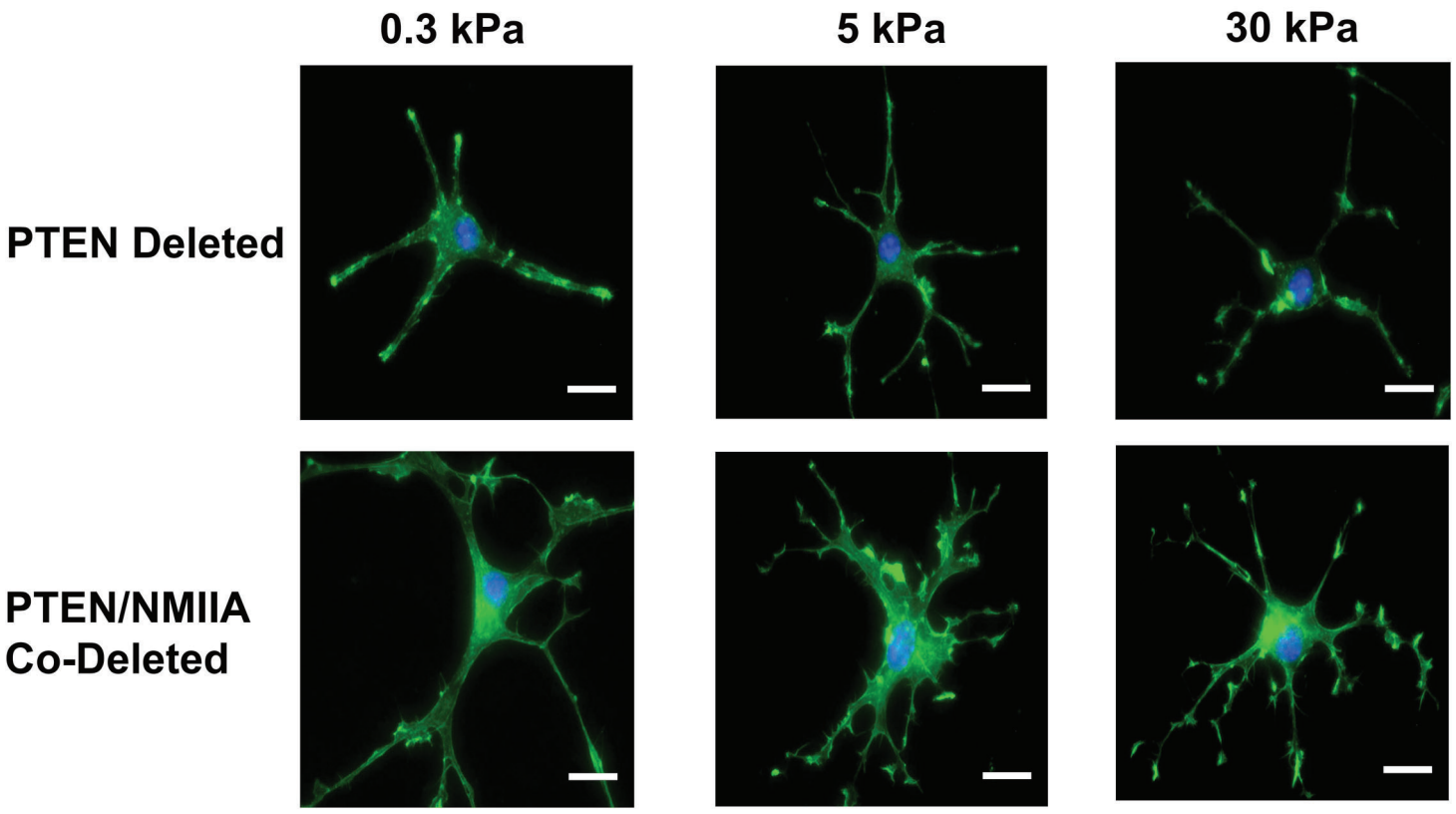

Figure S8

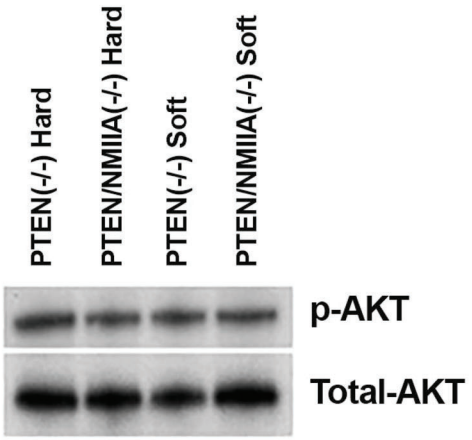
PTEN(-/-) Hard
PTEN/NMIIA(-/-) Hard
PTEN(-/-) Soft
PTEN/NMIIA(-/-) Soft
p-AKT
Total-AKT

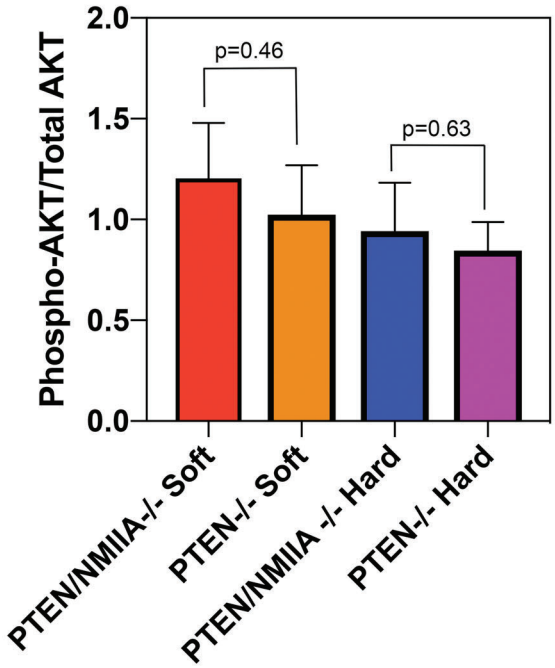
Phospho-AKT/Total AKT
2.0
1.5
1.0
0.5
0.0
p=0.46
p=0.63
PTEN/NMIIA-/- Soft
PTEN-/- Soft
PTEN/NMIIA -/- Hard
PTEN-/- Hard

Figure S9

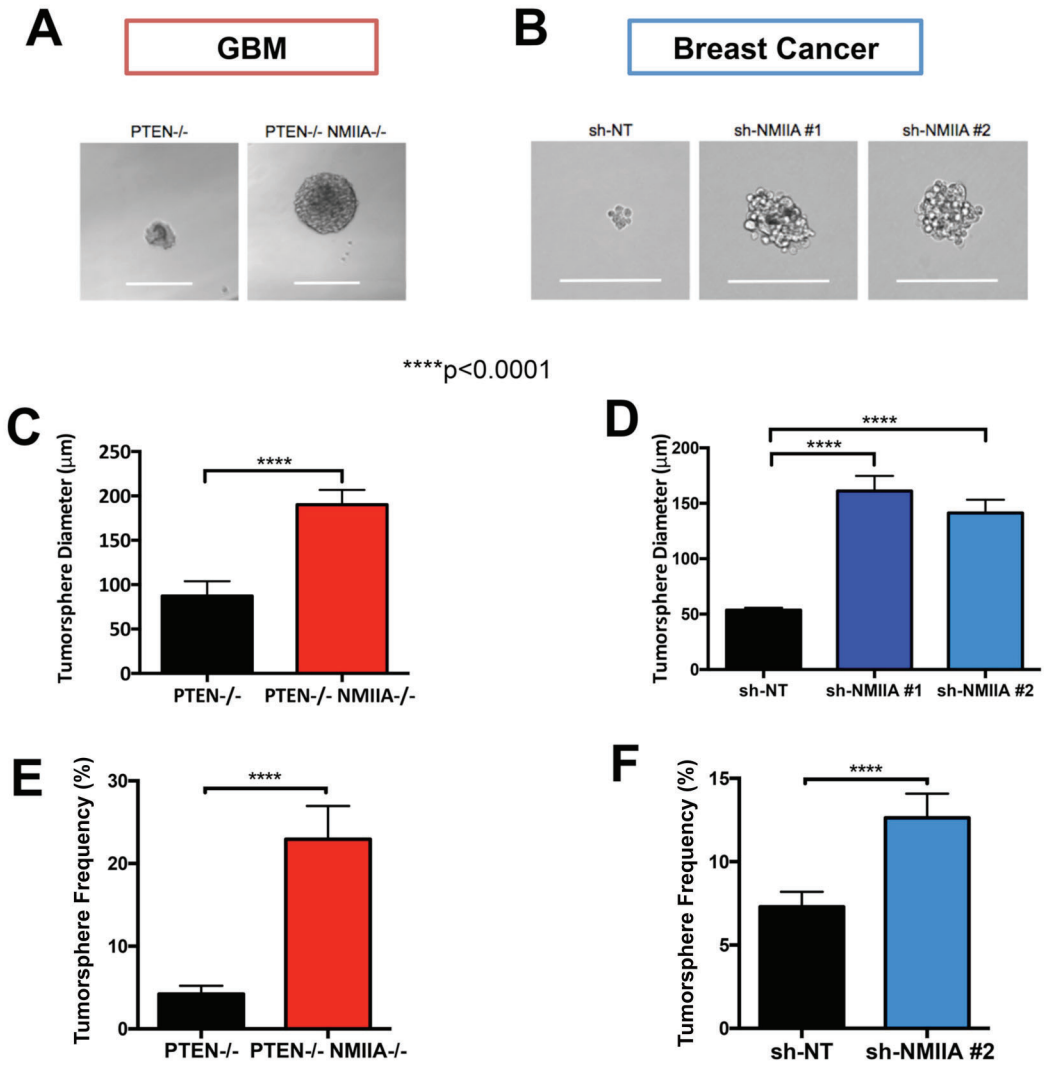
A
GBM
PTEN-/-
PTEN-/- NMIIA-/-
B
Breast Cancer
sh-NT
sh-NMIIA #1
sh-NMIIA #2
****p<0.0001
C
Tumorsphere Diameter (µm)
250
200
150
100
50
0
****
PTEN-/-
PTEN-/- NMIIA-/-
D
Tumorsphere Diameter (µm)
200
150
100
50
0
****
****
sh-NT
sh-NMIIA #1
sh-NMIIA #2
E
Tumorsphere Frequency (%)
30
20
10
0
****
PTEN-/-
PTEN-/- NMIIA-/-
F
Tumorsphere Frequency (%)
15
10
5
0
****
sh-NT
sh-NMIIA #2

Figure S10

SUPPLEMENTARY MOVIE LEGEND

Supplementary movie #1: Time-lapse video of cytokinesis of glioma cells deleted for PTEN and NMIIA. Cells express a RFP tagged Histone 2B. Images were acquired every 5 min using an UltraView VOX laser system PerkinElmer; DM1 6100 base Leica; 63× oil/NA 1.47 at 37°C and 5% CO_2.

Supplementary movie #2: Time-lapse video of cytokinesis of glioma cells deleted for PTEN and NMIIA and shRNA suppressed for NMIIB. CellsImages were acquired every 5 min using an UltraView VOX laser system PerkinElmer; DM1 6100 base Leica; 63× oil/NA 1.47 at 37°C and 5% CO_2.

Supplementary movie #3: Time-lapse video of PTEN-deleted glioma cells treated with a non-targeting shRNA and expressing cytoplasmic GFP, migrating toward a chemotactic gradient through 3D constrictions of a defined size. Images were analyzed using time-lapse spinning disk confocal microscopy (UltraView VOX laser system PerkinElmer; DM1 6100 base Leica; 63× oil/NA 1.47 at 37°C and 5% CO_2). Images were acquired every 10 min for 48 hours.

Supplementary movie #4: Time-lapse video of PTEN-deleted glioma cells treated with an shRNA directed NMIIA and expressing cytoplasmic GFP migrating toward a chemotactic gradient through 3D constrictions of a defined size. Images were analyzed using time-lapse spinning disk confocal microscopy (UltraView VOX laser system PerkinElmer; DM1 6100 base Leica; 63× oil/NA 1.47 at 37°C and 5% CO_2). Images were acquired every 10 min for 48 hours.

ARTICLE

High-throughput microfluidic micropipette aspiration device to probe time-scale dependent nuclear mechanics in intact cells

Received 00th January 20xx,
Accepted 00th January 20xx

DOI: 10.1039/x0xx00000x

Patricia M. Davidson,[ab] Gregory R. Fedorchak,[a] Solenne Mondésert-Deveraux,[c] Emily S. Bell,[a] Philipp Isermann,[a] Denis Aubry,[c] Rachele Allena [d] and Jan Lammerding *[a]

The mechanical properties of the cell nucleus are increasingly recognized as critical in many biological processes. The deformability of the nucleus determines the ability of immune and cancer cells to migrate through tissues and across endothelial cell layers, and changes to the mechanical properties of the nucleus can serve as novel biomarkers in processes such as cancer progression and stem cell differentiation. However, current techniques to measure the viscoelastic nuclear mechanical properties are often time consuming, limited to probing one cell at a time, or require expensive, highly specialized equipment. Furthermore, many current assays do not measure time-dependent properties, which are characteristic of viscoelastic materials. Here, we present an easy-to-use microfluidic device that applies the well-established approach of micropipette aspiration, adapted to measure many cells in parallel. The device design allows rapid loading and purging of cells for measurements, and minimizes clogging by large particles or clusters of cells. Combined with a semi-automated image analysis pipeline, the microfluidic device approach enables significantly increased experimental throughput. We validated the experimental platform by comparing computational models of the fluid mechanics in the device with experimental measurements of fluid flow. In addition, we conducted experiments on cells lacking the nuclear envelope protein lamin A/C and wild-type controls, which have well-characterized nuclear mechanical properties. Fitting time-dependent nuclear deformation data to power law and different viscoelastic models revealed that loss of lamin A/C significantly altered the elastic and viscous properties of the nucleus, resulting in substantially increased nuclear deformability. Lastly, to demonstrate the versatility of the devices, we characterized the viscoelastic nuclear mechanical properties in a variety of cell lines and experimental model systems, including human skin fibroblasts from an individual with a mutation in the lamin gene associated with dilated cardiomyopathy, healthy control fibroblasts, induced pluripotent stem cells (iPSCs), and human tumor cells. Taken together, these experiments demonstrate the ability of the microfluidic device and automated image analysis platform to provide robust, high throughput measurements of nuclear mechanical properties, including time-dependent elastic and viscous behavior, in a broad range of applications.

Introduction

The nucleus is the largest and stiffest organelle of eukaryotic cells. The mechanical properties of the nucleus are primarily determined by the nuclear lamina, a dense protein network comprised of lamins that underlies the inner nuclear membrane, and chromatin.[1–4] Chromatin mechanics dominate the overall nuclear response for small deformations, whereas the lamina governs the nuclear response for larger deformations.[3,4] In recent years, the mechanical properties of the nucleus have emerged as important predictors and biomarkers for numerous physiological and pathological conditions and functions, raising increased interest in probing nuclear mechanics. For example, the deformability of the nucleus determines the ability of migrating cells to pass through small openings,[5–8] which is highly relevant during development, immune cell infiltration, and cancer metastasis, where cells move through tight interstitial spaces and enter and exit blood vessels through openings only a few micrometre in diameter.[9] In stem cell applications, the morphology and mechanical properties of the nucleus can serve as label-free biomarkers for differentiation,[10–12] reflecting characteristic changes in the composition of the nuclear envelope and chromatin organization during differentiation.[10,13,14] Lastly, mutations in the genes encoding lamins give rise to a large family of inheritable disorders termed laminopathies, which are often characterized by reduced nuclear stability.[15]

The mechanical properties of cells and their nuclei are assessed using a range of techniques. Nuclear deformation can be observed by stretching cells cultured on flexible membranes and used to infer the mechanical properties of the nucleus, including the contribution of specific nuclear envelope

[a] Meinig School of Biomedical Engineering, Weill Institute for Cell and Molecular Biology, Cornell University, USA.
[b] Laboratoire Physico-Chimie Curie, Institut Curie; CNRS UMR 168; Université Paris Science et Lettres; Sorbonne Université, France.
[c] Laboratoire MSSMat UMR CNRS 8579, CentraleSupelec, Université Paris-Saclay, France.
[d] Arts et Metiers ParisTech, LBM/Institut de Biomécanique Humaine Georges Charpak, France

† Footnotes relating to the title and/or authors should appear here.
Electronic Supplementary Information (ESI) available: [details of any supplementary information available should be included here]. See DOI: 10.1039/x0xx00000x

proteins.[16–19] However, this technique relies on nucleo-cytoskeletal connections to transmit forces to the nucleus, which may be affected by mutations in nuclear lamins,[20] and stretching cells requires strong adhesion to the substrate. The latter fact limits the type of cells that can be studied, and can result in bias towards sub-populations of strongly adherent cells.[19] Single cell techniques, such as atomic force microscopy (AFM), nuclear stretching between two micropipettes,[4] and magnetic bead microrheology,[21] apply precisely controlled forces and measure the induced deformation, thus providing detailed information on nuclear mechanical properties. However, these techniques are time-consuming, technically challenging, and often require expensive equipment and training.

Micropipette aspiration remains one of the gold standards and most commonly used tools to study nuclear mechanics[22–24] and provides important information on the viscoelastic behaviour of the nucleus over different time scales.[13,25] Micropipette aspiration has been used to study a wide variety of phenomena, including the mechanical properties of the nucleus[2,25], the exclusion of nucleoplasm from chromatin,[26] and chromatin stretching[27] during nuclear deformation. However, micropipette aspiration is traditionally limited to a single cell at a time and performed with custom-pulled glass pipettes, which often vary in shape and diameter. In contrast, microfluidic devices enable high-throughput measurements of nuclear and cellular mechanics with precisely defined geometries.[28–30] Some microfluidic devices measure the stiffness of cells based on their transit time when perfused through narrow constrictions[31–34] or mimic micropipette aspiration,[35] but these approaches are often hampered by clogging due to particles, large cell aggregates, or cell adhesion in the constrictions. This problem can be alleviated in devices that use fluid shear stress to deform the cells rather than constrictions,[36] but the deformations achieved in these devices do not recapitulate the extensive deformations that can be achieved using physical barriers. Furthermore, in many of the current microfluidic perfusion assays, nuclear deformation is measured for only fractions of a second, making it difficult to observe viscoelastic responses with longer time-scales.

To overcome these challenges, we have developed an easy-to-use microfluidic device to measure time-dependent nuclear mechanical properties in a high-throughput manner. The device enables robust measurements of many cells in parallel, with easy loading and removal of cells from the aspiration sites, and requires minimal specialized equipment. Combined with a custom-developed automated image analysis MATLAB program to further accelerate the analysis and to provide consistent measurements, this experimental platform enables analysis of 100's of cells per hour, representing a 10- to 40-fold improvement over conventional manual micropipette aspiration.[37] We demonstrate the device's utility to quantify time-dependent nuclear and cell mechanics on a single-cell level, in a high throughput manner, in a broad range of applications and cell types.

Materials and Methods

Cells used for experiments. Mouse embryonic fibroblasts (MEFs) with homozygous deletion of the *Lmna* gene, which encodes lamins A/C, along with wild-type littermate controls, were generously provided by Dr. Colin Stewart.[38] Wild-type MEFs were stably modified with lentiviral vectors to express mNeonGreen-Histone 2B,[39] as described previously.[40] HT1080 cells were purchased from the DSMZ Braunschweig, Germany, and stably modified with lentiviral vectors to express the nuclear rupture reporter NLS-GFP, as described previously.[41] Induced pluripotent stem cells (iPSC) and healthy human skin fibroblasts were generously provided by Elisa di Pasquale and Gianluigi Condorelli (Humanitas Clinical and Research Center, Italy).[42] MDA-MB-231 cells were obtained from the American Type Culture Collection (ATCC). MEF, HT-1080, MDA-MB-231, and human fibroblast cells were maintained in Dulbecco's Modified Eagle Medium (DMEM) supplemented with 10 % (v/v) fetal bovine serum and 1 % (v/v) penicillin/streptomycin. iPSCs were maintained on matrigel-coated dishes in mTeSR medium (Stem Cell Technologies), prepared according to manufacturer's instruction. The dishes were prepared by diluting 50 µl matrigel (BD 354277) in 1 ml of mTeSR and incubating in 35 mm plastic petri dishes overnight at 4°C.

Design and microfabrication of the microfluidic devices. The mask and wafers were produced in the Cornell NanoScale Science and Technology Facility (CNF). The masks were fabricated using a Heidelberg DWL 2000 Mask Writer. Since the device contains features with different heights (5 µm for the micropipette channels and 10 µm for larger perfusion channels), two SU8 photolithography steps were used. A first 5-µm tall layer consisting of only the micropipettes channels was created by spinning SU-8 2005 to the correct thickness and exposing through the photomask using a GCA Autostep 200 DSW i-line Wafer Stepper, which allows precise realignment of the mask and wafer within 1 µm when using masks for the different SU-8 layers. The wafer was baked at 95°C for 30 minutes, cooled down and developed in SU-8 developer. A second layer of SU-8 2007 was spun to a thickness of 10 µm, and the larger device features were exposed on the stepper. The wafers were subsequently baked, developed following standard photolithography procedures,[40] and coated with trichloro(1H, 1H, 2H, 2H-perfluorooctyl)silane to facilitate demolding. PDMS replicas of the devices were cast using Sylgard 184 (Dow Corning), mixing in a 10:1 ratio and baking for two hours at 65°C. To minimize wear to the original wafer, the first PDMS cast was used to create a plastic mold from which all subsequent PDMS replicas were made, following a previously published protocol.[43] PDMS replicas were cut into individual devices and holes for perfusion were cut into the PDMS using a small (0.75 or 1.2 mm) biopsy punch to introduce tubing. The final PDMS devices were then mounted on glass slides using a plasma cleaner (Harrick Plasma) as described previously.[5,40]

Experimental acquisition. Immediately after plasma treatment, the PDMS devices were filled with 20 mg/ml bovine serum

albumin (BSA) and 0.2% (v/v) fetal bovine serum (FBS) in phosphate buffered saline (PBS) for 10 minutes to passivate the device. The same PBS solution was used as perfusion buffer and to create a cell suspension. The cell suspension (5 million cells/ml) was prepared in the PBS solution and kept on ice. Cell nuclei were stained by adding an aliquot of Hoechst 33342 at a dilution of 1:1000 to the cell suspension for a final concentration of 10 µg/ml and incubated on ice for ten minutes before being used for experiments. The vial with the cell suspension was connected via Tygon S3 E-3603 tubing (VWR, inner diameter 1/32"; outer diameter 3/32") to the cell entry port of the microfluidic device; a vial with cell free PBS solution (perfusion buffer) was connected to the buffer port. Additional tubing was connected to the outlet port (P_{atm} in Figure 1A) and drained into a small collection tube. The pressure applied to the vials with the cell suspension and the perfusion buffer was adjusted using an MCFS-EZ pressure controller (Fluigent) to regulate cell/buffer perfusion into the device. For the experiments, a pressure of 7.0 kPa was applied to the cell suspension and 1.4 kPa to the buffer solution. The outlet port tubing was open to atmospheric pressure.

Brightfield and fluorescence images of cells in the micropipette channels were acquired every 5 seconds using a 20×/NA 0.8 air objective and ORCA Flash 4.0 V2 Deep Cooling sCMOS (Hamamatsu) or alternatively CoolSNAP KINO CCD (Photometrics) digital camera to record nuclear deformation. At the start of each acquisition, cells present in the device were ejected from the micropipette channels, allowing new cells to enter the cell pockets and micropipette channels. To eject cells, pressure was applied to the outlet port with a syringe or pipette inserted in the tubing, causing transient reversal of the flow in the micropipette channels. As the pressure is greater at the cell port than the buffer port, the ejected cells were swept away from the vicinity of the micropipette channels towards the buffer port. After these cells had been removed (as observed through the microscope), the pressure at the outlet port was released, allowing new cells to enter the cell pockets and micropipette channels. The next round of data acquisition was then performed with these cells. By commencing the image acquisition before ejecting the cells, we ensured that all stages of cell and nuclear deformation were captured in the image sequences. The above procedure was repeated several times to capture data for a large number of cells at each experimental condition.

Modelling and experimental validation of fluid dynamics in the microfluidic devices. To determine the pressure exerted on the cells during nuclear deformation in the micro-channels, and because physical measurements inside the device are not feasible, we computationally modelled the pressure distribution inside the devices. Using the finite elements modelling software COMSOL Multiphysics 5.2, we designed a three-dimensional (3D) model that reproduced the geometry of the device. The fluid flow in the device was considered as laminar flow following the Navier-Stokes equation:

$$\rho(\boldsymbol{u}.\nabla)\boldsymbol{u} = \nabla(-p\mathbf{I} + \eta(\nabla\boldsymbol{u} + (\nabla\boldsymbol{u})^T)) \quad (1)$$

in which ρ is the volumic mass, $\boldsymbol{u}$ is the velocity, p is the pressure, $\boldsymbol{I}$ is the identity matrix and η is the dynamic viscosity of the fluid. The operator *T*, indicates the transpose operation on a tensor.

The hydrodynamic resistance of a tubular channel with laminar flow scales with the length of the channel and the inverse of the channel radius to the fourth power. Since the cross-sectional area of the tubing connecting the pressure controller to the device is orders of magnitude larger than the cross-sectional area of the channels in the microfluidic device, the hydrodynamic resistance of the microfluidic device is much greater than that of the connecting tubing. The pressure drop across the tubing outside of the microfluidic devices was therefore considered negligible relative to the pressure drop inside the device. The boundary conditions of the model were thus set to the pressure values applied to each solution in the device (P_{Cell} = 7 kPa; P_{Buffer} = 1.4 kPa). From this simulation, we computed the pressure distribution and the corresponding fluid flow profile in the device. The simulated velocity field was averaged over surfaces located above the centre of each pocket, to remove any effects due to variation in the geometry. To validate our computational model, we experimentally determined the flow rates from the streaks created by fluorescent beads (1.9 µm diameter) over a 3 ms exposure time. The length of the streaks was measured using ImageJ (National Institutes of Health, https://imagej.nih.gov/ij/). To minimize the effect of bead interactions with the walls, we analysed only beads in the centre of the channel. Given the small dimensions of the microfluidic channels, we calculated the effect of the beads on the effective viscosity of the fluid, using the work of Heinen et al.[44] and Einstein's formula:

$$\eta = \eta_s(1 + 2.5\phi) \quad (2)$$

in which η_s represents the dynamic viscosity of the fluid alone, and ϕ is the volume fraction of beads in the fluid. In our experiments, we used a 0.01% vol/vol suspension of beads with 1.9 µm diameter (Thermo-Fisher, Fluoro-Max G0200) in PBS solution with 20 mg/ml BSA. The viscosity for PBS containing 20 mg/ml BSA is η_s = 1.12 mPa.s.[44] Using the above equation, the dynamic viscosity of the bead/PBS suspension was determined from equation (2) to be η = 1.148 mPa.s. The flow rates in the channels were then computed from equation (1) using the bead velocity, pressure, and the viscosity of the bead solution.

Automated analysis of nuclear deformability measurements. A custom-written MATLAB program (available at: https://github.com/Lammerding/MATLAB-micropipette_analysis) was used to compute nuclear deformation into the microfluidic micropipette channels with only minimal user intervention. The MATLAB script converts time-lapse micropipette aspiration movies obtained using ZEN software (Zeiss) into multidimensional TIF stacks, separated according to color channels. The program can be readily adapted to import time-lapse sequences in other formats. The program automatically aligns the image sequence to a mask of the microfluidic device features to correct the images for rotational error, segment the individual microfluidic pockets, and determine the location of the micropipette channel

entrances. The user can make manual fine adjustments to the micropipette entrance line at any time using the arrow keys in the program interface. The program then thresholds the blue colour channel, which corresponds to the blue fluorescence from the DNA-binding Hoechst 33342 dye, to provide a trace of the nucleus during deformation. The threshold for the nuclear segmentation is based on a manual graphical user interface that provides a preview of the segmentation. To account for the heterogeneity in the Hoechst signal across different nuclei, the user selects a binary threshold value for each pocket from a histogram of pixel count versus intensity. After applying erosion and dilation processing to smooth the outlines of each thresholded nucleus, the program employs the MATLAB's *regionprops* function to track the nucleus' leading edge inside the micropipette and calculate the distance between the leading edge of the nucleus and the micropipette channel entrance for each frame. The program allows for visual inspection of the nuclear protrusion length analysis. After analysing all nuclei, the program exports the final matrix of nuclear protrusion values over time into a Microsoft Excel-compatible file, where rows correspond to the pocket number and columns to each image frame/time point. Empty pockets register as zeroes. Likewise, once a nucleus deforms past the end of the micropipette channel, it also registers as zero since the protrusion length is no longer measureable. For cells with highly deformable nuclei, multiple cells may sequentially enter and pass through a given micropipette channel during a single acquisition sequence. These cells are recorded as separate events. An additional MATLAB script, available upon request, was used to transpose the protrusion length versus time data to make it suitable for multilevel model analysis using JMP software.

Fitting the deformation data to models. The data obtained in the deformation experiments were fit to a number of viscoelastic models using the solver function in Microsoft Excel. Briefly, the function corresponding to the model studied was determined and approximate values for the variables were chosen as starting values. A computed value of the protrusion length was then obtained for each given deformation time, based on the function and variables. Each of these calculated values was subtracted from the value of the protrusion length obtained experimentally at each time point. This residual value was squared and the sum of squares for all time points was used as an indicator of goodness-of-fit. The solver function in Microsoft Excel was used to minimize the sum of the squared residuals by varying the variables within each model.

Each data set was modelled using six separate functions. We tested two functions for the power law model: $y = A * t^{\alpha}$ and $y = A * t^{\alpha} + c$. We tested four functions for the modified spring-and-dashpot model: the Kelvin–Voigt model (spring and dashpot in parallel) $y = A * (1 - \exp(B * t))$, the linear model (a spring followed by a spring and dashpot in parallel) $y = A - B*(1 - \exp(C * t))$, a Jeffreys model (a dashpot followed by a spring and dashpot in parallel) $y = A * (1 - \exp(B * t)) + C * t$, and a Burgers model (a spring and dashpot in series followed by a spring and dashpot in parallel) $y = A - B * (1 - \exp(C * t)) + D * t$. In the results section we report the second power law model and the Jeffreys model, which both showed significant improvements over more simple models. The Burgers model did not greatly improve the sum of the residuals, and thus we chose the Jeffreys model. The viscosity and elastic modulus were derived from these variables as detailed in the Supplementary information. We calculated and report the coefficient of determination (R^2) value for each model and cell type.

Statistical analysis. Statistical analysis was performed using Microsoft Excel and Igor Pro. We determined *p* values in student *t*-tests using the TTEST function in Excel. Igor Pro was used to obtain the confidence interval (one standard deviation) on the variables obtained from the fit of the data to the various models. Standard error propagation calculations were performed to obtain error values on the spring constants, elastic moduli, and viscosities, estimating that the error on the pressure is 0.3 kPa, and the error on the width and height of the micropipette channels is 0.5 μm. In all figures, error bars represent the standard error of the mean unless indicated otherwise. All data are based on at least two independent experiments.

Results and Discussion

Design of the microfluidic devices

The device consists of a series of 18 pockets with small micropipette channels, abutting a larger main channel used to perfuse cells into the device and the individual pockets (Figure 1A-D). The pockets are 20 μm wide and 10 μm tall, thus large enough to hold only a single cell. The micropipette channels are 3 μm wide and 5 μm tall, similar in size to micropipettes in conventional micropipette aspiration assays for probing nuclear mechanics, in which pulled glass pipettes with 3-5 μm inner diameter are used.[2,25,45] The micropipette channels connect to a large chamber at atmospheric pressure (P_{atm}). The cells are introduced into the device at the cell port under a pressure (P_{Cell}) that is higher than the pressure at the buffer port (P_{Buffer}), ensuring that the cells flow along the main channel (Figure 1A, C and D.) The two pressure inlets allow precise control of the velocity of the perfusion of the cells through the devices and the pressure applied on the cells in the pockets and micropipette channels. Microfluidic filters at each port, consisting of arrays of pillars, prevent large clusters of cells or dust to enter the main channel. As cells perfuse through the device, single cells flow into empty pockets and block the entrance of the micropipette channels, thereby preventing additional cells from settling into the same pocket. Cells located in the pocket then deform into the micropipette channels as they are subjected to the pressure difference between the main channel and atmospheric pressure. The large cell nucleus fills the entire cross-section of the micropipette channel (Figure 1E). The externally applied pressure is kept constant and the nucleus gradually enters the micropipette channel, closely resembling the creep behaviour observed in conventional micropipette aspiration assay.[22,37] The

deformation of the nucleus over time is recorded by time-lapse microscopy and used to infer the mechanical properties of the nucleus. Our micropipette dimensions are optimized for fibroblasts, myoblasts, and most cancer cells. The design can readily be adapted for smaller, more deformable cells (such as immune cells) if needed.

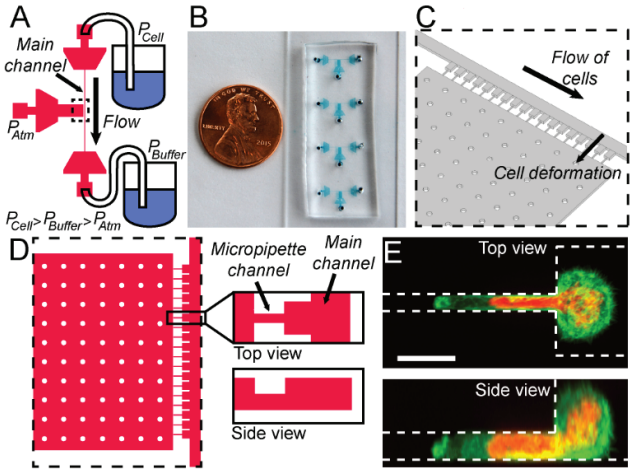

Figure 1: Overview of the micropipette devices. (**A**) Schematic overview of the device and the different pressures applied to the three ports. The dashed rectangle indicates the region shown as close-up in panels C and D. (**B**) Photograph of the actual devices in a typical experimental setup, with four devices mounted on a glass coverslip, allowing the measurement of four different cell types or replicates in rapid succession. A US 1 cent coin serves as reference for size. (**C**) Schematic 3-D close-up of the micropipette channels and the main channel, corresponding to the area outlined with a dashed line in panel A. (**D**) Schematic close-up of the device region with the individual pipettes channels, viewed from the top (left) and side (right). The side-view shows that the pipette channels have a lower height (5 µm) than the rest of the device (10 µm). (**E**) Representative image of cells expressing fluorescently labelled histones (red) to reveal the nucleus, and a fluorescent actin marker (LifeAct-GFP, green) to delineate the cytoplasm, entering the micropipette channel. (Scale bar: 10 µm.)

Automated image analysis

To measure nuclear deformations into the array of micropipettes in a quick and highly consistent manner, we developed a semi-automated MATLAB image analysis platform that requires only minimal user input (Figure 2). After initial image processing, a mask alignment step corrects the images for rotational error, segments the individual pockets, and determines the micropipette entrance (Figure 2B, vertical yellow line). To account for the heterogeneity in the nuclear fluorescence signal (e.g., DNA fluorescently labelled with Hoechst 33342), the user selects a binary threshold value for each pocket from a histogram of pixel count versus pixel intensity (Figure 2B, middle panel). Following additional erosion and dilation processing to smooth the segmented nuclei, the program tracks the leading edge of each nucleus (Figure 2B, red vertical line) and calculates the distance aspirated into the micropipette channel (i.e., the protrusion length) for each frame (Figure 2C). The program allows visual inspection of the

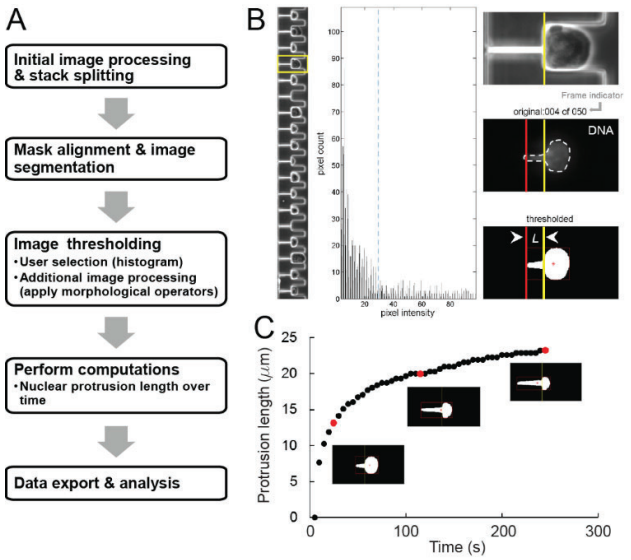

Figure 2: Custom-designed MATLAB software enables rapid analysis of nuclear deformability. (**A**) Schematic overview of the image analysis pipeline. The MATLAB program converts time-lapse micropipette aspiration movies into multidimensional image stacks and separates them by colour channel. The user aligns a mask to one of the image frames to segment the 18 pockets, enabling individual examination of each cell nucleus. (**B**) A graphical user interface ensures accurate measurement of the nuclear deformations within each pipette. The yellow box (left panel, fourth pocket) indicates the selected cell and corresponding nucleus, as visualized using Hoechst 33342 dye, which fluorescently labels DNA. The user sets a binary threshold value (blue dotted line) by clicking within the middle panel, a 60-bin histogram of image intensity values. Clicking the left mouse button previews the threshold by playing through the image sequence (right panel) at a user-specified sampling rate (every n^{th} frame). Additional erosion and dilation processing steps smooth boundaries and remove spurious pixels within the thresholded image. The program computes the nuclear protrusion length at each frame by drawing a bounding box around the thresholded nucleus (red box) and then computing the distance between the left edge (red vertical line) and the start of the micropipette channel (yellow vertical line). Once the thresholded image sequence (right panel, bottom) accurately depicts the original (right panel, middle), right clicking the mouse button saves the protrusion length values and proceeds to the next pocket. The values are exported to an Excel file where they can be plotted and analysed. (**C**) A plot of the nuclear protrusion length over time for a given cell, with the red data points corresponding to the thresholded nuclei in the frames shown below.

nuclear protrusion length in each pocket before proceeding. The program exports the final matrix of nuclear protrusion values over time for each pocket as an Excel-compatible file for subsequent statistical analysis or curve fitting.

Characterization of fluid dynamics and pressure gradients with the microfluidic device

The velocity of the cells moving along the main channel depends on the difference between the applied pressures, P_{Cell} and P_{Buffer}.

The larger the pressure gradient, the faster the cells will move through the device, ensuring rapid filling of available pockets. The pressure difference across the micropipette channels drives the cell and nuclear deformation. This pressure gradient is determined by the pressure in the main channel in front of the pipette (which depends on P_{Cell} and P_{Buffer}) and the atmospheric pressure, P_{atm}, at the other end of the micropipette channel. The deformation rates and flow velocities are thus readily tunable by varying the pressures applied to the cell port (P_{Cell}) and the buffer port (P_{Buffer}). To determine the pressure distribution within the device in more detail, including potential differences in the pressure exerted across the 18 parallel micropipette channels, we performed computational modelling of the fluid dynamics and pressure drop across the microfluidic device and then compared these model predictions with experimental measurements. We modelled two cases: one in which the micropipette channels are unfilled ("open"), and one in which the channels are blocked ("closed"). Typical experimental conditions during nuclear deformation measurements correspond to the "closed" scenario, as all of the micropipette channels are rapidly filled with cells that occupy the entire cross-section of the channels (Figure 1E) and thereby block fluid flow across the microchannels, in agreement with previous work.[46] In the closed case, the model predicts a linear decrease in pressure across the micropipette channels (Figure 3A, B), with the cells in the micropipette channels exposed to pressures between 3.8 and 4.4 kPa, corresponding to a difference of approximately 15% between the first and the last micropipette channel. In the case of the open micropipette channels, the model predicts a pressure drop across the main channel at the pipettes that decreases rapidly. In this case, the pressure difference from the first to the last micro-pipette channel decreases from 2.4 to 1.7 kPa (Supplemental Figure 1), a difference of >40%, which would imply a large variation from one micropipette channel to the next. In both the "open" and "closed" cases, the model indicates that the pressure drop across the filters at the ports is negligible compared to the pressure drop along the main channel (Figure 3A, B; large triangular shaped areas at each of the three outlets).

Experimental validation of the computational model

The small dimensions of the microfluidic device prohibit direct pressure measurements within the device. We therefore used experimental measurements of the fluid flow to infer the local pressure variation within the device. For these experiments, we perfused fluorescent beads through the microfluidic devices and determined the flow velocity inside the devices by quantifying the local velocity of the fluorescent beads. Measurements were obtained before and after the beads had clogged the microchannels, simulating the "open" and "closed" configurations, respectively. The experimental velocity measurements closely matched the predicted velocity from our computational model in the corresponding configurations (Figure 3B and Supp. Fig. 1). During actual micropipette aspiration experiments, all of the microchannels are simultaneously filled with cells, and thus experimental

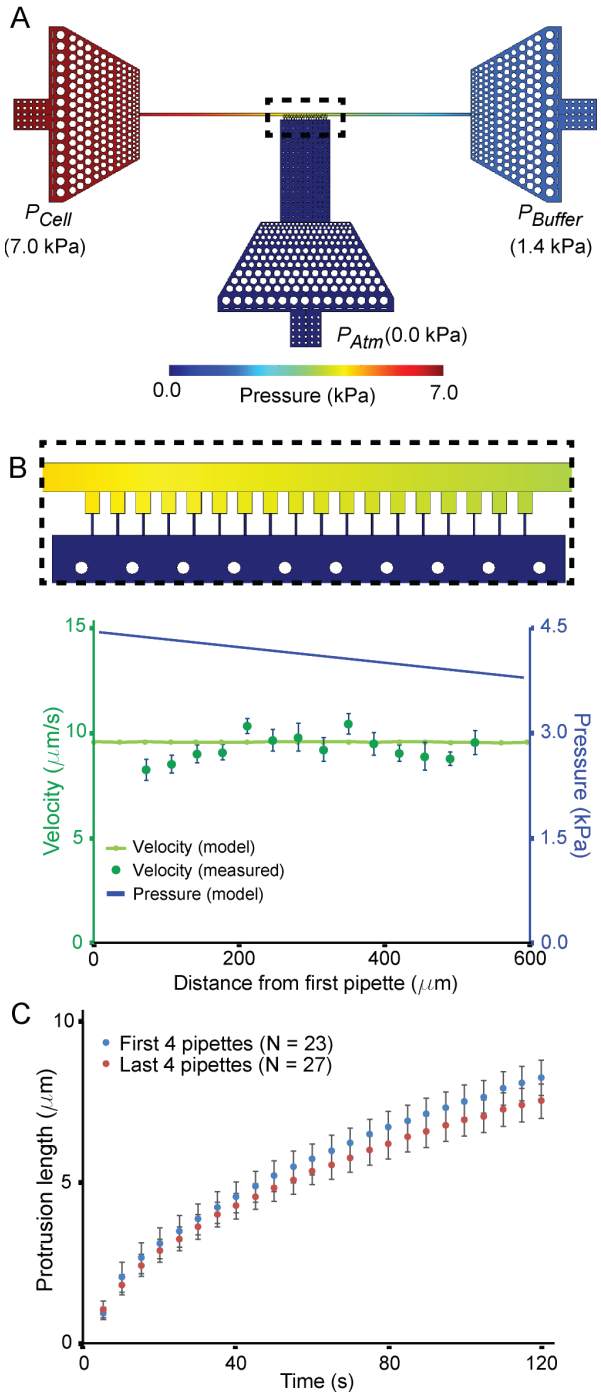

Figure 3: Modelling of the pressure distribution across the device. (**A**) Pressure distribution obtained from 3-D computational model in the condition in which the micropipette channels are closed, corresponding to experimental conditions in which all the channels are blocked by cells. (**B**) Comparison of the model predictions for the pressure distribution and resulting fluid velocity distribution in the main channel with experimental measurements. The velocity (light green line) determined from the pressure gradient (top figure and blue curve) was compared to the flow velocity determined from fluorescent beads (dark green points). (**C**) Deformation of wild-type MEFs in the first four

micropipette channels (blue) compared to the last four micropipette channels (red). The differences between the first four and the last four channels is not statistically significant, consistent with the predictions of the models. Similar results obtained from independent experiments with another cell line are included in Supp. Fig. 2A.

conditions resemble the "closed" case, resulting in a small, linear pressure drop along the length of the main channel. We tested whether the predicted small pressure difference between pipettes can affect the experimental readings depending on the position of the specific micropipette channel by performing experiments with mouse embryo fibroblast (MEF) cells and human breast cancer cells. The experiments did not reveal any statistically significant difference between the extent of nuclear deformation in the first 4 channels of the devices compared to the last four channels for either of the cell lines (Figure 3C; Suppl. Fig. 2A), indicating that the small drop in pressure along the main channel predicted by numerical simulations (Figure 3B) is negligible compared to the cell-to-cell variability of the experiment. If desired, the device design could be readily adapted to reduce further the pressure gradient across the section of the main channel containing the cell pockets, for example, by lengthening the other sections of the main channels, or altering its cross-section.

Device validation in cells with known nuclear mechanical properties

To validate our microfluidic micropipette devices, we measured the nuclear mechanical properties of lamin A/C-deficient (*Lmna*$^{-/-}$) and wild-type (*Lmna*$^{+/+}$) MEFs, which have been extensively characterized by micropipette aspiration[5] and nuclear strain experiments[1,47]. Consistent with previous studies, we found that lamin A/C-deficient MEFs had significantly more deformable nuclei than wild-type MEFs, as evidenced by the substantially more rapid deformation into the micropipette channels (Figure 4). Lamin A/C-deficient cells exhibited nuclear deformations 2.17 ± 0.02 times larger than wild-type controls, which is similar to the 2.05-fold increase in nuclear deformation observed in the same cell lines using substrate strain experiments,[1] and the 2.2-fold increase reported in a previous study comparing lung epithelial cells depleted for lamin A/C to non-depleted controls.[48]

For a more detailed analysis of the mechanical properties of these two cell types, we compared the time-dependent nuclear deformation into the micropipette channels using two alternative approaches. In the first approach, we modeled nuclear deformation into the micropipette channels under a constant pressure ('creep') using a power law proposed by Dahl and colleagues.[25] In this model, the nuclear protrusion length increases as a function of time to the power of an exponent, α, and the prefactor, A; the constant C accounts for uncertainty in the exact timing when the nucleus entered the channel ($t = 0$).

$$L(t) = A\,t^{\alpha} + C \qquad (3)$$

For viscoelastic materials, the exponent α is in the range of 0 to 1, and indicates whether the material behaviors more elastic(α closer to 0) or more viscous (α closer to 1).[25] In our

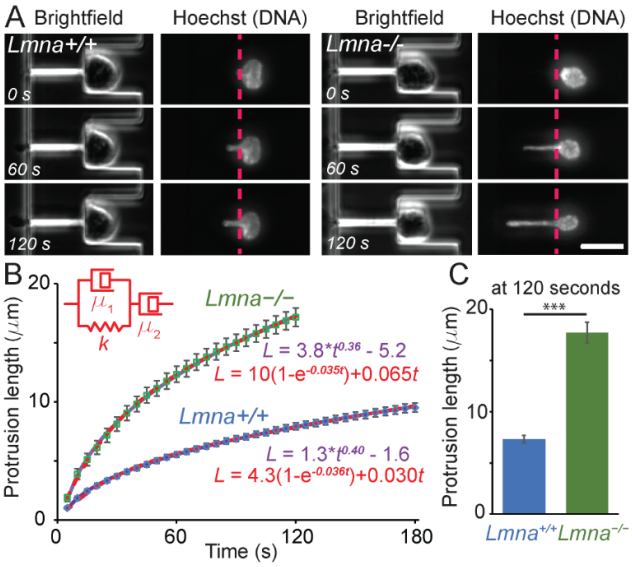

Figure 4: Validation of the devices the mechanical properties of nuclei. Wild-type (*Lmna*+/+, left) and lamin A/C-deficient (*Lmna*–/–, right) cells were deformed and the length of the protrusion was measured as a function of time. Brightfield images and images of the nucleus stain (Hoechst 33342) were acquired every five seconds. The *Lmna*–/– cells deformed more rapidly and more extensively than the wild-type controls. (**A**) Representative example images of the same cell at three different time points. (Scale bar 20 μm.) (**B**) The nuclear deformation (protrusion length) as a function of time modelled as a power law (purple line) or using the Jeffreys model (red dashed line). Only the first 120 seconds are shown for the *Lmna*–/– cells as many of these nuclei completely entered the micropipette channel at times longer than 120 seconds, and could thus not be used for analysis. (**C**) Comparison of the nuclear protrusion length at 120 seconds. ***, $p < 0.001$; $n = 70$ and 56 for *Lmna*+/+ and *Lmna*–/–, respectively

experiments (Figure 4B), lamin A/C-deficient and wild-type cells both fit power laws with similar exponents ($\alpha = 0.41 \pm 0.01$ and $\alpha = 0.37 \pm 0.01$ for wild-type cells and lamin A/C-deficient cells, respectively). This value is comparable to the one found by Dahl et al.[25] ($\alpha = 0.3$) for human adenocarcinoma-derived epithelial-like cells (TC7), and in agreement with a later study by the same group that found that reducing lamin A/C levels does not significantly affect the power law exponent for time-scales exceeding 10 seconds ($\alpha = 0.20$ for wild-type and 0.24 for lamin A/C-depleted lung epithelial cells).[48] Taken together, our data indicate that the microfluidic devices produce results consistent with those obtained using conventional micropipette aspiration.

In a second approach, we used classical "spring and dashpot" viscoelastic models to describe the time-dependent nuclear deformation into the micropipette channels. We tested several combinations of springs and dashpots (see Suppl. Fig. 3). The simplest model to adequately fit the observed viscoelastic creep behavior (with an increasing plateau at long deformation times)

is a dashpot in series with a Kelvin-Voigt element (spring and dashpot in parallel, Figure 4B). This 3-element model, known as a Jeffreys model, predicts the time-dependent deformation by the following equation:

$$L(t) = \frac{f}{k}\left(1 - e^{-t/\tau}\right) + \frac{f}{\mu_2}t \qquad (4)$$

where $L(t)$ is the strain (or, in this case, the nuclear protrusion), f is the aspiration force, k is the spring constant, μ is the dissipation coefficient of the dashpot element in series and τ is the relaxation time (equivalent to k/μ_1). To obtain quantitative data from this model, we balanced the aspiration force with the forces due to the elastic contribution (at short time scales) and the viscous flow through a small constriction (at long time scales) and obtained the following equation (see Supplementary Information for details on the derivation):

$$L(t) = \sqrt{\frac{HW}{\pi}}\frac{\Delta P}{E}\left(1 - e^{-\frac{E}{3\pi\eta_1}t}\right) + \sqrt{\frac{HW}{\pi}}\frac{\Delta P}{3\pi\eta_2}t \qquad (5)$$

Fitting the experimental data to the Jeffreys model we obtained values comparable to those reported previously in the literature (Table 1). Guilak et al.[49] measured an elastic modulus of 1 kPa and a viscosity of 5 kPa*s in isolated nuclei of pig chondrocytes, Dahl et al.[25] measured an elastic modulus of 5.7 kPa in isolated nuclei from lung epithelial cells, and Luo et al[50] found elastic moduli of 3.5 and 3 kPa in whole cell measurements of two tumor cell lines in microfluidic devices.

As expected, we detected significant differences between the lamin A/C-deficient and wild-type cells (Table 1). The elastic modulus of wild-type nuclei was more than two times larger for the lamin A/C-deficient nuclei, indicative of the importance of lamin A/C in determining the resistance to nuclear deformation.[1,4,13,17] Similarly, the two parameters describing the nuclear viscosity were approximately double in magnitude for wild-type cells compared to the lamin A/C-deficient cells, indicating that wild-type nuclei flow more slowly.

Parameter	*Lmna*+/+	*Lmna*–/–
A	1.34 (±0.05)	3.8 (±0.3)
α	0.41 (±0.01)	0.37 (±0.01)
E	2.1 (±0.3) kPa	1.0 (±0.1) kPa
η_1	6 (±1) kPa*s	2.8 (±0.4) kPa*s
η_2	33 (±4) kPa*s	15 (±2) kPa*s

Table 1. Lamin A/C-deficient cells have altered nuclear viscoelastic properties. Parameters for the Jeffreys model based on the least squares regression of the experimental data. The parameters A and α were obtained by measuring the protrusion length in μm and the time in seconds. The units of the parameter A are dependent on the magnitude of α; α is dimensionless.

Both the Jeffreys model and the power law model closely matched the experimental data (Figure 4B) and present complementary approaches to analyze nuclear deformation data. Taken together, the above experiments demonstrate that the microfluidic device is well suited to study nuclear mechanical properties, including the time-dependent behavior of nuclear deformation under force. Given the similar quality of fit and the fact that both viscoelastic models use the same number of tunable parameters (A, α, and c for the power law model; E, η_1, and η_2 for the Jeffreys model), the choice of a particular model will depend on the specific experiments and questions.

Measurements are independent of nuclear size or DNA labeling

To test the robustness of the microfluidic analysis platform in measuring nuclear mechanical properties, we analyzed the effect of two potentially confounding factors: (1) nuclear size; (2) the Hoechst 33342 dye commonly used to fluorescently label DNA, which could potentially affect nuclear deformability as it intercalates into the DNA. We found no significant correlation between the measured mechanical properties of the nuclei and the size of the nuclei (Suppl. Fig. 2C), indicating that the obtained measurements are independent of nuclear size. Furthermore, the addition of Hoechst 33342 dye did not alter the nuclear mechanical properties of cells expressing histone H2B fused to mNeonGreen to visualize nuclear deformation (Suppl. Fig. 2B), indicating that the DNA-intercalating dye does not alter mechanical properties under the experimental conditions used here.

Application of the device to laminopathy cells, stem cells, and tumor cells

To demonstrate the versatility of the microfluidic devices in a broad range of applications, we performed measurements of nuclear mechanical properties in a variety of cell types. In the first application, we compared human skin fibroblasts from an individual with dilated cardiomyopathy caused by a mutation in the *LMNA* gene (*LMNA*-DCM) with matching skin fibroblasts from a healthy family member.[42] *LMNA* mutations lead to a wide family of diseases, collectively referred to as laminopathies, that include *LMNA*-DCM, Emery-Dreifuss muscular dystrophy (EDMD), congenital muscular dystrophy, and limb-girdle muscular dystrophy.[15] One hypothesis to explain the often muscle-specific phenotypes in laminopathies is that the mutations affect the mechanical properties of the nucleus, rendering it less stable, and thus resulting in increased cell death in mechanically stressed tissues such as skeletal and cardiac muscle.[15] Supporting this hypothesis, fibroblasts expressing *LMNA* mutations associated with EDMD have more deformable nuclei than cells from healthy controls in membrane stretching assays.[20] Applying our microfluidic platform to skin fibroblasts from a laminopathy patient with *LMNA*-DCM and from a healthy family member, we found that the *LMNA*-DCM skin fibroblasts had significantly more deformable nuclei than the healthy controls (Figure 5A Table 2), indicating that the *LMNA* mutation reduces the mechanical stability of the nucleus in the *LMNA*-DCM cells. Analysis of the time-dependent creep deformation revealed that the nuclei of the *LMNA*-DCM fibroblasts were less viscous than the healthy controls, as visible in the steeper slope of the nuclear protrusion over longer time scales (Figure 5A; Table 2). This trend recapitulates our above findings in the lamin A/C-deficient and wild-type MEFs, where the loss of lamin A/C reduced the nuclear elastic modulus and viscosities (Table 1). While further studies will be necessary to determine if these phenotypes are

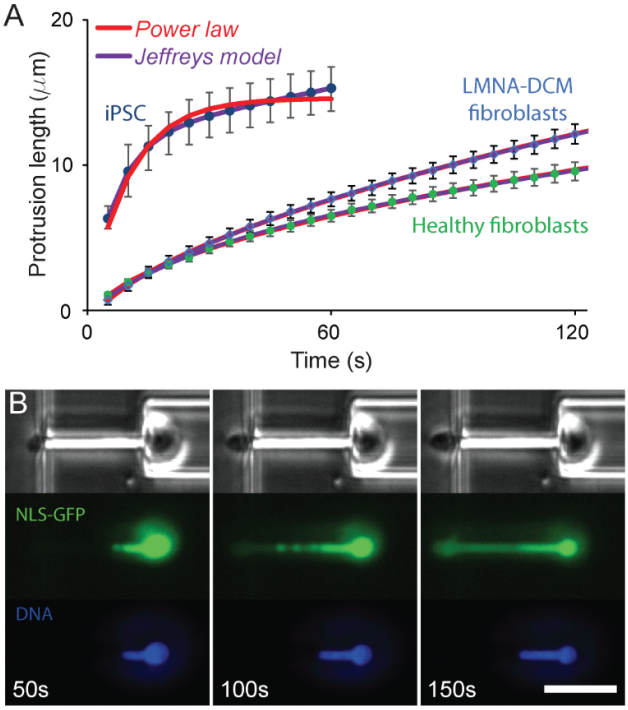

Figure 5. Comparison of the deformability of human cells. (**A**) Induced pluripotent stem cells derived from human skin fibroblasts have more deformable nuclei than human skin fibroblasts, reflecting the changes in chromatin organization and lower lamin A/C levels in the iPSCs. Human skin fibroblasts from an individual carrying a *LMNA* mutation that causes dilated cardiomyopathy have significantly more nuclear viscous flow at long deformation times. (**B**) Extensive nuclear deformation micropipette aspiration can result in nuclear envelope rupture, as visualized by the leakage of soluble green fluorescent proteins with a nuclear localization sequence (NLS-GFP) into the cytoplasm following nuclear envelope rupture. Time-lapse images show the extent of deformation and nuclear leakage with time, as a function of the onset of nuclear deformation. (Scale bar: 20 μm.)

	Healthy fibroblast	***DCM fibroblast***	***iPSC***
A	1.02 (±0.05)	0.83 (±0.02)	19 (±2)
α	0.49 (±0.01)	0.584 (±0.004)	0.012 (±200)
E	2.0 (±0.2) kPa	1.8 (±0.2) kPa	0.8 (±0.1) kPa
η_1	6 (±1) kPa*s	7 (±1) kPa*s	0.6 (±0.1) kPa*s
η_2	23 (±3) kPa*s	17 (±2) kPa*s	17 (±2) kPa*s

Table 2. Cells bearing *LMNA* mutations and in a reprogrammed differentiation state show altered nuclear mechanics. Parameters for Jeffreys model based on best fit to the experimental data from human skin fibroblasts from an individual with an *LMNA* mutation associated with dilated cardiomyopathy (DCM), a healthy control, and iPSCs derived from healthy human skin fibroblasts. The parameters A and α were obtained by measuring the protrusion length in μm and the time in seconds. The units of the parameter A are dependent on the magnitude of α; α is dimensionless.

recapitulated in other mutations and in *LMNA* mutant human cardiomyocytes, we have already used the microfluidic assay to demonstrate that myoblasts from mouse models of muscle laminopathies have reduced nuclear stability, and that the extent of the defect correlates with the disease severity.[51]

In a second application, we investigated the effect of stem cell differentiation on nuclear mechanical properties. As pluripotent stem cells differentiate into specific lineages, their nuclear stiffness increases for most lineages, likely due to a concomitant increase in the expression levels of lamin A/C and changes in chromatin organization.[10,22] We compared the deformability of human skin fibroblasts and induced-pluripotent stem cells (iPSCs) generated from skin fibroblasts, using our microfluidic devices. The iPSC cells had highly deformable nuclei (Figure 5A), resulting in many of the iPSCs passing through the micropipette channels within a few frames (less than 20 seconds). To avoid bias towards cells that passed through the channel more slowly, we restricted our comparison to the first 60 seconds of nuclear deformation and selected only cells whose nuclei had not completely entered the micropipette channel during time. The iPSCs had significantly more deformable nuclei than the skin fibroblasts (Figure 5A; Table 2), consistent with a previous study using conventional micropipette aspiration that found that nuclear stiffness increased during differentiation of human embryonic stem cells[22,52]. Comparing the data to both the power law model and the Jeffreys model, we found that the Jeffreys model provided a better fit for the iPSC data than the power law model, whereas both models provided equally good fits for the human skin fibroblast data (Figure 5A), consistent with our results for mouse embryo fibroblasts (Figure 4). The error on the power law exponent value is orders of magnitude greater than the exponent itself, symptomatic of the poor fit. Strikingly, the viscosity (η_2) of the iPSCs did not differ from the viscosity of the skin fibroblasts. This viscosity governs the deformation rate at long time scales. Our results suggest that reprogramming primarily alters the elastic properties of the nuclei.

Taken together, these examples demonstrate the use of the microfluidic device to measure the viscoelastic properties of nuclei in intact cells in a broad range of applications, producing results consistent with conventional micropipette aspiration assays or nuclear strain experiments, but at significantly higher throughput, and without the need for cell-substrate adhesion. The latter point is particularly relevant when studying tumour cells, which often have reduced adhesion strength,[53] and are thus not well suited for substrate strain experiments. Taking advantage of the novel microfluidic assay, we recently demonstrated that TGF-beta induced epithelial-to-mesenchymal transition in PyMT mouse breast tumour cells was associated with a decrease in nuclear stiffness, which, together with changes in focal adhesion organization, resulted in increased tumour cell invasion.[54] Notably, the device can also be used to study nuclear envelope rupture, which frequently occurs during migration of cells through confined environments.[26,41,55] As demonstrated in Figure 5B, the leakage of soluble green fluorescent protein with a nuclear localization sequence (NLS-GFP)[41] from the nucleus into the cytoplasm upon

nuclear envelope rupture can be clearly observed during large nuclear deformations.

Conclusions

We developed a novel microfluidic device and semi-automated imaging analysis pipeline in which we can observe and quantify the deformation of the nucleus at high resolution in intact cells, and with substantially higher throughput than conventional single cell micropipette aspiration experiments or atomic force microscopy measurements. We demonstrated the device's applicability to obtain precise viscoelastic information about the nucleus, including in mouse and human laminopathy cells and in human induced pluripotent stem cells and the corresponding original skin fibroblasts. Because the analysis platform presented here can perform measurements on large populations of cells, it can characterize the heterogeneity of samples, for example, to detect small mechanically distinct subpopulations of cancer cells or stem cells.

Conflicts of interest

There are no conflicts to declare.

Acknowledgements

This work was supported by awards from the National Institutes of Health [R01 HL082792 and U54 CA210184 to JL], the Department of Defense Breast Cancer Research Program [Breakthrough Award BC150580 to JL], the National Science Foundation [CBET-1254846 and MCB-1715606 to JL; GRFP-2014163403 to GRF], La Ligue contre le cancer [REMX17751 to PMD] the Fondation ARC [PDF20161205227 to PMD], and a ministerial doctoral fellowship of Paris Saclay University to SDM. This work was performed in part at Cornell NanoScale Facility (CNF), an NNCI member supported by NSF Grant NNCI-1542081. The authors thank Elisa di Pasquale and Gianluigi Condorelli for the human iPSCs and laminopathy patient fibroblasts, Colin Stewart for the lamin A/C-deficient and wild-type MEFs. The authors thank Karine Guevorkian and Francoise Brochard for helpful discussions.

References

1 J. Lammerding, P. C. Schulze, T. Takahashi, S. Kozlov, T. Sullivan, R. D. Kamm, C. L. Stewart and R. T. Lee, *J. Clin. Invest.*, 2004, **113**, 370–378.
2 K. N. Dahl, S. M. Kahn, K. L. Wilson and D. E. Discher, *J. Cell Sci.*, 2004, **117**, 4779–86.
3 A. D. Stephens, E. J. Banigan and J. F. Marko, *Nucleus*, 2017, **1034**, 1–6.
4 A. D. Stephens, E. J. Banigan, S. A. Adam, R. D. Goldman and J. F. Marko, *Mol. Biol. Cell*, 2017, **28**, 1984–1996.
5 P. M. Davidson, C. Denais, M. C. Bakshi and J. Lammerding, *Cell. Mol. Bioeng.*, 2014, **7**, 293–306.
6 T. Harada, J. Swift, J. Irianto, J. W. Shin, K. R. Spinler, A. Athirasala, R. Diegmiller, P. C. D. P. Dingal, I. L. Ivanovska and D. E. Discher, *J. Cell Biol.*, 2014, **204**, 669–682.
7 K. Wolf, M. te Lindert, M. Krause, S. Alexander, J. te Riet, A. L. Willis, R. M. Hoffman, C. G. Figdor, S. J. Weiss and P. Friedl, *J. Cell Biol.*, 2013, **201**, 1069–1084.
8 A. L. McGregor, C.-R. R. Hsia and J. Lammerding, *Curr. Opin. Cell Biol.*, 2016, **40**, 32–40.
9 P. Friedl, K. Wolf and J. Lammerding, *Curr. Opin. Cell Biol.*, 2010, 1–10.
10 S.-J. Heo, T. P. Driscoll, S. D. Thorpe, N. L. Nerurkar, B. M. Baker, M. T. Yang, C. S. Chen, D. A. Lee and R. L. Mauck, *Elife*, 2016, **5**, e18207.
11 W. Cheng, H. Shi, Z. Poon, L. Myint, T. Kaushik and G. V Shivashankar, , DOI:10.1073/pnas.1402306111.
12 X. Mao, N. Gavara and G. Song, *Stem Cell Rev Rep*, 2015, 804–812.
13 J. D. Pajerowski, K. N. Dahl, F. L. Zhong, P. J. Sammak and D. E. Discher, *Proc. Natl. Acad. Sci. U. S. A.*, 2007, **104**, 15619–15624.
14 B. Burke and C. L. Stewart, *Functional Architecture of the Cell ' s Nucleus in Development* , Elsevier Inc., 1st edn., 2014, vol. 109.
15 P. M. Davidson and J. Lammerding, *Trends Cell Biol.*, 2014, **24**, 247–256.
16 J. Lammerding, J. Hsiao, P. C. Schulze, S. Kozlov, C. L. Stewart and R. T. Lee, *J. Cell Biol.*, 2005, **170**, 781–91.
17 J. Lammerding, L. G. Fong, J. Y. Ji, K. Reue, C. L. Stewart, S. G. Young and R. T. Lee, *J. Biol. Chem.*, 2006, **281**, 25768–80.
18 N. Caille, Y. Tardy and J. J. Meister, *Ann. Biomed. Eng.*, 1998, **26**, 409–16.
19 P. Isermann, P. M. Davidson, J. D. Sliz and J. Lammerding, *Curr. Protoc. cell Biol.*, 2012, **Chapter 22**, Unit22.16.
20 M. Zwerger, D. E. Jaalouk, M. L. Lombardi, P. Isermann, M. Mauermann, G. Dialynas, H. Herrmann, L. L. Wallrath and J. Lammerding, *Hum. Mol. Genet.*, 2013, 1–15.
21 S. Sen and S. Kumar, *J. Biomech.*, 2010, **43**, 45–54.
22 J. D. Pajerowski, K. N. Dahl, F. L. Zhong, P. J. Sammak and D. E. Discher, *Proc. Natl. Acad. Sci.*, 2007, **104**, 15619–15624.
23 J. Swift, I. L. Ivanovska, A. Buxboim, T. Harada, P. C. D. P. Dingal, J. Pinter, J. D. Pajerowski, K. R. Spinler, J.-W. Shin, M. Tewari, F. Rehfeldt, D. W. Speicher and D. E. Discher, *Science (80-.).*, 2013, **341**, 1240104–1240104.
24 K. N. Dahl, P. Scaffidi, M. F. Islam, A. G. Yodh, K. L. Wilson and T. Misteli, *Proc. Natl. Acad. Sci. U. S. A.*, 2006, **103**, 10271–6.
25 K. N. Dahl, A. J. Engler, J. D. Pajerowski and D. E. Discher, *Biophys. J.*, 2005, **89**, 2855–64.
26 and D. E. D. Jerome Irianto, Charlotte R. Pfeifera, Rachel R. Bennetta, Yuntao Xiaa, Irena L. Ivanovskaa, Andrea J. Liua, Roger A. Greenberga, *Mol. Biol. Cell*, 2016, **in press**, 1–30.
27 J. Irianto, Y. Xia, C. R. Pfeifer, R. A. Greenberg and D. E. Discher, *Biophys. J.*, 2016, **in press**, 1–4.
28 A. C. Hodgson, C. M. Verstreken, C. L. Fisher, U. F. Keyser, S. Pagliara and K. J. Chalut, *Lab Chip*, 2017, **17**, 805–813.
29 J. Zhang, X. A. Nou, H. Kim and G. Scarcelli, *Lab Chip*, 2017, **17**, 663–670.
30 J. Guck, S. Schinkinger, B. Lincoln, F. Wottawah, S. Ebert, M. Romeyke, D. Lenz, H. M. Erickson, R. Ananthakrishnan, D. Mitchell, J. Käs, S. Ulvick and C. Bilby, *Biophys. J.*, 2005, **88**, 3689–98.

31 A. C. Rowat, D. E. Jaalouk, M. Zwerger, W. L. Ung, I. a Eydelnant, D. E. Olins, A. L. Olins, H. Herrmann, D. a Weitz and J. Lammerding, *J. Biol. Chem.*, 2013, **288**, 8610–8.

32 K. D. Nyberg, M. B. Scott, S. L. Bruce, A. B. Gopinath, D. Bikos, T. G. Mason, J. W. Kim, H. S. Choi and A. C. Rowat, *Lab Chip*, 2016, **16**, 3330–3339.

33 Z. S. Khan, J. M. Santos and F. Hussain, *Biomicrofluidics*, 2018, **12**, 014102.

34 K. D. Nyberg, K. H. Hu, S. H. Kleinman, D. B. Khismatullin and M. J. Butte, *Biophysj*, 2017, **113**, 1574–1584.

35 L. M. Lee and A. P. Liu, *Lab Chip*, 2015, **15**, 264–73.

36 J. S. Dudani, D. R. Gossett, H. T. Tse and D. Di Carlo, *Lab Chip*, 2013, **13**, 3728–3734.

37 J. Lammerding, K. N. Dahl, D. E. Discher and R. D. Kamm, *Methods Cell Biol.*, 2007, **83**, 269–294.

38 T. Sullivan, D. Escalante-Alcalde, H. Bhatt, M. Anver, N. Bhat, K. Nagashima, C. L. Stewart and B. Burke, *J. Cell Biol.*, 1999, **147**, 913–20.

39 N. C. Shaner, G. G. Lambert, A. Chammas, Y. Ni, P. J. Cranfill, M. A. Baird, B. R. Sell, J. R. Allen, R. N. Day, M. Israelsson, M. W. Davidson and J. Wang, , DOI:10.1038/nmeth.2413.

40 P. M. Davidson, J. Sliz, P. Isermann, C. M. Denais and J. Lammerding, *Integr. Biol.*, 2015, **7**, 1534–1546.

41 C. M. Denais, R. M. Gilbert, P. Isermann, A. L. McGregor, M. te Lindert, B. Weigelin, P. M. Davidson, P. Friedl, K. Wolf and J. Lammerding, *Science (80-.).*, 2016, **352**, 353–358.

42 R. Roncarati, C. Viviani Anselmi, P. Krawitz, G. Lattanzi, Y. von Kodolitsch, A. Perrot, E. di Pasquale, L. Papa, P. Portararo, M. Columbaro, A. Forni, G. Faggian, G. Condorelli and P. N. Robinson, *Eur. J. Hum. Genet.*, 2013, 1–7.

43 S. P. Desai, D. M. Freeman and J. Voldman, *Lab Chip*, 2009, **9**, 1631.

44 M. Heinen, F. Zanini, F. Roosen-Runge, D. Fedunová, F. Zhang, M. Hennig, T. Seydel, R. Schweins, M. Sztucki, M. Antalík, F. Schreiber and G. Nägele, *Soft Matter*, 2012, **8**, 1404–1419.

45 a C. Rowat, J. Lammerding and J. H. Ipsen, *Biophys. J.*, 2006, **91**, 4649–64.

46 P. Preira, M. P. Valignat, J. Bico and O. Théodoly, *Biomicrofluidics*, 2013, **7**, 1–17.

47 J. Lammerding, L. G. Fong, J. Y. Ji, K. Reue, C. L. Stewart, S. G. Young and R. T. Lee, *J. Biol. Chem.*, 2006, **281**, 25768–25780.

48 J. D. Pajerowski, K. N. Dahl, F. L. Zhong, P. J. Sammak and D. E. Discher, *Proc. Natl. Acad. Sci.*, 2007, **104**, 15619.

49 F. Guilak, J. R. Tedrow and R. Burgkart, *Biochem. Biophys. Res. Commun.*, 2000, **269**, 781–6.

50 Y. N. Luo, D. Y. Chen, Y. Zhao, C. Wei, X. T. Zhao, W. T. Yue, R. Long, J. B. Wang and J. Chen, *Sensors Actuators, B Chem.*, 2014, **202**, 1183–1189.

51 A. J. Earle, T. J. Kirby, G. R. Fedorchak, P. Isermann, J. Patel, S. Iruvanti, G. Bonne, L. L. Wallrath and J. Lammerding, *bioRxiv*, 2018, 364778.

52 K. J. Chalut, M. Höpfler, F. Lautenschläger, L. Boyde, C. J. Chan, A. Ekpenyong, A. Martinez-Arias and J. Guck, *Biophys. J.*, 2012, **103**, 2060–70.

53 A. Fuhrmann, A. Banisadr, P. Beri, T. D. Tlsty and A. J. Engler, 2017, 736–745.

54 A. H. Mekhdjian, F. Kai, M. G. Rubashkin, L. S. Prahl, C. C. Dufort, G. Ou, A. C. Chang, L. Cassereau, S. J. Tan, M. W. Pickup, J. N. Lakins, X. Ye, M. W. Davidson and J. Lammerding, *Mol Biol Cell*, 2017, **28**, 1467–1488.

55 M. Raab, M. Raab, M. Gentili, H. De Belly, H. R. Thiam, P. Vargas, A. J. Jimenez, F. Lautenschlaeger, N. Manel and M. Piel, *Science (80-.).*, 2016, **352**, 359–62.

Supplemental Information

Derivations

We derived the elastic modulus and the viscosities of the viscoelastic model as laid out in previous work,[56] with adaptations for a rectangular channel and our chosen model. The Jeffreys model consists of three elements: a dashpot in series with a Kelvin-Voigt element, i.e., a spring and a dashpot in parallel. For this model, the creep is described by the following equation:

$$L(t) = \frac{f}{k}\left(1 - e^{-t/\tau}\right) + \frac{f}{\mu}t$$

Where *f* is the force, *k* is the spring constant, τ is the relaxation time ($\tau = \frac{k}{\mu}$) and μ is the viscosity of the dashpot in series. At short time scales, the first term dominates, resulting in a rapidly rising curve, while at long time scales, the second term dominates, leading to a linear regime.

The aspiration force is given by:

$$f = \pi R_p^2 \Delta P$$

Where R_p is the radius of the micropipette and ΔP is the applied pressure.

At short time scales, the force is balanced by the elastic deformation and is given by the following equation:

$$\frac{f}{A} = CE\frac{\delta}{R_p}$$

Where *A* is the cross-sectional area of the pipette, *C* is approximately equivalent to 1,[56] *E* is the elastic modulus and δ is the elastic deformation at short times. We thus obtain $f = \pi R_p E \delta$.

The definition of the spring constant (*k*) is the relationship between the force and the extension: $f = k \times \delta$, and thus $\frac{f}{\delta} = k = \pi R_p E$.

At long time scales, the force is balanced by viscous flow. The dissipative force due to the plug at the entrance of the capillary is given by the following equation:

$$f = 3\pi^2 \eta R_p \frac{dL}{dt}$$

Where μ is the viscosity and R_p is the radius of the pipette. At long time scales, the second term of equation 1 dominates and we obtain: $\frac{dL}{dt} = \frac{f}{\mu}$, thus $\mu = \frac{f}{dL/dt} = 3\pi^2 \eta R_p$

Inserting these expressions into equation 1, we obtain the following:

$$L(t) = \frac{f}{k}\left(1 - e^{-t/\tau}\right) + \frac{f}{\mu}t = \frac{\pi R_p^2 \Delta P}{\pi R_p E}\left(1 - e^{-\frac{E}{3\pi\eta}t}\right) + \frac{\pi R_p^2 \Delta P}{3\pi^2 \eta R_p}t = \frac{R_p \Delta P}{E}\left(1 - e^{-\frac{E}{3\pi\eta}t}\right) + \frac{R_p \Delta P}{3\pi\eta}t$$

Here we replace the radius of the pipette by the effective radius for a rectangular channel, given by $R_{eff} = \sqrt{\frac{HW}{\pi}}$, Where H is the height and W is the width of the channel.[57]

We thus obtain:

$$L(t) = \sqrt{\frac{HW}{\pi}}\frac{\Delta P}{E}\left(1 - e^{-\frac{E}{3\pi\eta}t}\right) + \sqrt{\frac{HW}{\pi}}\frac{\Delta P}{3\pi\eta}t$$

By fitting the data, we can obtain values for the elastic modulus and the viscosities.

Supplementary Figures

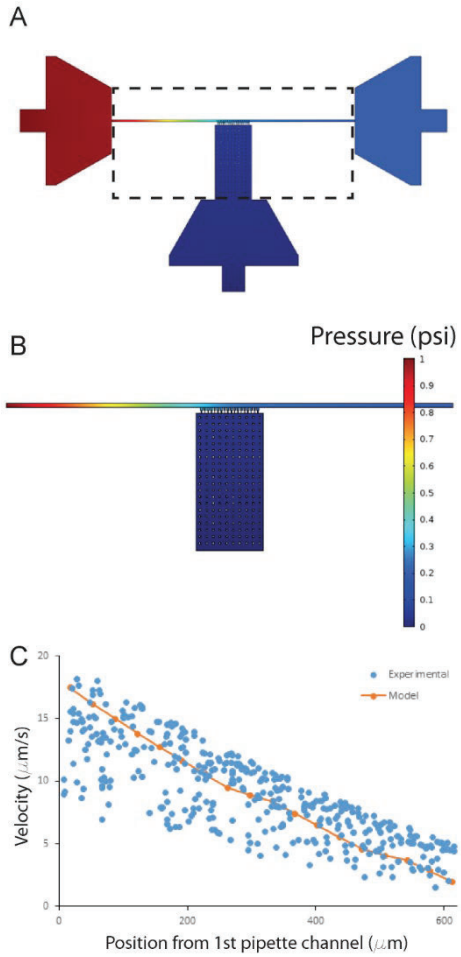

Supplementary Figure 1: Simulation on micropipette channels in "open" configuration. (**A**) Overview of the simulated pressure distribution in the entire microfluidic device. (**B**) Close-up of the area containing the micropipette channels (area surrounded by dashed line in panel A) showing a rapid decrease of the pressure upstream of the micropipette channels. (**C**) Comparison of the velocity obtained from the simulation (orange line) and measured velocities obtained from the streak length of fluorescent beads in the microfluidic device (blue points).

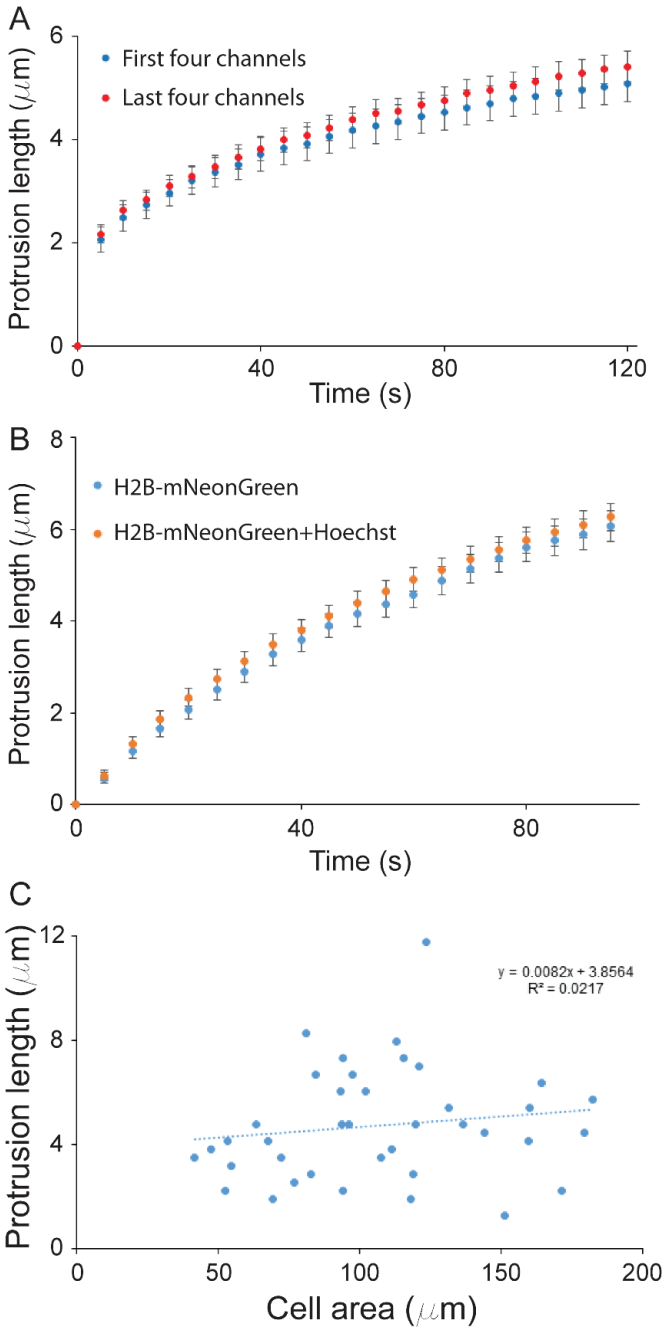

Supplementary Figure 2. Effect of microchannel position, Hoechst labeling, and cell size on nuclear deformation measurements. (A) The deformation rate as a function of microchannel position. We compared the deformation rate or MDA-MB-231 cells in the first four and last four micropipette channels. Similar to the results shown in Figure 3C, the position of the cells does not have a significant influence on the deformation rate of the cells. **(B)** Effect of a DNA intercalating agent on the deformability measurements. The deformability of cells was not significantly different when Hoechst 33342 was added at the concentrations we use in our experiments. (**C**) Effect of nuclear size on deformability of the nucleus. We compared the cross-sectional area and the protrusion length at 60 s in individual cells. Using a regression analysis, we determined that the slope of the linear regression (0.008) was smaller than the 95% confidence interval (0.018) associated with it, indicating that the slope is not significantly different from 0.

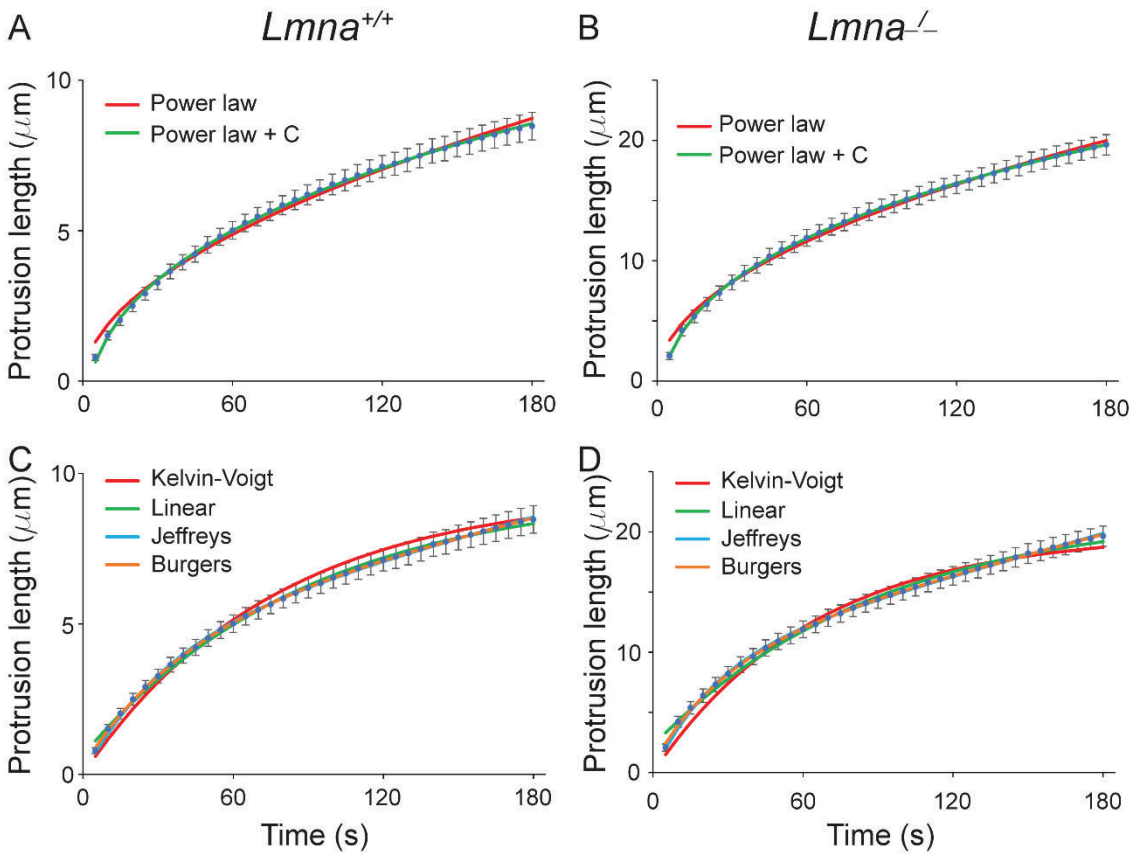

Supplementary Figure 3. Comparison of the models used to fit the data. (**A, B**) The data was fit with a simple power law ($y=At^{\alpha}$) and a power law with an additional constant ($y=At^{\alpha}+C$) to account for error in the first time point. The simpler model does not follow the data well at small time points due to the uncertainty in time zero, resulting in a flattening of the curve and thus a large change in the exponent value. The second model is a better fit at short time points. (**C, D**) The four viscoelastic (spring and dashpot) models. The Kelvin-Voigt and Standard Linear Solid models include a spring in parallel and thus do not result in a viscous linear increase with time. We thus didn't chose these models as our data increases linearly at long time points (indicative of a dashpot in series). The Jeffreys model is made up of a dashpot in series with a Kelvin-Voigt element and thus is the simplest element to accurately describe our data. Accordingly, the R^2 values are smaller for the Jeffreys model than the first two models. (See Suppl. Table 1.) The Burgers model includes an additional element, and consequently exhibits a better fit, but is only a minimal improvement.

Supplementary Tables

Model	*# of Variables*	*Lmna*$^{+/+}$		*Lmna*$^{-/-}$	
		R^2	Residuals	R^2	Residuals
Power law	2	0.99345	1.1	0.99520	3.7
Power law with C	3	0.99941	0.11	0.99989	0.13
Kelvin-Voigt	2	0.99401	2.4	0.98903	13
Linear	3	0.99800	0.32	0.99639	3.9
Jeffreys	3	0.99963	0.082	0.99921	0.68
Burgers	4	0.99980	0.031	0.99941	0.37

Supplementary Table 1: Values of the Coefficient of Determination (R^2) and residuals calculated for each condition